

The Effects of Skin Moisturizers using Electrical Impedance Spectroscopy

Son Nguyen Thanh, BEng.

Department of Electrical and Electronic Engineering

Thesis submitted to the University of Nottingham

for the degree of Doctor of Philosophy

December, 2015

Abstract

Skin Electrical Impedance Spectroscopy (EIS) is a method that involves the injection of an AC current into human tissue and measurement of the resulting voltage drop. By measuring the tissue over a range of frequencies, the impedance spectrum can then be used to detect changes in the underlying nature of the skin tissue. One potential application is in monitoring the effects of over the counter products such as skin moisturisers on human skin. This can be useful for cosmetics companies in new product development where users of the cosmetic product could use such a device in their own home.

A low cost, portable, custom-made bio-impedance analyser based on a four-point probe sensor has been constructed for measuring the skin impedance over short and long time periods. Long term measurements are motivated by manufacturer claims that the effects of moisturisers last up to 24 hours and hence a custom made device has been developed to carry out long term monitoring. The system is based around a dsPIC33F board that contains a DSP processor, Analogue Frontend and analogue stimulus all connected to a 4-point probe sensor. 100µA AC current (according to Medical Standard 60601-1) is passed to the skin through two outer probes and a voltage drop measured across the two inner probes. A DSP controls the analogue frontend, processes the measured data and transfers data to a PC for real time display. The portable custom-made device is validated against a Solartron 1260 + 1294 impedance analyser and achieved a within 5% error.

Four different commercial skin creams: Bio-oil, Nivea, Palmer's Olive Butter and Cocoa Butter have been investigated. Under controlled environmental conditions, four kinds of cream were applied to an allocated area of the arm for 1 minute. The

EIS was then measured for up to 5 hours on these regions by the four point probe sensors captured by the custom-made device.

Nivea, Cocoa Butter and Olive Butter have a similar response as they are type II humectants which attract water from deeper dermis to the stratum corneum. Bio oil however, can be classified as a type I occlusives as it blocked water vaporized from stratum corneum. The Impedance results can discriminate between Bio-oil/ Bare skin (Type I) and the other three Type II moisturizers (Nivea, Olive and Cocoa). This discrimination is appointed in two clear features: firstly, the impedance values from the type II creams have a much reduced variability when compared to the bare skin and Bio-oil; secondly, the plots of R versus X showed for the Type II creams to have a non “constant phase element” dominance whilst bare skin and Bio-oil showed no such behavior. Phase results demonstrated additional capacitance effects of Bio oil compared to other moisturizers. Simulation models are provided to compare with these practical results with the model fitting process.

Acknowledgement

Firstly, I would like to sincerely thank my supervisors Prof. Barrie Hayes-Gill and Prof. Steve Morgan for their continued support and guidance along the course of this work.

I would like to thank my labmates Matthew Butler for his support on the work of designing the analogue frontend PCB board, James Carpenter for his help on signal processing algorithms and all other labmates for their efforts to provide me the best conditions for completing this research.

I would like to acknowledge and thank all staff members and technicians in the Faculty of Engineering, especially in the Department of Electrical and Electronic Engineering, who helped me with ethics, administration, technical expertise and experimental setup.

I also want to thank all my friends and volunteers who helped me to conduct the experiments during my studies.

This work has been financially supported by the Faculty of Engineering, University of Nottingham.

Finally, I would especially like to thank my family for the endless support and encouragement. Thanks to my wife, Ms. Khoa Pham, and other friends for their support that has made this work possible.

Contents

Abstract ii

Acknowledgement iv

Contents v

List of Abbreviations x

Chapter 1 Introduction 1

1.1 Introduction 2

1.2 Introduction to Electrical Bio-Impedance 2

1.2.1 Background 2

1.2.2 Electrical Bio-Impedance 3

1.2.3 Tissue Impedance 4

1.3 Overview of Electrical Impedance Spectroscopy 7

1.3.1 Electrical Impedance Spectroscopy 7

1.3.2 Frequency dependence on skin tissue 8

1.3.3 Model of skin impedance 11

1.4 Motivations of the project 12

1.5 Novelty and Contribution of this project 13

1.6 Project Objectives 15

1.7 Outline of the Thesis 16

Chapter 2 Overview of Electrical Impedance Spectroscopy 17

2.1 Introduction 18

2.2 A brief introduction to bioimpedance measurement system theory and implementation 18

2.3 Comparison between bipolar and tetra-polar technique 20

2.3.1 Kelvin Probe or Two point probes 20

2.3.2 Four point probe or Tetra-polar probes 22

2.3.3 Comparisons, advantages and disadvantages of these techniques 23

2.3.4 Tetra-polar probes implementation and design 24

2.4 Drive circuit design 26

2.4.1 Voltage controlled current source 26

2.4.2 Source of errors in drive circuits 35

2.4.3 Improvement in drive circuits 37

2. 5 Sense circuit design 39

2.5.1 Instrumentation amplifier 42

2.5.2 Sources of error in sense circuits 51
2.5.3 Improving the performance of the voltage sense circuits 53
2.5.4 Noise and minimum detectable signal 60
2.6 Review of EIS measurement systems 66
2.7 Review of bio-electrical models 70
2.7.1 Basic models 74
2.7.2 RC networks including 2 resistors and one capacitor 77
2.7.3 Constant phase element (CPE) 80
2.7.4 Cole equation 85
2.7.5 Finite elements methods 88
2.8 Experimental Studies 89
2.8.1 Cervical cancer detection by Brown et al 91
2.8.2 Friction and Electrical Impedance in measuring the effects of lotions 94
2.8.3 Skin assessment and moisturization by Martinsen 97
2.8.4 Skin admittance for dry electrodes and skin moisturisation by Yamamoto . 100
2.8.5 Skin moisturizers assessment by Lodén 103
2.9 Conclusion 105
Chapter 3 System Overview: Implementation, Design and Validation 107
3.1 Introduction 108
3.2 System design: DSP Unit, Analogue Frontend and Sensor 108
3.2.1 High level schematic of Bio-impedance Measurement System 110
3.2.2 Schematic Design 112
3.2.3 Layout Design 124
3.3 Finite Element Method Modelling for bioimpedance electrodes 127
3.3.1 Creation of a forward model 128
3.3.2 Adding the stimulating pattern 130
3.3.3 Estimating penetration depth 131
3.3.4 Penetration depth calculations 132
3.3.5 Electrode optimisation 135
3.3.6 Conclusion 137
3.4 Digital signal processing: Digital Filter, Lockin Amplifier and Discrete Fourier Transform 137
3.4.1 Digital Filter 138
3.4.2 Lock-in Amplifier 141

3.4.3 Discrete Fourier Transform 145
3.5 Impedance measurement at multiple frequencies 147
3.6 Characterization with DUT (Device under test) 149
3.6.1 Calibration resistor and capacitor network 151
3.6.2 Calibration with solution 151
3.7 Results from resistors and capacitors networks 153
3.8 Results in calibration solution 157
3.9 Validation of data measurement using the Solartron impedance analyser 160
3.9.1 Validation with resistors network 164
3.9.2 Validation with resistor and capacitor network 169
3.9.3 Validation with calibration solution 174
3.9.4 Validation with human skin impedance 179
3.9.5 Valid Impedance and Phase Range Measurement 180
3.10 Conclusion 185
Chapter 4 Skin Measurements 187
4.1 Introduction 188
4.2 Methodology 188
4.2.1 Materials 188
4.2.2 Experiment Protocol 189
4.3 Instantaneous measurement results 194
4.3.1 Bare skin impedance: 194
4.3.2 Skin impedance effects of Cocoa Butter Cream: 199
4.3.3 Skin impedance effects of Olive Butter Cream: 203
4.3.4 Skin impedance effects of Nivea Cream: 207
4.3.5 Skin impedance effects of Bio-oil: 211
4.3.6 Comparison of skin creams' effect: 215
4.4 Short term measurement 219
4.4.1 Short term bare skin impedance versus skin temperature: 219
4.4.2 Short term skin impedance using moisturizers: 220
4.4.3 Short term skin impedance with continuous contact of electrodes: 223
4.5 Long term measurement 223
4.5.1 Long term bare skin impedance 224
4.5.2 Long term skin impedance using Nivea 224
4.5.3 Long term skin impedance using Cocoa: 226

4.5.4 Long term skin impedance using Bio-oil: 227
4.5.5 Summary of long term monitoring 230
4.6 Discussion 232
4.7 Conclusions 235
Chapter 5 Data Analysis and Modelling 237
5.1 Introduction 238
5.2 Skin impedance model 238
5.2.1 Biological Skin Layers 238
5.2.2 Overview of several skin models 240
5.2.3 Proposed skin models 245
5.3 Simulation models and comparison method 248
5.4 Comparison between models and skin measurement results 250
5.4.1 Two component model compared with measured result 250
5.4.2 Three component model compared with measured results 252
5.4.3 Cole model vs measured data 255
5.4.4 Modified Cole model vs measured data 258
5.4.5 CPE model vs measured data: 261
5.5 Discussion about the simulation model and practical results 265
5.6 Limitation of the simulation results with results data. 268
5.6.1 Limitation in practical measurement results 268
5.6.2 Limitation in experimental setup experiment 270
5.6.3 Limitation in Z plane fitting process 270
5.7 Conclusion 271
Chapter 6 Discussion and Conclusions 272
6.1 Introduction 273
6.2 Sensors design 274
6.3 Analogue frontend design 275
6.4 Software for real time measurement 276
6.5 Application Protocol 276
6.6 Summary of in-vivo measurement results 277
6.7 Modelling 278
6.8 Suggestions for future work 279
6.9 Summary of Findings 283
References 286

Appendix A: Exploratory research on skin impedance.....300
Appendix B: Case Report Form.....303
Appendix C: Participant Information Sheet.....304
Appendix D: Consent Form.....306
Appendix E: Safety regulations.....307
Appendix F: Long term skin impedance using moisturizers on five volunteers.....311
Appendix G: Details of skin moisturizers using in the experiments.....321
Appendix H: Group of volunteers for different experiments..... 323
Appendix I: Short term measurement with continuous contact of electrodes on skin using different moisturizers.....325

List of Abbreviations

AC	-	Alternating current
ADC	-	Analogue to Digital Converter
BIS	-	Bioelectrical Impedance Spectroscopy
CPE	-	Constant Phase Element
CPA	-	Constant Phase Angle
CMRR	-	Common mode rejection ratio
CMOS	-	Complementary Metal Oxide Semiconductor
CIN	-	Cervical Intraepithelial Neoplasia
DC	-	Direct current
DAC	-	Digital to Analogue Converter
DUT	-	Device under test
DSP	-	Digital Signal Processor
DFT	-	Discrete Fourier Transform
EIS	-	Electrical Impedance Spectroscopy
EIT	-	Electrical Impedance Tomography
ECG	-	Electrocardiography
FET	-	Field Effect Transistor
FEM	-	Finite Element Method
JFET	-	Junction Field Effect Transistor
IPG	-	Impedance Plethysmography
PCB	-	Printed Circuit Board
PPG	-	Photoplethysmography
SPI	-	Serial Peripheral Interface
SNR	-	Signal to Noise ratio
SPF	-	Sun Protection Factor

TEWL	-	Transepidermal water loss
THD	-	Total Harmonic Distortion
VCCS	-	Voltage Controlled Current Source

Chapter 1 Introduction

1.1 Introduction

This chapter introduces the subject of electrical bio-impedance and provides an overview of electrical impedance spectroscopy. In addition, this chapter also provides the motivation, novelty and contribution of this work, its background of design methods and outlines the structure of this thesis.

1.2 Introduction to Electrical Bio-Impedance

1.2.1 Background

Bio-impedance, bio-electricity and the electrical properties of biological tissue are similar concepts. Bio-impedance is concerned with the passive electrical properties of biological tissue e.g. the characteristics of the tissue when electric current is passed through it. Bioelectricity deals with the properties of a body that generates electricity, for example Electrocardiography (ECG). The electrical properties of biological tissue may be considered as a mixture of volume conductor and dielectric. At low frequency (e.g. 20 Hz), the dielectric properties of tissue are dominant, however at higher frequency, the tissue characteristic becomes closer to that of the internal water of the tissue. It has been shown that the electrical properties of tissue are dominated by current flow in the extracellular water at low frequency and in both extracellular and intracellular water of the tissue at high frequency [1].

Impedance is the ratio between voltage and current. It is applied to both direct current (DC) and alternating current (AC). However, because the direct current (DC) can cause the electrochemical reactions on biological tissue, it is not recommended to use DC on biological tissues. Bio-impedance is about biomaterials such as those which contain living tissues, e.g. plants, fruit, fish, animals and the human body. The

basic building block is the living cell, which is surrounded by electrolyte solution. Because of this electrolyte solution, the living tissue contains ions, which support ionic conduction. Therefore, a specific conductive part in biological tissue called conductance is created. In addition, the cell membranes also cause capacitive coupling (permittivity) in tissue. In general, cell tissue contains conductivity and permittivity.

1.2.2 Electrical Bio-Impedance

Bioelectrical impedance spectroscopy (BIS) is used to measure the properties of biological tissue (resistive and capacitive characteristics) of animals including the human body. The mechanism of BIS is that living cells must be contained or surrounded by aqueous electrolytes, such as in blood, which contains the most important cations such as H^+, Na^+, K^+, Ca^{++} , and Mg^{++} and anions such as Cl^-, HCO_3^-, protein$^-$, HPO_4^{--}, SO_4^{--}. Protein in the blood is considered as a negative (macro)-ion. These electrolytes mean that the whole human body can conduct [1]. The BIS measurement can be made using either two point probes or four point probes configuration. In the two point probe technique, the current injected and voltage drop measured use the same two terminals. This thesis however, uses four electrodes (or probes): the two outer electrodes connect to a current source that passes a small current through the body whilst the two inner electrodes measure the resulting voltage drop across the body. For measuring the impedance, the human body needs to be assumed to be a conductor, which contains a resistance component (R) in series with a reactance component (X). The total impedance can be measured by $Z = \sqrt{R^2 + X^2}$ and $\tan(\sigma) = X/R$.

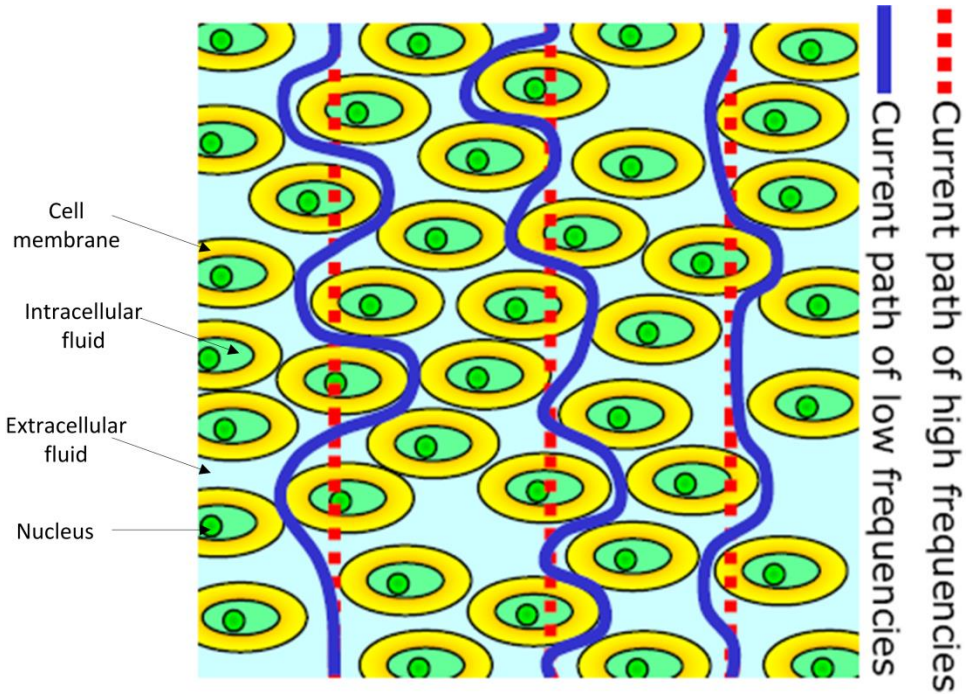


Figure 1.1: The characteristic of low and high frequency currents passing through the biological tissues [2].

In Figure 1.1, the structure of the biological tissue is shown including the cell nucleus, intracellular fluid, cell membrane and extracellular electrolyte. The membrane around living cells has electrochemical properties because it contains ions and allows certain ions to travel through the membrane. Moreover, the intra- and extracellular spaces consist mainly of electrolytes and have primarily resistive properties. Thus, biological tissues have both capacitive and resistive properties, and the impedance of biological tissues is highly frequency dependent. Generally, the low frequencies are affected by the extracellular space (i.e. electrolyte) and high frequencies are affected by the properties of the intracellular space (the cells).

1.2.3 Tissue Impedance

McAdams and Jossinet [3] provided a useful overview of the historical development of tissue impedance and this is briefly summarized below.

Following the appearance of Ohm's law in 1827, various trials were performed to measure the electrical properties of living tissues. However, because of the frequency dependent characteristics of biological tissue, the task is not straightforward. From 1848 to 1860, early work from Bois Reymond and others showed that the 'resistance' of animal tissue decreased with the increase of frequency, which demonstrated the effect of the capacitive behavior in tissue. In 1896, Oliver Heaviside introduced the concept of electrical impedance, which was established to investigate the electrical impedance of biological tissue i.e. impedance plethysmography, and body composition techniques. In 1902, Bernstein proposed that biological tissue consisted of the conductive cell surrounded by insulating membranes. Later, in 1910, after conducting experiments in which the cell membranes had been destroyed, Hober found that the resistivity of tissue was frequency independent. Therefore, Hober concluded that the internal cell resistivity was measured at the high frequency whilst the high resistance measured at low frequency was due to intact cells, which included the membranes that enclosed the cells.

In 1921, Phillipson described tissue impedance in terms of a resistor-capacitor model. Later, Fricke and Morse [4] refined this into an equivalent circuit model to represent the electrical properties of cell suspensions as shown in Figure 1.2.

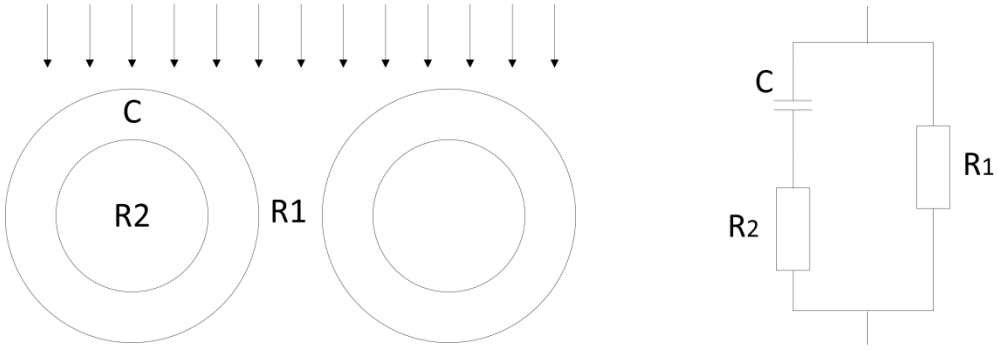


Figure 1.2: The electrical model of cell suspension by Fricke and Morse [4].

In 1941, Cole and Cole [5] proposed a empirical expression to represent the electrical properties of the tissue and membranes. The Coles' 1941 formula [5] described an important step change in the history of the tissue impedance:

$$Z = R_\infty + \frac{\Delta R}{1+(j\omega\tau_Z)^\alpha}\ [\Omega] \quad \text{where } \Delta R = R_0 - R_\infty \tag{1.2.1}$$

where R_0 is the impedance value at low frequency, R_∞ is the impedance value at high frequency, τ_z is equal to $1/\omega_c$, where ω_c is the characteristic frequency defined at the apex of the impedance circular arc. α is a dimensionless numerical constant with a value between 0 and 1. For example, $\alpha = 1$ will form a semicircular arc whose center lies on the real axis. If $\alpha < 1$, this will form of a semicircular arc whose center lies below the real axis. The typical value of α is ~0.5. The Cole model will be discussed in more detail in Chapter 2.

Equation 1.2.1 can also be written in terms of complex impedance, which mathematically describes the frequency properties of Fricke and Morse's electrical circuit, with the capacitor replaced by a "Constant Phase Angle" (CPA) or Constant Phase Element (CPE), which has frequency dependent components such as C(f) and R(f) where resistor and capacitor values change with frequency. Specifically, the frequency dependent components can be modelled so that the phase of the immittance is independent of frequency [1]. Biological tissue is therefore often represented by the Cole equation [5]. For example, the complex impedance |Z| of tissue can be expressed as a function of frequency in order to characterise the tissue.

Electrical Impedance Spectroscopy (EIS) can involve measuring the electrical impedance Z and the phase θ, which can be transferred into constant phase elements such as R_{cpa} and C_{cpa}. Some equivalent circuits are used to describe the components

of the particular tissue impedance. However, the representation of specific tissue is not always easy as it requires the complex combination of R_{cpa} and C_{cpa}, which are represented by the conductive and insulating parts of the cell. In Chapter 2 and Chapter 5, some specific circuit models, such as an RC (resistor and capacitor) circuit, will be described and simulated in order to compare them with the measurement results.

1.3 Overview of Electrical Impedance Spectroscopy

1.3.1 Electrical Impedance Spectroscopy

EIS or BIS has the potential to be used in many applications such as hydration monitoring for human skin, cancer detection or glucose monitoring.

There are many methods to measure the hydration of the human body: nutrition and metabolism, urine and plasma osmolality, saliva flow rate, and bioelectrical impedance spectroscopy [6]. Bioelectrical Impedance Spectroscopy (BIS), using the basic theory that human body contains water ions which can conduct electricity, has the potential to be an indicator of the hydration status of the human body but it is necessary to decouple it from other effects such as blood flow and the change of body temperature.

One of the better established applications of EIS is the ability to diagnose cervical intraepithelial neoplasia (pre-cancerous stage in cervix) in the human uterine cervix developed by Brown et al [7]. In addition, EIS could potentially become a non-invasive method for monitoring glucose levels in patients with diabetes [8][9].

Electrical Impedance Tomography (EIT) is a related impedance technique, which can be implemented in a similar way to EIS. This method also drives alternating current

into the body and measures the voltage drop between arrays of electrodes. The impedance spectrum given by EIT represents impedance image of the object at one particular frequency that helps to track the changes in the underlying nature of tissue. Multi-frequency EIT is also called EIS as the system uses multiple frequencies to better differentiate between normal or abnormal tissue because in general higher frequency current will go deeper into the tissue. EIT is one promising method by which breast tumours could be diagnosed using impedance spectroscopy based on 3D reconstruction images [10][11][12][13].

This thesis focuses on the investigation of moisturizer's effects on the skin using EIS. More specifically, the four point probe technique is applied to measure the impedance of the skin. From the impedance results of the four point probe, the effect of moisturizers on human skin can be evaluated and analyzed.

1.3.2 Frequency dependence on skin tissue

Assuming that an electrical current passes through a homogeneous tissue of area A, thickness x with the conductivity (σ) and relative permittivity (ε_r), the electrical properties of the tissue can be represented by a model containing a resistance in parallel with a capacitance as shown in Figure 1.3:

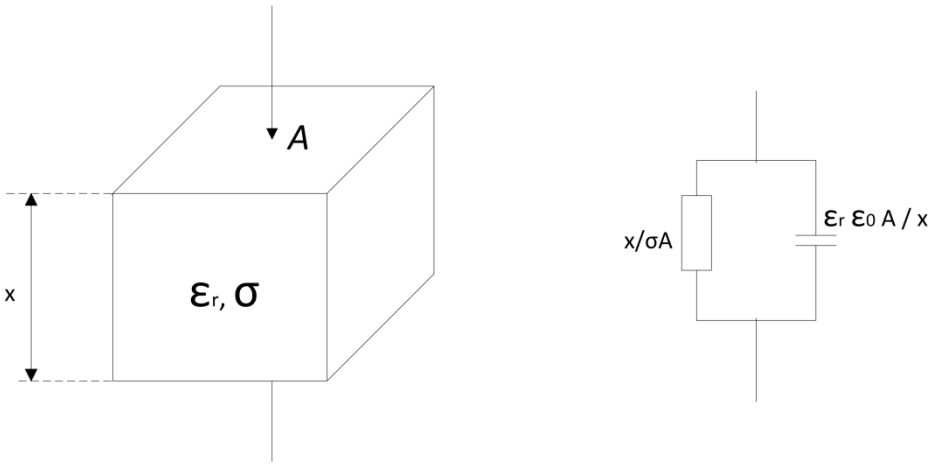


Figure 1.3 : The electrical properties of the tissue can be represented by a model containing a resistance in parallel with a capacitance [14]

Therefore, the formula of resistance and capacitance can be given by:

$$R = \frac{x}{\sigma * A} \qquad C = \frac{\varepsilon_r * \varepsilon_0 * A}{x} \tag{1.3.1}$$

In which A is the area, x is the thickness, σ is the conductivity, ε_r is the relative permittivity and ε_0 is the permittivity of free space (8.85 x 10^{-12} F/m).

However, both the conductivity σ and permittivity ε_r are found to be a function of frequency and this is known as 'dispersion'. Dispersion occurs from low frequencies through to extremely high frequencies and for biological tissue can be divided into three regions: α (alpha), β (beta) and γ (gamma) as shown in Figure 1.4.

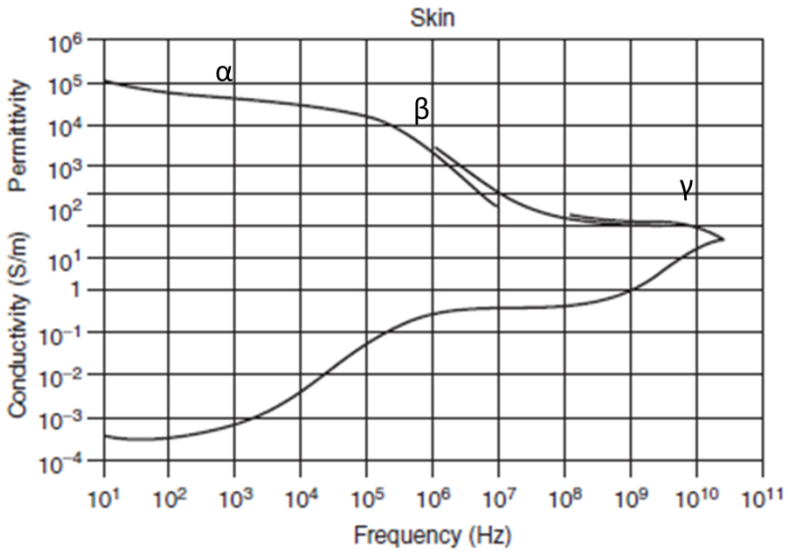


Figure 1.4: The frequency variation of the relative permittivity ε_r and conductivity σ with frequency for a typical skin tissue [15][16].

There are three different regions of dispersion:

- α dispersion (10Hz - few KHz): Associated with polarization of tissue interfaces. (It should not be confused with the alpha α in the Cole model)

- β dispersion (100 KHz – few MHz) Associated with cell membrane from capacitive charging effect.
- γ dispersion (greater than 10GHz): Associated with the dielectric relaxation of free water.

The stratum corneum, also called the horny layer, contains fully keratinized, dead cells (corneocytes). The purpose of the stratum corneum is to form a barrier to protect underlying tissue from infection, dehydration, chemical and mechanical stress. Figure 1.5 represents the average resistivities and relative permittivities in stratum corneum and viable skin measured in experiments by Yamamoto and Yamamoto [17]. Because the measurement is usually made on the skin, the frequency used to monitor the state of stratum corneum is from a few Hz to a few KHz.

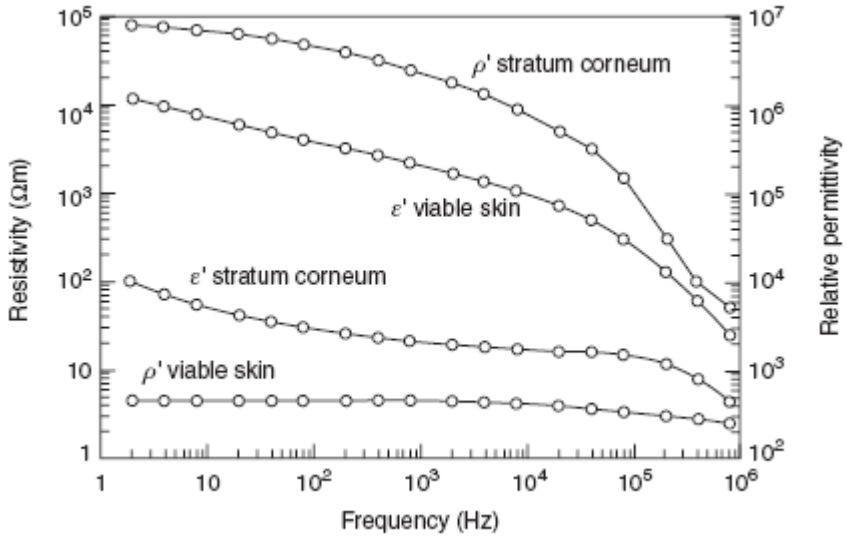


Figure 1.5: Average resistivities and relative permittivities in stratum corneum and viable skin [17].

Clearly, from Figure 1.5, the resistivity of the stratum corneum is much higher than the resistivity of deeper tissue. At low frequency (1 Hz), the ratio can be up to 10^5 times between stratum corneum and viable skin. On the other hand, the permittivity

of stratum corneum is much lower than that of viable skin. Therefore, generally, the skin impedance measured at low frequency is dominated by stratum corneum and it is known that increased frequency will enable measurements to be made deeper into the skin layers.

1.3.3 Model of skin impedance

An alternative model of skin impedance is to use two resistors and a capacitor. The resistor R_s is in series with the network of the resistor $R_{p\ in}$ parallel to capacitor C (Figure 1.6).

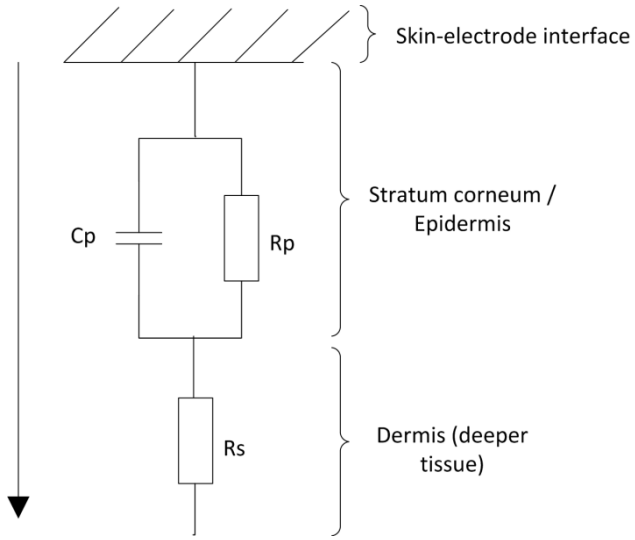


Figure 1.6 : Electrical model of human skin

The skin impedance is given by:

$$Z = Z_s + Z_p \text{ in which } Z_s = R_s \text{ and } Z_p = R_p / (1 + j\omega C_p R_p). \qquad (1.3.2)$$

From Equation 1.3.2 and the model of skin impedance, the easy thing to recognize here is that at the low frequency, the flow of current will mainly be through the resistors R_s and R_p. This means that the current flows mainly on the stratum corneum layer of the skin at low frequency. In contrast, at higher frequencies, the capacitor C_p become dominant, and the current will mainly go through R_s and capacitor C_p, which means deeper layers (dermis) inside the skin.

There are several ways to apply EIS to biological tissues. In this project, two methods are considered: two point probes (bipolar technique) and four point probes (tetra-polar technique). This will be discussed in more detail in Chapter 2.

1.4 Motivations of the project

There are two motivations for this project. Firstly, it is becoming more important to establish how moisturizers affect human skin impedance and EIS is a promising approach for doing this. Secondly, it is important to monitor the effects over long periods of time and a portable monitor would be highly beneficial for making practical long term measurements. Long term measurements are motivated by manufacturer claims that the effects of moisturizers last up to 24 hours and so a portable, low cost device has been developed to carry out long term monitoring and to help to investigate this claim.

Water is essential to skin function and the degree of hydration is closely linked to the vital plasticity and barrier function of the skin [18][19]. For this and other reasons, a great majority of people apply moisturizers to their skin on a daily basis. As a result, 'skin moisturizers', are nevertheless frequently promoted in the cosmetic market. The moisturizing effect of most of these products is unpublished, and according to Martinsen [20], this is due to the lack of appropriate measuring instrumentation.

For companies developing new cosmetic products it is important to be able to reliably characterize the properties of the skin in order to measure the effects of new products. Usually such monitoring is carried out in test laboratories using volunteers (Test laboratories equipment using volunteers https://www.bootsvolunteers.com/). This enables the availability of such as instrument for regulatory bodies to become involved and allows the authorities to validate the products' claims. Developing a

low cost method of monitoring the skin in a volunteer's home would allow more frequent measurements to be made and provide more efficient evaluation of products in a desired setting. It could (although not the subject of the work presented in this thesis) also allow home monitoring of the effects of skin disorders such as psoriasis or eczema and the performance of medication on these conditions as patients can be monitored without frequent visits to the hospital or GP surgery.

There are several other applications of the technology that could be investigated e.g. body hydration. However, in this PhD research, the effects of skin cream on skin impedance over time will be investigated by designing and constructing a low cost, portable device using EIS to measure the impedance change.

1.5 Novelty and Contribution of this project

Long term measurements are motivated by manufacturer claims that the effects of moisturizers last up to 24 hours. This thesis presents a low cost portable device that makes it possible to perform long term impedance measurements of the skin. This device operates over the frequency range from 20 Hz to 100 kHz. By using a voltage source for the source driver and a current sense for measuring the resulting current injected, this device can determine the skin impedance from ~10 MΩ down to ~1 kΩ.

This device has been validated against a Solartron (Solartron 1260 + Solartron 1294) commercial bioimpedance analyzer using: passive components such as resistors and capacitors; a Hanna Instrument series of calibration solutions; and human skin. Together with the hardware platform, the embedded software carries out digital filtering, lock-in amplifier techniques and distortion measurement. This low cost portable device demonstrates highly comparable performance to that of much larger

and more expensive commercial counterparts thereby providing a platform for future deployment of wearable EIS techniques.

The tetrapolar electrode sensor arrangement has been modelled through the EIDORS FEM software in order to investigate the human skin penetration depth. Results indicate that larger separation makes the voltage difference smaller in the four electrode configuration, and as probe separation increases, the penetration depth also increases.

Several skin cream products, such as water based cream (Cocoa butter, Olive butter and Nivea) and oil based cream (Bio Oil), are used to conduct both short term (up to 2 hours) and long term (up to 5 hours) measurements on 16 volunteers. The effects of different skin cream types could be detected. For example water based cream decreases the skin impedance significantly. The Z plot obtained when a water based cream is applied to skin creates a semicircle shape instead of a straight line plot from bare skin. In long term measurement, the skin impedance is maintained at a constant impedance value; when the skin cream of any type is applied, the impedance drops significantly and then gradually increases back to its original value as the effects of the skin cream wears off.

Finally, this work has demonstrated that with the application of water based skin creams (Cocoa butter, Olive butter and Nivea) a change in the electrical skin properties from a classical constant phase elemental model to a more traditional RC non-constant phase element occurs.

So to summarise this thesis has contributed the following novel aspects to the literature:

1. The realization of a portable EIS tetrapolar instrument

2. Investigating the optimum configuration of the tetrapolar sensors using modelling.

3. The timeline effects of skin creams in terms of EIS measurements.

4. Demonstration that certain water based skin creams create “non-constant phase” models

1.6 Project Objectives

The overall objectives of this PhD research is to develop a low cost portable EIS system based on a four point probe to measure the short term and long term effects of different moisturizers. The objectives are divided into five specific tasks:

i) Create a specific tetra polar probe in order to measure human skin in terms of electrical impedance spectra.

ii) Build a custom-made bio-impedance analyzer device with high input impedance to make the measurement on skin. The bio-impedance analyzer is to operate over the frequency range from 20 Hz to 100 KHz.

iii) Validate the results of the custom made impedance analyzer with a Solartron unit (Solartron Analytical, Farnborough, UK) using passive RC (resistors and capacitors) network load, calibration solutions and human bare skin.

iv) Conduct short term and long term measurement with different skin creams on skin using the custom made device and compare the results with the Solartron system.

v) Model and analyze the results to classify the different effects on skin of different skin creams.

1.7 Outline of the Thesis

Chapter 2 provides a detailed literature review on the use of the four point probe sensors. This chapter will also review the voltage generator part, current sense part of the bio-impedance measurement system and multi-frequency EIS measurement. Finally, Chapter 2 generalizes the models to be used to fit with measurement results from bio-impedance analyzers.

Chapter 3 will describe the design, implementation and validation of the custom made system. The optimization of the tetrapolar sensors using modelling will be also given. A calibration process contains measurements with resistor and capacitor networks, calibration solution liquid and a comparison with the Solartron Impedance Analyzer (models 1260 + 1294).

Chapter 4 will focus on instrumentation and measurement in vivo. It includes the set-up protocol, the carrying out of the measurements on human skin and the results given by different skin care/ moisturizers when they were applied to skin. Short term and long term measurement results will be demonstrated.

Chapter 5 describes data analysis and modeling. Data from skin measurements will be processed and analyzed for comparison with the chosen model. A model of skin impedance will be proposed and compared with the results from measurement. Moreover, it will include the limitations of the system.

The final chapter, Chapter 6, contains the discussions and conclusions of the work, and any suggestions for further work.

Chapter 2 Overview of Electrical Impedance Spectroscopy

2.1 Introduction

This chapter provides an overview of Electrical Impedance Spectroscopy. Sections 2.1-2.5 provide an overview of different circuits applied in bioimpedance measurements. Section 2.6 reviews the EIS measurement systems. Sections 2.7 and 2.8 provide a review of different models and experimental studies from previous research respectively.

2.2 A brief introduction to bioimpedance measurement system theory and implementation

In general, the electrical impedance is represented as the ratio between the voltage and current applied in the circuit network. The bio-impedance is measured by injecting a current into biological tissue and it is estimated quite simply from Ohm's law:

$$Z = \frac{V}{I}[\Omega] \tag{2.2.1}$$

One approach in obtaining the bio-impedance is to measure the voltage drop caused by a known current that is injected into the biological tissue. Another is to measure the bio-admittance, which is the inverse of the bio-impedance. Although both of these approaches, defined as deflection methods [22], are usually used to measure the bio-impedance, it can also be measured by a Wheatstone bridge - known as null methods [22]. However, the Wheatstone bridge or null method does not measure the current flowing into the load but adjusts the voltage to balance the potential between a reference resistor and the load.

This project concentrates on injecting a known current into the object and measuring the generated voltage drop across the tissue under test via skin contact probes. There

are two different configurations for these skin contact probes namely two point probes (Kelvin probes) and four point probes (tetra-polar).

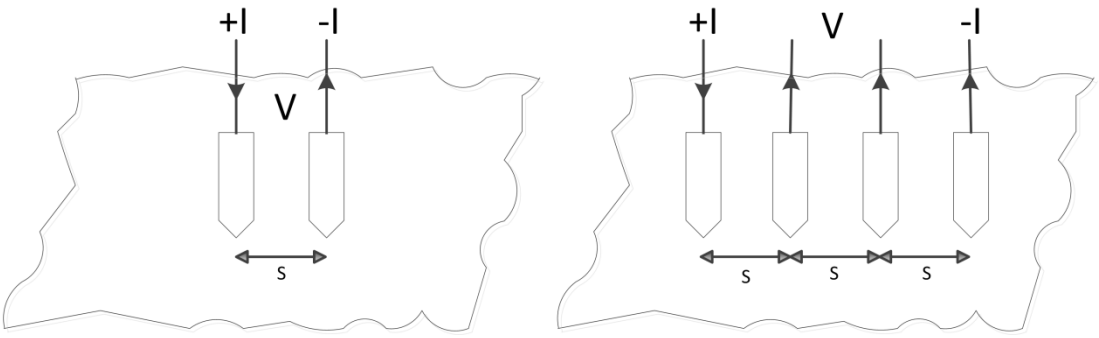


Figure 2.1: A two point probe setup (left) and four point probe setup (right).

Figure 2.1 shows on the left the two point probe configuration. Here, the injected current and voltage drop measurement deploys the same two contact points on the tissue. The four point probe setup on the right of Figure 2.1 uses the two outer probes for the injection of current and the two inner probes for the measurement of the resulting voltage drop.

Since the bio-impedance is taken on biological tissue in animals or humans, for safety reason the applied current or voltage must fulfil the requirement of the British Standard 60601-1 [23]. For example, the current allowance will not exceed more than 10 µA DC or 100 µA AC. The accumulation of charges within the tissue must be avoided, hence it is recommended to apply limited DC current on living subjects Generally, for frequencies less than 1 KHz where the load impedance is much higher than 10kΩ, the maximum allowable current is around 100 µA AC. However, for frequencies higher than 1 KHz, the allowance current can be up to 1 mA as the load impedance is approximately 1kΩ. A detailed explanation of these safety regulations can be found in Appendix E.

2.3 Comparison between bipolar and tetra-polar technique

2.3.1 Kelvin Probe or Two point probes

Kelvin probes are very popular in measuring the sample impedance in materials such as calibration solutions, water, and metals. The two point probe technique is easier to implement than the four point probe technique. However, the results from two point probes are not reliable because of electrode contact resistance. Therefore, in applications where high accuracy is not required, Kelvin probes are preferred. Because of the low safety current, the large contact resistance can dominate that of the sample and result in significant errors.

A voltmeter, such as a differential or instrumentation amplifier, usually has very high input impedance, so that as long as it is much greater than the load impedance then it will accurately measure the voltage drop between the two points. Figure 2.2 shows the two point probe configuration for measuring the impedance based on the V/I method. This figure contains a current source injecting a known current I_m into the device under test (DUT) through two electrodes, the instrumentation amplifier measures the voltage drop across the same two contact points assuming that its input impedance Z_{in} is infinite.

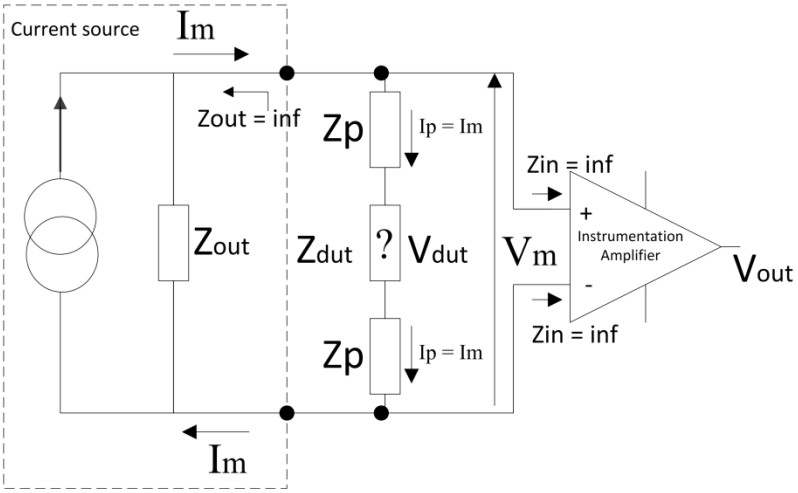


Figure 2.2: Two point probe configuration for measuring the impedance [24].

$$\boldsymbol{Zm = \frac{Vm}{Im}\ ;\ Vm = Vp + Vdut + Vp\ ;\ Vp = Im\ Zp\ ;\ Vdut = Im\ Zdut\ ;\ Zm = Zdut + 2\ Zp.}$$

In Figure 2.2, the electrode sensors have their own polarization impedance Z_p, which adds to the measured impedance Z_m. The impedance of the device under test is Z_{dut}. I_m is the current from the current source into the device under test and I_p is the current flowing through electrode impedance Z_p. However, because of the electrode impedance Z_p, the current flows through electrode impedance before reaching Z_{dut}. Note that in Figure 2.2, the measured impedance $Z_m = Z_{dut} + 2Z_p \neq Z_{dut}$. Clearly, the impedance of the device under test Z_{dut} is not equal to the measured impedance Z_m, hence it gives an error in the measurement.

According to [56], skin impedance Z_{dut} was measured for a wide range of frequencies ranging from 1 Hz to 1MHz using bipolar electrodes with a surface area of $1cm^2$ by measuring and subtracting the skin electrode impedance Z_p. The skin impedance varied from 10kΩ to 1MΩ at 1Hz, 10kΩ to 100kΩ at 100 Hz and approximately about 120Ω at 1 MHz. In another publication, the skin-electrode impedance Z_p was also studied by Rahal et al [25]. Six different types of Ag/AgCl bipolar electrodes

were evaluated over the frequency range between 10 Hz and 1 MHz. For frequencies below 1 kHz the electrode-tissue impedance (Zp) was higher than 10kΩ, and reduced to approximately 5 kΩ at 10 kHz, 337 Ω at at 1 MHz. Dozio et al [26] investigated the electrical properties of the skin electrode interface of dry ECG electrodes. They reported that the electrode impedance of Z_p varied from 41kΩ to 458kΩ, stratum corneum/epidermis layer impedance Z_{dut} from 168kΩ to 1590kΩ and deeper tissue from 800Ω to 1.9kΩ at low frequency 0.016 Hz.

In contrast, the four point probe technique overcomes these problems by eliminating the electrode impedance.

2.3.2 Four point probe or Tetra-polar probes

In the four point probe technique shown in Figure 2.3, the injected current from two outer probes flows through two electrodes of impedance Z_p and the impedance under test (Z_{dut}). Again, I_m is the current from current source into the device under test and I_p is the current flowing through the electrode impedance $Z_{p.}$ As the input impedance of the differential or instrumentation amplifier is very high, there is no current going into the non-inverting and inverting terminals of the amplifier. Therefore, the instrumentation amplifier measures the voltage drop between the two inner probes, without affecting the current flow from the two outer probes.

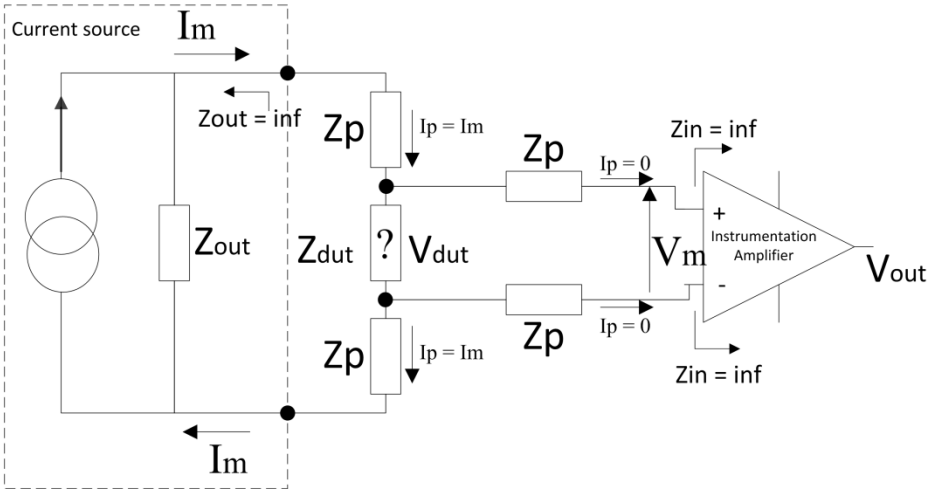


Figure 2.3: Four point probe configuration for measuring the impedance [24]

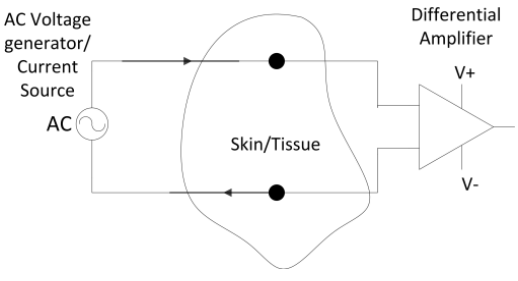
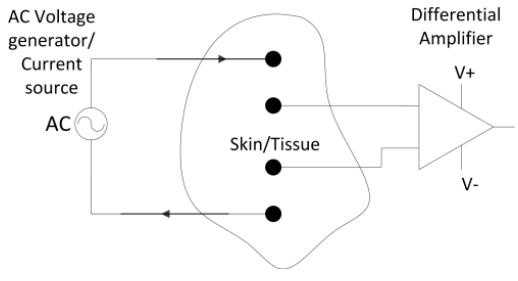
$$Zm = \frac{Vm}{Im}\ ;\ Vm = Vp + Vdut + Vp\ ;\ Vp = Ip\ Zp = 0 \text{(for two horizontal Zp)}\ ;$$

$$Vdut = Vm\ ;\ Zm\ = Zdut$$

The effect of electrode Z_p is avoided and Z_m is equal to Z_{dut}. As this method can eliminate the contributions of electrode polarization impedance, it is therefore the preferred method to perform bio-impedance measurement [27][28][29].

2.3.3 Comparisons, advantages and disadvantages of these techniques

Table 2.1 summarizes the advantage and disadvantage of two techniques: two point probes and four point probes. It also includes applications of these methods.

	
Properties: Uses 2 connections to the DUT.	**Properties**: Uses 4 connections to the DUT.
Pros: Easier to implement than the four	**Pros:** More reliable as it eliminates the

point probe technique. It is suitable for applications which do not require high accuracy. **Cons:** the main problem is the error due to the electrode impedance. It contains an error due to an imperfect current source or voltage sensing.	electrode impedance (Zp). Results are given in higher accuracy. **Cons:** This technique is more complicated than the 2 point probe. It still contains the error due to an imperfect current source or voltage sensing (i.e. non infinite input impedance of the op-amp.).
Application: measuring a sample impedance of materials such as calibration solutions, water, and metals.	**Application:** measuring a sample impedance such as materials, calibration solutions, water, metals and biological tissue.

Table 2.1: Comparison between two point probe (left column) and four point probe (right column) techniques

2.3.4 Tetra-polar probes implementation and design

Consider the case of measuring the conductivity of a thick biological tissue [21] shown in Figure 2.4.

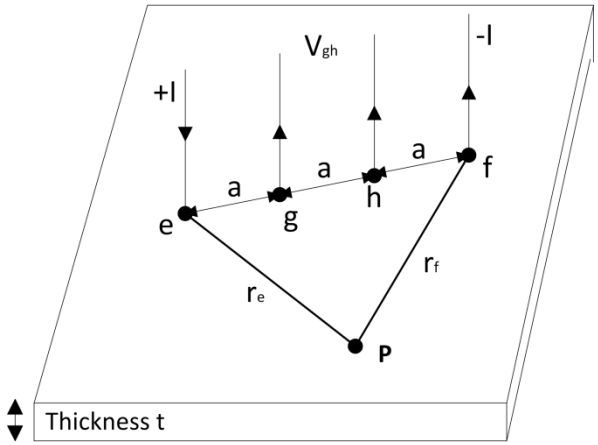


Figure 2.4: Four electrode technique for biological impedance measurement [21]

It can be seen that the electrode system consists of four equally spaced point electrodes, two outer electrodes inject a current while the inner electrodes are used to measure the voltage V_{gh}. Suppose that the electrode system is measuring a tissue which is uniform and the thickness "t" is large compared with electrode spacing "a" (t>>3a), then the current from "e" and "f" is spread out along a radial path. The

current density at a point "P" can be calculated by dividing the total current to the area of the hemisphere drawn through point "P". The current density due to electrode "e" and "f" is:

$$J_e = \frac{I}{2\pi r_e^2} \tag{2.3.1}$$

and

$$J_f = \frac{I}{2\pi r_f^2} \tag{2.3.2}$$

Where r_e and r_f are distances of the field point "P" from each respective current source.

The potential difference between "g" and "h" is the superposition of the potential difference due to each current source acting separately and is found by integrating the electric field (current density divided by conductivity) between "g" and "h".

The potential contribution from electrode "e" by integrating the electric field across "g" and "h" gives:

$$(V_{gh})_e = \int_a^{2a} \frac{I}{2\pi\sigma r_e^2}\, dre = \frac{I}{2\pi\sigma} \int_a^{2a} (r_e^{-2})\, dr_e$$

$$= \frac{I}{2\pi\sigma} \times \left(\frac{1}{a} - \frac{1}{2a}\right) = \frac{I}{4\pi\sigma a} \tag{2.3.3}$$

Then, the potential contribution from electrode "f" by integrating the electric field across "h" and "g"gives:

$$(V_{gh})_f = \int_a^{2a} \frac{I}{2\pi\sigma r_f^2} = \frac{I}{2\pi\sigma} \int_a^{2a} r_f^{-2}\, dr_f$$

$$= \frac{I}{2\pi\sigma} \times \left(\frac{1}{a} - \frac{1}{2a}\right) = \frac{I}{4\pi\sigma a} \tag{2.3.4}$$

Therefore, the total potential between "g" and "h" is $V_{gh} = (V_{gh})_e + (V_{gh})_f = \frac{I}{2\pi\sigma a}$

(2.3.5)

The conductivity of biological tissue can therefore be measured by $\sigma = \frac{I}{2\pi a V_{gh}}$

(2.3.6)

However, this is the ideal theory for a four point probe with uniform biological materials. Many biological tissues are anisotropic as the conductivity in different directions is not the same [30]. Other factors that affect the impedance measurement are the electrode size, geometry and hydration state of the biological tissue. One method of reducing error is to use a calibration solution in order to obtain the resistivity of the measurement even if the geometry or size of electrodes is not well defined [31]. The calibration solution contains a mixture of a high purity, ionizable component (such as Sodium Chloride) designed for specifying the measured resistivity volume of electrodes. In this thesis, the four point probe electrodes are characterized using a calibration solution as described in Chapter 3.

2.4 Drive circuit design

2.4.1 Voltage controlled current source

In order to measure the sample impedance a current source is required and most techniques use a Voltage Controlled Current Source (VCCS) that converts a voltage into a current and directs it through the DUT. Figure 2.5 shows a simple model of a voltage controlled current source:

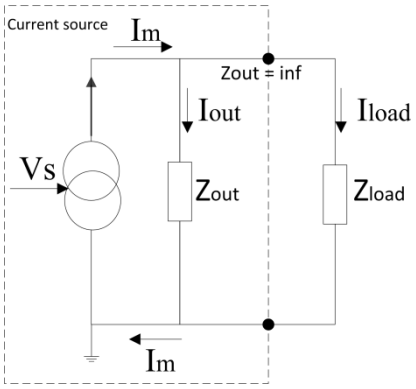


Figure 2.5: A simple model of a voltage controlled current source

As seen in Figure 2.5, the voltage generator output V_s is converted into an output current I_m. If it is assumed that the output impedance of the current source is very high ($Z_{out} = \infty$) and is much higher than the load impedance ($Z_{out} >> Z_{load}$), the output current I_m is equal to the load current I_{load} i.e. I_m flows through Z_{load} and hence $I_{out} = 0$. In the case of finite Z_{out} then I_{load} is given by:

$$I_{load} = \frac{1}{1+\frac{Z_{load}}{Z_{out}}}.I_m \qquad (2.4.1)$$

In practice, Z_{out} is not infinite and varies with frequency, usually decreasing with higher frequencies due to parasitic or stray capacitances, hence the load current I_{load} also decreases with increasing frequency.

There are several ways to inject a current into an object. Usually a waveform generator injects either voltage or current into the object and the voltage drop between two inner probes and the current out from the last outer probe is measured. The technique used by Solartron Analytical [32] is shown for biomaterial impedance measurement in Figure 2.6 and Figure 2.7. In order to make the measurement on bio materials, it is required to have a FRA (Frequency Response Analyzer), such as a Solartron 1260 or 1255 linked to an Impedance Interface Solartron 1294 and then connected to four contact points of the test sample as shown in Figure 2.6.

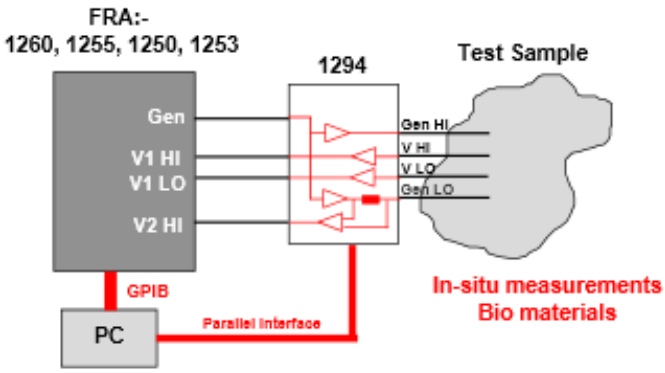


Figure 2.6: Block diagram of the bio-impedance measurement system [32]

The four contact points of the test sample are shown in detail in Figure 2.7. The first contact is called "Generator" (either voltage or current). The second and third contact is the voltage drop measurement, and the final contact is for current measurement. Figure 2.7 also includes the impedance models of each connection point.

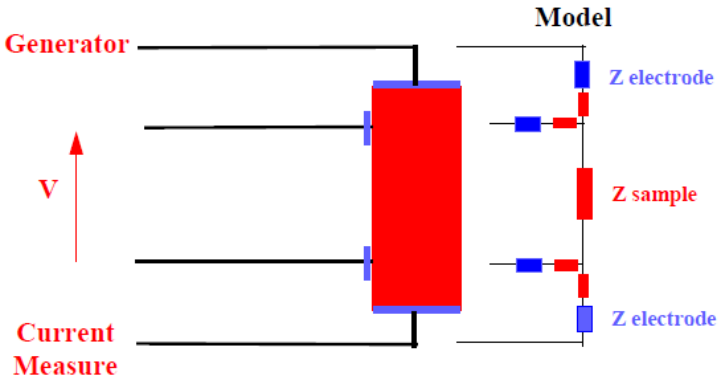


Figure 2.7: 4 terminal setup measurement from Solartron [32]. Blue resistors are represented for electrode impedance $Z_{electrode}$ and red resistors are for sample impedance.

The majority of voltage controlled current sources used in EIS are based on the Howland Circuit [33]. The "Basic Howland Current Pump" was first presented by Prof. Bradford Howland of MIT in 1962, and the invention was disclosed to his colleague George A. Philbrick (the analog computer pioneer who was head of

Philbrick Researches, Boston MA at that time). This circuit was not patented. This can use a single operational amplifier (in a Basic Howland Current Configuration) as shown in Figure 2.8.

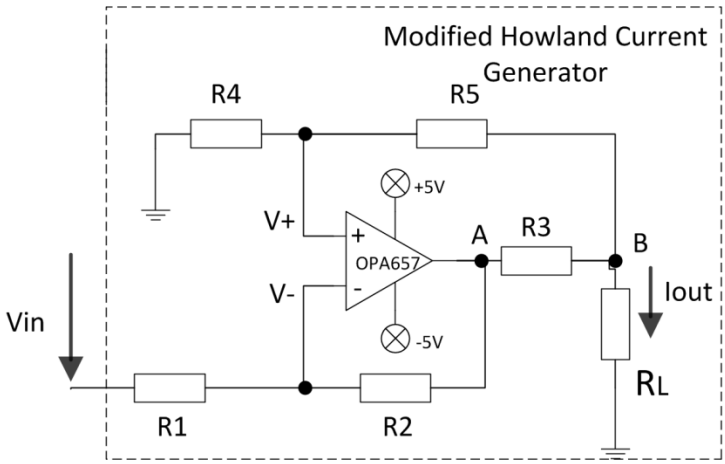


Figure 2.8: Single Modified Howland Current Generator

In order to determine the output current (I_{out}), a nodal analysis is carried out at the positive and negative terminals of the amplifier. If we assume that the current flowing into the positive and negative terminals of the amplifier is negligible then:

$$\frac{\text{Vin} - V_-}{R1} = \frac{V_- - V_A}{R2} \rightarrow V_A = -V_{in} \times \frac{R2}{R1} + V_- \left(1 + \frac{R2}{R1}\right) \qquad (2.4.2)$$

$$\frac{0 - V_+}{R4} = \frac{V_+ - V_B}{R5} \rightarrow V_B = V_+ \times \left(1 + \frac{R5}{R4}\right) \qquad (2.4.3)$$

By applying Kirchoff currents law, the sum of the currents at one node will equal zero.

$$\frac{V_A - V_B}{R3} + \frac{V_+ - V_B}{R5} + \text{i}_{\text{out}} = 0 \qquad (2.4.4)$$

Substituting the equation (2.4.2) and (2.4.3) to (2.4.4), then:

$$\frac{1}{R3} \times \left(-V_{in} \times \frac{R2}{R1} + V_- \left(1 + \frac{R2}{R1}\right) - V_+ \times \left(1 + \frac{R5}{R4}\right)\right) + \frac{-V_+}{R4} + \text{i}_{\text{out}} = 0$$

$$\rightarrow -V_{in} \times \frac{R2}{R1R3} + V_- \left(1 + \frac{R2}{R1}\right) \times \frac{1}{R3} - V_+ \times \left(\frac{1}{R3} \times \left(1 + \frac{R5}{R4}\right) + \frac{1}{R4}\right) + \text{i}_{\text{out}} = 0$$

$$\rightarrow -V_{in} \times \frac{R2}{R1R3} + V_- \times \left(\frac{R2}{R1R3}\right) - V_+ \times \left(\frac{R5}{R4R3} + \frac{1}{R4}\right) + \frac{1}{R3} \times (V_- - V_+) + \text{i}_{\text{out}} = 0 \quad (2.4.5)$$

Assuming that $V_+ = V_-$ to (2.4.5), then

$$V_+ \frac{1}{R3}\left(\frac{R2}{R1} - \frac{R3+R5}{R4}\right) + \frac{R2}{R1R3}V_{in} = i_{out} \qquad (2.4.6)$$

If we set the value of R4 equal to the sum of R3 and R5, and also set the values of R1 and R2 to be identical then, the output current will be equal to:

$$i_{out} = \frac{R2}{R1R3}V_{in} = \frac{V_{in}}{R3} \qquad (2.4.7)$$

Hence the output current can be set by the value of R3 and V_{in}. In order to maintain the output current dependence on input voltage, the ratio of the resistors R1,R2,R3,R4 and R5 in the equation $\frac{R2}{R1} - \frac{R3+R5}{R4}$ used at the node voltage calculation from positive and negative amplifier terminals have to be tightly matched.

The error due to the tolerance of the components creates a mismatch and reduces significantly the output impedance of the Howland Current Generator. In order to obtain the output impedance, it is assumed that V_{in} in Figure 2.8 is grounded. Then, the output impedance of Modified Howland Current Generator can be calculated from the equations above as:

$$R_{out} = \frac{V_B}{i_{out}} = \frac{V_{out}}{i_{out}} = \frac{R3\,(1+\frac{R5}{R4})}{\frac{R2}{R1} - \frac{R3+R5}{R4}} \qquad (2.4.8)$$

The denominator $\frac{R2}{R1} - \frac{R3+R5}{R4}$ can be used to set the output impedance of the Howland Current Generator in Figure 2.8. For example if the denominator is maintained at zero, the output impedance can be infinite. The denominator controls the output impedance and in order for it to hold high then these resistors' values need to be carefully selected.

The Howland Circuit does have some disadvantages. Most application notes indicate the ratio of R1/R2 must be equal to (R3 + R5)/R4. For achieving high accuracy, it is

necessary to use very high precision resistors such as 0.1% or even 0.01% tolerance resistor [33] with a trim pot to adjust for matching.

On the other hands, voltage source could be used to put a known voltage into the object and measure the current output.

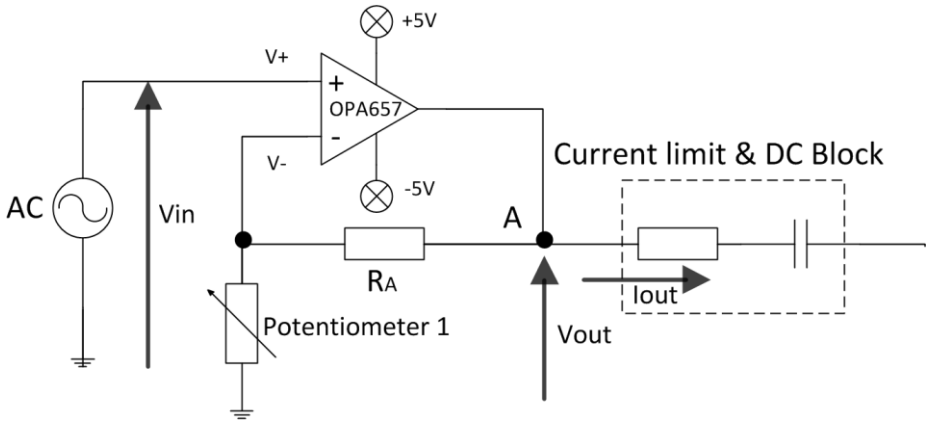


Figure 2.9: Voltage Source generating current

As shown in Figure 2.9, in addition to the Voltage Source, a non-inverting amplifier with a potentiometer is used to adjust the gain in order to generate different values of output voltage. Finally, an optional resistor is used to limit the current out which is in series with a capacitor to block the DC. Compared with the Howland Current Generator, the Voltage Generator combined with a Buffer Amplifier is more straight-forward to implement. Moreover, it does not require high precision resistors (such as 0.1% tolerance) to balance out the feedback of the op-amp as in the Howland Circuit. On the other hand, the Voltage Source Configuration requires a high control in current measurement in order to adjust the current into the DUT accurately.

According to Figure 2.9, the output voltage from the non-inverting amplifier can be calculated as:

$$V_+ = V_- = V_{in} \qquad (2.4.9)$$

$$\frac{V_-}{R_1} = \frac{V_A - V_-}{R_A} \qquad (2.4.10)$$

Then using (2.4.9) and (2.4.10),

$$\rightarrow V_A = V_{out} = V_- \times (1 + \frac{R_A}{R_1}) = V_{in} \times (1 + \frac{R_A}{R_1})$$

$V_{out} = A_0 \times V_{in} - i_{out} \times R_0 + \frac{Vin}{R1} \times R_0$ where A_0 is open loop gain, R_0 is internal resistance of the op-amp from Figure 2.10. Therefore,

$$\rightarrow V_{out} \times (1 + A_0 \times \frac{R_1}{R_1+R_A} + \frac{R_0}{R_1+R_A}) = - i_{out} \times R_0$$

$$R_{out} = - \frac{Vout}{iout} = \frac{R_0}{1+A_0 \times \frac{R_1}{R_1+R_A} + \frac{R_0}{R_1+R_A}} \qquad (2.4.11)$$

From equation (2.4.11), because the A_0 is very large (>1000000) that makes the denominator is also large (mismatches between resistors can be ignored), therefore output impedance R_{out} can be considered very small.

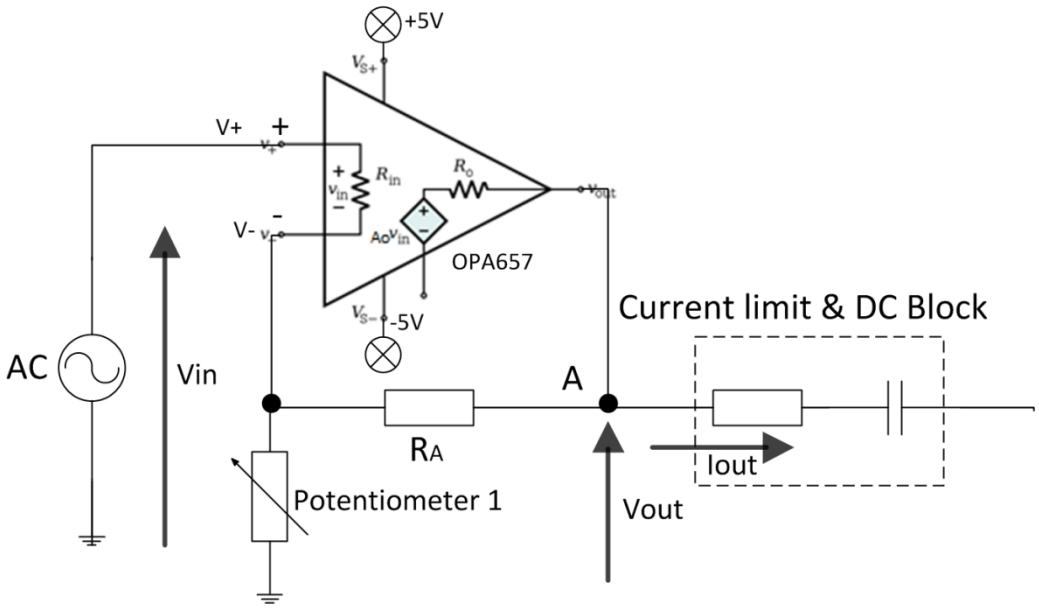


Figure 2.10: An equivalent circuit of an operational amplifier that models some resistive non-ideal parameters such as input impedance R_{in} and internal output impedance R_o.

In theory, the output impedance of an operational amplifier is very small and the input impedance is extremely high. For instance, Texas Instruments Op-amp OPA657 has an output impedance 0.025Ω at 100 kHz and is ~4Ω at 100 MHz. The

voltage source with the OPA657 operational amplifier can be represented as in Figure 2.11:

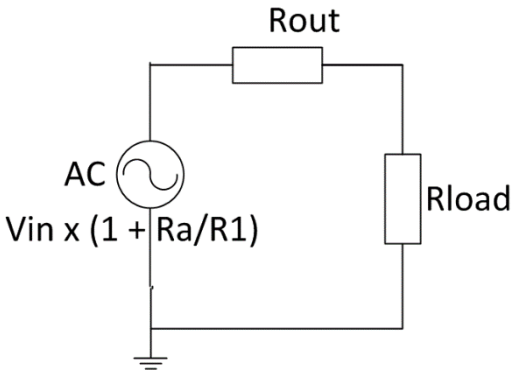


Figure 2.11: Basic AC analysis of voltage source of Figure 2.9 including R_{out}, R_{load} and V_{in}

Because R_{out} of the OPA657 is very small (0.025Ω - 4Ω), it can be assumed that the voltage applied to the load is equal to $V_{in} \times (1 + \frac{R_A}{R_1})$. Also, the output current can be calculated as

$$I_{out} = \frac{V_{in} \times (1 + \frac{R_A}{R_1}).}{Rload + R_{out}} \approx \frac{V_{in} \times (1 + \frac{R_A}{R_1}).}{Rload} \qquad (2.4.12)$$

In order to satisfy the Medical electrical safety standard, EN 60601-1, an output resistor is used to limit the AC current out which is in series with a capacitor to block any DC (Direct Current) as shown in Figure 2.12.

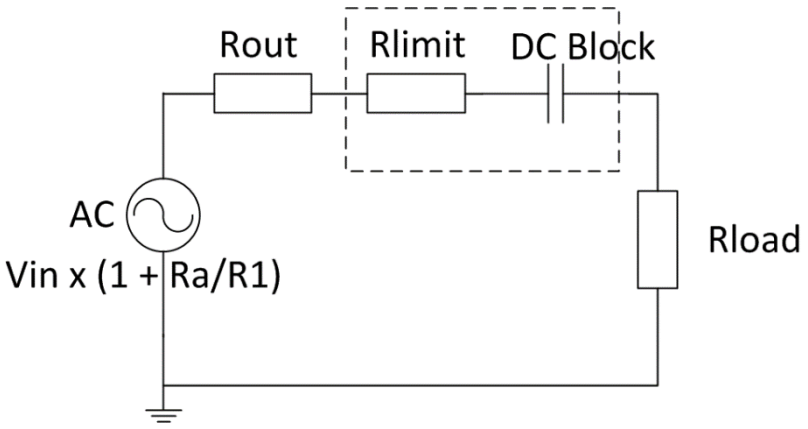


Figure 2.12: AC analysis of voltage source including R_{out}, R_{load} and V_{in} with addition of R_{limit} and DC_{block} capacitor

$$I_{out} = \frac{V_{in} \times (1 + \frac{R_A}{R_1}).}{R_{load} + R_{out} + Z_{limit\&DC}} \approx \frac{V_{in} \times (1 + \frac{R_A}{R_1}).}{R_{load} + Z_{limit\&DC}} \qquad (2.4.13)$$

Where, $Z_{limit\&DC} = R_{limit} + 1/j\omega C$

For instance, at frequency f = 10 Hz, R_{limit} = 50 kΩ and C = 1μF, then $Z_{limit\&DC}$ = 52.471 kΩ. In the case where R_{load} is equal to zero, the maximum current flow through R_{load} will be equal to

$$I_{out} = \frac{V_{in} \times (1 + \frac{R_A}{R_1}).}{Z_{limit\&DC}} \qquad (2.4.14)$$

If maintaining the output voltage of the voltage source V_{in} = 1V rms, $Z_{limit\&DC}$ = 52.471kΩ, and $\frac{R_A}{R_1}$ = 4, then I_{out} = 95.29 μA rms, which satisfies the maximum allowable current flow through biological tissue according to British Standard 60601 at 10Hz. However, if V_{in} is increased above 1V rms then the allowable current will be exceeded. In addition in order to implement EIS it is necessary to know the value of the current applied. Hence for voltage sources used in an EIS arrangement it is necessary for both EIS measurement and for safety purposes to measure the current flowing in the subject.

Both Howland Current Generator and the Voltage Source Configuration need to achieve sufficient output impedance in order to measure the impedance load i.e. Current Source needs to maintain high Z_{out}, while Voltage Source requires low R_{out}. It also requires ensuring that current injected to the sensor is the same as the current being generated. However, in practice, Z_{out} is not infinite or R_{out} in some cases it is not low enough, making it dependent on the impedance of the load and frequency range.

2.4.2 Source of errors in drive circuits

In reality, the output impedance Z_{out} is not infinite and its non-linear characteristic over the range of frequency leads to errors in the current injected into the load. It usually decreases with increasing frequency. Therefore, it is necessary to define the operating frequency range of the application and to estimate the maximum limit impedance load used in the measurement system.

The second source of error is with the parasitic capacitances contained in either the current design circuit or the sensor, which can dramatically reduce the operating range of the drive circuit. The parasitic / stray capacitance can be caused by bad design or coupling from the signal line or ground line on the board (Figure 2.13).

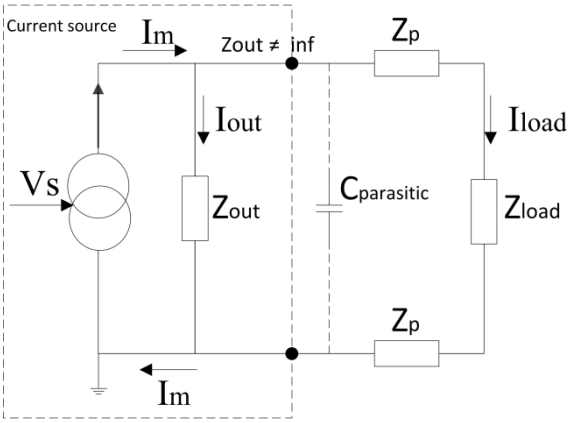
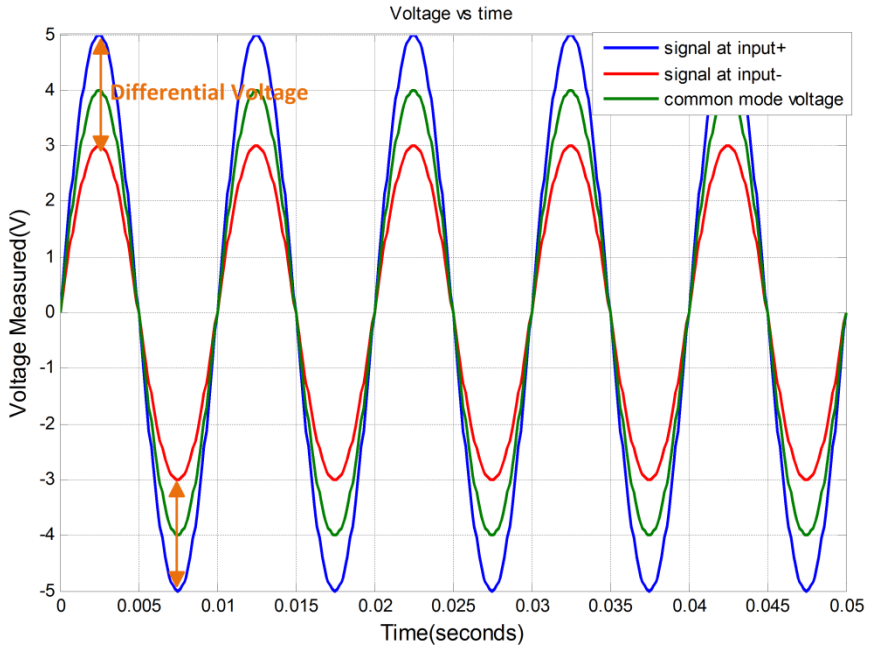


Figure 2.13: The non-ideal output impedance and parasitic / stray capacitance in the current source design.

In Figure 2.13, the imperfect output impedance and parasitic / stray capacitance can significantly decrease the measurement capability not only in high frequencies but also high impedance loads. Since the current generated from the current source is different from the current flowing through the load ($I_m \neq I_{load}$), then this will lead to errors in the measurement.

Finally, the common-mode voltage is related to the potential voltage across the two electrode impedance Z_p and load impedance Z_{load} to ground, which means that the common mode voltage can have amplitude higher than the differential voltage across the load to be measured. Therefore, the amplifier cannot differentiate the voltage drop between input+ and input- and it then rejects the voltage [14]. Figure 2.14 illustrates the built-up common mode voltage problem in the amplifier.



$$V_{cm} = \frac{V_+ + V_-}{2}$$

Figure 2.14: Common-mode voltage and differential voltage appear in the inputs of the differential amplifier.

In Figure 2.14, the voltage at input+ is shown in blue and the voltage at input- is shown in red. The common mode voltage is shown in green and equal to (V+ + V-)/2. The common mode voltage is an oscillating version that follows the signal at input+ and input- with its peak amplitude at half the sum of voltages at the two inputs. The difference voltage, which is expected at the output of the amplifier, is shown in orange. In this case, the common mode voltage acceptance from the op-

amp is lower than the built up common mode voltage, and the amplifier cannot discriminate the voltage drop between input+ and input-. Therefore, the output voltage is zero as it is being rejected by the amplifier.

Solutions of output impedance mismatch, parasitic capacitance and common-mode voltage are discussed in the next section.

2.4.3 Improvement in drive circuits

In order to increase the output impedance, there are some modifications possible in the design implementation. For instance, it is vital to design a drive circuit to avoid the signal from current being in parallel with another signal route or ground plane because of the capacitive coupling effect. Separating the drive source with other parts of the circuit helps to ensure that the effects of additive noise and coupling are significantly reduced.

For parasitic / stray capacitances contained on the sensor, it is suggested that one should drive the cable shield with the same signal which is on the core by a voltage follower [14]. Because of the same voltage potential, there is no current flow out through the cable capacitance [14]. In addition, the cable length should be minimized as the longer the cable, the higher the stray capacitance [14][24]. Moreover, designing the drive circuit and sense electronics close to the electrodes will minimize the stray capacitance and increase the operating frequency range of the current source [14].

As stated in section 2.4.2, the common mode voltage can have amplitude higher than the differential voltage. Therefore, the amplifier cannot differentiate the voltage drop between input+ and input-. One of the solutions is to minimize the common-mode voltage by using a bipolar current source (two oppositely phased current sources)

[14]. However, this can create a mismatch between the two current sources causing different stray capacitances on each side [14]. Another suggestion is to increase the power supply for the amplifier, so it can increase the ability to accept larger input common-mode voltages. Figure 2.15 shows the input common-mode voltage vs output voltage in an Instrumentation Amplifier AD8429 (Analog Device) as a function of the power supply voltage.

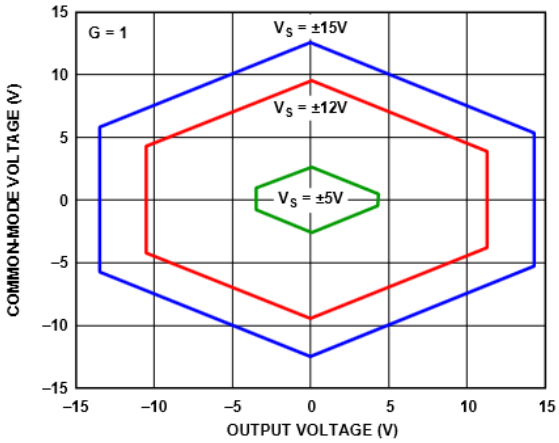


Figure 2.15: Input Common-Mode Voltage vs. Output Voltage,
Dual Supply, VS= ±5 V, ±12 V, ±15 V (Gain = 1) (AD8429, Analog Device)

In the Figure 2.15, with voltage supply ±15 V, the common-mode voltage can accept up to ±12.5V. However, it has raised one problem that in order to supply this amplifier, a DC to DC converter that can convert from a low voltage to a high voltage is required. For example, the Texas Instrument LM2611 Cuk Converter (Texas Instrument) has been used to convert low voltage (±5 V) to high voltage (±15V) with output current up to 300 mA, which can supply all the op-amps and instrumentation amplifiers in the current source and voltage sense design circuit. By increasing the voltage supply, the common-mode voltage acceptance for the amplifier is also increased. However, this method still contains disadvantages such as the converter's switching frequency and high in-rush current (LM2611, Texas

Instrument). The switching frequency used in the Cuk converter can be amplified and combined with the signal if it is not isolated. Also, a Cuk Converter has a high in-rush current, which is required to be compensated by a complex circuit in order to ensure the stabilization and protection of all design circuit elements.

The next section will be an overview of the sense circuit design with differential or instrumentation amplifiers.

2. 5 Sense circuit design

The voltage drop between the two inner electrodes (tetrapolar) is measured in the sense circuit. It depends highly on the current level injected into the skin tissue, the performance of the instrumentation amplifier and also the skin characteristics. The signals need to be amplified before going to an Analogue to Digital Converter (ADC) in order to increase the resolution and accuracy. Such small signals are therefore vulnerable to noise and interference before the amplification stage. This section will discuss in detail the voltage sense part before going on to discuss the ADC.

There are two common instrumentation amplifier architectures: the two op-amp instrumentation amplifier circuit and the classic 3 op-amp instrumentation amplifier circuit.

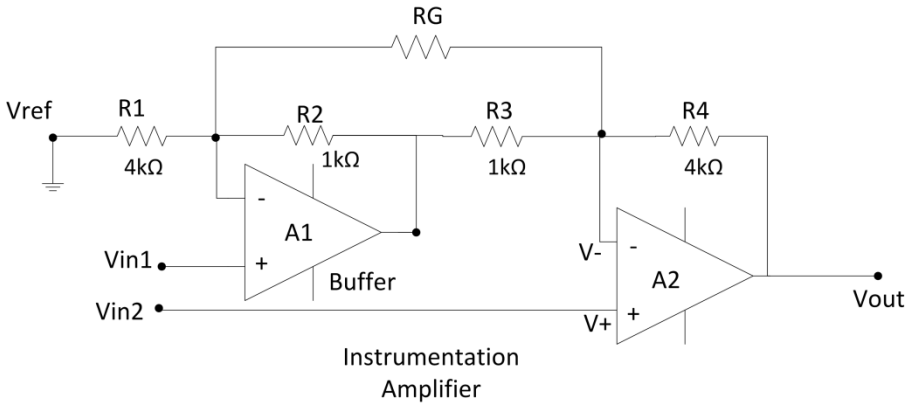


Figure 2.16: The typical two op-amp instrumentation amplifier

The gain of the 2 op-amp instrumentation amplifier (Figure 2.16) is given by [34]

$$V_{out} = (V_{in1} - V_{in2}) \times (1 + \frac{R4}{R3} + \frac{2R4}{RG}). \qquad (2.5.1)$$

This two op-amp in-amp circuit has the obvious advantage of requiring only two rather than three op-amps, thereby offering a saving in cost and power consumption. However, one of the most notable disadvantages is the lower CMRR compared with the 3-op amp design shown in Figure 2.17.

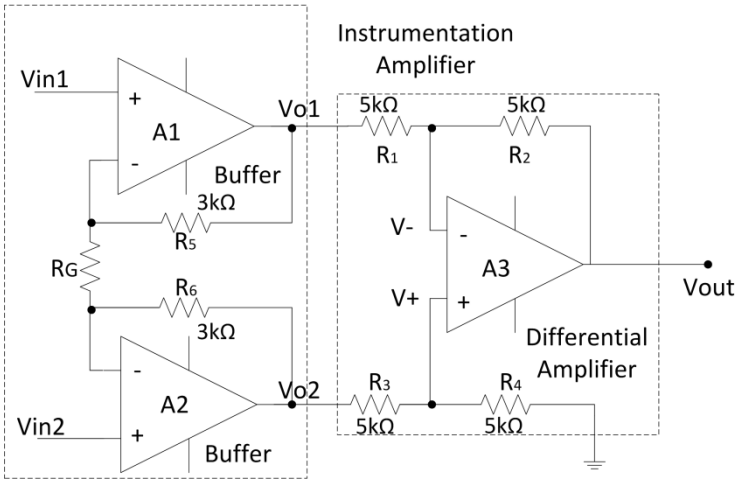


Figure 2.17: the classic 3 op-amp instrumentation amplifier [34]

The gain of the 3 op-amp instrumentation amplifier is given by $V_{out} = (V_{in1} - V_{in2}) \times \frac{R2}{R1} \times (1 + \frac{2R5}{RG})$. The calculation of this gain will be discussed in the next section.

Current feedback Amplifier at input stage of Instrumentation Amplifier

In many instrumentation amplifiers, the current feedback amplifier topology is applied to the input stage.

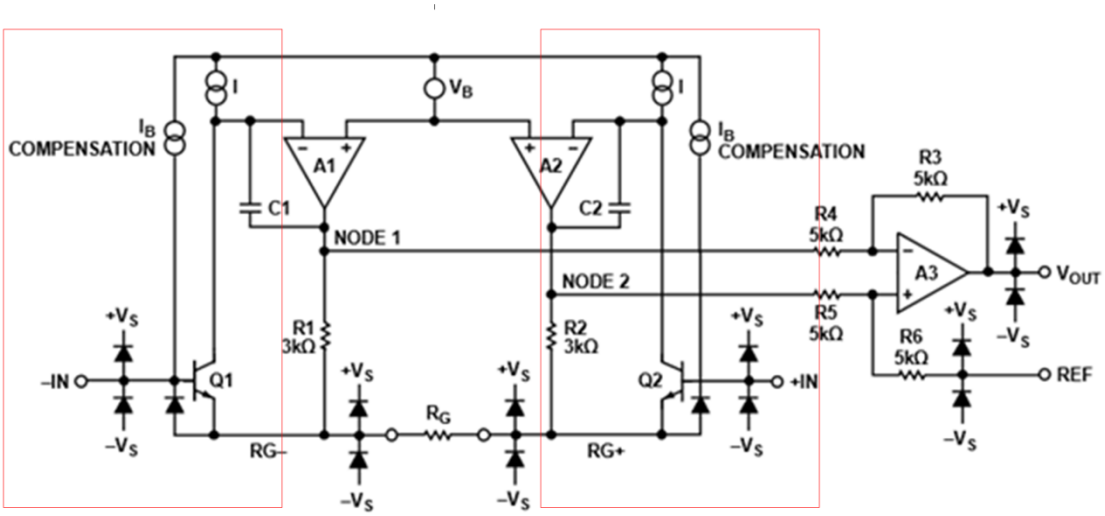


Figure 2.18: Current feedback amplifier at the input stage of the instrumentation amplifier (AD8429, Analog Device)

Input transistors Q1 and Q2 are biased at a constant current to compensate the bias current at the input. Any differential signal at input IN- and IN+ will force the output voltages from A1 and A2 to be equal. A signal applied to the input will create a current through $R_{G,}$ R_1 and R_2, which makes the output of A1 and A2 deliver the correct voltage. The pair of Q1, A1, R1 and Q2, A2, R2 can be seen as the current feedback amplifier. The amplified signals (both differential and common mode signal) after A1 and A2 are applied to difference amplifier A3. As a result the common mode voltage is rejected, and presents only the differential voltage to the output. By using the current feedback amplifier at the input stage, the instrumentation amplifier performance is greatly increased in terms of a higher input impedance, lower bias current, low offset current, low drift and low noise.

Table 3-1. Latest Generation Analog Devices In-Amps Summarized[1]

Product	Features	Power Supply Current Typ	–3 dB BW Typ (G = 10)	CMR G = 10 (dB) Min	Input Offset Voltage Max	V_{OS} Drift (µV/°C) Max	RTI Noise[2] (nV/√Hz) (G = 10)	Input Bias Current (nA) Max
AD8221	Precision, high BW	0.9 mA	560 kHz	100[3]	60 µV	0.4	11 max	1.5
AD620	General-purpose	0. 9 mA	800 kHz	95[3]	125 µV	1	16 max	2
AD8225	Precision gain = 5	1.1 mA	900 kHz[4]	83[4, 5]	150 µV	0.3	45 typ[4]	1.2
AD8220	R-R, JFET input	750 µA	1500 kHz	100	250 µV	5	17 typ	10 pA
AD8222	Dual, precision, high BW	1.8 mA	750 kHz	100[3]	120 µV	0.4	11 max	2
AD8230	R-R, zero drift	2.7 mA	2 kHz	110	10 µV	10	240 typ	1
AD8250	High BW, programmable gain	3.5 mA	3.5 MHz	100	100 µV	1	13 typ	15
AD8251	High BW, programmable gain	3.5 mA	3.5 MHz	100	100 µV	1	13 typ	15
AD8553	Auto-zero with shutdown	1.1 mA	1 kHz	100	20 µV	0.1	150 typ	1
AD8555	Zero drift dig prog	2.0 mA	700 kHz[6]	80[6]	10 µV	0.07	32 typ	22
AD8556	Dig prog IA with filters	2.0 mA	700 kHz[6]	80[6]	10 µV	0.07	32 typ	54
AD622	Low cost	0.9 mA	800 kHz	86[3]	125 µV	1	14 typ	5
AD621	Precise gain	0.9 mA	800 kHz	93[3]	250 µV[7]	2.5[7]	17 max[7]	2
AD623	Low cost, S.S.	375 µA	800 kHz	90[3]	200 µV	2	35 typ	25
AD627	Micropower, S.S.	60 µA	80 kHz	100	250 µV	3	42 typ	10

Figure 2.19: Analogue Devices Instrumentation Amplifiers [34]

Power consumption is highly dependant on the instrumentation amplifier architecture, the required bandwidth, input bias current, and voltage offset. According to Figure 2.19, the AD627 micropower, single supply instrumentation amplifier consumes only 60 µA in current supply. AD627 deploys a two op-amp architecture instead of the classic three op-amp. Other characteristics however are compromised such as: the bandwidth of AD627 at a gain of 10 is only achieved at 80 kHz; high offset voltage 250 µV; voltage noise of 42 nV/$\sqrt{Hz}$; and an input bias current 10 nA. Another example, the precision high bandwidth AD8221 with three op-amp architecture uses 0.9mA current supply (15 times higher than AD627), but the performance is outstanding compared with AD627 such as 560 kHz bandwidth, voltage offset 60 µV, voltage noise of 11 nV/$\sqrt{Hz}$ and 1.5 nA input bias current.

2.5.1 Instrumentation amplifier

An instrumentation amplifier is connected across the two inner probes of the four point probe configuration. The instrumentation amplifier is typically used as this difference amplifier as it has very high input impedance, Z_{in}, which ideally tends to infinity. Hence no AC current flows out of the two inner measurement electrodes

ensuring a zero electrode voltage drop and all of the measured voltage of the skin tissue appears across the instrumentation amplifier. Figure 2.20 shows the arrangement of the AD8429 instrumentation amplifier which uses the classical 3 operational amplifier arrangement. The differential gain, common mode gain and the Common Mode Rejection ratio (CMRR) are all determined next:

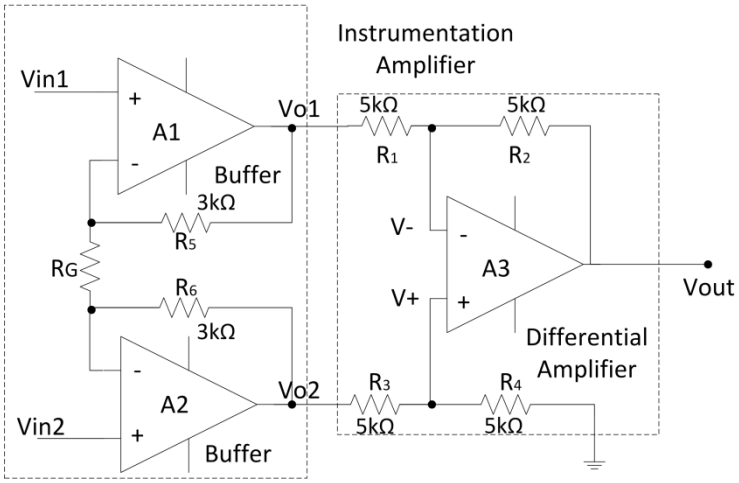


Figure 2.20: The instrumentation amplifier AD8429 schematics

In the stage of Differential Amplifier A3, the output voltage V_{out} is calculated as:

$$\frac{V_{out} - V_-}{R2} = \frac{V_{01} - V_-}{R1} \rightarrow \frac{V_{out}}{R2} - \frac{V_{01}}{R1} = \frac{V_-}{R2} - \frac{V_-}{R1} \qquad (2.5.2)$$

$$\frac{V_{o2} - V_+}{R3} = \frac{0 - V_+}{R4} \rightarrow \frac{V_{o2}}{R3} = \frac{V_+}{R3} - \frac{V_+}{R4} \qquad (2.5.3)$$

Adding (2.5.2) and (2.5.3), yields

$$\frac{V_{out}}{R2} - \frac{V_{01}}{R1} + \frac{V_{o2}}{R3} = \frac{V_-}{R2} - \frac{V_-}{R1} + \frac{V_+}{R3} - \frac{V_+}{R4} \qquad (2.5.4)$$

Using $V_+ = V_-$, $R_1 = R_3$, $R_2 = R_4$ to (2.5.4), the output of differential amplifier stage:

$$\frac{V_{out}}{R2} = \frac{V_{01}}{R1} - \frac{V_{o2}}{R3} \rightarrow \frac{V_{out}}{R2} = \frac{(V_{01} - V_{o2})}{R1} \rightarrow V_{out} = \frac{R2\,(V_{01} - V_{o2})}{R1} \qquad (2.5.5)$$

By applying the Superposition theorem, if $V_{in2} = 0$, then the node between R_G and R_6 is virtual ground (as zero). Then,

$$V_{o1} = V_{in1}\left(1 + \frac{R5}{RG}\right) \qquad (2.5.6)$$

Assume that there is no current flow into negative terminal of A1 and A2, then

$$\frac{V_{o1}}{R5+RG} + \frac{V_{o2}}{R6} = 0 \rightarrow V_{o2} = \frac{-V_{o1} \times R6}{R5+RG} \qquad (2.5.7)$$

Replacing V_{o1} (2.5.6) and V_{o2} (2.5.7) to (2.5.5), the output voltage V_{out} becomes

$$V_{out1} = \frac{R2\,(V_{o1} - V_{o2})}{R1} = \frac{R2}{R1} \times \left(V_{o1} + \frac{V_{o1} \times R6}{R5+RG}\right) = \frac{R2}{R1} \times \left(1 + \frac{R6}{R5+RG}\right) \times V_{in1}\left(1 + \frac{R5}{RG}\right)$$

$$= V_{in1} \times \frac{R2}{R1} \times \left(1 + \frac{2R5}{RG}\right) \qquad (2.5.8)$$

Again, applying the Superposition theorem, if $V_{in1} = 0$, then $V_{o2} = V_{in2}\left(1 + \frac{R6}{RG}\right)$ and

$V_{o1} = \frac{-V_{o2} \times R5}{R6+RG}$, yields

$$V_{out2} = \frac{R2\,(V_{o1} - V_{o2})}{R1} = \frac{R2}{R1} \times \left(-V_{o2} - \frac{V_{o2} \times R5}{R5+RG}\right) = -V_{in2} \times \left(1 + \frac{R5}{R6+RG}\right) \times \left(1 + \frac{R6}{RG}\right) =$$

$$- V_{in2} \times \frac{R2}{R1} \times \left(1 + \frac{2R6}{RG}\right). \qquad (2.5.9)$$

Because R5 = R6, therefore, $V_{out2} = - V_{in2} \times \frac{R2}{R1} \times \left(1 + \frac{2R5}{RG}\right)$. (2.5.10)

Then the total V_{out} will be equal to:

$$V_{out} = V_{out1} + V_{out2} = (V_{in1} - V_{in2}) \times \frac{R2}{R1} \times \left(1 + \frac{2R5}{RG}\right) \qquad (2.5.11)$$

The differential gain is calculated as:

$$A_d = \frac{R2}{R1} \times \left(1 + \frac{2R5}{RG}\right) \qquad (2.5.12)$$

The common mode gain is also calculated from Figure 2.20: $V_{in1} = V_{in2} = V_{cm}$

$$V_+ = \frac{R_4}{R_4+R_3} \times V_{o2} \qquad (2.5.13)$$

$$V_- = \frac{R_1}{R_1+R_2} \times (V_o - V_{o1}) + V_{o1} = V_{o1} \times \left(1 - \frac{R_1}{R_1+R_2}\right) + \frac{R_1}{R_1+R_2} \times V_o \qquad (2.5.14)$$

Because $V_+ = V_-$, using (2.5.13) and (2.5.14), then

$$\frac{R_4}{R_4+R_3} \times V_{o2} = V_{o1} \times \left(1 - \frac{R_1}{R_1+R_2}\right) + \frac{R_1}{R_1+R_2} \times V_o$$

$$V_o = \left(\frac{R4}{R3+R4} \times \frac{R1+R2}{R1}\right) \times V_{o2} - \frac{R2}{R1} \times V_{o1} \qquad (2.5.15)$$

Consider the current flowing in $R_5 - R_G - R_6$:

$$\frac{V_{o1}-V_{in1}}{R_5} = \frac{V_{in2}-V_{o2}}{R_6} = \frac{V_{in1}-V_{in2}}{R_G} \qquad (2.5.16)$$

From $\frac{V_{o1}-V_{in1}}{R_5} = \frac{V_{in1}-V_{in2}}{R_G} \rightarrow V_{o1} = \frac{R_5+R_G}{R_G}V_{in1} - \frac{R_5}{R_G}V_{in2}$ (2.5.17)

From $\frac{V_{in2}-V_{o2}}{R_6} = \frac{V_{in1}-V_{in2}}{R_G} \rightarrow V_{o2} = \frac{R_6+R_G}{R_G}V_{in2} - \frac{R_6}{R_G}V_{in1}$ (2.5.18)

Because $V_{in1} = V_{in2} = V_{cm}$, subtituding to (2.5.17) and (2.5.18), then yields $V_{o1} = V_{o2} = V_{cm}$. Applying to (2.5.15), becomes:

$$\rightarrow V_o = \left(\frac{R4}{R3+R4} \times \frac{R1+R2}{R1}\right) \times V_{cm} - \frac{R2}{R1} \times V_{cm} \qquad (2.5.19)$$

$$A_{cm} = \frac{V_o}{V_{cm}} = \frac{R4}{R3+R4} \times \frac{R1+R2}{R1} - \frac{R2}{R1} \qquad (2.5.20)$$

The common mode rejection ratio is derived as:

$$CMRR = \frac{Ad}{|Acm|} = \frac{\frac{R2}{R1} \times \left(1 + \frac{2R5}{RG}\right)}{\frac{R4}{R3+R4} \times \frac{R1+R2}{R1} - \frac{R2}{R1}} \qquad (2.5.21)$$

A_{cm} is zero in theory if $R_1 = R_2 = R_3 = R_4$, but in practice the resistors cannot be perfectly matched. In precision instrumentation amplifiers, the resistors are laser trimmed to get the smallest error of its normal value such as 0.01% or even 0.001%. Differential or instrumentation amplifiers are usually used to measure the voltage drop in the sense part. Figure 2.21 shows the instrumentation amplifier INA118 (Texas Instrument) with two pre-amplifiers. This instrumentation amplifier contains two pre-amplifiers connected to two difference inputs from another amplifier with single ended output. The two pre-amplifiers create the high input impedance and increase the common-mode rejection ratio (CMRR) for the instrumentation amplifier. In the measurement, the two inputs from the instrumentation amplifier are in contact with skin tissue and measure the potential difference across it. The

reference input is set as the reference potential for the amplifier and it is usually held at 0 V.

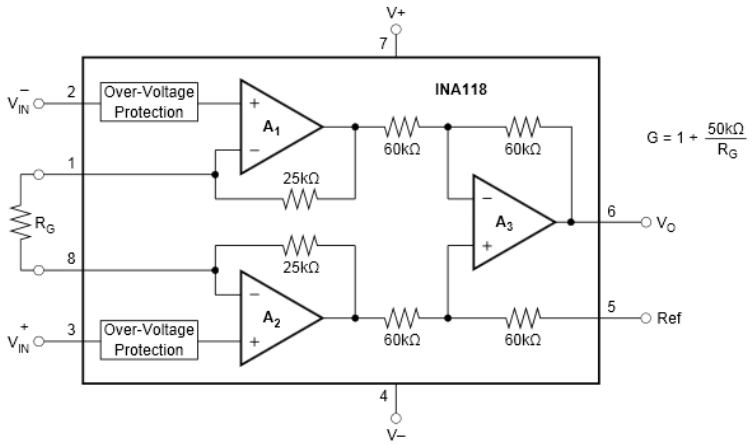


Figure 2.21: Schematic of Instrumentation amplifier INA118 (Texas Instrument) with two pre-amplifiers and differential output, where G is the differential gain equal to $\boldsymbol{G = 1 + \frac{50k\Omega}{R_G}}$ and R_G is the resistor used to set the gain.

As derived for the AD8429 above, the output voltage from the Instrumentation Amplifier for differential input signals is expressed as

$$V_{out} = (V_{in1} - V_{in2}) \times \frac{R2}{R1} \times (1 + \frac{2R5}{RG})$$

$$\text{Differential Gain} = \frac{R2}{R1} \times (1 + \frac{2R5}{RG})$$

In the case of the INA118, $R_1 = R_2 = 60\ k\Omega$, $R_5 = 25\ k\Omega$, therefore the differential gain will be equal to $\boldsymbol{G = 1 + \frac{50k\Omega}{R_G}}$.

The two differential inputs V_{in}^+ and V_{in}^- are connected to the electrodes, which are placed on the skin. The output voltage V_o is equal to the product of the gain G and difference of the two inputs ($V_{in}^+ - V_{in}^-$). There are four important factors of instrumentation amplifier specification: high input impedance, low noise, high common-mode rejection ratio (CMRR) and low input bias current.

Firstly, for the input impedance, ideally the operational amplifier should have input impedance Z_{in} that tends to infinity, but it does not happen in practice. A typical operational amplifier always has high input impedance from a few MΩ to hundreds of MΩ. In some instrumentation amplifiers with two pre-amplifiers, the input impedance can go up to GΩ e.g. Texas Instrument's Precision Low Power Instrumentation Amplifier INA118 has an input impedance of 10 GΩ.

The second factor is noise in the instrumentation amplifier.

The total noise of the Instrumentation Amplifier (In-Amp) depends on three main contributors of noise: the source resistance noise, the voltage noise of the In-amp and the current noise of the In-amp. When calculating noise the value is often referred to the input (RTI) and therefore everything is calculated as if it appeared at the amplifier input. The noise at the amplifier's output is then calculated by multiplying the RTI noise with the gain of in-amp. The instrumentation amplifier noise model is shown in Figure 2.22.

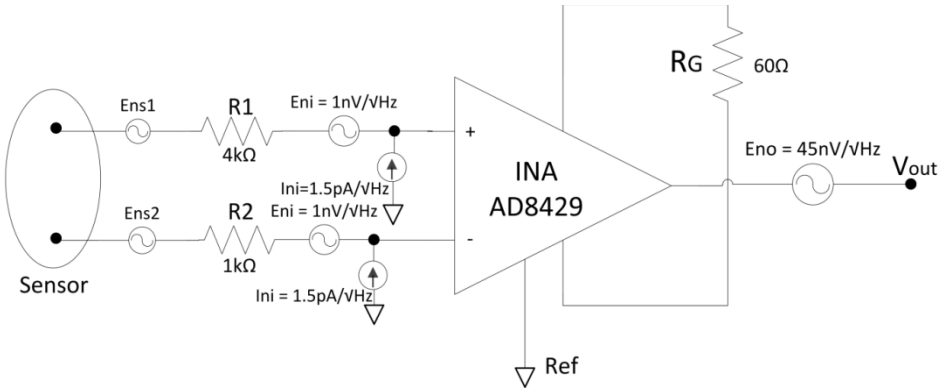


Figure 2.22: Instrumentation Amplifier Noise model

a) Source Resistance Noise

The source resistances are labelled R_1 and R_2 in Figure 2.22. Any resistors contain a level of noise such as thermal noise. The thermal noise (in nV/$\sqrt{Hz}$.) is proportional to the square root of the resistor value i.e. $E_{noise} = \sqrt{4kTR}$.

For example, in Figure 2.22, with a source resistance on the positive input of 4 kΩ and on the negative input of 1 kΩ, the noise from source resistances E_{ns1} and E_{ns2} is calculated as

Source Resistance Noise voltage = $\sqrt{Ens1^2 + Ens2^2}$

$= \sqrt{4kTR1 + 4kTR2}$ (2.5.22)

$= 10^{-9} \times \sqrt{4 \times 3 \times 4 \times 1.38 + 4 \times 3 \times 1.38} = 10^{-9} \times \sqrt{6 + 16.56} = 8.9\text{nV}/\sqrt{Hz}$.

Where k is Boltzmann's constant (1.38×10^{-23} JK^{-1}) and T is the temperature in Kelvin (i.e. 300 K).

b) Voltage Noise of the In-amp

The voltage noise from In-amp is calculated using input voltage noise E_{ni}, output voltage noise E_{no} and resistor gain R_G noise. For example, for In-amp AD8429, E_{ni} = 1nV$\sqrt{Hz}$, E_{no} = 45nV$\sqrt{Hz}$, gain G = 100, R_G = 60Ω at frequency 1 kHz according to the datasheet AD8429.

Voltage Noise = $\sqrt{\left(\frac{Output\ noise}{G}\right)^2 + (Input\ noise)^2 + (RG\ noise)^2}$

$= \sqrt{\left(\frac{Eno}{G}\right)^2 + (Eni)^2 + \left(\sqrt{4kTRG}\right)^2}$ (2.5.23)

$= 10^{-9} \times \sqrt{\left(\frac{45}{100}\right)^2 + (1)^2 + \left(4 \times \sqrt{0.0604}\right)^2} = 1.5\ \text{nV}/\sqrt{Hz}$.

c) Current Noise of the In-amp

Current noise is calculated by multiplying the source resistance by the current noise. In the case of AD8429, the input current noise I_{ni} = 1.5 pA/$\sqrt{Hz}$ and the source resistance R_1 = 4 kΩ and R_2 = 1 kΩ, the current noise is derived as

Current Noise = $\sqrt{(R1 \times Ini)^2 + (R2 \times Ini)^2}$ (2.5.24)

= $10^{-9} \times \sqrt{(4 \times 1.5)^2 + (1 \times 1.5)^2}$ = 6.2nV/$\sqrt{Hz}$.

d) The Total Noise Density, referred to the input, is calculated as the sum of squares of source resistance voltage noise, amplifier voltage noise and amplifier current noise.

Total noise density

= $\sqrt{(voltage\ noise)^2 + (current\ noise)^2 + (source\ resistance\ noise)^2}$

= $10^{-9} \times \sqrt{(8.9)^2 + (1.5)^2 + (6.2)^2}$ = 11 nV$\sqrt{Hz}$. (2.5.25)

In the case when the Gain is 1000, the total noise density, referred to input, is approximately 11 nV$\sqrt{Hz}$. If the bandwidth is set at 1000 Hz, then the total noise is the product of total noise density and bandwidth equals to 11 µV rms.

It is necessary for instrumentation amplifiers to have low noise in the sense configuration for EIS circuitry. It will be set up to have a high gain, therefore amplification of the noise can be a problem in the high precision system. A low noise instrumentation amplifier (such as the AD8429) has noise as low as 1 nV/$\sqrt{Hz}$(Analog Device) .

For the third factor, the common-mode rejection ratio (CMRR) is one of the most important parts in the instrumentation amplifier for this application. For each instrumentation amplifier configuration, the CMRR highly depends on the set up gain and frequency range. Usually, CMRR decreases with respect to increasing frequency. The common-mode rejection ratio is calculated in dB (decibels) by:

$$\text{CMRR} = 20\log_{10}\left(\frac{A_d}{|A_{cm}|}\right) \text{ dB} \qquad (2.5.26)$$

in which A_d is the differential gain, and A_{cm} is the common mode gain.

CMRR is based on the ratio of the differential gain and common-mode gain. It is a positive number and a higher number shows a better CMRR. For example, the CMRR versus frequency of the AD8429 (Analog Device) is shown in Figure 2.23.

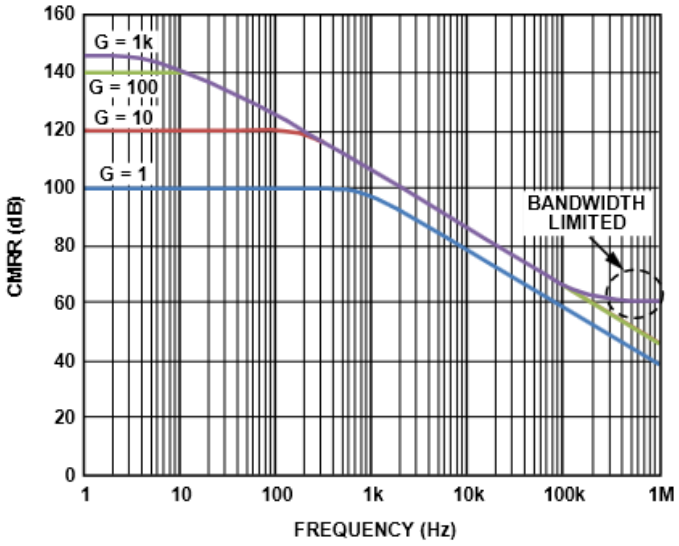


Figure 2.23: CMRR versus frequency of the instrumentation amplifier AD8429 (Analog Device)

In Figure 2.23, the CMRR is shown to be dependent on the gain and frequency range, and can be high (100 dB) at low frequencies and low (40 dB) at high frequencies.

The final important factor of the instrumentation amplifier is the input bias current. Ideally, there should be no DC current flow into the input terminals of the op-amp. However, in practice, there always is a small current flow into the terminals of the op-amp called the input bias current. The input bias current can typically vary from fA to µA [35]. Because the inputs of instrumentation amplifiers are connected directly to the electrodes to measure the voltage across the tissue, they will cause DC errors in the results assuming that some current flows into the amplifier. Figure 2.24 shows the input bias current flowing into the inputs of an op-amp.

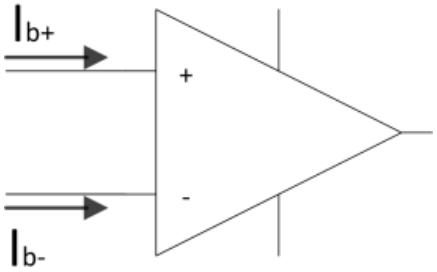


Figure 2.24: Op Amp Input Bias Current [35]

Many technologies have been used in the fabrication of the front end of an instrumentation amplifier such as Bipolar Junction Transistor (BJT) buffer inputs, Field Effect Transistor (FET) inputs (including CMOS inputs), and Junction Field Effect Transistor (JFET) inputs . In the next section, several sources of errors due to each method will be discussed.

2.5.2 Sources of error in sense circuits

Power supply sockets that used 240V- 50 Hz AC voltages (such as in the United Kingdom) are one of the interferences that can affect the sense circuit. Moreover, crosstalk, such as Electromyography (EMG) ranging from 0 to 500 Hz and Electrocardiography (ECG) ranging from 0.05 Hz to 120 Hz, can also affect the voltage measurement [14]. However, the amplifier can minimize the effects of these

interferences with appropriate with filter circuits. Again, the common-mode voltage can cause a problem as the output voltage of the instrumentation amplifier contains a differential voltage (V_{in}^{+} - V_{in}^{-}) and a common-mode voltage. Moreover, the built up potential voltage (as described in section 2.4.2 across two electrode impedances Z_p and load impedance Z_{load} to ground (Figure 2.14) makes the common mode voltage amplitude higher than the differential voltage across the load to be measured.

Noise caused by the operational amplifier and electrodes' resistance should also be considered in the system. The operational amplifier itself can generate low or high noise dependent on different configurations, such as with the same gain G = 100, AD8429 can have a low noise of 1 nV/$\sqrt{Hz}$ (AD8429, Analog Device) from 10Hz to 100kHz or INA118 generates approximately 11 nV/$\sqrt{Hz}$ (INA118, Texas Instrument) from 10Hz to 10kHz. In addition, the electrode resistance causes some noise in the voltage sense part; however it is demonstrated in Section 2.3.2 that this is not critical in the four point probe technique. The electronic amplifiers are not ideal and have finite input impedance. Also, the parasitic capacitances can be associated with the PCB board, or with the input and ground planes. These capacitances significantly reduce the input impedance of the instrumentation amplifiers especially in high frequencies around 100 kHz or above. This makes the current through the measurement electrodes non zero and causes the voltage gain to drop. The usage of FET or even JFET inputs can make the input impedance from the amplifier extremely high and ensure that there is no current flow into the amplifier through the electrode leads [28].

Finally, input bias currents can also cause a problem in the sense voltage measurement part because the larger bias current drawn by the amplifier, the more

unwanted voltage offset is created on the impedance measurement loads. Hence, one with a low input bias current should be selected, for example, the INA118 (Texas Instrument) has an input bias current of typically 1 nA, or a maximum 10 nA, however AD8429 (Analog Device) can have input bias current as high as 300 nA . For an application that requires small input bias currents, clearly the AD8429 is hard to adapt to the requirements such as for measuring impedances above 1MΩ because it withdraw a lot of bias current. However, the AD8429 (Analog Device) can achieve wider bandwidths up to 100 kHz compared with the INA118 for example. For this reason, the AD8429 was used to implement in the analogue frontend board described in Chapter 3.

2.5.3 Improving the performance of the voltage sense circuits

According to the sources of errors in the section 2.5.1, the op-amps in Figure 2.20 play an important role in a successful measurement of EIS. Wide bandwidth, high input impedance, high CMRR, low noise, and low input bias current are all necessary for a high quality EIS working system.

The function of the differential input stage of the op-amp is to amplify the input difference between positive (V_p) and negative (V_n) terminal and convert this into an output signal proportional to (V_p - V_n). Three different types of op-amp differential stages exist namely: Bipolar Transistor input, JFET input or CMOS input.

Bipolar Transistor Input Stage

Figure 2.25 shows the bipolar transistor input stage of the operation amplifier. In this bipolar input stage, there are four BJT transistors made up of two NPN and two PNP. The two NPN transistors Q1 and Q2 are called a differential pair amplifier, which

convert the input voltage V_p and V_n into currents I_{C1} and I_{C2}. Then two of transistors Q3 and Q4 are created as a current mirror. This current mirror ensures that the collector currents flowing into Q3 and Q4 are equal to I_{C1}.

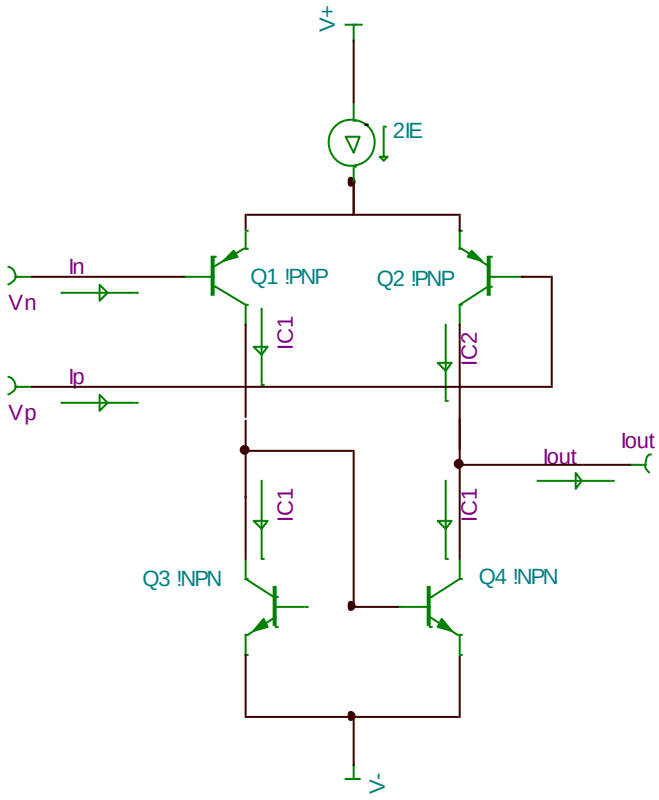


Figure 2.25: Biopolar transistor input stage [34][36]

The current source 2IE is divided between Q1 and Q2. Depending on the input voltage from V_p and V_n, the current flowing into emitters of Q1 and Q2 are different. If $V_p > V_n$, the current IC_1 is higher than IC_2. The current mirror Q3 and Q4 forces $I_{out} = IC_2 – IC_1$ to flow into the collector-collector junction of Q2 and Q4. Again, if $V_p < V_n$, the current IC_1 is higher than IC_2. The current mirror Q3 and Q4 forces $I_{out} = IC_1 – IC_2$ to flow into the collector-collector junction of Q2 and Q4. The output from input stage of op-amp is proportional to the differential input $V_p - V_n$, such as $I_{out} = gm \times (V_p - V_n)$, where gm is the transconductance gain of the input stage set by the transistors Q1, Q2.

However, because of the BJT bipolar input stage, the bias currents are somewhat high due to the base current that starts to flow with an input voltage of about 0.7 V. As can be seen the bias currents are directly from the base currents of the two input transistors. By introducing the internal current source, as shown in Figure 2.26, the bias current is classified as an internally compensated input stage.

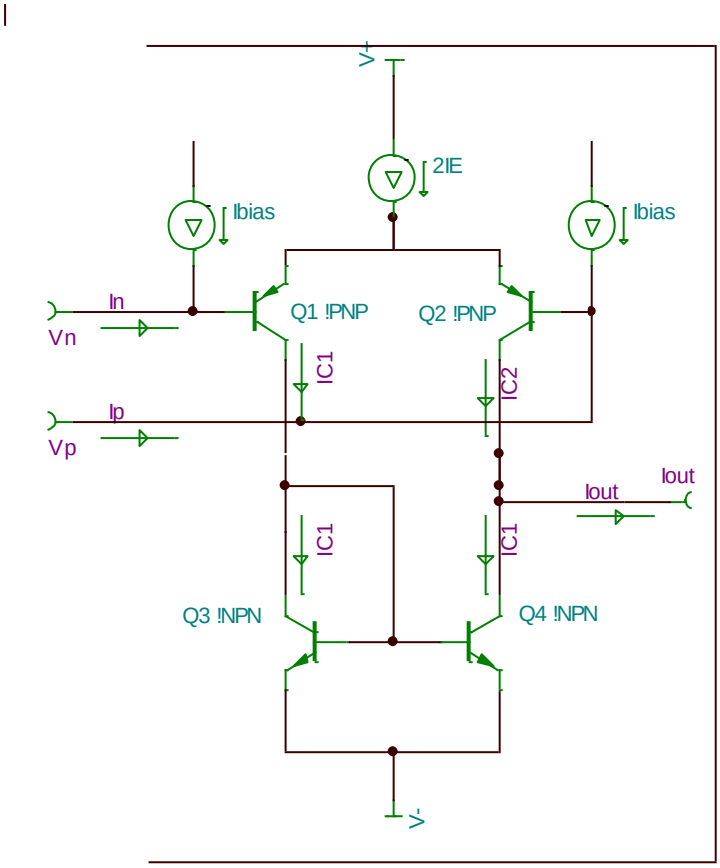


Figure 2.26: Bias current compensated bipolar input stage [34][36]

On the other hand, the compensated bias current can introduce noise into the input stage. As a result, the output current inevitably has some noise. The effective method to reduce this is with a FET input stage, which is discussed in the next section.

JFET input stage

Field-Effect Transistors (FET) have a much higher input impedance than bipolar junction transistor (BJT). In fact, FETs offer high input impedance, low bias current (due to the current required at gate is nearly zero (pA)), good high frequency performance and much lower current noise.

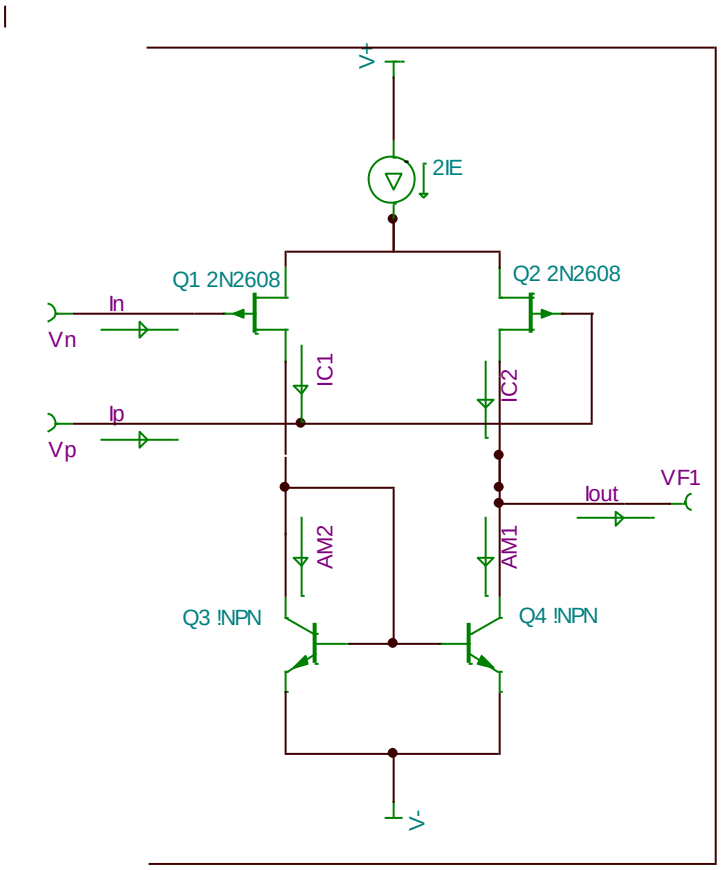


Figure 2.27: JFET input stage of operational amplifier [34][36]

In Figure 2.27, by providing two JFET (Junction Field Effect Transistors) at the differential input stage, the bias current problem can be solved as the current required at the gate is nearly zero. The current mirror can either use a FET or BJT, however, in practice, the combined Bipolar/JFET technology in op amps achieves improved performance compared to an op-amp using purely FETs [34]

CMOS Input Stage

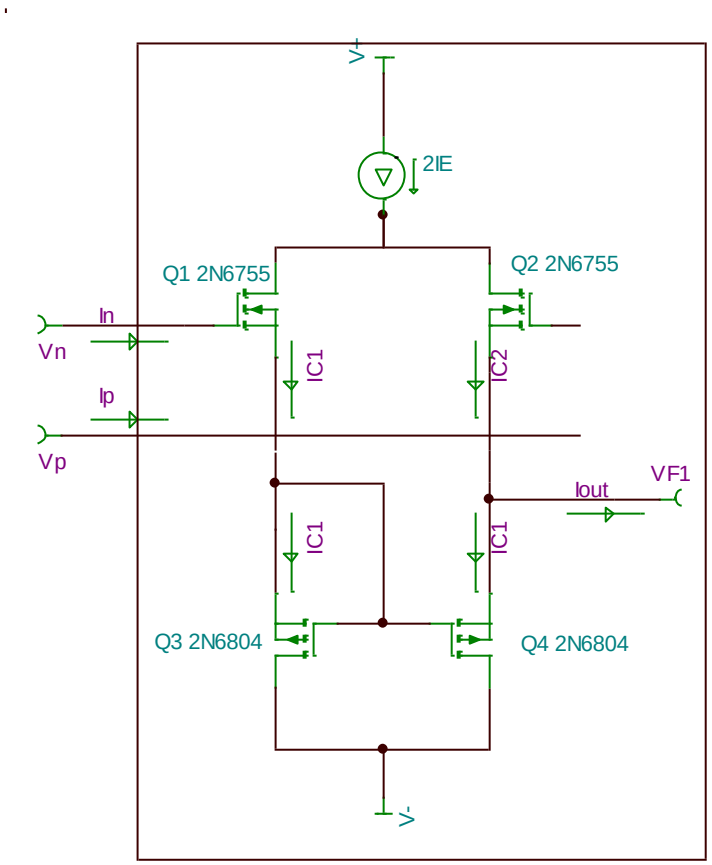


Figure 2.28: CMOS input stage of operational amplifier [34][36]

Figure 2.28 illustrates a differential CMOS input stage of op-amp. This arrangement enables low power consumption and rail-to-rail application. Like JFETs, CMOS offers low bias current, high input impedance and reasonable performance in high frequency.

An input using FET or JFET in the op-amp can provide the instrumentation amplifier with both a high input impedance and high CMRR. Some reports indicate a 60 dB CMRR at 1 MHz using FET buffered inputs [36]. Whilst some new CMOS input instrumentation amplifiers can achieve very high input impedances of the order of 10^{13} Ω (INA332/2332, Texas Instruments).

For low input bias currents, the FET input op-amp is typically a few hundreds of pA and the CMOS input op-amps (INA332/2332, Texas Instruments) can achieve as low as a few pA. However, in order to take advantage of a high input impedance, high CMRR and low input bias current, there is a trade-off with bandwidth.

Therefore, the improved instrumentation system is comprised of two optimised stages. For the first stage, two single FET input op-amps play the role of buffer as FET op-amps can achieve extremely high input impedances, high CMRR and low input bias current. Because they work as a buffer with small gain, the FET op-amp can easily achieve bandwidths up to multiples of MHz. The second stage is an instrumentation amplifier, which has low noise and high bandwidth. Figure 2.29 shows the two stage combination instrumentation amplifier in order to combine the high CMRR, input impedance, bias current, low noise and wide bandwidth.

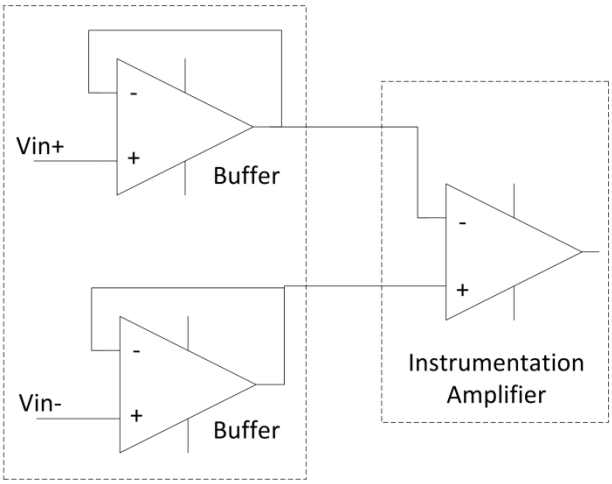


Figure 2.29: Two stage combination instrumentation amplifier

The effect of common-mode voltage in the sense part is also needed to be reduced in order to improve the system. Among the solutions, the usage of rail to rail and dual supply op-amps increases the acceptance of common-mode signals in the

instrumentation amplifier. Therefore, two FET input, rail to rail op-amps were used as buffers for the first stage, and connected together with AD8429 for the second stage.

Parasitic / stray capacitance degrades the input impedance of the sense circuit especially at high frequencies. Also, parasitic capacitances arise in the measurement apparatus such as between the cable leads and ground, the injecting electrodes and the sensing electrodes as well as the patient and ground [24]. In order to increase the reliability in the presence of parasitic capacitance, the actual input current value should be measured using a reference resistor connected in series with the DUT Figure 2.30 shows the diagram of this "Two Reading Method" setup [22] for impedance measurement.

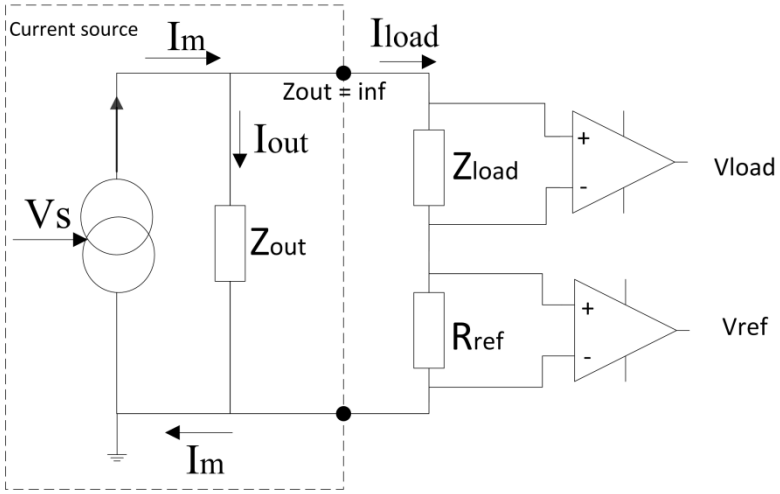


Figure 2.30: Diagram of two reading method setup

The measured impedance is given by the product of the reference resistor and quotient of the two voltage readings from the formula [22]:

$$Z_{load} = R_{ref} \frac{Vload}{Vref} (\Omega) \qquad (2.5.27)$$

Both instrumentation amplifiers in Figure 2.30 must have the same characteristics such as frequency response and bandwidth. However, the gains of the two instrumentation amplifiers are different. i.e. the first amplifier uses a gain G of 5 to measure voltage drop at the impedance load Z_{load}, however second amplifier has a gain G of 1000 in order to sense the small current flowing through the reference resistor R_{ref} in cases where the impedance load Z_{load} has very high impedance. This therefore creates an imbalance between the amplifiers as the characteristics (CMRR, bandwidth, input impedance) of the same instrumentation amplifier is different at different set up gains.. A two stage amplifier will help to reduce this problem by sharing the gain using a cascading setup such as a buffer amplifier having a gain G_1 = 100 and the instrumentation amplifier having gain G_2 = 10, so the total gain is 1000.

Resistor R_{ref} is used not only for measuring the current injected into the tissue but also for checking the current flow through the tissue following the British Standard safety regulation [23]. In order to remove the common mode voltage problem whilst measuring the current, this reference current is passed through a series resistor after the DUT. In this manner, the series resistor is close to ground and hence the magnitude of the potential across the resistor is limited. According to Figure 2.30 above, the actual current is measured in series after the DUT and near the ground line in order to avoid the common mode voltage problem.

2.5.4 Noise and minimum detectable signal

Introduction to Electronic noise

Electronic noise originates both from the components within a circuit and also from external sources which can be noise or unwanted signals such as mains and radio interference. The amount of noise in a circuit can determine the minimum detectable

signal. In analogue circuits, noise can be reduced but never eliminated completely through analogue or digital filtering along with signal averaging. It is nevertheless best to minimise noise in the original signal as much as possible before any filtering takes place.

Noise type and origin

Firstly, it is important to explain the units of noise. The noise power in the time domain is proportional to the bandwidth, B, of noise in the frequency domain. The noise power spectral density is defined as $V_n^2 = \frac{Vnoise^2}{B}$ (V^2/Hz). The noise voltage density is therefore given by $V_n = \frac{Vnoise}{\sqrt{B}}$ ($V/\sqrt{Hz}$). Similar to noise voltage density, the noise current density is given by $I_n = \frac{I_{noise}}{\sqrt{B}}$ ($A/\sqrt{Hz}$).

With this in mind the various electronic noise sources are as follows:

(a) Johnson or Thermal Noise: This is the electronic noise arising from the thermal random motion of carriers present in conductors and resistors.

The noise voltage due to this thermal noise is given by: $V_{noise} = \sqrt{4kTBR}$; where T is the temperature in Kelvin (K), k is Boltzmann's constant (1.38×10^{-23} JK^{-1}), B is the bandwidth and R is the resistance in Ohms. The equivalent thermal current noise is expressed as: $I_{noise} = \frac{Vnoise}{R} = \sqrt{\frac{4kTB}{R}}$ and is illustrated in Figure 2.31.

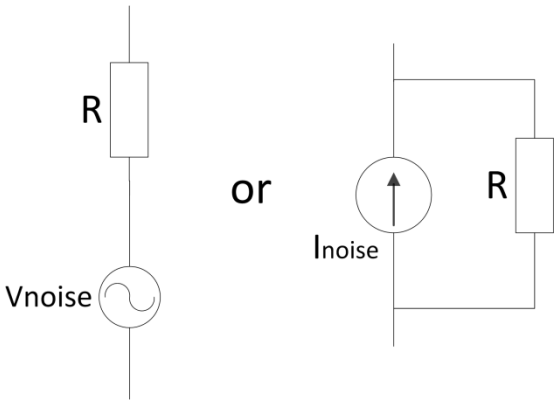


Figure 2.31: Equivalent models of thermal noise voltage and thermal noise current in a resistor

(b) Shot Noise: This is dictated by the randomness of the DC current and is present in diodes and transistors. The rms shot noise is represented by a noise current and is given by: $I_{noise} = \sqrt{2qIB}$, where q is the electron charge and I is the DC current and B is the bandwidth. In a diode for example shot noise is represented as a noise current source I_{noise} in parallel with the dynamic resistance of the diode - see Figure 2.32:

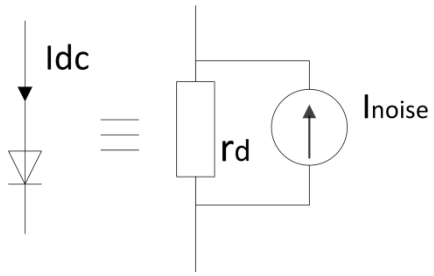


Figure 2.32: Shot noise in the diode.

Where $r_d = \frac{kT}{qIdc}$ and $V_{shot} = I_{shot} \cdot r_{d.}$

Both thermal noise and shot noise are white which means that its noise spectral density does not depend upon frequency as illustrated in Figure 2.33:

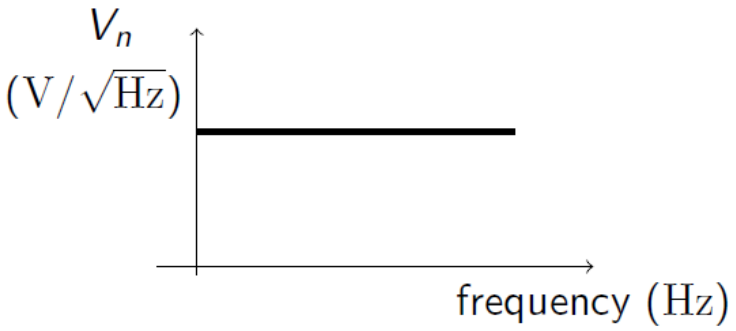


Figure 2.33: Thermal or shot noise voltage density over frequency is white.

(c) **Flicker noise:** 1/f or flicker noise is caused by many factors. One of these factors is Charge Trapping. Charge trapping occurs in diodes and transistors due to crystal defects. The flicker noise is represented by a current given by $I_{flicker} = \sqrt{K_1 \frac{I^a}{f^b} B}$, where B is the bandwidth at frequency f, I is DC current flowing, K_1 is constant for particular device, a is exponent in the range 0.5-2, b is exponent of around unity i.e. 1/f. The Flicker noise spectrum is shown in Figure 2.34.

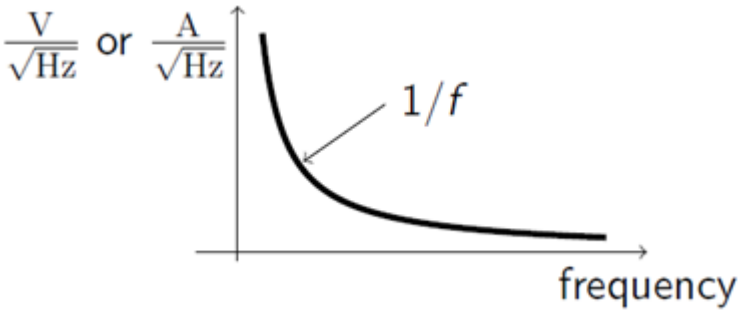


Figure 2.34: Flicker noise voltage or current density over frequency

Burst noise: is found in integrated circuits and transistors. This noise is thought to come from the defects and contamination in the device.

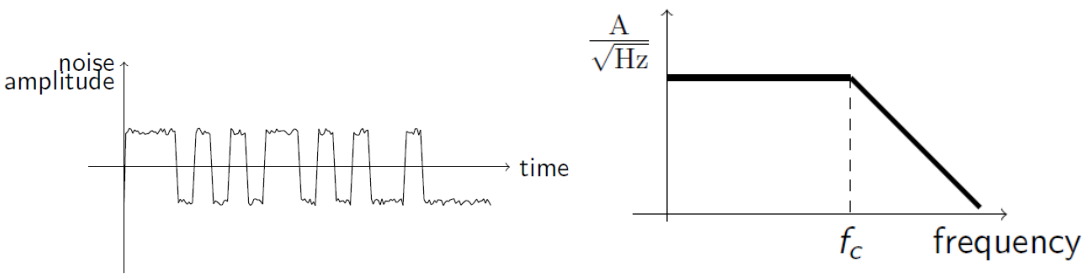


Figure 2.35: Burst noise in time and frequency domain.

Operational Amplifier noise voltage and current:

By way of example the noise of an inverting amplifier shown in Figure 2.36 using the OPA657 (Texas Instrument) op amp is illustrated next. From the data sheet the voltage and current noise of the OPA657 is V_n = 4.8nV/$\sqrt{Hz}$ and I_n = 1.3fA/$\sqrt{Hz}$ respectively (OPA657, Texas Instrument). Assuming the temperature T = 300˚K and Boltzmann's constant k = $1.38.10^{-23}$ JK^{-1}, then the thermal noise for Ri and Rf can be added to the circuit leaving R_i and R_f as noiseless resistors.

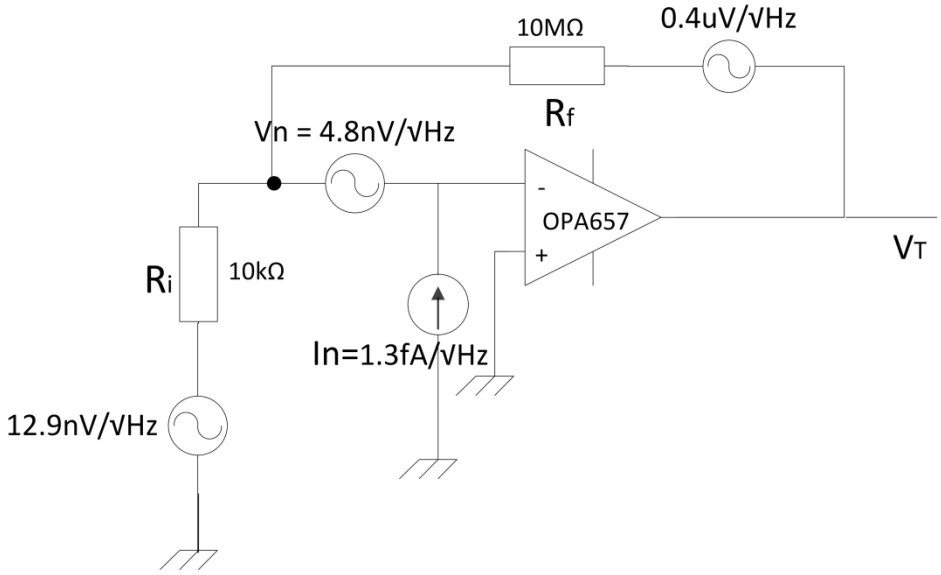


Figure 2.36: An example of noise in inverting amplifier configuration using OPA657

The total noise density is given by $V_T = \sqrt{V_1^2 + V_2^2 + \cdots + V_N^2}$ and deriving each noise component as follows:

Noise voltage density in the resistor R_i: at the input $V_{Ri}^{input} = \sqrt{4kTRi}$ = 12.9 nV/$\sqrt{Hz}$. This voltage will be amplified with G = $\frac{Rf}{Ri}$ = 1000 at the output. The

output noise voltage density due to R_i will be V_{R1}^{output}= G × V_{R1}^{input} = 1000 × 12.9 nV/$\sqrt{Hz}$ = 12.9μV/$\sqrt{Hz}$.

Noise voltage density in the resistor R_f: The noise density of R_f is already at the output of the amplifier, therefore it is not amplified and its contribution at the output is: V_{Rf}^{output} = $\sqrt{4kTRf}$ = 0.4 μV/$\sqrt{Hz}$.

Noise from input current density I_n : This current flows through the resistor R_f and is presented as a voltage at the output of value: $V_{noise\ current}^{output}$ = I_n × R_f = 1.3 × 10^{-15} × 10^6 = 1.3 nV/$\sqrt{Hz}$.

Noise from input voltage density V_n of OPA657 at the output: V_n^{output} = V_n × $\frac{R1+Rf}{R1}$ = 4.8 nV/$\sqrt{Hz}$ ×1001 = 4.8 μV/$\sqrt{Hz}$.

The total noise seen at the output of the amplifier OPA657 is V_T = $\sqrt{(V_{R1}^{output})^2 + (V_{Rf}^{output})^2 + (V_{current}^{output})^2 + (V_n^{output})^2}$ = 13.8 μV/$\sqrt{Hz}$.

To determine the corresponding noise density at the input to the amplifier, the output total noise is divided by the gain of the amplifier V_T^{input} = 13.8 / 1000 = 13.8 nV/$\sqrt{Hz}$. The bandwidth B is defined as the cut off frequency of the lock-in amplifier. The lock-in amplifier is set to cut off at B = 20 Hz. The corresponding input noise voltage is V_{RMS}^{input} = V_T^{input} × $\sqrt{B}$ = 13.8 nV/$\sqrt{Hz}$ × $\sqrt{20}$ = 61 nV rms. The theoretical minimum detectable signal voltage at the input needs to be higher than the corresponding input noise voltage. i.e. typically three times higher than the rms corresponding input noise voltage. For example, if the input voltage is 30 nV rms, then it cannot be distinguished from noise background. However, 90 nV rms should be adequate for minimum detectable signal in this circuit.

2.6 Review of EIS measurement systems

Voltage source versus current source in EIS/EIT

There are two kinds of generator source in EIS: voltage source (VCVS) and current source (VCCS). The conventional way is the use of a current source, which is used in the majority of existing bioimpedance EIT/EIS systems. It converts the reference voltage to an applied current, and then passes this into the tissue theoretically at a constant amplitude. The major existing EIT systems are operating in the region 20 Hz to 1MHz [38][39][40][41][42][43][44] as reported in the review table 2.1.

The use of voltage sources or voltage controlled voltage source (VCVS) is also reported in literature [45][46][47][48][49][50]. A voltage source applies a voltage to the tissue and the resulting current due to the tissue's impedance is monitored. An advantage of a voltage source over its current source counterpart is the ability to achieve a higher frequency of operation with higher accuracy in the injected current [51][52]. This is due to the fundamental principle behind the operation of a voltage source relative to a current driver: ie the voltage source has a low output impedance whilst a current source has a high one. In addition, the voltage source can measure a larger load ($\geq$ 50kΩ) with a stable bandwidth compared to a current source [53]. Consequently, any associated parasitic capacitance will further degrade the output impedance characteristic of a current driver compared to a voltage source. Conclusively, a voltage source therefore is able to perform higher accuracy for a higher bandwidth with a higher range of load impedances. It can be seen from the literature that the existing EIS systems based on voltage are operating from 100 Hz to 10MHz [45][46][47] [48][49] as reported in table 2.1.

Theoretically the choice of a current driver does not require constant monitoring of the injected signal and can be used to set the current up to the safety limit. In contrast, the voltage source requires constant monitoring of the injected current as it could reach over the safety limit and in addition knowledge of the current is necessary in order to determine the impedance of the DUT.

Voltage driven system and current driven system are different in terms of output impedance due to the electrical characteristics of each system. i.e. the current source needs to maintain high output impedance, but the voltage source has low output impedance.

The review table shown in Table 2.1 illustrates the performance of both current source EIT/EIS and voltage source EIT/EIS systems.

Author	Sheffield systems by (Brown et al[38][39]) (2001)	UCL mark I (Yerworth et al [41]) (2002)	Kyung Hee KHU mark I system [40] (2007)	Rensselaer Polytechnic Institute ACT 3 (Gary et al[42]) (1994)	Yang et al [43] (2006)	UCL new system by Hong et al[44] (2009)	Dartmouth system (Hartov et al [45][46][47]) (2004)	Kyung Hee new KHU mark II system[48][49] (2012)	Rensselaer Polytechnic Institute new ACT4 Gary et al[13] [50] (2007)
Method	CS	CS	CS	CS	CS	CS	VS	VS	VS
Output current (I_0)	Max 1 mA	100µA @≤1kHz to max 3mA	0.2 to 2 mA	Max 0.5mA	Max 140 µA	Max 500 µA	Max 50 mA peak	Max 1.85mA	Max 1mA
Bandwidth	1kHz – 1MHz	4.8–77 kHz	10Hz – 500khz	300Hz – 1MHz	20 kHz to 1 MHz	10 kHz – 1MHz	0 to 10MHz	10 Hz to 2.2 MHz	3.33 kHz to 1 MHz
Output Impedance (Z_0)	670kΩ@ 100kHz 330kΩ@ 300kHz	537kΩ@ 225Hz 73 kΩ@ 77kHz	3MΩ@10Hz 4MΩ@55kHz 3.8MΩ@ 250kHz	~64MΩ@ 30 kHz	N/a	>1MΩ@ 100kHz, >160kΩ@ 1MHz	0.135Ω@ 10kHz, 13.5Ω@ 1MHz	Estimated 0.3 Ω@ up to 1MHz, 3Ω @10MHz	Estimated 50 Ω@ up to 1 MHz
Impedance load test	50Ω - 1kΩ	330Ω - 1kΩ	Max 1kΩ	0 - 1kΩ	9Ω-5.7kΩ	100Ω to 1kΩ	Up to 1kΩ	10Ω - 10kΩ	Up to 1kΩ
THD or SNR	40 dB SNR	50 dB SNR	0.0002%THD, 76-99dB SNR	104 dB SNR	N/a	0.79%THD,	~0.316 %THD (-50 dB),77 – 96dB SNR	≤1 %THD, ≥60 dB SNR@1MHz	106 dB SNR
Voltage supply	10 V	N/a	N/a	N/a	≥10V	3V-5V	≥10V	≥10V	N/a
Application	Lung, cervix, thorax tissue	Brain	Brain, chest, abdomen.	Thorax tissue	N/a	Lung	Breast tissue	Breast	Breast

Table 2.1: the review table of existing EIT/EIS measurement systems (CS: Current Source Configuration, VS: Voltage Source Configuration)

The output current $\mathbf{I_o}$ from current source configuration could reach a maximum of 3mA in UCL Mark I system. However, the output current from the voltage source can reach up to 50mA in the Dartmouth system. The voltage source EIS/EIT systems generally have higher output current compared with current source systems.

The bandwidth using the current source systems reported in [38][39][40][41][42][43][44] from table 2.1, shows the maximum bandwidth achieved was up to 1MHz in the Sheffield system, Rensselaer system, and Yang; while the bandwidth using the voltage source system reported in [45][46][47] can go up to 10MHz.

The output impedance of current source EIS/EIT systems such as the UCL system by Hong et al can achieve higher than 160kΩ at 1MHz, the Sheffield system can achieve 330kΩ at 300kHz, while Kyung Hee KHU mark I system can have output impedance 3.8MΩ at 250kHz. On the other hand, the voltage source systems maintained a low output impedance e.g. Dartmouth system has 13.5Ω at 1MHz, Kyung Hee new KHU mark II system has up to 3Ω @10MHz.

The impedance load tests in review table 2.1 are up to 1kΩ in most of the systems using a current source. However, Yang et al [43] used up to 5.7 kΩ load test, Kyung Hee new KHU mark II system [48][49] using voltage source can measure up to 10kΩ load test. The reason why systems used 1kΩ impedance load test could be that most of the biological tissues have quite low impedance. Gabriel *et al* [49] reviewed the literature and found 75% of biological tissues have impedance in the range of 50Ω to 1 kΩ [49] except for the skin, fat and bone. According to the resistivities for various tissues from Faes et al [54], the resistivities of the tissue covered a large range from 10^2 to 10^9 Ω. Human skin conductivity could go up to 10^{-5} S/m at 10Hz by Yamamoto [17]. Within a particular tissue, however, the range was comparatively

small, with the exception of the stratum corneum results (Yamamoto [17]), the skin results from Gabriel et al [15] and also in observations for bone and muscle [54]. In other words, the resistivities of skin can cover a large range, which may be not suitable for low impedance (i.e. 1kΩ) measurement systems.

In terms of signal to noise ratio (SNR), the Sheffield system is 40 dB, UCL Mark I is 50 dB, Kyung Hee KHU mark I system is 76-99 dB, Rensselaer Polytechnic Institute ACT 3 is 104 dB, Rensselaer Polytechnic Institute new ACT4 can achieve up to 106 dB, Kyung Hee new KHU mark II system has even higher 60 dB SNR at 1MHz.

The systems in the table 2.1 are used for imaging applications such as in lung, cervix, thorax, brain, chest, abdomen or breast tissue. There is no human skin application.

To conclude, the voltage source configuration offers the possibility to measure higher load with higher bandwidth compared with a current source [53]. The current impedance load test of the EIS system may be not suitable for human skin, which can cover a large range of impedance. Also, the applications of EIS/EIT systems for human skin, which can be benefit for skin care products or dermatology studies, are insufficient. Therefore, for human skin applications at low frequency 10Hz to 100 kHz, the voltage source is a preferred choice.

2.7 Review of bio-electrical models

This section is an overview of the electrical models that have been used in general biological tissue and in particular, human skin tissue. The extracellular fluid, intracellular fluid and cell membrane in the biological tissue represent the resistive and capacitive properties in the electrical system. In this review, there is an

assumption that an ideal current source and voltage meter are used to measure the electrical properties of these electrically equivalent models as shown in Figure 2.37

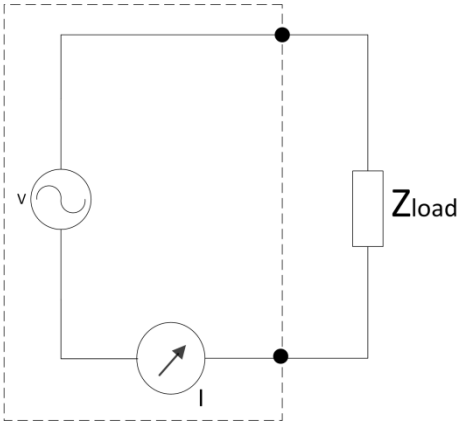


Figure 2.37: Ideal voltage source and current measurement in impedance measurement.

Extra and intra-cellular fluid

The mechanism of ionic conductivity in biological tissue is that living cells must be contained or surrounded by aqueous electrolytes, such as in blood, which contains the most important cations such as H^+, Na^+, K^+, Ca^{++} , and Mg^{++} and anions such as Cl^-, HCO_3^-, $protein^-$, HPO_4^{--}, SO_4^{--}[1].

Cations (mmol/L) (millimole per Litre)			**Anions (mmol/L) (millimole per Litre)**		
	Extracellular	**Intracellular**		**Extracellular**	**Intracellular**
Na^+	142	10	Cl^-	103	4
K^+	4	140	HCO_3^-	24	10
Ca^{2+}	5	10^{-4}	$Protein^-$	16	36
Mg^{2+}	2	30	HPO_4^{2-} + $SO4^{2-}$ and organic acids	10	130

H^+	4×10^{-5}	4×10^{-5}			
Sum	**153**	**180**	**Sum**	**153**	**180**

0.9% NaCl is 154 mmol/L.(Concentration in mmole/litre of NaCl aqueous solution 0.9% to show the correlations between extracellular and intracellular fluid)

Table 2.2: The cations and anions concentration in extra-cellular and intra-cellular fluid [1]

The major intracellular cation is K^+ and the major extracellular cation is Na^+. The most important ions for extracellular conductance are Na^+ and Cl^- (0.9% NaCl in water means 9 g/1000 g = 9 g/L). From the relative atomic mass, the gram weight per mole is Na = 23g/mole and Cl = 35.5g/mole. Hence, 1 mol NaCl = 58.5g. 0.9% NaCl = 154 mmol/L. According to the molar conductivity of Na = 50 Scm^2/mol and Cl = 76 Scm^2/mol, the conductivity of 0.9% NaCl can be calculated by (50 + 76).0.154 $\times$ 10^{-1} = 1.94 S/m. The actual conductivity may be lower or higher due to nonlinearity in concentration i.e. sweat concentration is lower, while urine concentration is higher.

In general, different biological tissues of the body contain different conductivity values. Table 2.3 shows the conductivity of different biological tissue at low frequency 1 Hz – 10kHz:

Bio-material/ Biological tissue	**Conductivity σ (S/m)**
NaCl in water, 0.9% at 37 ℃	2
Blood at 37 ℃	0.7
Muscle	0.4
Liver	0.2
Human skin	10^{-4}

Fat	0.05
Lung	0.05 – 0.4
Urine	0.5 – 2.6
Brain	0.03 – 0.4

Table 2.3: Tissue conductivities in low frequency 1 Hz – 10kHz.[1]

In table 2.3 the skin conductivity is the lowest compared to other biological tissues. According to Gabriel [15] and Yamamoto [17], the conductivity of skin tissue varies from 10^{-4} S/m (1Hz) to 10^{-1} S/m (100kHz). As a result, several conductivity solutions were chosen for calibration purposes such as de-ionized water 7×10^{-4} S/m, Hanna Instrument calibration solution 46×10^{-4} S/m, 96×10^{-4} S/m, 580×10^{-4} S/m, and 1376×10^{-4} S/m. These conductivity solutions approximately cover the conductivity of typical human skin from low frequency to high frequency.

Skin Pigmentation

Human skin gets its colour from a pigment called melanin. Melanin is produced within the skin in cells called melanocytes and it is the main determinant of skin colour. The pigment producing cell is anchored to the basement membrane at the epidermal – dermal junction.

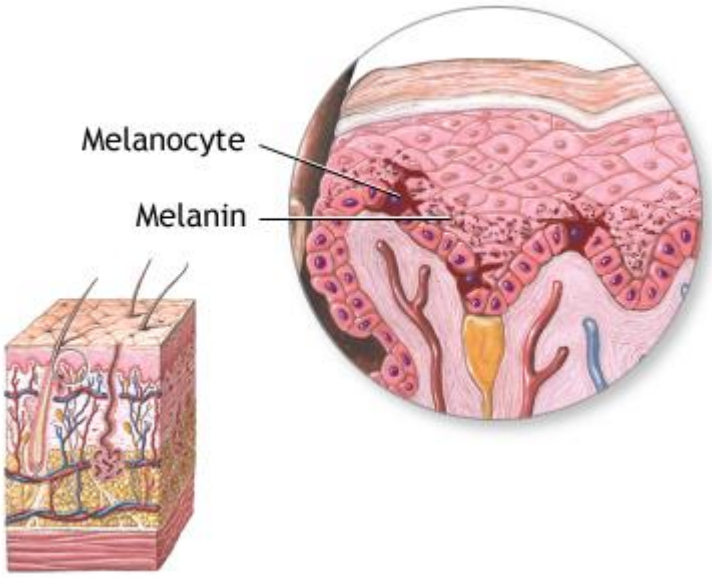


Figure 2. 38: Melanin of pigment is located at the basement membrane between epidermis and dermis.

If the body makes too much melanin, the skin will get darker. If the body makes too little melanin, the skin gets lighter. The melanin can absorb efficiently the UV radiation of the sun and thereby protect the DNA from the damaging effects of UV radiation [55]. There is no evidence or proof that shows the pigment might affect the skin impedance.

2.7.1 Basic models

The simplest equivalent circuit is the combination of one resistor and one capacitor: in parallel and in series. Table 2.2 shows the calculation of the impedance and the phase of the two-component circuits.

Parallel version	Series version

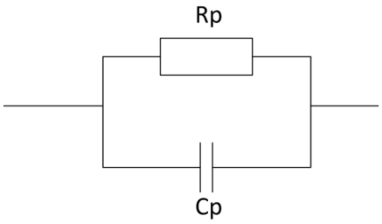
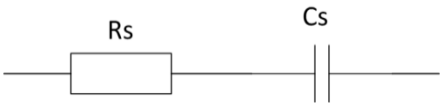
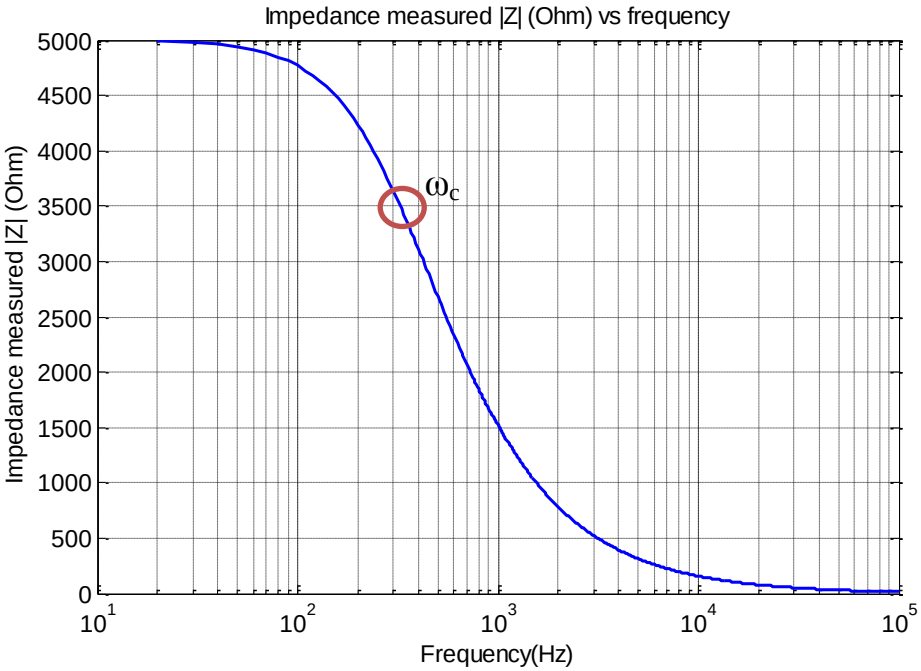
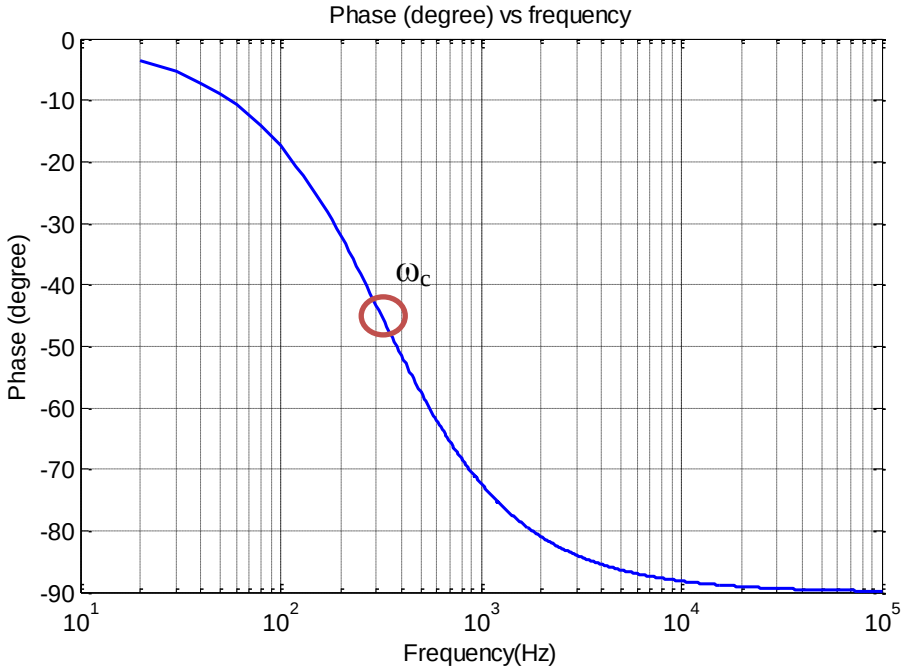
<table>
<tr><td>
</td><td>
</td></tr>
<tr><td>Reactance $X_c = 1/\omega Cp$
Impedance $Z = RpX_c / (\sqrt{Rp^2 + X_c^2})$
Phase $\theta = \tan^{-1}(Rp/Xc)$</td><td>Reactance $X_c = 1/\omega Cs$
Impedance $Z = \sqrt{Rs^2 + X_c^2}$
Phase $\theta = \tan^{-1}(Xc/Rs)$</td></tr>
<tr><td colspan="2">The Q factor between parallel and series RC:
$Q = \omega R_p C_p = 1/ (\omega R_s C_s)$
$C_p = C_s . (\frac{Q^2}{1+Q^2})$
$R_p = R_s . (1+ Q^2)$</td></tr>
</table>

Table 2.2: Calculation of the impedance and the phase of the two-component circuits in parallel and series.

The parallel version and series RC circuits have a mutual relationship to each other through the correlation Q factor [1]. Rosell et al [56] measured the skin impedance from 1Hz to 1MHz and reported that skin impedance can be modeled as a resistor in parallel with a capacitor in the low frequency range. The capacitance corresponds to that of the barrier layer of skin (Figure 1.3), whilst the resistance corresponds to that of this barrier layer (Figure 1.3). Also, Neuman [57] together with Yamamoto [17] represented the epidermis layers of the skin by an RC parallel version equivalent circuit. This comes from the fact that skin tissue contains resistivity and capacitive effects. Figure 2.39a shows the absolute impedance versus frequency whilst Figure 2.39b illustrates the phase versus frequency of a parallel RC arrangement with R_p = 5kΩ and C_p = 100nF (with cut off frequency $\omega_c = 1/(2\pi R_p C_p)$ = 318 Hz). Figure 2.40 shows this RC model plotted in real and imaginary graph.



(a) The impedance versus frequency of parallel version R_p = 5kΩ and C_p = 100nF.



(b) The phase versus frequency of parallel version R_p = 5kΩ and C_p = 100nF.

Figure 2.39: Impedance (a) and phase (b) versus frequency of of parallel version R_p = 5kΩ and C_p = 100nF.

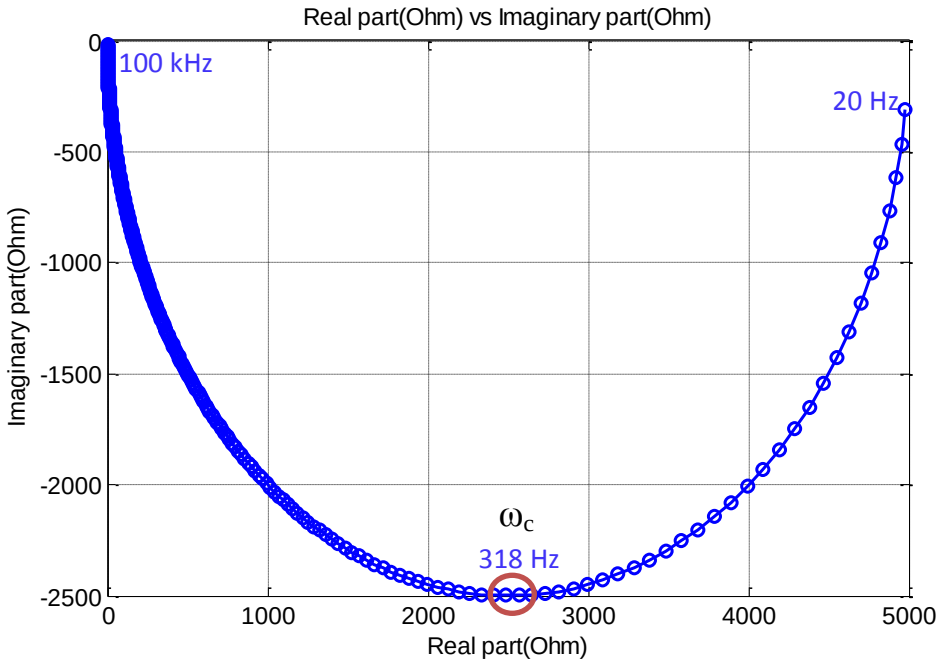


Figure 2.40: The real and imaginary parts of an RC parallel circuit with R_p = 5kΩ and C_p = 100nF.

From the impedance Z and phase in Figure 2.39, a real component versus the imaginary component can be plotted as shown in Figure 2.40. This has a semi-circular shape because it represents a characteristic of traditional RC circuit. For example, the complex impedance Z = $\sqrt{R^2 + X^2}$, which contains a resistance component (real) R with a reactance component (imaginary) X, can usually create the semicircle in real vs imaginary plot. On the other hand, using a simple RC circuit to model the skin may not accurately represent the electrical characteristics of the skin. It is therefore necessary to have a more detailed model in order to generalize the electrical properties of skin. In the next section, a three element component is discussed to try to model the skin tissue more accurately.

2.7.2 RC networks including 2 resistors and one capacitor

Unfortunately, the two-component circuit described above is too simple to generalize the frequency dependent skin impedance [1]. Therefore, it is suggested that a three-

component or more model can be used to represent the skin impedance [1]. It may contain two resistors and one capacitor or two capacitors and one resistor in either parallel or series. Lapicque et al [3] investigated a 2R-1C series version, to model different biological materials such as nerve membrane, blood cells and other tissues. In addition, Frickle and Morse saw the impedance of red blood cells accurately fitted with the 2R-1C parallel version [3]. In this section, only two 2R-1C versions are discussed as its electrical properties have often been used for biological tissue such as extracellular fluid, intracellular fluid and the cell membrane [1] (Figure 1.2).

Specifically, the parallel version, in which one resistor R_s is in series with a capacitor C_s and two of them in parallel with R_p is best characterized by admittance. It has been used for cells and living tissue, with C_s for cell membranes, R_s for intracellular fluids and R_p for extracellular fluids [1] (refer to Figure 1.6).

On the other hand, the series version is best characterized by impedance. It has often been used as a skin electrical equivalent circuit, R_s for deeper tissue in series with the skin composed of R_p and C_p [1]. Table 2.3 below shows the impedance and the phase calculation for parallel and series 2R-1C circuit.

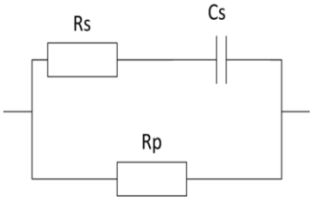
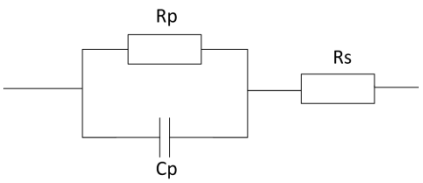
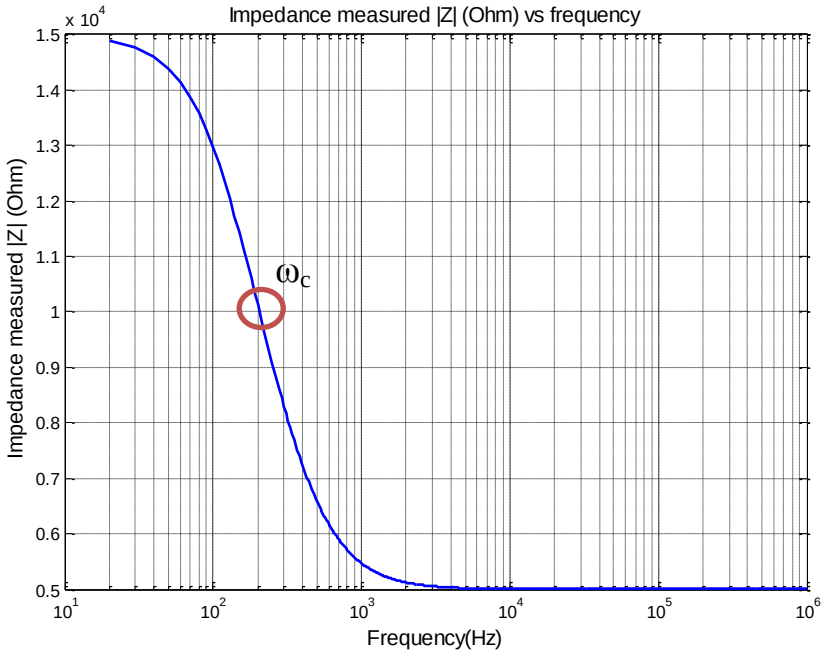
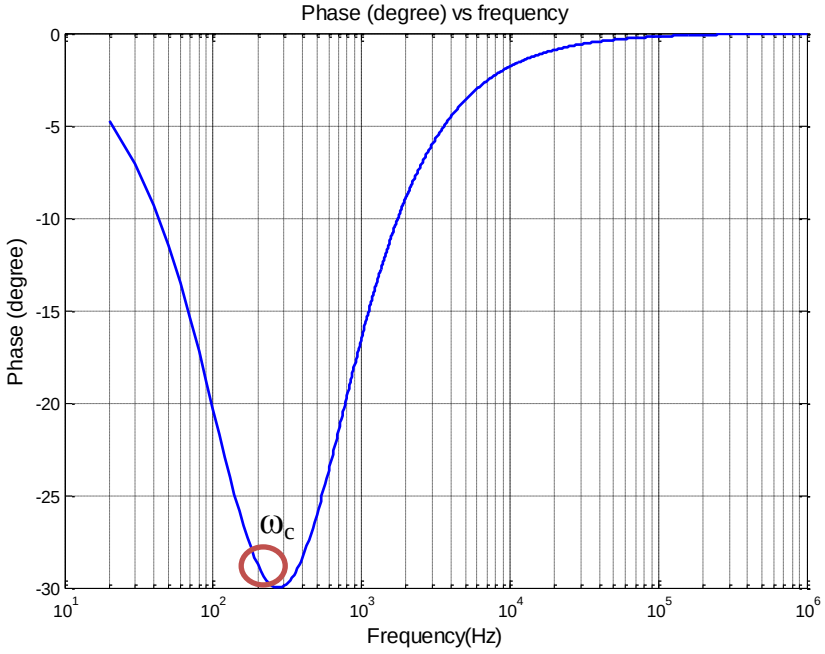
Parallel version	Series version
	
$R_p = 1/G$ impedance: $Z = [G + \omega^2C^2R(1 + RG) - j\omega C]/[G^2 + \omega^2C^2(1 + RG)^2]]$ phase: $\theta = \arctan(\omega C/[G + \omega^2C^2R(1 + RG)])$	$R_p = 1/G$ impedance: $Z = R + (G - j\omega C)/(G^2 + \omega^2C^2)$ Phase: $\theta = \arctan(\omega C/(G(1 + RG) + \omega^2C^2R))$

Table 2.3: The impedance and phase calculation of parallel and series 2R-1C circuit.



(a) the impedance versus frequency of the series version



(b) the phase versus frequency of the series version

Figure 2.41: The impedance (a) and phase (b) versus frequency of the series version of a three component skin model R_p = 10 kΩ, R_s = 5 kΩ, and C_p = 100nF.

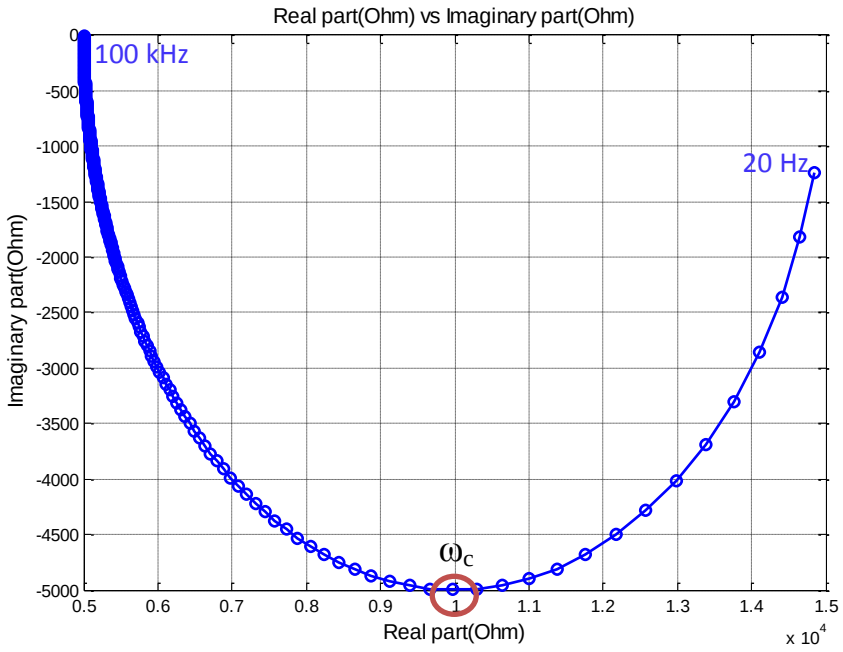


Figure 2.42: The real versus imaginary plots of a 2R-1C series circuit R_p = 10 kΩ, R_s = 5kΩ and C_p = 100nF.

In Figure 2.42, the semicircle in real vs imaginary plot can also be seen like the plot in RC model.

However, Fricke has shown that the three frequency-independent components model only satisfies red blood cells [3]. Therefore, it was proposed that a frequency dependent cell (R and C are themselves frequency dependent components) existed. Cole also observed that many cell membranes contained a frequency dependent capacitance and resistance [3]. In the next section, the frequency dependent C and R create a "Constant Phase Element".

2.7.3 Constant phase element (CPE)

Again, the three component models described above may be too simple to represent real biomaterials at all frequencies [1] since there maybe frequency dependent R and C components. According to Martinsen [1], a much better method uses non-ideal R

and C components that vary with frequency. It is assumed that this is a conductor in parallel with a susceptor, so the frequency dependence admittance Y = G + jB.

The phase angle ($\phi_{CPE} = \arctan B / G$) becomes frequency independent B_{cpe} / G_{cpe} = k, a constant. It is clear that in order to keep the phase angle constant, both G and B must depend on the frequency in the same way:

$$G_{cpe} = (G_{\omega=1})\omega^m \qquad B_{cpe} = (B_{\omega=1})\,\omega^m. \tag{2.7.1}$$

The units of G_{cpe} and B_{cpe} is siemens (S), so the units of $G_{\omega=1}$ and $B_{\omega=1}$ are [S/ω^m] or [$S.s^m$]. According to Martinsen [1], the introduction of τ with the dimension of time and forming the product $\omega\ \tau$ is of interest for two reasons:

1. τ represents a useful frequency scale factor.
2. The product $\omega\ \tau$ is dimensionless (an angle).

Equation 2.9 is changed to:

$$G_{cpe} = G_1\,(\omega\ \tau)^m \qquad B_{cpe} = B_1(\omega\ \tau)^m \tag{2.7.2}$$

Where G_1 and B_1 are values at $\omega\ \tau = 1$. Therefore,

$$Y_{cpe} = (\omega\ \tau)^m\,(G_1 + jB_1) \tag{2.7.3}$$

$$\phi_{cpe} = \arctan({}^{B_1}/_{G_1}). \tag{2.7.4}$$

Equation 2.11 and 2.12 determine a general CPE, which depends on $\omega\ \tau$, m, G_1 and B_1. If the m-values are restricted to positive values in the range $0 \le m \le 1$, then the admittance $\mathbf{Y}_{cpe}$ increases with frequency, in accordance with what is found for biological tissue. Also, the susceptance is the capacitive effect, meaning that B = ωC, and $B_1 = \frac{1}{\tau}C_1$ ($C_1 = C_{\omega\ \tau=1}$).

Therefore,

$$Y_{cpe} = (\omega\ \tau)^m G_1 + j\,\omega^m\,\tau^{m-1}C_1 \tag{2.7.5}$$

$$\Phi_{cpe} = \arctan {}^{C_1}/_{\tau\, G_1} \quad (2.7.6)$$

$$C_{cpe} = C_1(\omega\ \tau)^{m-1} \quad (2.7.7)$$

Let us examine the limits of frequency:

When $f \to \infty$, $\mathbf{Y}_{cpe} \to \infty$, even when C cpe → 0.

When $f \to 0$, $\mathbf{Y}_{cpe} \to 0$, even when $C_{cpe} \to \infty$.

Now examine the limits of m = 0 and m = 1:

m = 0: $G_{cpe} = G_1$, an ideal (frequency independent) resistor.

$C_{cpe} = C_1 / \omega\ \tau$: a frequency dependent capacitor

m = 1: $G_{cpe} = G_1\, \omega\ \tau$: a frequency dependent resistor

$C_{cpe} = C_1$, an ideal (frequency independent) capacitor.

In both cases the constant phase characteristic is valid with $\phi_{cpe} = \arctan C_1 / \tau\, G_1$.

With $G_1 = 0$ so $\phi_{cpe} = 90°$; and with $C_1 = 0$: $\phi_{cpe} = 0°$.

The series impedance version shows similar properties to the parallel version.

$$Z_{cpe} = (\omega\ \tau)^{-m} R_1 + j\,\omega^{-m}\,\tau^{-m+1} C_1 \quad (2.7.8)$$

$$\phi_{cpe} = \arctan {}^{-\tau}/_{R_1 C_1} \quad (2.7.9)$$

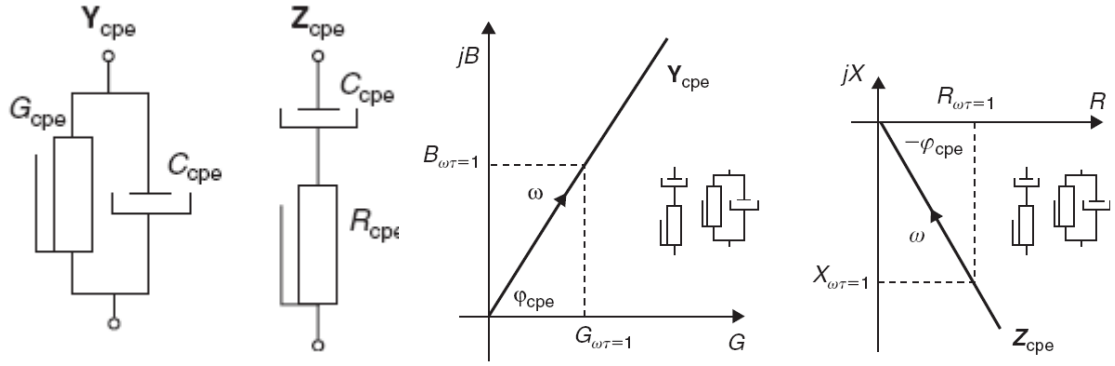
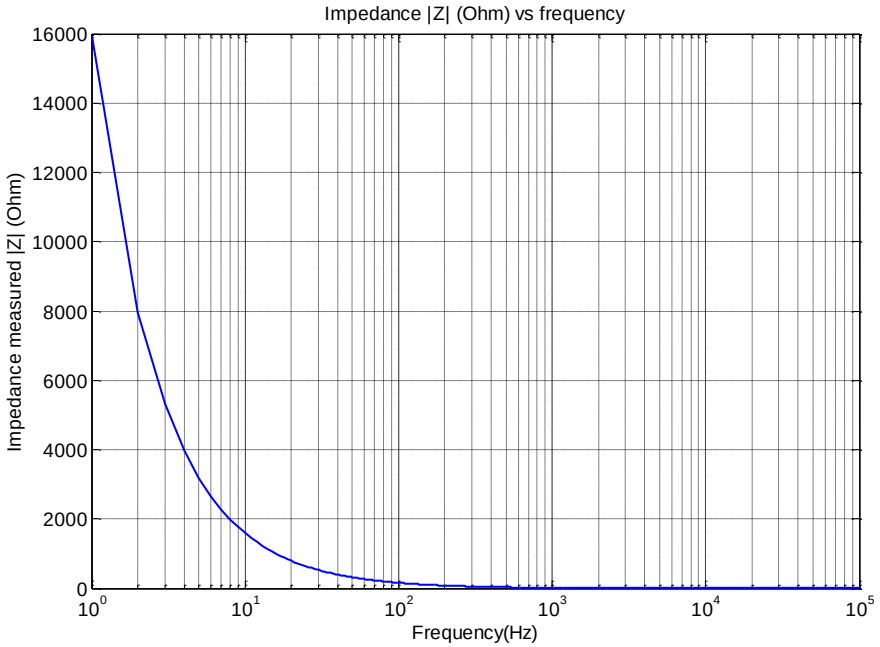


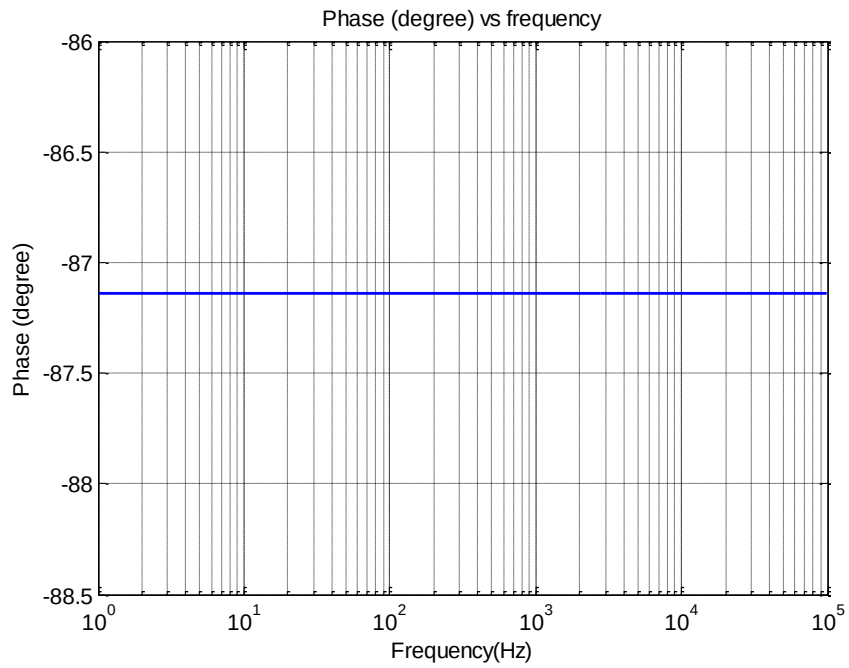
Figure 2.43: Equivalent circuits of Admittance Y_{cpe} (parallel version) and Impedance Z_{cpe} (series version) representations with the phase φ_{cpe} included for both models [1].

In Figure 2.43, the Admittance Y_{cpe} (parallel version) gives a constant slope of phase φ_{cpe} in the plot using real (G) versus imaginary part (jB). It also occurs with the phase slope φ_{cpe} of Impedance Z_{cpe} in the plot using real (R) versus imaginary part (jX). Compared to the two components and three components model, the phase of CPE is constant with frequency, therefore it is called a frequency independent component and it does not have the semi-circular shape.

For example, for the series version of the CPE circuit based on equation 2.7.8 and 2.7.9, with $\omega\ \tau\ = 1,\ \tau\ = 1$, m = 1, X = 1/ωC, R_1 = 5kΩ and C_1 = 10μF. The impedance, phase, real and imaginary part plots are shown in figures 2.24 and 2.25:



(a) The impedance versus frequency of CPE for the series version of equation 2.7.8 and 2.7.9



(b) The phase versus frequency of CPE for the series version of equation 2.7.8 and 2.7.9 showing constant phase through the frequency range.

Figure 2.44: The impedance (a) and phase (b) versus frequency of CPE for the series version of equation 2.7.8 and 2.7.9 with m = 1, X = 1/ωC, R = 5kΩ and C = 10μF

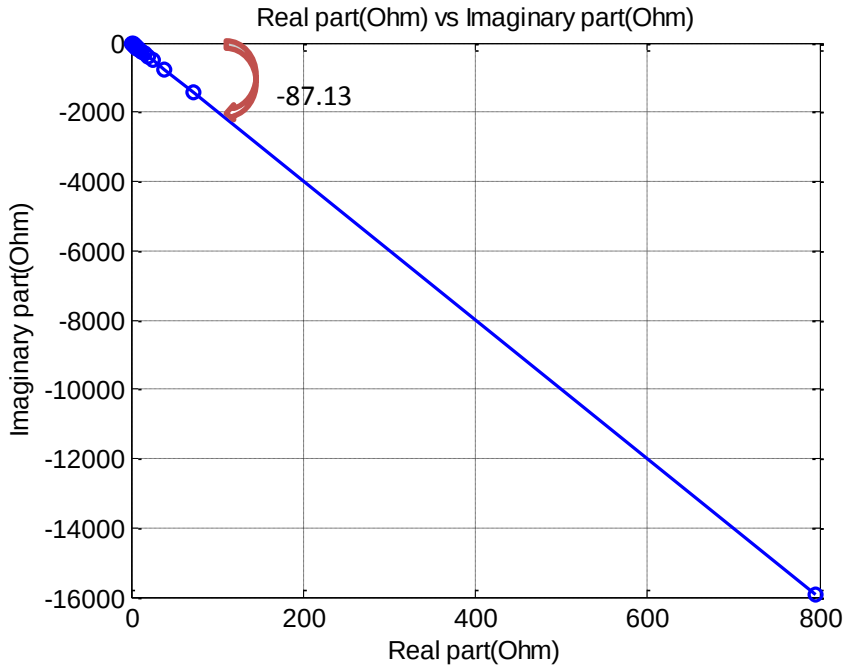


Figure 2.45: The real part versus imaginary part of CPE for the series version of equation 2.7.8 and 2.7.9 with m = 1, X = 1/ωC, R = 5kΩ and C = 10μF – note the constant phase results in a straight line slope plot.

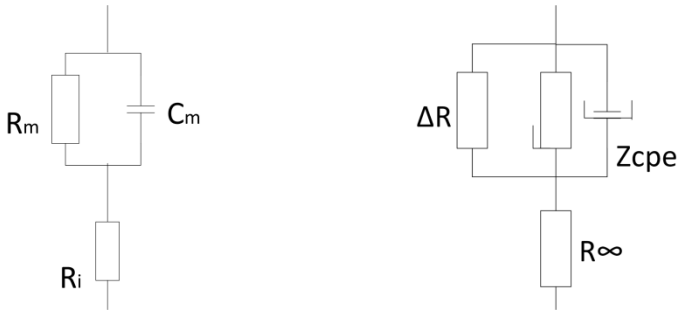
Since the appearance of the CPE, McAdams et al [58] used the "constant phase element" impedance Z_{cpa} to model several layers such as the electrode-electrolyte interface, epidermis and even dermis. Also, Cole had applied the CPE into his Cole equation [5] to model electrical properties of tissues and membranes.

2.7.4 Cole equation

After the CPA (Constant Phase Angle) concepts were popularized, Cole and Fricke published diagrams and equations based on a frequency independent phase angle [3][59][60][61][62]. Cole and Cole [3][61] proposed an empirical expression representing the electrical properties of the tissue and membranes. Cole and Cole [5] in 1941 showed an important turning point in the history of the tissue impedance modelling by demonstrating:

$$\mathbf{Z} = R_{\infty} + \frac{\Delta R}{1+(j\omega/\omega_0)^{\alpha}}\ \mathbf{[\Omega]} \quad \Delta R = R_0 - R_{\infty} \qquad (2.7.10)$$

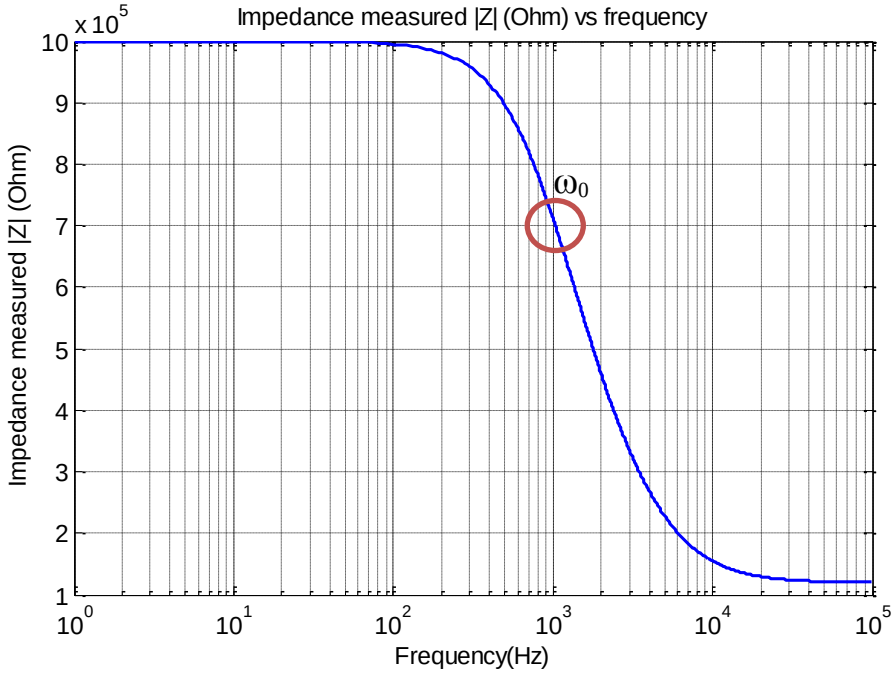
in which Z is the biological tissue impedance, R_{∞} is the resistance at very high frequency, R_0 is the resistance at low frequency, $\Delta R = R_0 - R_{\infty}$ and Z_{cpe} is a constant phase angle impedance. This equation can also be written in terms of complex impedance, which mathematically describes the frequency properties of Lapicque's electrical circuit, with the capacitor replaced by a CPA element [3] as shown in Figure 2.46. Since then, the biological tissue could be represented by Cole equation [5] proved a useful discovery in measurement of the electrical properties of tissues and membranes. Hence, the Cole model had been widely used to represent the electrical properties of biological tissue and other materials and interfaces [3]**.** More specifically, the complex impedance |Z| of tissue can be expressed as a function of frequency in order to characterise the tissue. Figure 2.46 shows the model of typical complex impedance for biological tissue. The physical terms of these parameters are later described in Chapter 5.



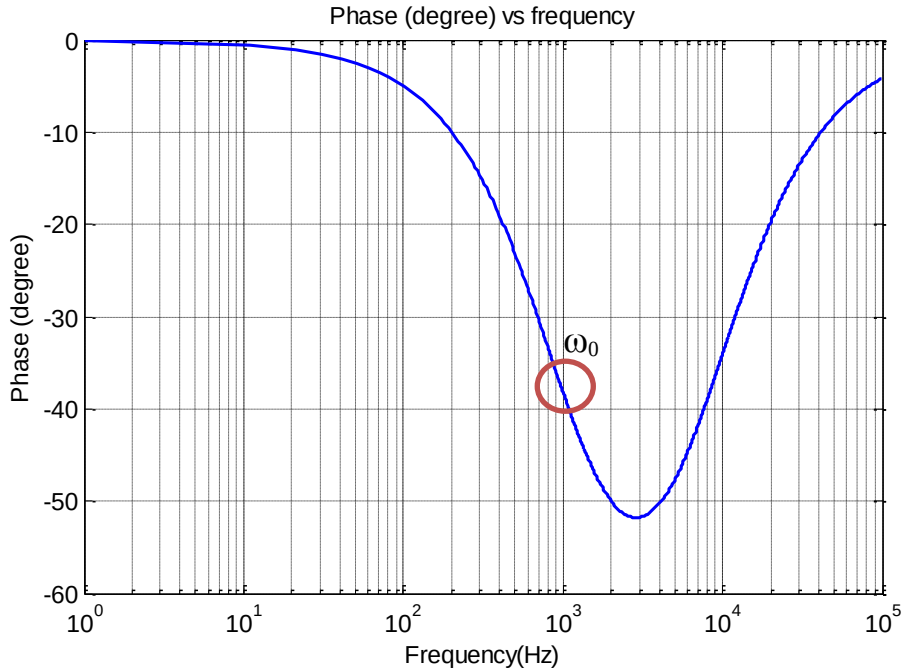
(a) **(b)**

Figure 2.46: The Lapicque equivalent circuit model (a) and the complete Cole model system (b), in which R_∞ is the resistance at very high frequency, R_0 is the resistance at low frequency, $\Delta R = R_0 - R_\infty$ and Z_{cpe} is constant phase angle impedance.

For instance, if the resistance $R_\infty = 1M\Omega$, $R_0 = 120k\Omega$, $f_0 = 1$ KHz, $\omega_0 = 6280$ rads/s, $\alpha = 1$, the impedance and phase versus frequency are shown in Figure 2.47, the real versus imaginary plot obtained is shown in Figure 2.48 .



(a) The impedance versus frequency of the Cole model



(b) The phase versus frequency of the Cole model

Figure 2.47: The impedance (a) and phase (b) versus frequency of the Cole model with $R_\infty = 1M\Omega$, $R_0 = 120k\Omega$, $f_0 = 1$ KHz, $\omega_0 = 6280$, $\alpha = 1$.

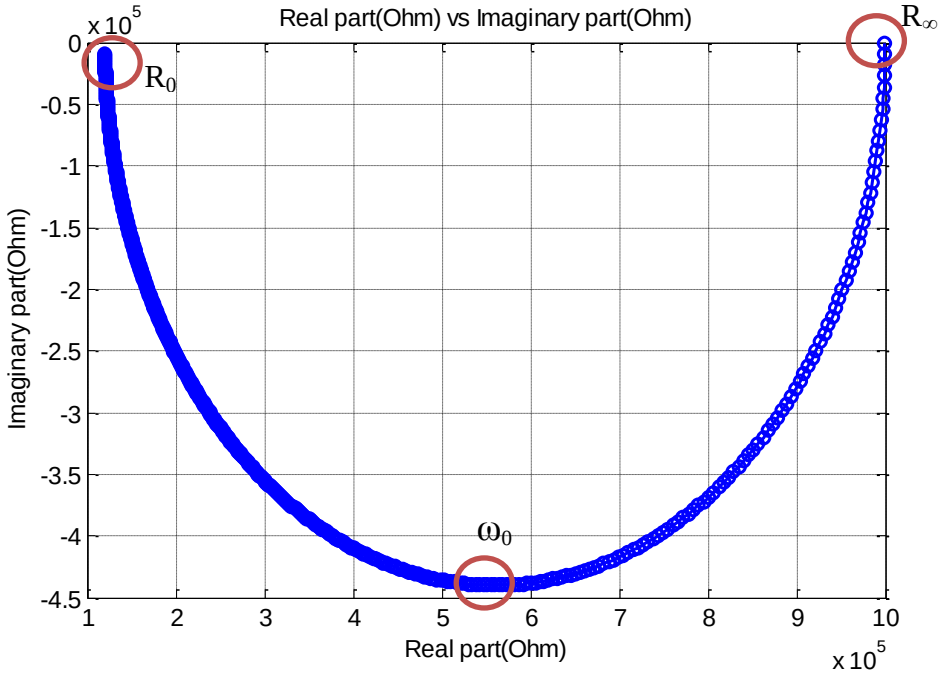


Figure 2.48: The real part versus imaginary part of the Cole model with R_∞ = 1MΩ, R_0 = 120kΩ, f_0 = 1 KHz, ω_0 = 6280, α = 1.

However, according to Grimnes and Martinsen [63], the Cole equation contains parameters which are incompatible with the theory of relaxation, and maybe not a good choice to fit with the experimental results. Also, a modification in the Cole model improved the modeling [63]. By introducing R_0 - R_∞ = 1/ΔG, the Cole equation from equation 2.18 becomes:

$$\mathbf{Z} = R_\infty + \frac{1}{\Delta G + \Delta G(j\omega/\omega_0)^\alpha}\ [\mathbf{\Omega}] \qquad (2.7.11)$$

By suggesting an independent ideal conductance G_{var} instead of ΔG, the equation then becomes

$$\mathbf{Z} = R_\infty + \frac{1}{Gvar + G1(j\omega/\omega_0)^\alpha}\ [\mathbf{\Omega}] \qquad (2.7.12)$$

The comparison between experimental and modelling results will be explored in Chapter 5.

2.7.5 Finite elements methods

The FEM (Finite Element Method) simulation can be used to model Maxwell's equations in biological tissue and provides a good approximation to model different geometries and allow for the evaluation of impedance values. However, there are several limitations to this method. There is a great variability in the contact impedance which occurs due to mismatches such as the area of contact for flat electrodes or the penetration depth for electrodes [64]. Biological effects, such as half-cell potentials and electrochemical processes [65] caused by AC currents with charge exchange between electrons and ions, can be difficult to model using FEM compared with the equivalent electrical circuits. In addition, sweat-gland activity

moistens the underlying skin and decreases the impedance [66], hence making it even harder to model [64]. This can be better approximated with an electrical circuit approach as discussed in the Cole model. For these reasons, the equivalent electrical models are preferred however FEM is useful for obtaining penetration depth and is used in Chapter 3.

2.8 Experimental Studies

The non-invasive contact of the EIS device with the skin makes its operation appealing for applications such as skin care, monitoring athletes and health/wellness assessment [74][75][76].

Body impedance, particularly when combined with the epidermal differential impedance sensors in a single system, can be valuable in human healthcare and wellness evaluation [74]. In this paper, an impedance analyser is used with epidermal differential impedance sensors to measure the changes in hydration level of skin. Using a commercial moisture meter (MoistureMeterSC Compact Delfin Inc), skin hydration level changes from 30 (dry) to 110 (wet) in arbitrary unit were measured. The experimental results demonstrated that the impedance results correlate with the arbitrary unit results when compared with moisture meter as shown in Figure 2.49.

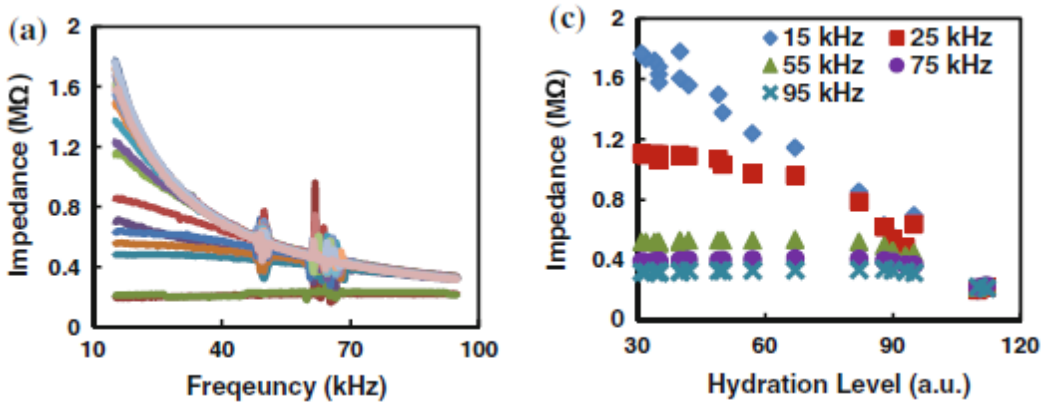


Figure 2.49: The correlation between impedance results and different hydration levels. (Right) the typical responses of changes in skin hydration at frequency 15 kHz to 95 kHz at various skin hydration level (different colors). (Left) Hydration level depends on the impedance amplitude at several selected frequencies [74].

Figure 2.49 shows the changes in impedance with skin hydration levels at selected frequencies. As the hydration increases, the skin impedance reduces significantly. For examples, when hydration level is 30, the skin impedance can reach up to 1.8 MΩ, and about 100 kΩ when hydration level is at 110. The highest sensitivity (change) is obtained at low frequency (i.e. 15 kHz) in this experiment. By comparing with the moisture meter, the assumption of low or high impedance values from the impedance meter can possibly represent the dry or wet status of the skin; therefore it is possible that this technique can be applied in healthcare and wellness measurement [74][75]. Hydration monitoring has significant value in performance during training and competition but also offers medical personnel the opportunity to reduce heath risks for atheletes [75]. It is also suggested that the moisture of skin is particularly sensitive in low frequency measurement.

EIS or Bioelectrical impedance spectroscopy (BIS) has the potential to be used in several applications. For example, BIS can measure the total body water and therefore it is in principle possible to derive the hydration status of the human body

[75][76]. One of the established applications of EIS is the ability to diagnose cervical intraepithelial neoplasia in the human uterine cervix developed by Brown et al [7][67][68][69][70][71][72][73]. In addition, it has been suggested that EIS could potentially become a non-invasive method for monitoring glucose levels in patients with diabetes [8][9].

Interestingly, BIS can be used to assess the condition of the skin, and so it also has the potential to measure the effect of specific creams on human skin [77]. For companies developing new cosmetic products it is important to be able to reliably characterize the properties of the skin in order to measure the effects of new products. The following sub-sections review some of the studies most closely related to the work in this thesis.

2.8.1 Cervical cancer detection by Brown et al

Cancer of the cervix is the second most common cancer affecting women in the world [7]. By applying the electrical current into human tissue, the resulting current flow can be used to determine the shape, arrangement and internal structure of tissue cell by relating the measurements to an appropriate model [7]. Brown et al have published several studies relating to the development and application of EIS for detecting cervical pre-cancers [7][14][37][67][68][69][70][71][72][73]. This method involves measuring the electrical impedance of human tissue through a range of frequencies and analyzes the inverse model of the resulting measurements.

A pencil-sized probe (with diameter 5 mm) with four gold probes arranged in a tetra-polar configuration has been used to measure the electrical impedance spectrum on the cervix. A colposcopy (a medical diagnostic procedure to examine an illuminated, magnified view of the cervix for detecting abnormalities) was also made together

with impedance measurement data on volunteers in order to compare two kinds of results [7]. The impedance measurements were made at eight different frequencies between 4.8 kHz and 614 kHz using the "Sheffield multi-frequency EIT system" [7][71]. A current of 10 μA was passed between a pair of electrodes, and the resulting potential was measured between the two remaining electrodes. Figure 2.50 shows the cervical measurement probe for cancer detection.

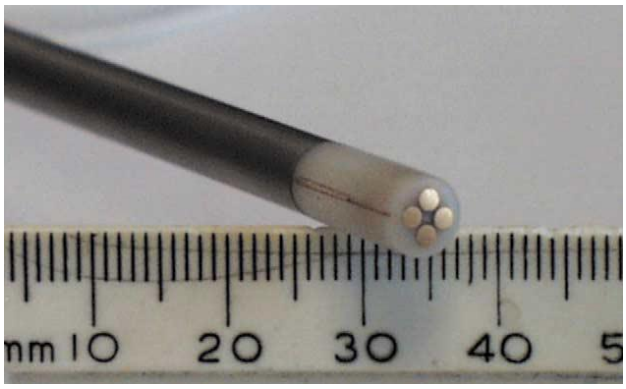
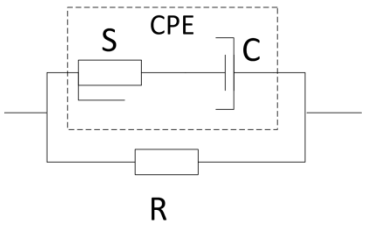


Figure 2.50: A pencil-sized cervical measurement probe used by Brown [7].

More specifically, colposcopy measurements were recorded by video allowing comparison with impedance measurements [7]. The Cole equation with an electrical circuit model has been used to form the impedance spectrum and then used to try to fit into the model described in section 2.7.4. By using a least square deviation method to the Cole equation, Brown et al [7] derived the formula for impedance as:

$$Z = R_{\infty} + \frac{(R_0 - R_{\infty})}{(1 + [jF/Fc])^{1-\propto}} \qquad (2.8.1)$$

In which R_0 is the impedance at very low frequency, R_{∞} is the impedance at very high frequency, F_c is the cut off frequency, and α is assumed as zero. The electrical circuit model is presented in Figure 2.51.



$$R_0 = R, \quad R_\infty = \frac{RS}{R+S}$$

$$F_c = \frac{1}{2\pi C(R+S)}$$

Figure 2.51: Electrical model in cervical measurement modelling by Brown et al [7]

In Figure 2.51, for modelling biological tissue, resistor R is related to the extracellular fluid, S is related to intracellular fluid and C to the cell membrane. According to [7][68][69], pre-cancerous phase stages, called cervical intraepithelial neoplasia (CIN), are divided into 3 stages: CIN1 (low grade), CIN2 and CIN3 (high grade). Brown et al made colposcopy and impedance measurements on 124 women and related this to the difference between normal tissue and CIN tissue shown in Figure 2.52.

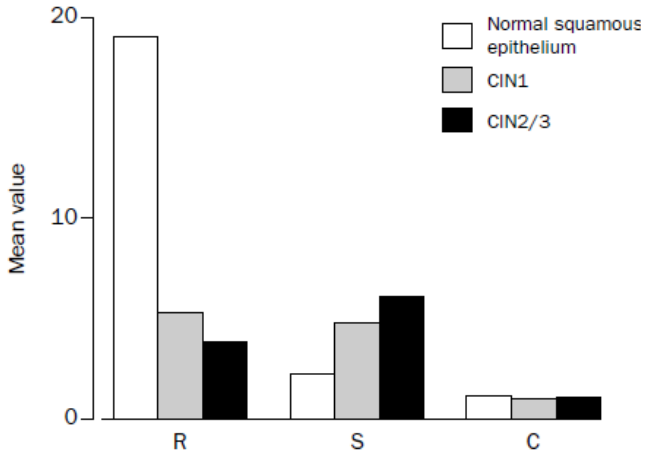


Figure 2.52: Mean value of R (Ω.m), S (Ω.m), and C (μF/m) in normal tissue, CIN1 tissue, and CIN2/3 tissue [7].

Brown et al [7] found that R is measured higher in the normal tissue, while R is lower in the case of CIN1 or CIN2/3. In contrast, S is lower in normal tissue and

higher in the CIN1 or CIN2/3. Finally, the C is shown unchanged in either normal tissue or CIN1 and CIN2/3.

The findings of Brown et al demonstrated the potential of electrical techniques using four point probes as a method of detecting precancerous stages in the cervix. Also, the results from the electrical impedance system suggested an explanation for the changes of cell arrangements and cell nuclei in biological tissues such as layering or the size of cell nuclei [7].

From the studies of Brown, it can be seen that it is important to have a custom made device to measure the skin impedance with respect to the specific application area. AC current, multi-frequency bioimpedance analyzer could measure the electrical spectrum of the skin, and would be appropriate for use in the skin tissue. Also, the four point probe sensor was demonstrated to be useful for detecting the change of the electrical properties of skin tissue. Based on the Cole equation, correlating the measurement results and modelling is also important for analysing the data.

2.8.2 Friction and Electrical Impedance in measuring the effects of lotions

The Centre for Tribology [78][79][81] in Campbell, California have conducted experiments to evaluate the effect of lotions on skin properties using friction and electrical measurement. This uses the two point probe technique described in section 2.3.1 in order to measure the surface resistance. Specifically, the friction coefficient and the electrical measurements are monitored simultaneously using a Biomedical Micro-Tribometer. In electrical measurement, a current of 10 μA with a frequency of 10 kHz was applied and the resulting voltage was measured across the probe [78]. According to their claims [78][79], the results allow for a quick assessment of skin conditions such as hydration, dryness, moisturization, and diagnosis of skin diseases.

In Figure 2.53, the friction and electrical impedance measurement is shown using a Tribometer system.

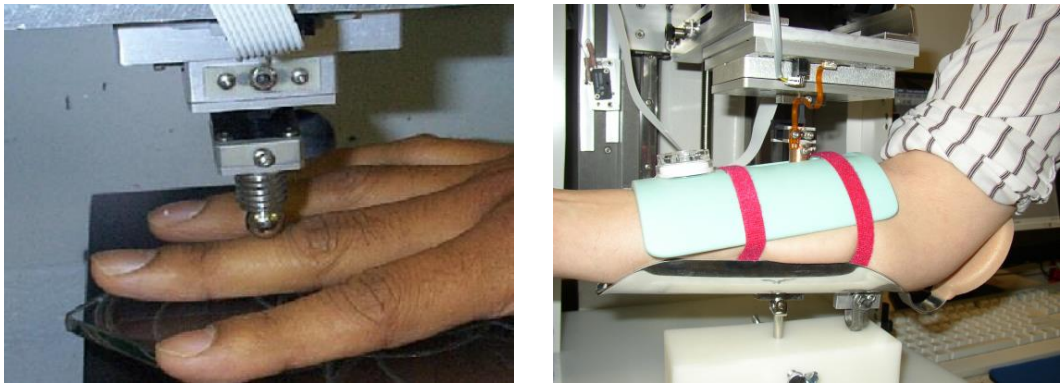


Figure 2.53: The Biomedical Micro-Tribometer measures the skin friction coefficient and electrical impedance of surface contact on finger (left) and forearm (right) [78][79].

The protocol was set to compare three different moisturizers in short term and long term measurement. Volunteers were tested on the same location on their right and left forearm [78]. The reference levels were measured before cream application. After the application of skin cream on volunteers, the friction (by strain-gauge sensor with constant load of 0.2N when skin testing) and electrical surface impedance were measured every 5 minutes for 1 hour, then after 5 hours and finally 24 hours [78].

According to [78][79], the results showed that the consistency and comprehensiveness of test data is higher than those obtained in previously known skin measuring instrumentation. Figure 2.54 and Figure 2.55 show the test results on the effects of different lotions on skin properties with friction coefficient and surface electrical impedance.

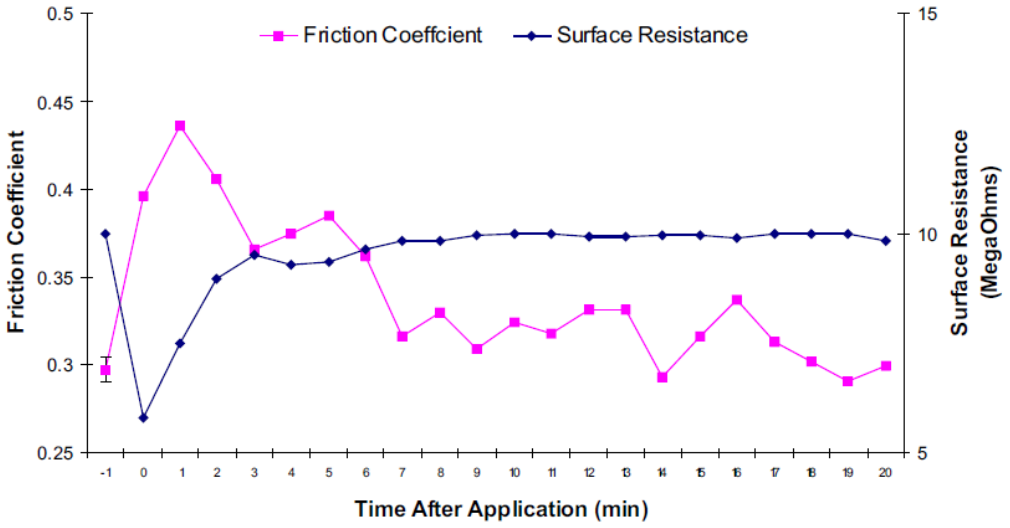


Figure 2.54: Friction and Electrical Surface Resistance after application of Lubriderm Skin Therapy Moisturizing lotion to the left Dorsal Middle Finger over a short period of 20 minutes [78][79].

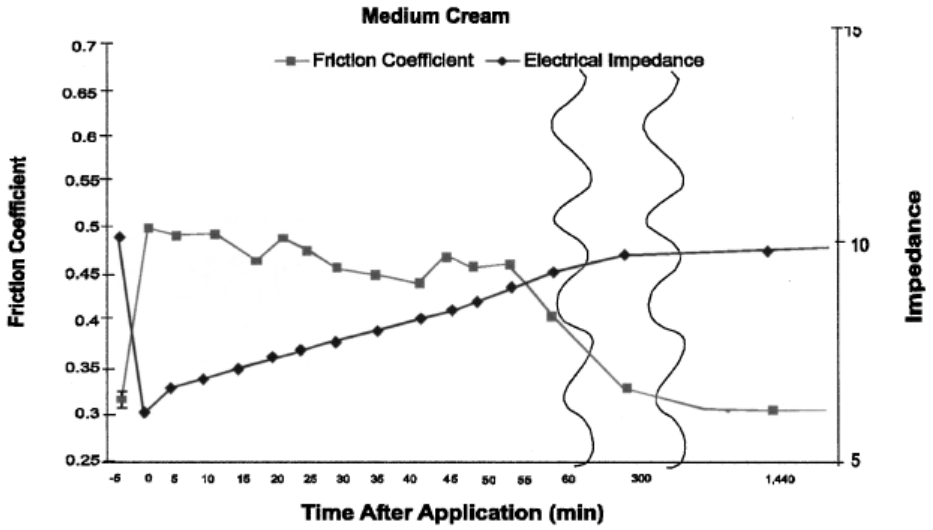


Figure 2.55: Friction and Electrical Surface Resistance after application of the medium cream for long term measurement [78]

A comparison of different lotions was measured simultaneously with electrical impedance and friction results. In Figure 2.54, the effect of the skin moisturizer is shown at time t = 0, when surface resistance dropped and friction coefficient increased rapidly. After the application from time t = 0 minutes to time t = 20 minutes, friction drops down and fluctuates while surface resistance increases

correspondingly. In Figure 2.55 , the long term friction and electrical measurements are shown after 1 hour, 5 hours and then 24 hours. The results illustrate that the cream moisturizer strongly affects the skin at t = 0 and the effect gradually decreases over 24 hours. These experiments also showed the different performance characteristics for different kinds of lotions [78]

In general, the Centre for Tribology in California has carried out excellent experiments in measuring the lotion's effect using friction and electrical resistance with a well-designed protocol. However, there is variability in the friction measurements at times after the application of moisturiser but these are not seen in the electrical resistance results. The base line time t = -1 minute is a single measurement before application making it difficult to ascertain when the impedance returns to base line. Ideally the base line should be measured several times before application of the lotion in order to ascertain the base-line variability.

2.8.3 Skin assessment and moisturization by Martinsen

Martinsen et al has performed many bio-impedance studies on human skin [1]. According to Martinsen et al [1][82][83], skin moisture is closely related to skin function, and by monitoring the hydration state of the stratum corneum, diagnosis of nonvisible skin conditions may be accomplished.

In one of the studies, the effects of moisturizers were studied by monitoring several different parameters of treated skin sites [82] using a Corneometer and bioimpedance measurements using two and three electrode measurements. The measured parameters were the arbitrary units of the Corneometer CM820 using a capacitance measurement technique. The electrical susceptance and conductance at 8 and 88 Hz using both two and three electrodes measurements were used and also the two and

three electrodes measurement of electrical admittance at 10 KHz using a Princeton Applied Research 5210 lock-in amplifier. The voltage was sinusoidal with amplitude of 20 mV.

According to the experiment [82], the moisturizers used were distilled water and Spenol liposome suspension. In the protocol, before each measurement series, the volunteers rested in the laboratory for 15 minutes. Pre-values at time t = -1 min were taken on test skin sites before every treatment. 0.1 ml of moisturizer was applied onto the test skin site and rubbed in gently for 60 seconds [82]. Then, a paper towel was used to remove the excess.

The measurements were carried out successively and immediately after the treatment t = 1 min, then after each 1 min until t = 10 minutes. These measurements continued at t = 30, 60, 120, 240, 360 minutes.

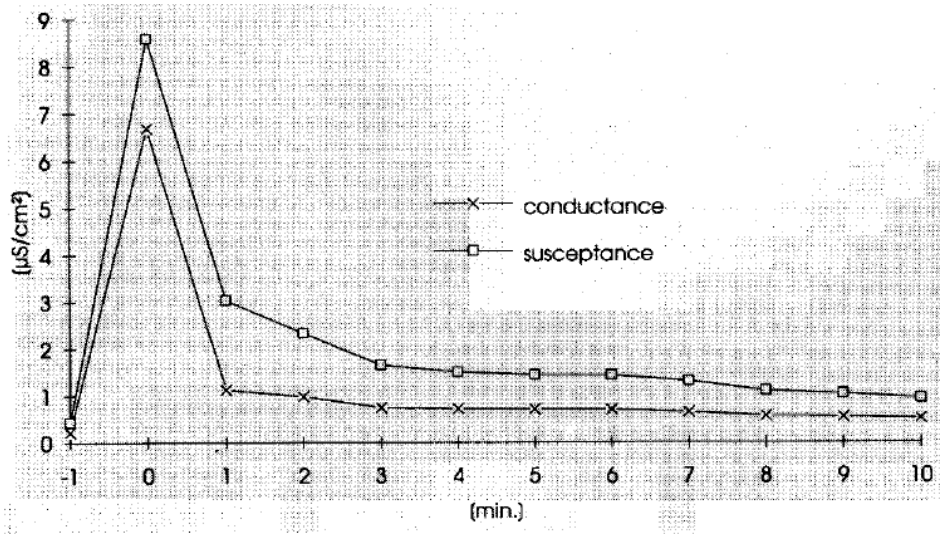


Figure 2.56: 88-Hz conductance and susceptance after water treatment in first 10 minutes [82].

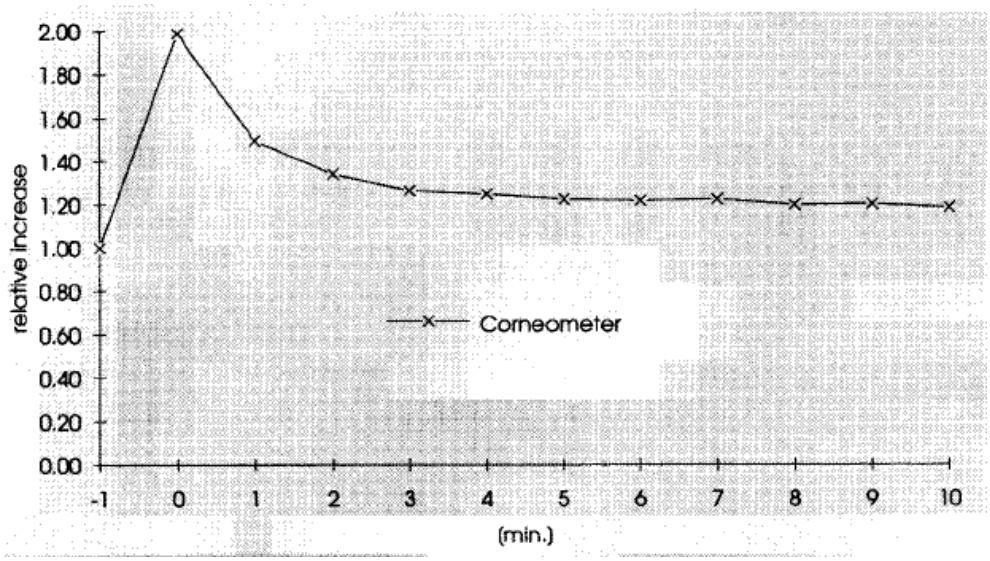


Figure 2.57: Relative increases in Corneometer units after water treatment first 10 minutes [82].

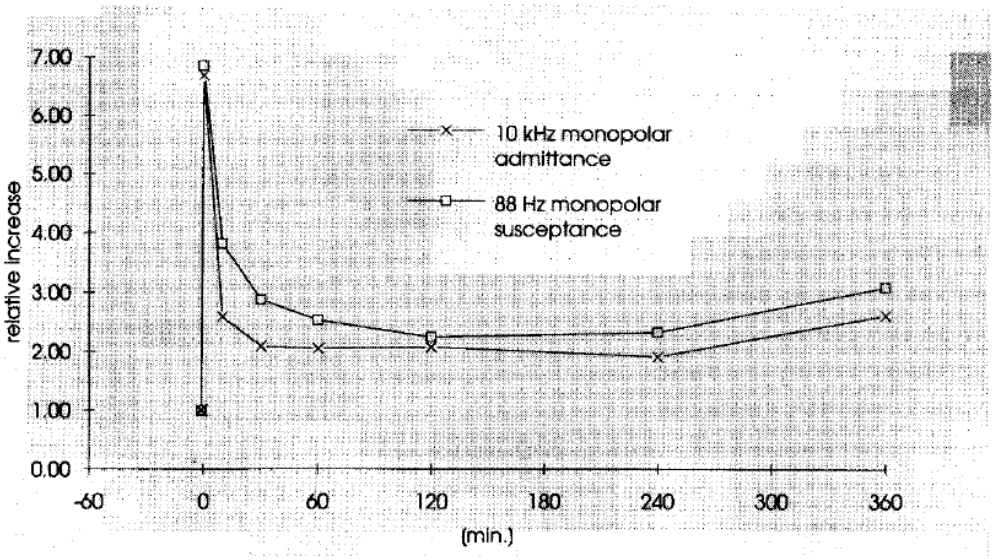


Figure 2.58: Relative increase in 88 Hz susceptance and 10 KHz admittance after Spenol treatment in 360 minutes [82].

In order to compare these methods, Martinsen plotted the relative increase in Corneometer units after water treatment shown in Figure 2.57, and the corresponding 88 Hz and 10 KHz results shown in Figure 2.58. All methods used showed the results significantly changed after the application of moisturizers. The results illustrated the

decreasing trend lasting 5 min after the water application and after 10 minutes there was still a small increase in the hydration level compared to the pre-values [82].

In conclusion, Martinsen demonstrated that electrical impedance was the preferred method of electrical skin moisture assessment compared with the capacitance technique of the corneometer. This electrical method appeared to be more sensitive to changes in the hydration compared with the high frequency method using a Corneometer [82].

Martinsen designed a very good protocol to examine the moisture changes reflected in the electrical skin impedance using a Corneometer and a Lock-in amplifier based bioimpedance measurement system. However, the results from the Corneometer are in arbitrary units and it is not possible to compare with results from the lock-in amplifier impedance system as two different techniques were used. Also, the sensor, which was a two point probe or three electrodes, was not reliable as it contained the electrode polarization impedance unlike with a four point probe technique. Moreover, the base line impedance measurement was measured only one time (t = -1 minutes) making the base line results potentially unreliable. It is recommended that the base line should be measure several times before application because the base line may be not stable in time.

2.8.4 Skin admittance for dry electrodes and skin moisturisation by Yamamoto

Yamamoto has also performed a considerable amount of research on the skin's electrical properties [17][84][85][86]. According to one study [84], the skin admittance Y was investigated to measure the moisture effects on skin. The relative permittivity and resistivity of the skin can be derived from the admittance [84]. A concentric electrode was implemented to measure the skin impedance [84] using the

two point probe method. The electrode was connected to a Wien bridge oscillator generating a sinusoidal voltage of 2V at 100 kHz. The measuring circuit was connected to an ADC and the data was downloaded to a computer. By using a custom made bio impedance measurement system on skin, Yamamoto intended to measure the hydration and dehydration effects on the skin through the admittance results [84]. However, it was found that the contact between dry electrodes and stratum corneum is the dominant factor producing the change of skin admittance caused by the water content on the skin surface. Also, the impedance of the skin at low frequencies largely influenced the results and caused problems in general use [84]. In addition, the water contained on the skin is possibly changed as the stratum corneum could absorb or vaporize the water by activities such as washing or bathing [84].

Yamamoto et al [84] found that a concentric electrode with a diameter of 5 mm was suitable for measuring the skin admittance in order to avoid variability in the observed value. According to experimental data from Yamamoto [84], it was preferred to use a frequency above 10 kHz for moisturisation measurement [84]. The constant pressure used should be 100 gcm^{-2} and this was achieved by coil spring. The relationship between the skin admittance and skin moisturisation was examined to investigate the hydration and dehydration process [84]. The protocol used was to place the forearm ventral side in warm water for 5 minutes, then wipe off the water and make a measurement of admittance versus time. The results of the experiment for hydration and dehydration process obtained are shown by plotting the admittance versus time in Figure 2.59.

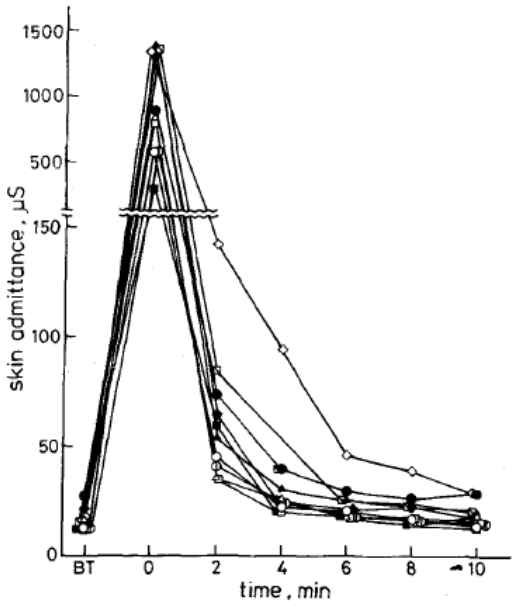


Figure 2.59: Changes of skin admittance during process of dehydration. (BT: Before treatment) [84].

The skin admittance was markedly increased by hydration and decreased with the process of dehydration in Figure 2.59. Thus, there are several conclusions that can be drawn. Firstly, it could be confirmed that skin admittance is strongly correlated with water content of the skin. Secondly, frequencies higher than 10 KHz are preferred for skin admittance measurement. Thirdly, skin admittance could be used to obtain the relative permittivity, resistivity and the thickness of the stratum corneum (according to a derived equation (2) in [84]). However, the different sizes of electrodes affect the variations (through the experiment using different electrode's sizes on skin) on the observed admittance values according to Yamamoto [84]. Finally with the automatic measuring system, the variations in the obtained data were reduced and the results were improved to be more reliable [84].

In general, Yamamoto has carried out some excellent innovative experimental studies about the skin hydration in the 1980's. The protocol designed was simple as it only involved dipping the subjects' forearm into water for 5 minutes, then removing

the forearm from the water and making the measurement continuously. The protocol could be expanded to using different moisturizers. The results are quite relevant to those shown in this thesis, however, a two point probe was used which introduced errors in measurement due to the electrode polarization impedance.

2.8.5 Skin moisturizers assessment by Lodén

Previous studies on short-term treatment have shown that moisturizers can weaken or strengthen skin barrier function and also influence skin barrier recovery [89]. For examples, urea containing moisturizers seemed to improve skin barrier function, however, sodium lauryl sulfate disrupted the skin barrier and is an irritant [89]. Knowledge of the effects on skin barrier function of long-term treatment with moisturizers is still relatively scarce and needs further exploration. Lodén et al [77][80][87][88][89] carried out a significant amount of experiments to examine the human skin with different moisturizing creams including evaluating the skin barrier effect in patients with atopic dermatitis.

In one of the experiments, Lodén measured the transepidermal water loss (TEWL) by using a Tewameter and the skin capacitance using a Corneometer to investigate the impact of long term treatment with moisturizers [77]. In the protocol, Lodén et al chose several skin creams with different elements, for example glycerine, urea and alcohol [77], to design the experiments with the aim of examining different effects of different skin creams on human skin in general and on atopic dermatitis patients in particular. One of the protocols was to apply the skin moisturizer on the forearms of patients twice daily for 20 days and to measure the effects [77]. The cream deployed was Canoderm and contains 5% urea in an oil-in-water emulsion. TEWL and skin capacitance were recorded at the start of study and after 10 and then 20 days as shown in Figure 2.60.

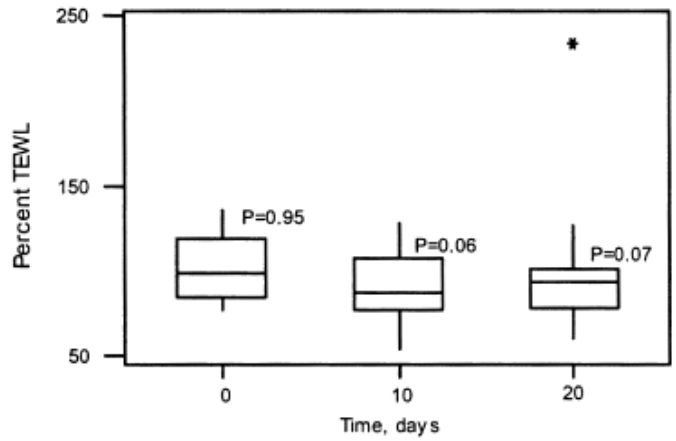


Figure 2.60: Transepidermal water loss (TEWL) in the treated arm as a percentage of the values in the control arm, n = 15, using box plots [77].

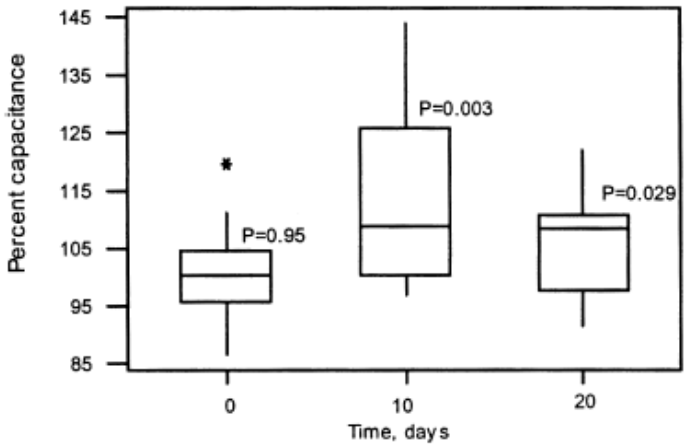


Figure 2.61: Skin capacitance in treated skin as a percentage of the values in control skin, n=15, using box plots [77].

After the treatment with cream, the TEWL tended to be lower on the treated arm compared with the untreated, while the skin capacitance increased on the treated arm compared with the untreated arm. Hence, Lodén drew the following conclusions. Lipids act as occlusives as it blocked water vaporization from the stratum corneum [77]. Humectants in moisturizers, which attracted water from deeper dermis to the stratum corneum, are believed to increase skin hydration by attraction of water [77]. Finally, it seems that certain moisturizers could improve skin barrier function (by Corneometer measurements) not only in normal skin but also in atopic skin.

Lodén has carried out many dermatology studies about the human skin with moisturizers. However, the results from a Corneometer make them difficult to compare with other instruments as Corneometer uses arbitrary units and relates this to hydration. A four point probe with lock-in amplifier or bio-impedance analyzer may offer more accurate measurement.

2.9 Conclusion

Electrical Impedance Spectroscopy or Bioelectrical Impedance Spectroscopy is a method that involves the injection of a constant current into human skin and measurement of the voltage drop. The impedance is then calculated and then related to the resistivity value of the skin. One example is in monitoring the effects of products (e.g. moisturisers) on the skin. This can be useful for cosmetics companies in new product development where users of the cosmetic product could use such a device in their own home.

In the past, other methods such as TEWL, Corneometry, and the two point probe technique have been used to investigate the water loss, skin capacitance and skin impedance change in order to find out the effect of skin cream. Using EIS (Electrical Impedance Spectroscopy) to investigate the skin cream effects on human skin is a potential method as this approach is non-invasive, quick and portable. Also, the characteristic of EIS include the absolute impedance $|Z|$ and phase change θ, therefore it can not only track the change of skin capacitance (skin barrier change) but also detect the change of the skin resistance (sweat activity, hydration). In addition, the EIS technique used with a four point probe sensor can help to increase the reliability and accuracy compared with the Kelvin two point probe system. The overview of the electronic design for EIS is given in detail together with explanation

of advantages, disadvantages and improvements. Also, the differences between RC components model and CPE component model is demonstrated in impedance, phase and especially in real vs imaginary plot.

From previous experimental research, many used the skin capacitance method or the two point probe technique to measure the skin moisture with different skin creams. It is of interest to assess whether the four point probe technique could perform well when compared with traditional techniques. Therefore, it is suggested that a low cost, portable, custom-made bio-impedance analyser based on a four-point probe sensor should be constructed for measuring skin impedance over short and long term. Long term measurements are motivated by manufacturer claims that the effects of moisturisers last up to 24 hours (such as Nivea) and so a portable, low cost device is developed to carry out long term monitoring.

Chapter 3 System Overview: Implementation, Design and Validation

3.1 Introduction

In this chapter, the custom-made bio impedance measurement unit, which follows the general bio impedance measurement demonstrated in Chapter 2, is implemented with a specific sensor and corresponding frontend. The processing unit inside the DSP board is programmed to control the analogue frontend and process the measured data. Moreover, a Matlab coding interface is written to communicate with the DSP board to control the output voltage into the skin and to receive the results from the measurement. Finally, the data is collected and shown in real time on a computer. A finite element model is used to investigate the effects of probe separation on the penetration depth of the measurements.

In order to validate the system performance, three phantoms have been tested together with comparison between the custom made device and a commercial device (Solartron Impedance Analyzer 1260 + 1294). These phantoms are resistor-only networks, resistor and capacitor networks and calibration solutions. After calibration with three phantoms, human skin impedance measurement is also validated. The custom-made device and the Solarton gave results which matched well in three kinds of test. The Solartron system gave more accurate results (approximately 1%) compared with the custom made device with 5% accuracy. Nevertheless, this demonstrates the potential for a portable, low cost device that is compatible with long term or home monitoring.

3.2 System design: DSP Unit, Analogue Frontend and Sensor

The bio impedance analyzer comprises a Microchip dsPIC33F (Microchip dsPIC33FJ256GP710 Digital Signal Controller) and PCB interface card connected to the four point probe sensor.

Although the Solartron is a better choice for purely bench top studies, the custom-made device could do an acceptable job depending on the application. In this case, skin impedance ranges from about 1MΩ at low frequency (20Hz) to around 1kΩ at high frequency (100 kHz). Figure 3.1 illustrates the complete process of skin impedance measurement and includes the skin-electrode interface, analogue frontend, DSP Unit and real-time display.

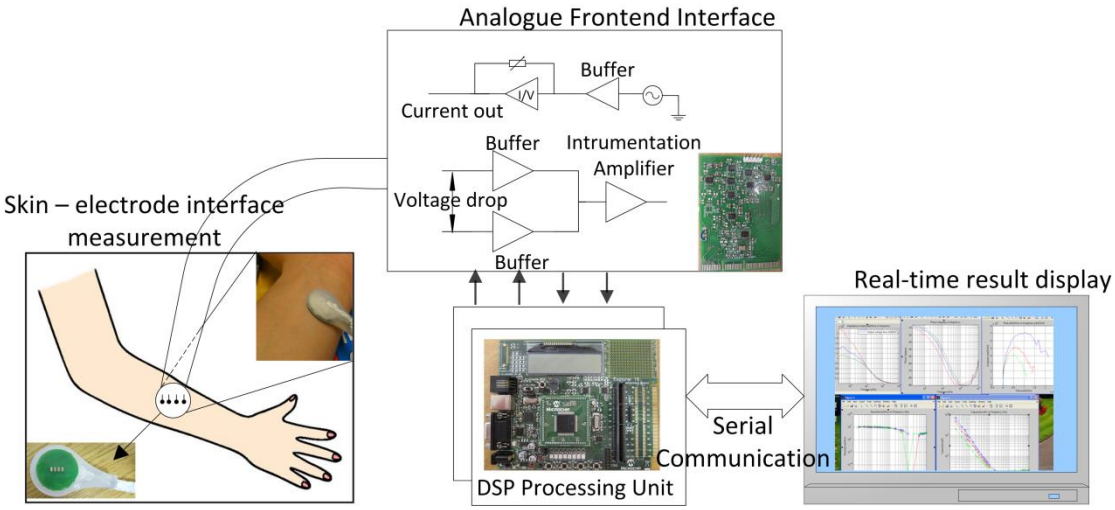


Figure 3.1: Block diagram of the bioimpedance measurement process.

The sensor interface is a four point probe gold electrode constructed in a PCB. The cable connects the sensor to the analogue frontend and is a driving shield to minimize the leakage current.

As seen in Figure 3.1, the analogue frontend contains two parts: part one is a Voltage Controlled Voltage Source and part two is Voltage Measurement. In the first part, the board is designed to implement a voltage source into the two outer probes of the sensor. The second part is the implementation of the Instrumentation Amplifier to capture the voltage drop between the two inner probes of the sensor and send it to an ADC part of the DSP. Current is measured at one of the outer probes using a current measurement circuit followed by transfer of the signal to another ADC. The analogue

frontend is controlled by the DSP Unit. Figure 3.2 gives the general concepts of the custom made bio-impedance analyzer using four point probe technique.

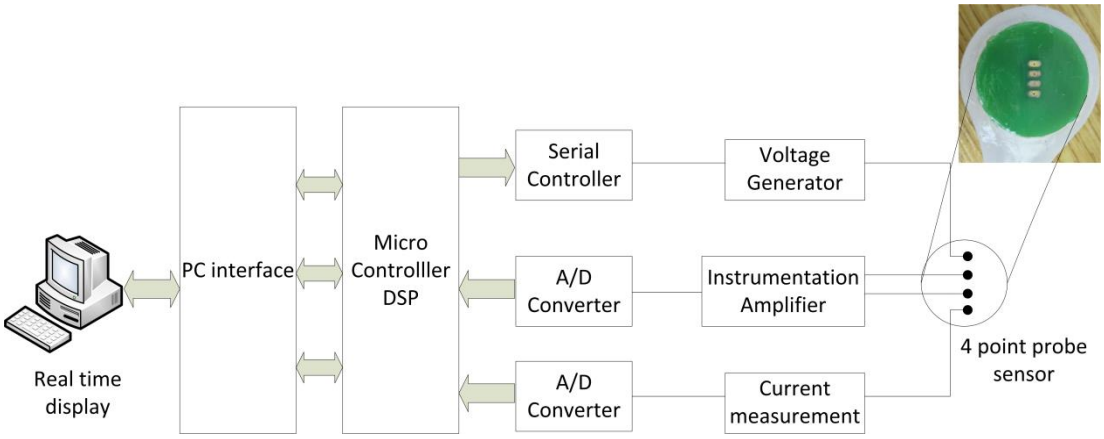


Figure 3.2: General concepts of the custom made system using tetra-polar technique.

Once data are stored in the memory, the DSP uses a series of mathematical operations such as a digital filter, lock-in amplifier and discrete Fourier Transform in order to obtain the absolute impedance $|Z|$ and phase θ. Then, the DSP sends the processed data to a PC/ Laptop for real time display through PC interface RS232. The current is limited according to Medical Safety British Standard 60601-1 [23] which is described in Appendix E.

3.2.1 High level schematic of Bio-impedance Measurement System

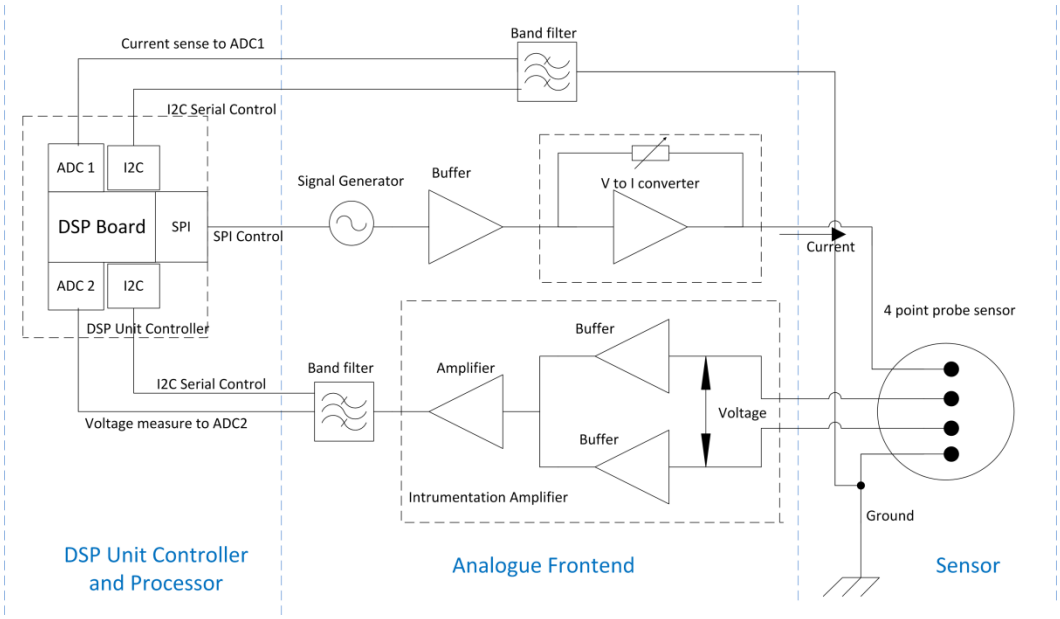


Figure 3.3: High level schematic of the bio impedance measurement system

In Figure 3.3, four point probe sensors are constructed into two layers; the top layer of the sensor is connected to the human skin to measure the skin impedance; the bottom layer is connected via a cable to the analogue frontend followed by the dsPIC board to capture and process the data.

In the high level schematic of Figure 3.3, the analogue frontend contains fundamentally two parts: part one is Voltage Source and part two is Voltage Measurement. In part one, the board is designed to implement a Programmable Waveform Generator combined with a Buffer Amplifier with variable gain to generate different voltage levels (0 - 5V) and frequencies (20Hz – 100 KHz). In order to source current into the two outer probes of the sensor, a simple Voltage Controlled Voltage Source (a Signal Generator connected to a potentiometer) is used. The second part of the frontend is the implementation of an Instrumentation Amplifier to capture the voltage drop between the two inner probes of the sensor.

3.2.2 Schematic Design

Schematic designs are divided into two parts: the sensor design and analogue frontend design. The sensor design has two layers: the top layer, used as the contact interface with human skin, and the bottom layer, used to connect to the analogue board. Secondly, the analogue interface board is designed with different electronic blocks including waveform generator, voltage to current converter, instrumentation amplifier measurement, band-pass filter and ADC level shifter.

Part 1: Sensor design:

Based on the electrode design of Campbell [100] and Brown et al [7], the custom made electrodes sensors for impedance measurement are made with four gold electrodes of 2mm x 1mm spaced equally on a circle of radius 10mm. The four gold electrodes sensor is designed to minimize destruction by oxidation or electrochemical reaction and is shown in Figure 3.4.

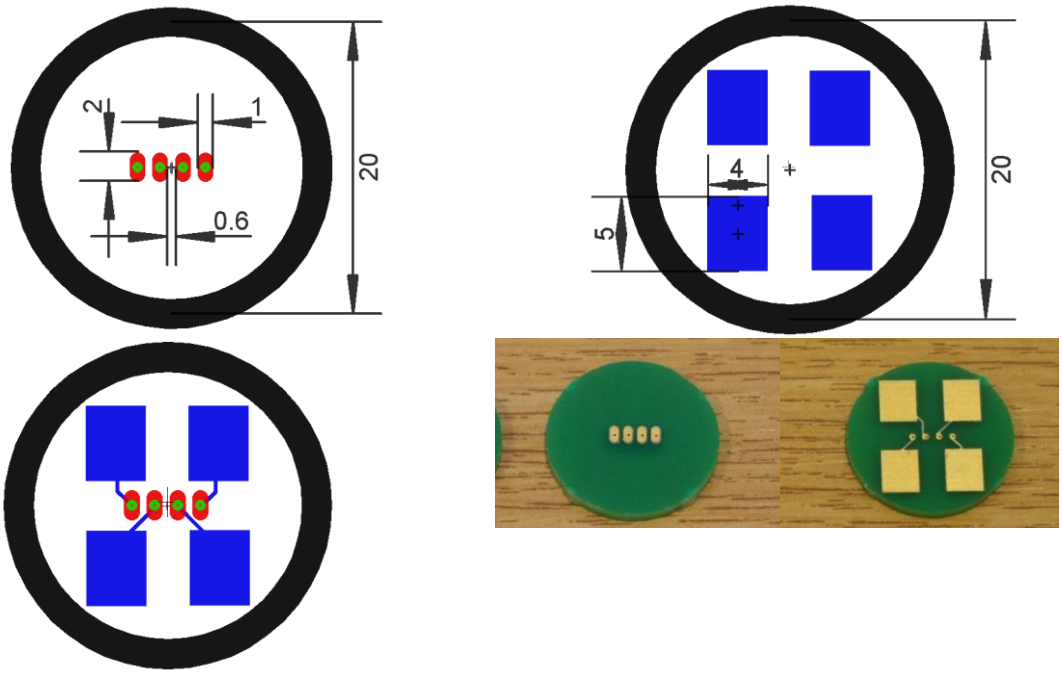


Figure 3.4: Top (red) and bottom (blue) layers dimensions of the four point electrodes (unit in millimeters)

In Figure 3.4, the blue color is the bottom design layer and red color is the top design layer. The two layers are connected through vias (green color). The picture on the left is the PCB design for the electrodes and on the bottom right hand side is the fabricated PCB board. The gold four point electrodes have diameter of 20mm. In the top layer, each probe point has 2 mm length x 1 mm width, the spacing between each probe point is 0.6 mm. In the bottom layer, there are four square gold pads with dimension 5 mm in length x 4 mm in width. The bottom of the electrode is then soldered to the cable and covered in silicone rubber.

Part 2: Analogue frontend interface

There are four parts to the schematic design of the Analogue Frontend: Voltage source, current limit and DC blocks, an instrumentation amplifier, and a band-pass filter combined with a level shifter.

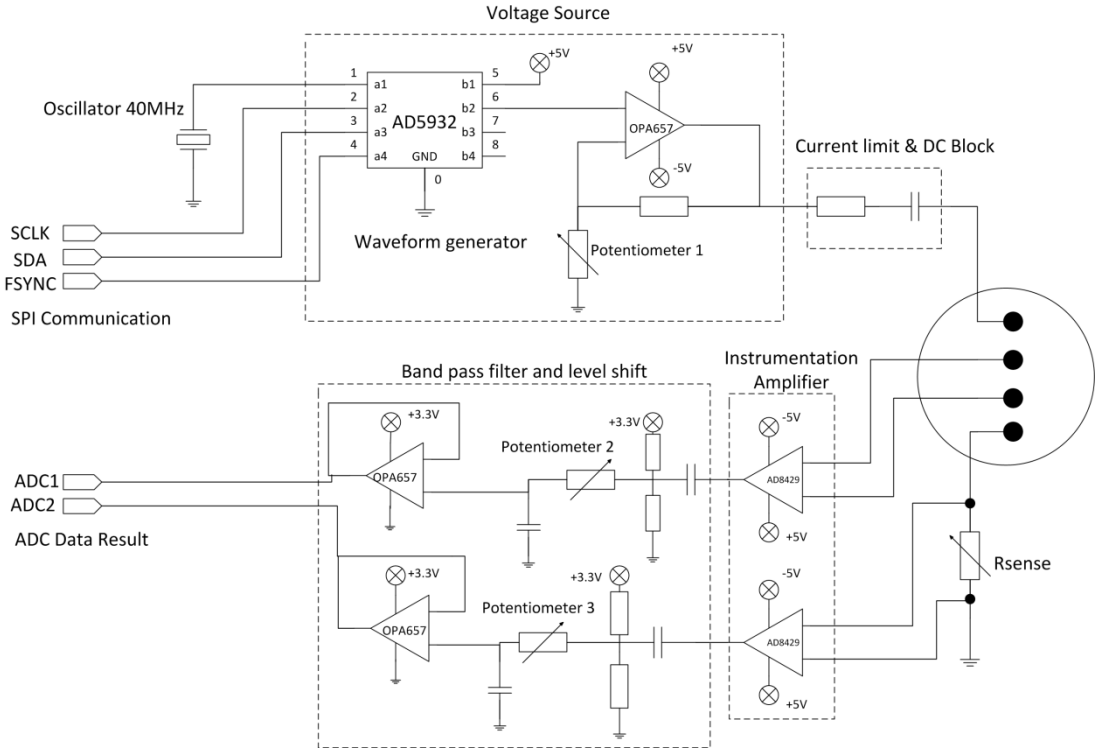


Figure 3.5: Schematic of Analogue Frontend Interface

The analysis of the analogue frontend circuit is given in detail below:

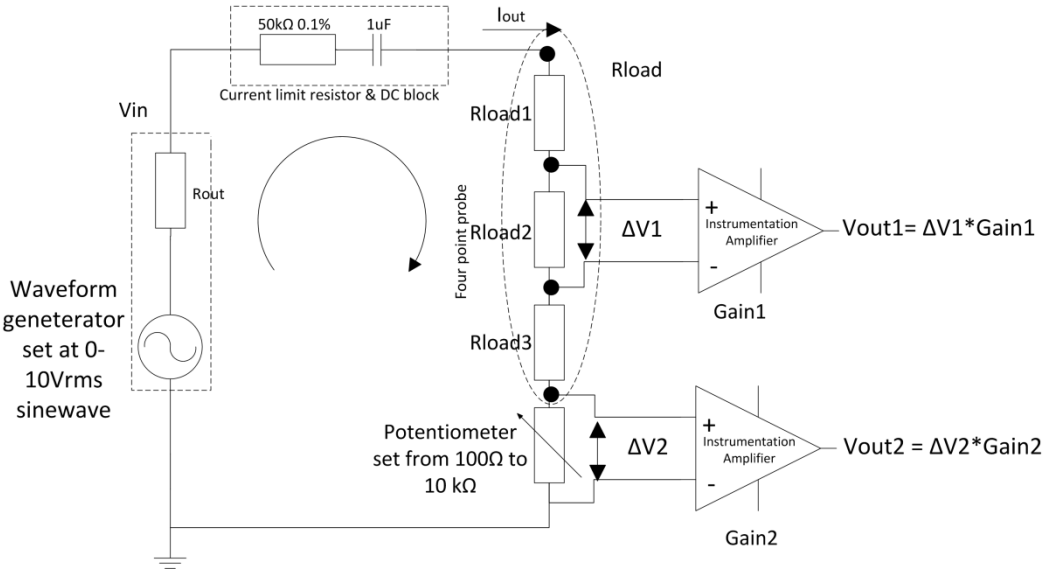


Figure 3.6: The analysis of the analogue frontend circuit

As the technique used deploys a voltage source, the output current is highly dependent on the load and hence must be measured in-situ. According to the analogue frontend design, the output current can be calculated as

$$I_{out} = \frac{V_{in}}{R_{out} + Z_{limit\&DC} + Rload + Rpot} \qquad (3.2.1)$$

where $Rload = Rload1 + Rload2 + Rload3$, $Z_{limit\&DC} = R_{limit} + 1/ j\omega C$ is the impedance current limit resistor (50kΩ) and a DC capacitor block (1uF).The chosen capacitor value relates to the impedance $Z_{limit\&DC}$. For example: if a smaller value capacitor is chosen i.e. 100nF, the $Z_{limit\&DC}$ will be much higher at low frequency. R_{out} is the output impedance from the voltage source and buffer (less than10Ω) taken from the datasheet of OPA657 (Texas Instrument) explained in section 2.4.1 (Voltage Source output impedance), R_{load} is the impedance across the four point probe electrode and R_{pot} is the current sense resistance value set by the digital potentiometer (from 100Ω to 10kΩ).

There are two instrumentation amplifiers to capture the voltage across the load (INA1) and current output (INA2). The first instrumentation amplifier captures the voltage across the middle load and amplifies by Gain1 (set by R_G resistor). Then, $V_{out1} = \Delta V_1 \times$ Gain1 is sent to ADC1. The second instrumentation amplifier measures the voltage across the current sense potentiometer, and amplifies this by Gain2 before passing to ADC2.

Loop gains calculation:

a) Gain calculation at Instrumentation Amplifier 1

$$A_1 = \frac{V_{in}}{V_{out1}} = \frac{V_{in}}{\Delta V_1 \times Gain1}$$

$$= \frac{V_{in}}{\frac{V_{in}}{Rout+Z_{limit\&Dc}+(Rload1+Rload2+Rload3)+R_{pot}} \times Rload2 \times Gain1}$$

$$= \frac{Rout+Z_{limit\&Dc}+(Rload1+Rload2+Rload3)+R_{pot}}{Gain1 \times Rload2} \qquad (3.2.2)$$

b) Gain calculation at Instrumentation Amplifier 2

$$A_2 = \frac{V_{in}}{V_{out2}} = \frac{V_{in}}{\Delta V_2 \times Gain2}$$

$$= \frac{V_{in}}{\frac{V_{in}}{Rout+Z_{limit\&Dc}+(Rload1+Rload2+Rload3)+R_{pot}} \times R_{pot} \times Gain2}$$

$$= \frac{Rout+Z_{limit\&Dc}+(Rload1+Rload2+Rload3)+R_{pot}}{Gain2 \times R_{pot}} \qquad (3.2.3)$$

For instance, at frequency f = 10 Hz, R_{limit} = 50 kΩ and C = 1μF, then $Z_{limit\&DC}$ = 52.5 kΩ. Setting R_{load} to 3kΩ such as Rload1 = Rload2 = Rload3 = 1 kΩ, R_{pot} = 100Ω, V_{in} = 1Vrms, the current flow through R_{load} will be equal to $I_{out} = \frac{V_{in}}{R_{out} + Z_{limit\&DC} + Rload + Rpot} = \frac{1}{55581}$ = 18 μArms.

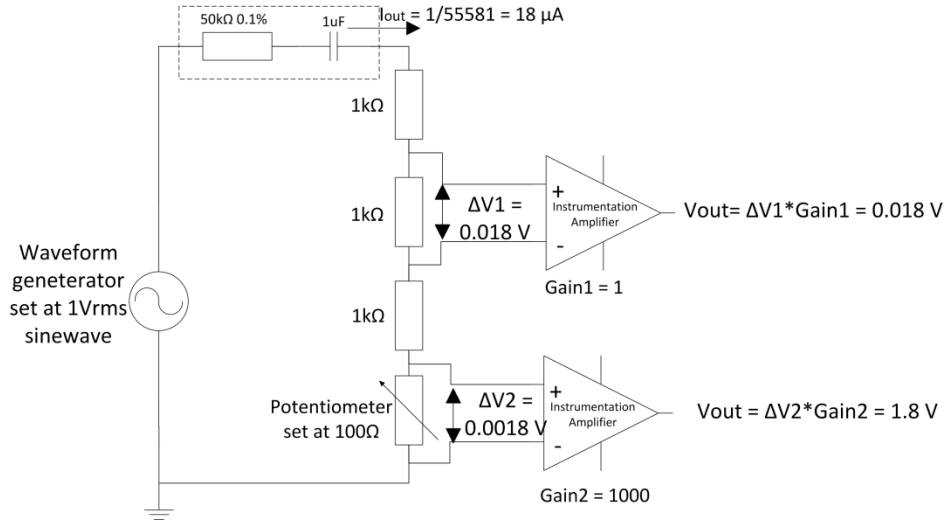


Figure 3.7: Bio-impedance analyser with 3kΩ load measurement

In order to measure the voltage across the load and the current output, the gains of INA are set as 1 and 1000 respectively which generates voltages of V_{out1} = 18 mV and V_{out2} = 1.8 V at the ADC inputs. The microcontroller is then programmed to calculate the load impedance by the equation:

$Z_{out} = \frac{Vout1}{Vout2} \times \frac{Gain2}{Gain1} \times R_{pot} = \frac{0.018}{1.8} \times \frac{1000}{1} \times 100 = 1000\ (\Omega)$.

Consider another example where R_{load} is equal to zero and hence the maximum current flow through R_{load} will be equal to

$$I_{out} = \frac{V_{in}}{Z_{limit\&DC} + Rpot + Rout} \qquad (3.2.4)$$

If V_{in} = 5 Vrms, f = 10 Hz, $Z_{limit\&DC}$ = 52471 Ω, R_{pot} = 100 Ω, then I_{out} = 95.09 µArms, which satisfies the maximum allowable current flow through biological tissue according to British Standard 60601. The current limit resistor R_{limit} = 50 kΩ is needed to maintain accuracy i.e. 0.1% tolerance, otherwise the output current can exceed the maximum allowable current. For example, if 10% tolerance resistor is used, that can make R_{limit} = 45 kΩ in the worst case, then at f = 10 Hz, $Z_{limit\&DC}$ = 47471 Ω, then I_{out} = 105 µArms, which exceeds levels recommended in the Standard.

The application of the various frequency and input magnitudes of Vin is controlled by the DSP PIC microcontroller. Figure 3.8 illustrates the functional description whilst Figure 3.9 provides the associated flow chart of the firmware.

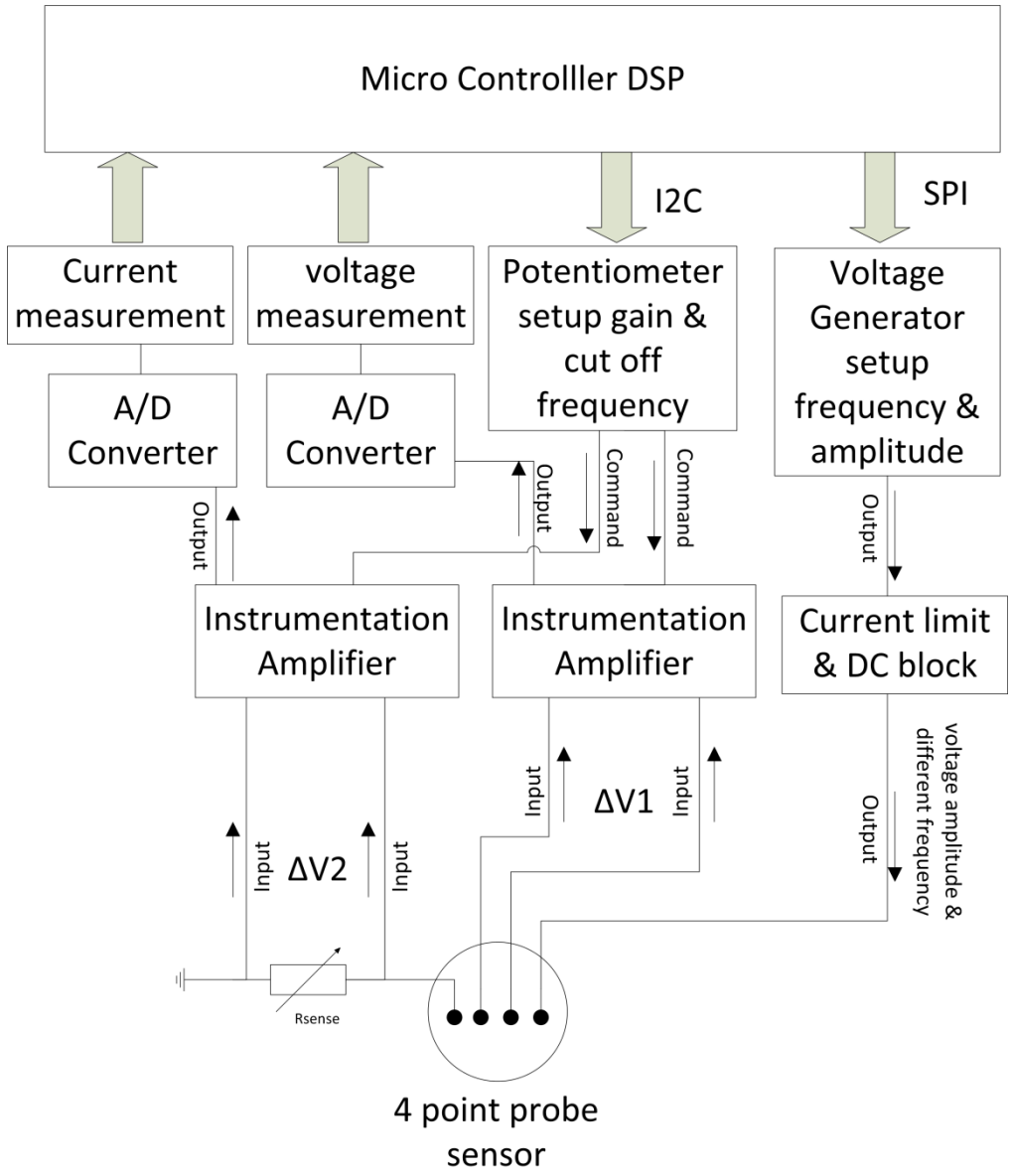


Figure 3.8: Functional description of the analogue frontend design

In Figure 3.8 the DSP is set up to send commands through I^2C and SPI to control the digital potentiometer in order to set up the gain of the amplifier, the cut off frequency of the anti-aliasing filter, value of the current sense resistor, and the amplitude and frequency of the input voltage. The measuring voltage drops at the two inner probes

and at the current sense are captured by the instrumentation amplifiers, and this is then sent to the ADC converter of the DSP. At this point, all analogue signals of voltage and current measurement are converted to a digital value in order to carry out signal processing such as THD confirmation, digital filtering and lock-in amplification. In Figure 3.9, the current firmware flow chart is provided.

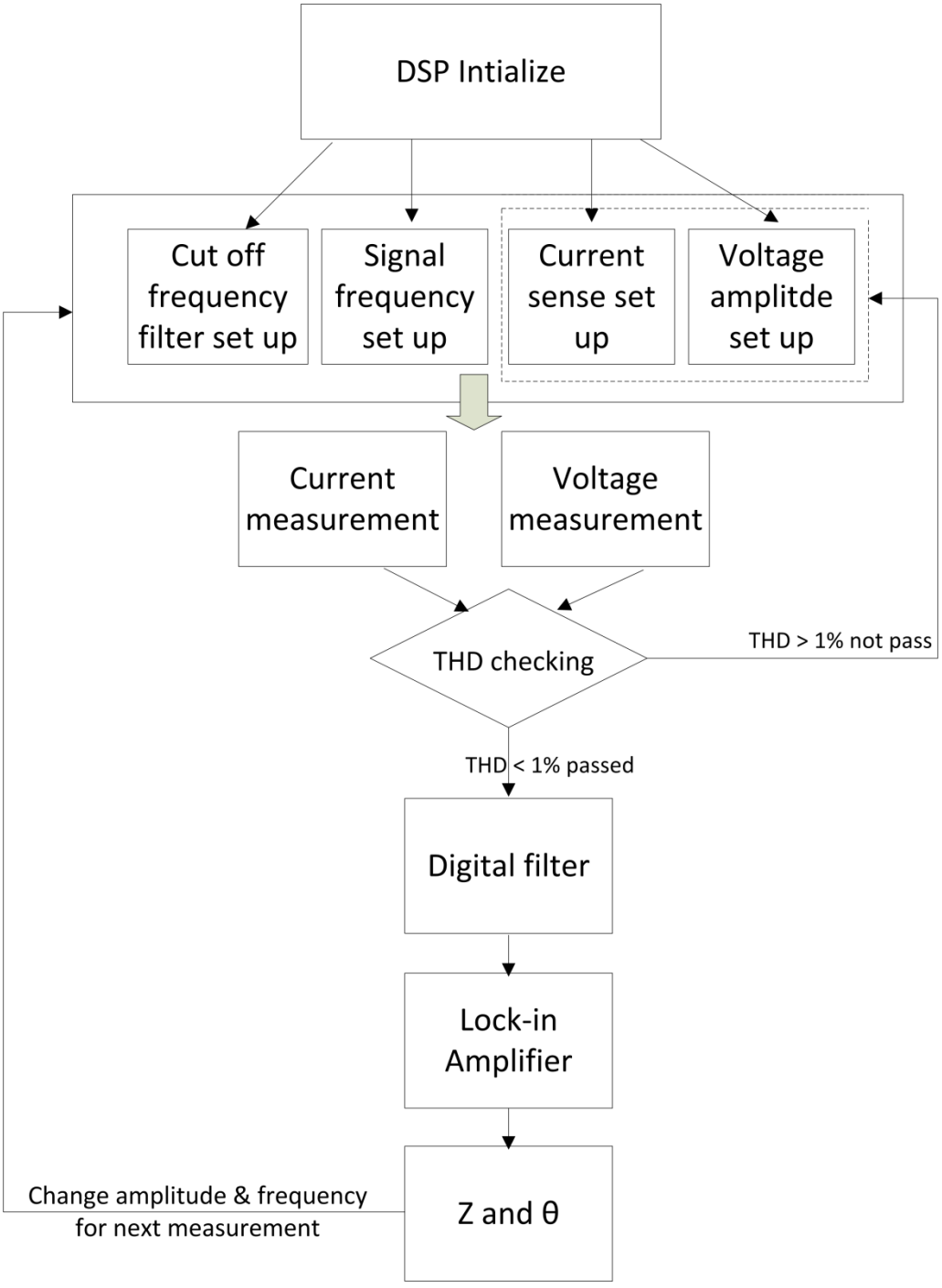
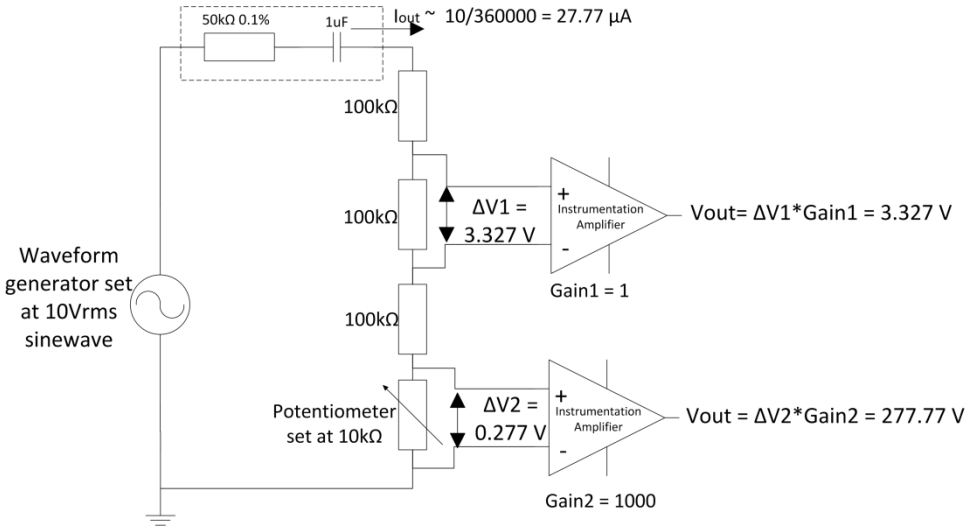
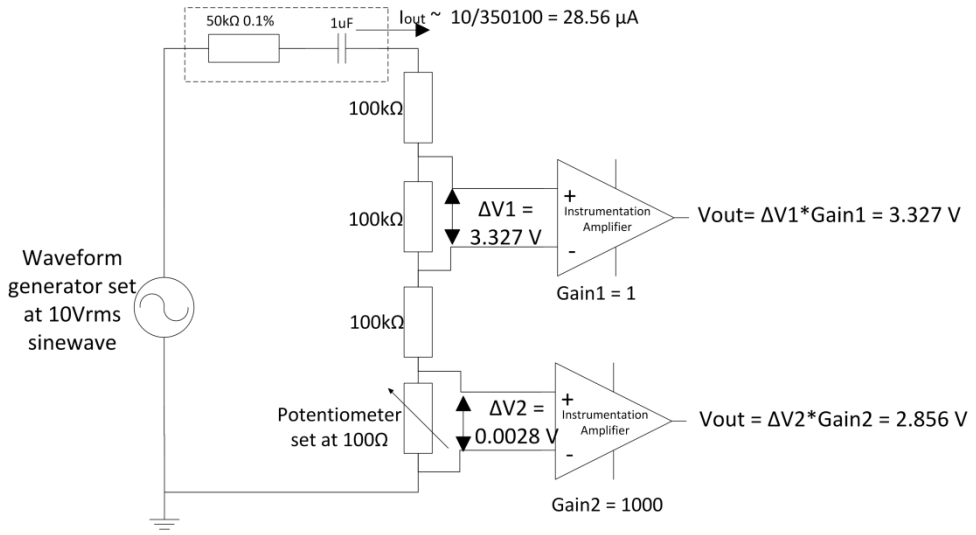


Figure 3.9: Firmware flow chart of the analogue frontend design controlled by the DSP

After the DSP initialisation, the voltage amplitude and frequency, current sense resistor and cut off frequency of the anti-aliasing filter are all set up for measurement. The resulting voltage drop between the two inner probes is measured together with the current sense at the final probe. These signals are converted to a digital signal through the ADC and then passed through the THD checking process. Since this ADC can only receive a voltage from 0 to 3.3V, potentiometers 1,2,3 and Rsense need to be adjustable so that the receive voltage will not saturate the ADC. For example in Figure 3.10, in the measurement of a 100kΩ load , if Rsense is set at 10kΩ and this passes through the gain of the amplifier, the expected output is 277.77 V. This of course can never happen as the ADC can only receive a voltage of 0-3.3V. As a result the signal received by the ADC will be saturated. By reducing Rsense to 100Ω, the signal received will therefore not be saturated anymore and hence the true distortion can be detected via THD measurement.



(a)



(b)

Figure 3.10: Measurement with 100kΩ load measurement with distortion (a) and without distortion signal (b)

If THD distortion is higher than 1%, then the signal is defined as "distorted" and therefore the input voltage amplitude and current sense will be adjusted until the THD < 1%. After passing through the THD process, the undistorted signal will then go through a digital filter to filter out the noise. The final stage is a lock-in amplifier, applying in-phase and quadrature phase signal, to derive the absolute impedance and phase difference of device under test. The lock in amplifier also acts like band pass filter to further reduce the noise from the receive signal together with digital filter.

Section 1: Voltage Source

As shown in Figure 3.5 the waveform generator consists of a combination of the programmable waveform generator AD5932 and a buffer amplifier. The waveform generator AD5932 generates sinusoidal/triangular/square waves with frequency up to 25 MHz (square wave only) [110]. AD5932 contains a 10-bit DAC (Digital to Analogue Converter), frequency controller with sine wave ROM (Read Only Memory), 3-wire SPI (Serial Peripheral Interface) to communicate with the DSP

(Digital Signal Processor), and Master Clock using a standalone crystal oscillator with a frequency of 40 MHz. In addition, the waveform generator is connected at its output to a buffer amplifier with controlled gain to generate different current levels.

The waveform generator is controlled through the SPI communications protocol (SCLK for serial clock, SDA for serial data input, FSYN for frame synchronization). The purpose of this communication is to send control signals to the AD5932 [110]. Data control is two 16-bit binary and can be written in the DSP in the form of hexadecimal commands. The DSP sends two 16-bit binary signals to control the Sine Wave ROM of the AD5932. The timing diagram of SPI Communication is shown in Figure 3.11.

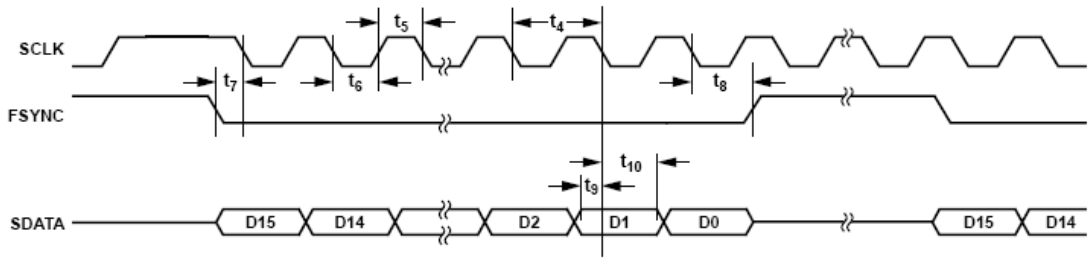


Figure 3.11: Serial timing for SPI Data Control [110]

For example, in order to generate a 1 KHz sine wave output, the hexadecimals need to be sent from the DSP are 0xC1A3 for the 16 LSB (Least Significant Bits) and 0xD000 for the 16 MSB (Most Significant Bits). With the combination of the waveform generator, buffer amplifier and current limit resistor, a sine wave can be generated with frequencies ranging from 20 Hz to 100 KHz together with different current levels from 0.1µA to 100µA, controlled by Digital Potentiometer 1 (explained in detail in section 4 in 3.2.2).

Section 2: Current limit and DC block:

The second part of the analogue frontend is a Current limit and DC block. The resistor is adjusted to guarantee that the current level limits below 100 µA. The capacitor after the resistor blocks DC from the Voltage to Current Converter. According to analogue frontend design, the output current can be calculated as

$$I_{out} = \frac{V_{in}}{R_{out} + Z_{limit\&DC} + Rload + Rsense} \qquad (3.2.5)$$

R_{out} = 10Ω, R_{limit} = 50 kΩ and C = 1µF, f = 10 Hz then $Z_{limit\&DC}$ = 52.471 kΩ. For example, when R_{load} is equal to 3kΩ and R_{sense} = R_{pot} = 100Ω, the output current I_{out} = 18 µA. R_{sense} is set by the digital potentiometer in order to monitor the drive current. A high impedance load generates a smaller current and hence a higher gain is required on the instrumentation amplifier. Alternatively, a low impedance load generates a larger current and the inst-amp gain can be reduced. By setting the current sense resistor together with the current limit resistor and the DC block capactior the current level can be limited below 100 µA rms. It should be noted that the limit resistor can not be used as $R_{sense.}$ This is because if it is placed before the load, it will have a large AC common mode voltage present at the input of the inst-amp and hence will degrade its ability to differentiate the voltage difference across R_{sense}. If R_{sense} is set at the position after the load and near the ground, the common mode voltage of the instrumentation amplifier is minimized.

Section 3: Instrumentation Amplifier

The third part of the analogue frontend is the Instrumentation Amplifier AD8429 (Analog Device). There are two Instrumentation Amplifiers in the analogue frontend: one is for current sensing and another is for voltage drop measurement. AD8429 has very good specifications such as very high input impedance (1.5 GΩ), low noise (1

nV$\sqrt{Hz}$), high slew rate (22 V/us), excellent AC performance (80dB CMRR (Common mode reject ratio)) up to 5 KHz (Gain = 1), 15MHz bandwidth (Gain = 1), THD (Total Harmonic Distortion) = -130dBc (at 1 kHz, Gain = 1). The Instrumentation Amplifiers are shown in Figure 3.5.

In the current sense part, the resistor R_{sense} is used to convert from current to voltage so the AD8429 (Analog Device) can detect the voltage drop between R_{sense} and calculate the current applied to the four point probe. The second instrumentation amplifier is designed to capture the voltage drop between the two inner probes of the sensor. These two outputs from the instrumentation amplifier are passed through the band-pass filter and level shifter before reaching the ADC of the DSP.

Section 4: Band pass filter and level shift

In the band-pass filter (also used as an anti-aliasing filter) and level shift gain control is achieved by the use of the digital potentiometers AD5241/AD5242 (Analog Device). These are also used to control the input current level to the four point probe as shown in Figure 3.5.

The band-pass filter is designed using a RC high pass filter cascaded with a RC low-pass filter. To set different cut-off frequencies, the digital potentiometers are programmed to adjust the resistance level according to the frequency of the input signal source to the four point probe. As a rule of thumb, the cut off frequency was set to four times higher than the input frequency. Digital potentiometers are set to communicate with the DSP through an I^2C interface (Inter-Integrated Circuit). In total, the DSP will send 3×8-bits to AD5241/5242 through I^2C communication. Figure 3.12 illustrates the write process using I^2C.

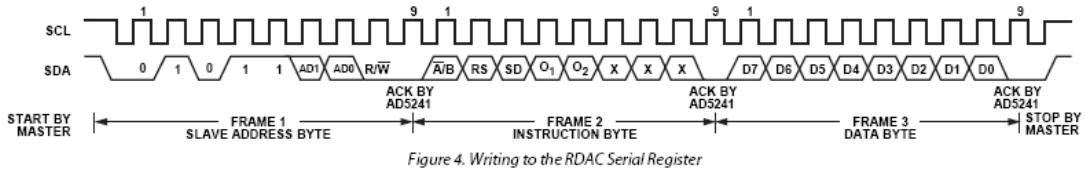


Figure 4. Writing to the RDAC Serial Register

Figure 3.12: I^2C writing timing diagram on AD5241 (AD5241, Analog Device)

The digital potentiometer has 256 positions corresponding to 256 Resistor levels. As the ability to change to different resistance levels is controlled by the DSP, the AD5242 was exploited to set various current levels and cut off frequencies of the anti-aliasing filter. As stated earlier, the measurement frequency is from 20 Hz to 100 KHz, therefore the anti-aliasing filter was set to have a cutoff frequency range from 80Hz to 400 KHz (four times higher than the input signal). It is set at the frequency higher than Nyquist theory (cut off frequency is set only two times higher than signal frequency) because the practical imperfection of the anti-aliasing filter can possibly filter out the output signal. The level shifter is a buffer with two symmetric resistors to lift the signal up to 1.65Vdc ($\frac{3.3V}{2}$) which is about half of voltage operation range (0-3.3V) of the ADC of the DSP. This level shift ensures that the signal can achieve maximum dynamic range (maximum swing) without distortion when it reaches the ADC.

3.2.3 Layout Design

The interface part with DSP called a Pictail Plus Board is used to plug into the pin connectors of Explorer 16 Board (contains dsPIC33F) to process the data shown in Figure 3.13.

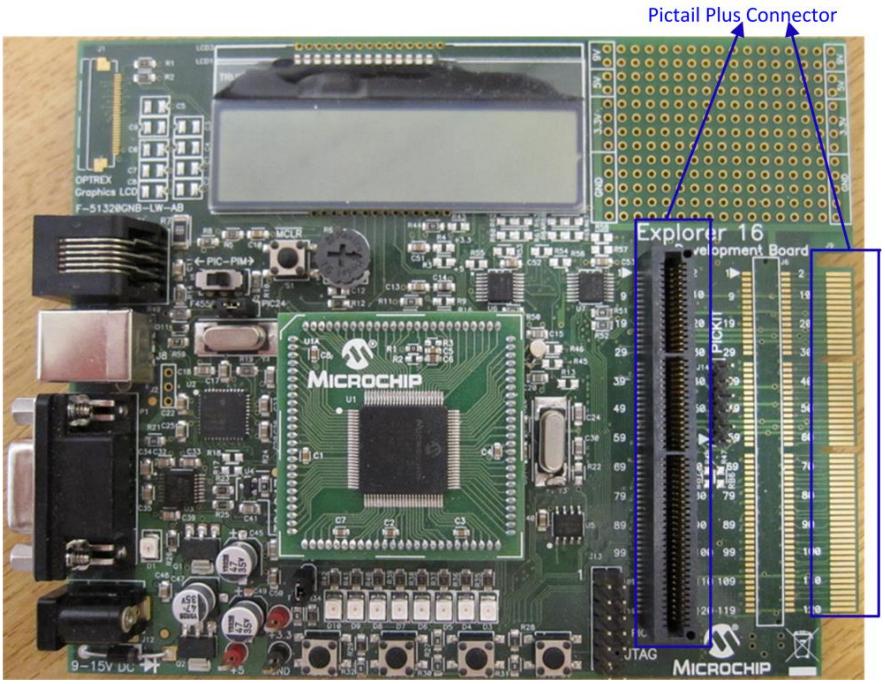


Figure 3.13: Microchip Explorer Kit 16 Board with Pictail Plus Connector

For the analogue frontend interface, the PCB Board is two layers in which the top layer is used for the main components design layout and bottom layer is used for coupling capacitors, resistors to set gain for amplifier and waveform generator. The board has dimensions of 85W×60H mm. Figure 3.14 presents a picture of the top layer design board with the main components labeled.

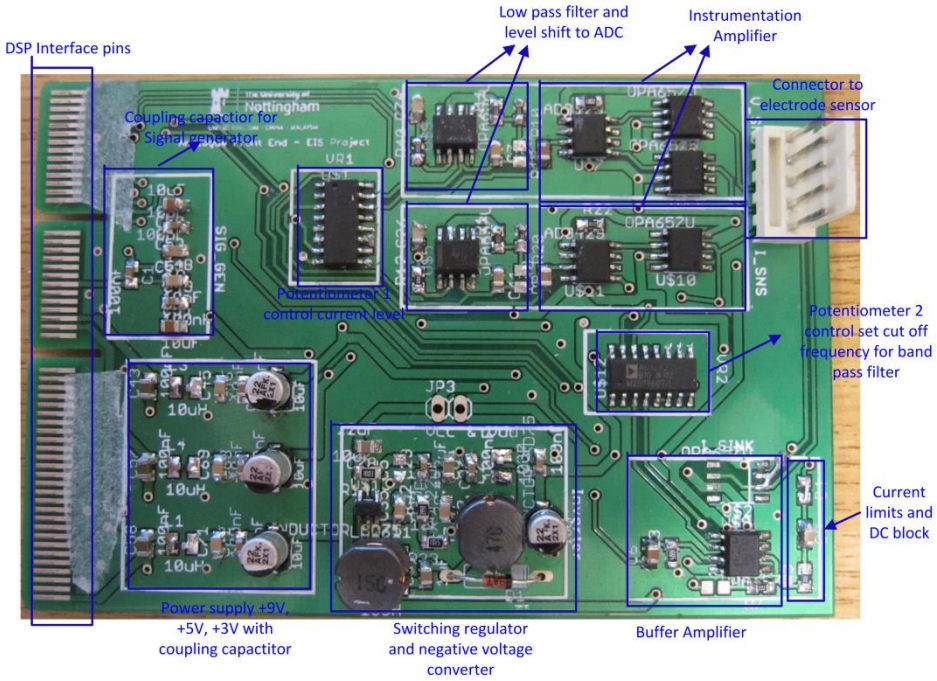


Figure 3.14: Top layer of the designed Interface Card

The top layer also contains the DSP interface pins, power supply, switching regulator with negative voltage converter, buffer amplifier, current limit and DC block, instrumentation amplifier, band-pass filter and level shifter. In addition, there are two programmable digital potentiometers: potentiometer 1 controls the current level and potentiometer 2 controls the cut off frequency for the band pass filter.

The bottom layer of the interface board is shown in Figure 3.15.

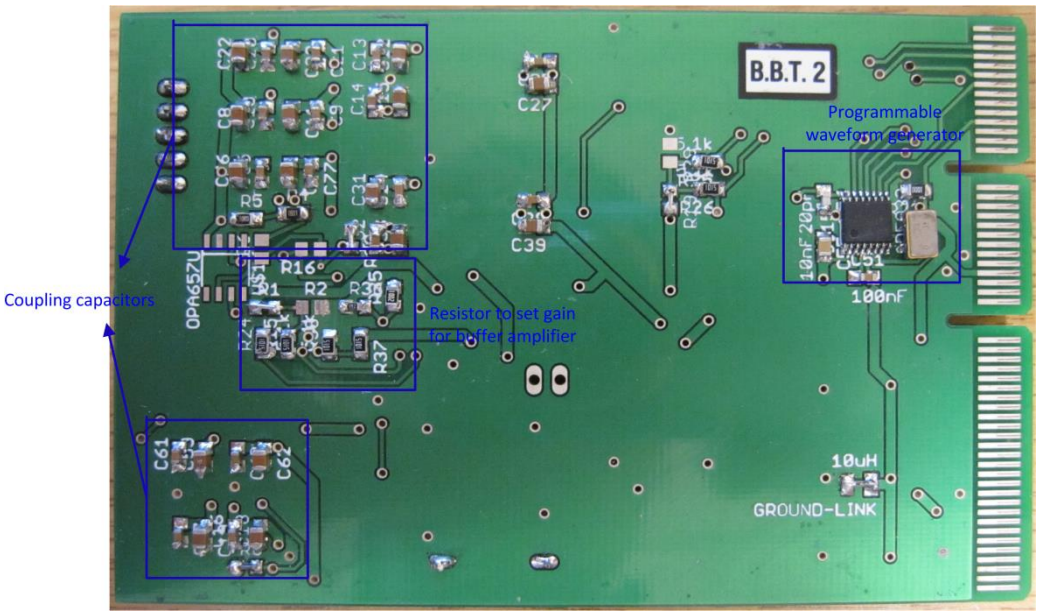


Figure 3.15: Bottom layer of the designed Interface Card

On this side of the board, programmable waveform generator, coupling capacitors maintaining the power supply for the op-amps and resistors to set gain for buffer amplifier are located and labeled in the Figure 3.15. The next section details the modelling of tetrapolar electrodes that used in this project.

3.3 Finite Element Method Modelling for bioimpedance electrodes

The electrode configuration (Figure 3.4) was originally designed to minimize destruction by oxidation or electrochemical reaction. In order to better understand measurements of moisturisers, it is of interest to estimate the depth of penetration of this configuration and a useful tool is EIDORS. EIDORS (http://eidors3d.sourceforge.net) [90][91] is an open source finite element method (FEM) software suite for image reconstruction in both electrical impedance tomography and diffuse optical tomography. It is written into Matlab code program to facilitate collaboration, testing and new research in these fields. This software structure is aimed to simplify FEM usage (compared for example to the more

complex FEM software such as COMSOL) and provides a uniform interface thereby allowing easier modification and customization.

Several research groups have deployed FEM on EIT based problems to image the acquired data. For example, Pedro et al [92][93] used EIT to investigate the sensitivity distribution of the tetrapolar probes by moving a sphere from the surface of electrodes to inside a semi-infinite homogeneous medium. Measurements of the thorax using EIT were taken by Frerichs et al [94][95] for monitoring lung injury from pigs. Heinrich et al [96] used an EIT system to acquire the body and head effects on regional lung ventilation in neonates lying in the prone position. Wolf et al [97] used EIT to estimate the extent of acute lung injury during ventilation whilst Adler et al [98] described an approach to perform linear image reconstruction in lung EIT. The data of these researchers were all acquired and reconstructed with EIDORS. Other application examples exist of the usage of EIDORS in imaging conductivity changes in the abdomen [99].

3.3.1 Creation of a forward model

The work presented in this section focuses on the voltage sensitivity distribution of the four point probe electrodes. The four point probe model and the conductivity volume were created by using the forward model in EIDORS version 3.7.1 together with Netgen Mesh Generator version 5.3.1. The simulated 3D models generated by Netgen Mesh Generator consist of a homogeneous volume of conductivities that can be varied from 0.14 S/m to 0.0001 S/m. The geometry extends from 0 mm to 10 mm in the x-axis, between 0 and 5 mm in the y axis and -5mm to +5mm in the z-axis. In this initial specification, each electrode has a rectangular shape of 2mm length x 1mm width, the line of symmetry is the x = 5mm line; a simulated 1mA current was injected between the two outer electrodes, and the simulation voltage is measured at

the two inner electrodes. Figures 3.16 and 3.17 illustrate the model set up for a probe separation of 0.1mm.

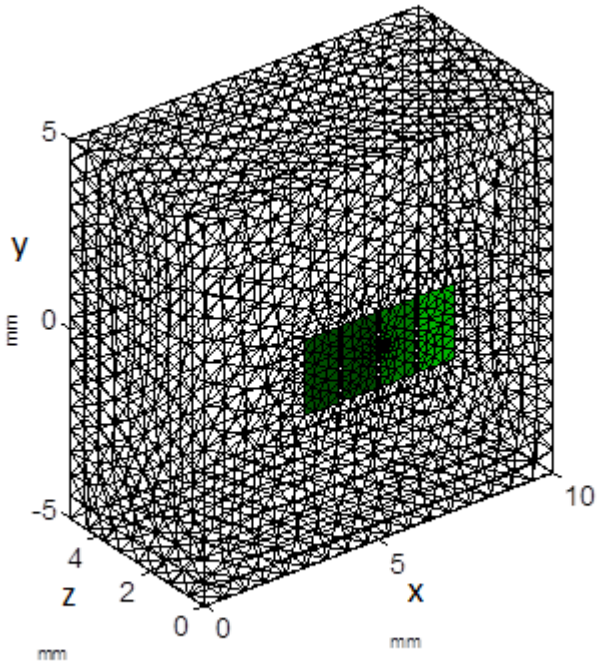


Figure 3.16: 3D FEM model with four point probe electrodes (in green)

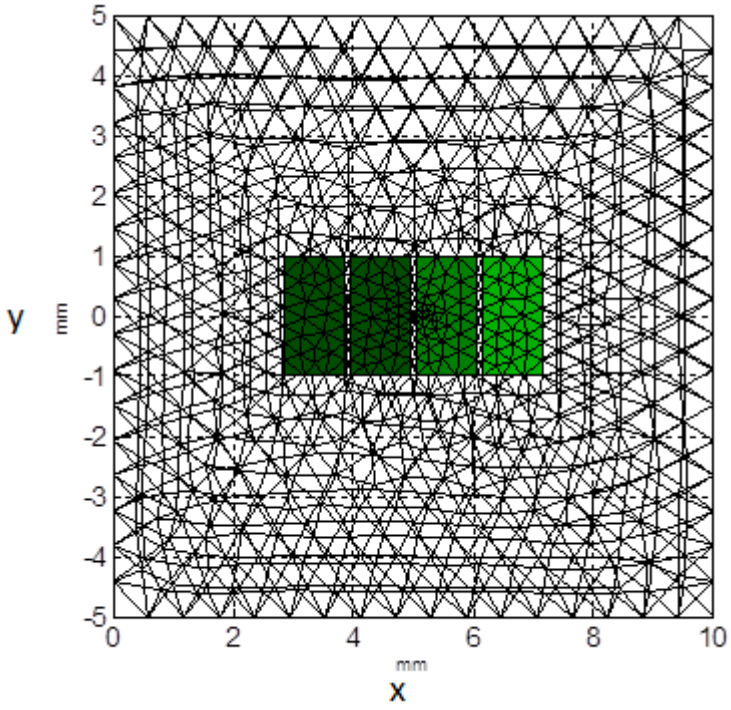


Figure 3.17: Four point probe shown only in X-Y axis with a probe separation of 0.1mm

The injecting electrodes are positioned at x = 6.65mm and 3.35mm, the measuring electrodes are located at x = 5.55mm and 4.45mm. The mesh of the 3D model constructed had 4,790 mesh points and 20,040 triangular elements.

For these simulations, equally spaced electrodes were used with separations "s" of s = 0.1mm, 0.2mm, 0.5mm, 0.6mm, 1mm, 1.5mm and 2mm. The overall aim of these simulations was to ascertain the spatial voltage distribution in terms of depth for various probe separations.

3.3.2 Adding the stimulating pattern

The current is injected into two outer probes as illustrated in Figure 3.18. The amplitude of current injected was set at 1mA. The positive voltage distribution is shown in the red colour area whilst the negative voltage distribution is shown in blue.

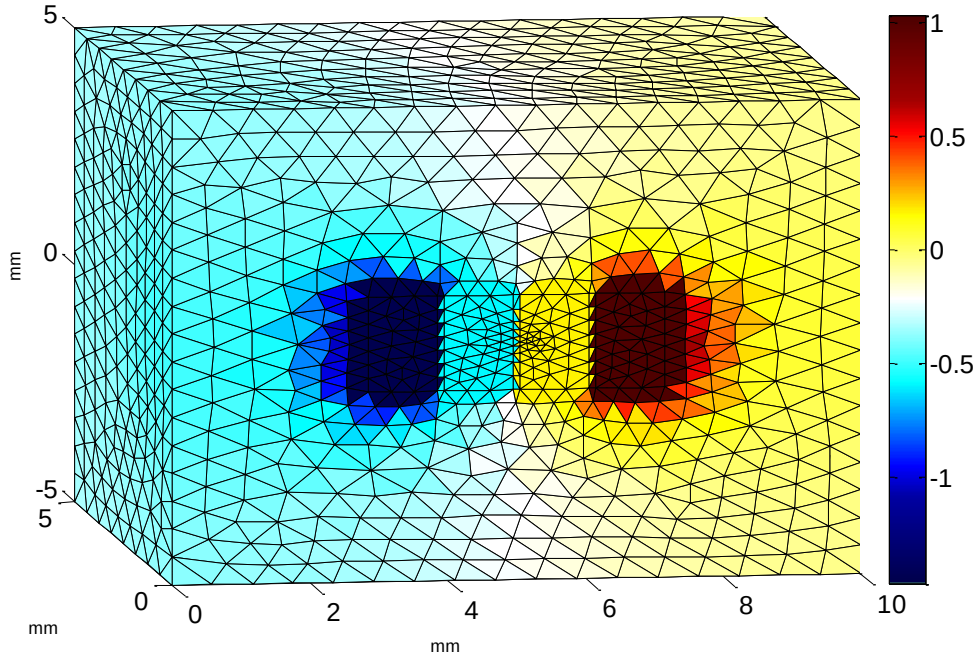


Figure 3.18: Stimulation pattern using EIDORS. Red is positive voltage distribution volume and blue is negative voltage distribution volume.

In this case, the pattern simulates the injecting current in the two outer electrodes, and the measuring voltage is on the two inner electrodes.

3.3.3 Estimating penetration depth

In order to estimate the depth of penetration of the applied current a small object with different conductivity from the background medium is moved from the surface to deep inside the medium (see Figure 3.19). This follows a method described in detail by [92][93]. The rationale is that if there is no significant difference in the measured voltages in the absence and presence of the object then the current will not have reached those depths. For example an object near the surface will have a large effect on the measured voltage and this will descrease as the object moves deeper into the tissue away from the surface. Subtracting the inhomongeneous (with object) and homogenous (without object) cases provide a voltage difference with object depth whose 1/e value corresponds to the penetration depth (37% of the original value). This procedure is repeated for different electrode separations and for different conductivities of the volume.

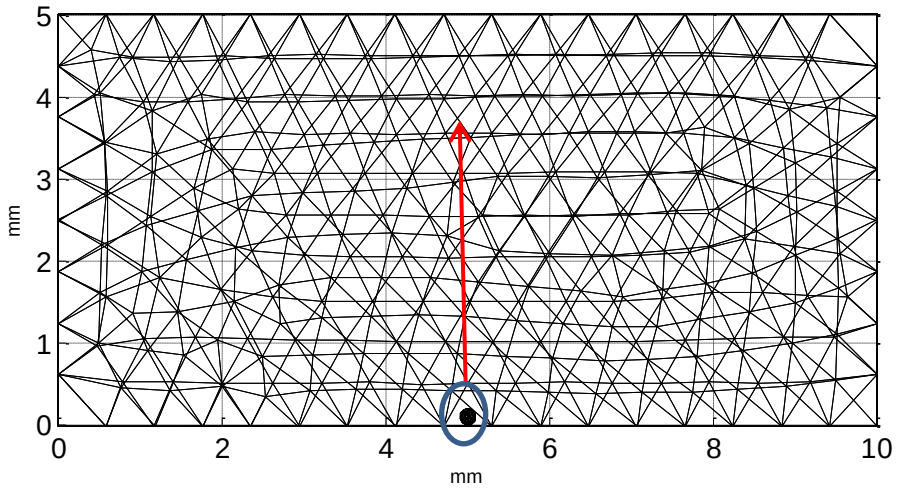


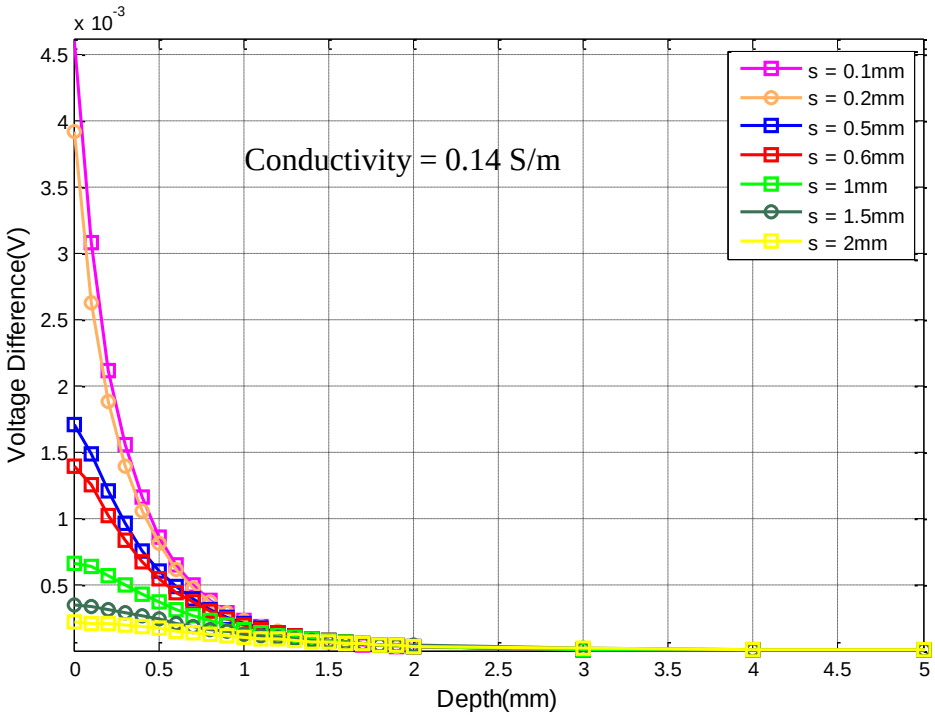
Figure 3.19: Moving an object from the surface to deeper inside the volume to obtain the voltage sensitivity distribution.

The voltage differences are obtained from:

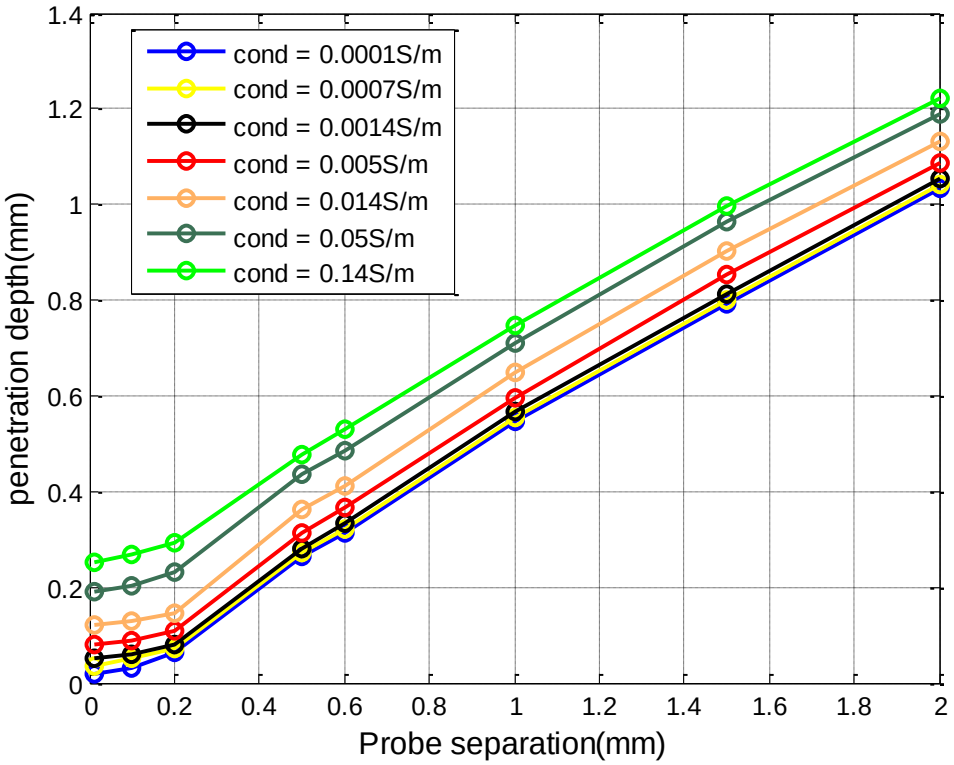
$$\Delta V = | V_{homogenous} - V_{non\text{-}homogenous} |$$

3.3.4 Penetration depth calculations

In Figure 3.20a, the voltage difference between the homogenous and inhomogenous cases is shown for different object depths and different electrode source separations (conductivity of the volume = 0.14 S/m, current = 1mA). When the object is positioned at the surface (object depth = 0, Figure 3.20a), the voltage measured between the two inner electrodes is at its highest. This is because the object has the greatest effect on the current near the surface due to the high current density. As the object moves deeper inside the volume, the voltage distribution becomes smaller as the contribution of the current to the detected signals decreases and eventually becomes negligible. Higher signals can be seen when the probes are close together but the pentration depth increases with increasing separation. In Figure 3.20b, the penetration depth is plotted against conductivity for different separations. It can be seen that as the probe separation increases, the penetration depth also increases. Also, the low conductivity medium makes the penetration depth smaller and high conductivity medium makes the penetration depth larger.


x 10^-3
Conductivity = 0.14 S/m
s = 0.1mm
s = 0.2mm
s = 0.5mm
s = 0.6mm
s = 1mm
s = 1.5mm
s = 2mm
Voltage Difference(V)
Depth(mm)

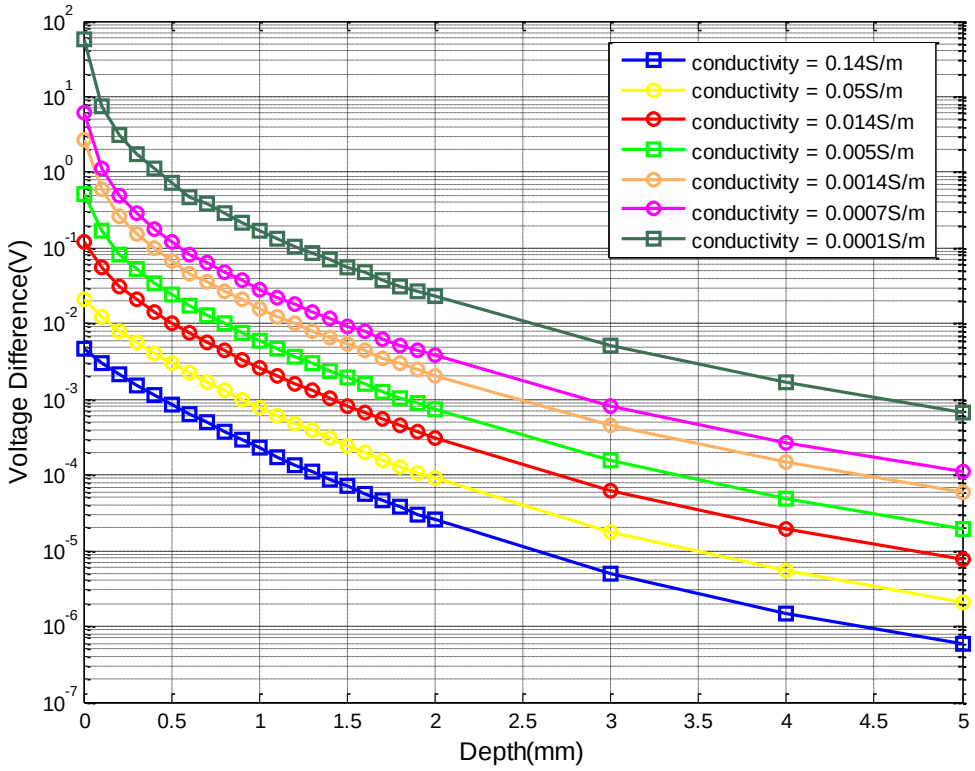
(a)


cond = 0.0001S/m
cond = 0.0007S/m
cond = 0.0014S/m
cond = 0.005S/m
cond = 0.014S/m
cond = 0.05S/m
cond = 0.14S/m
penetration depth(mm)
Probe separation(mm)

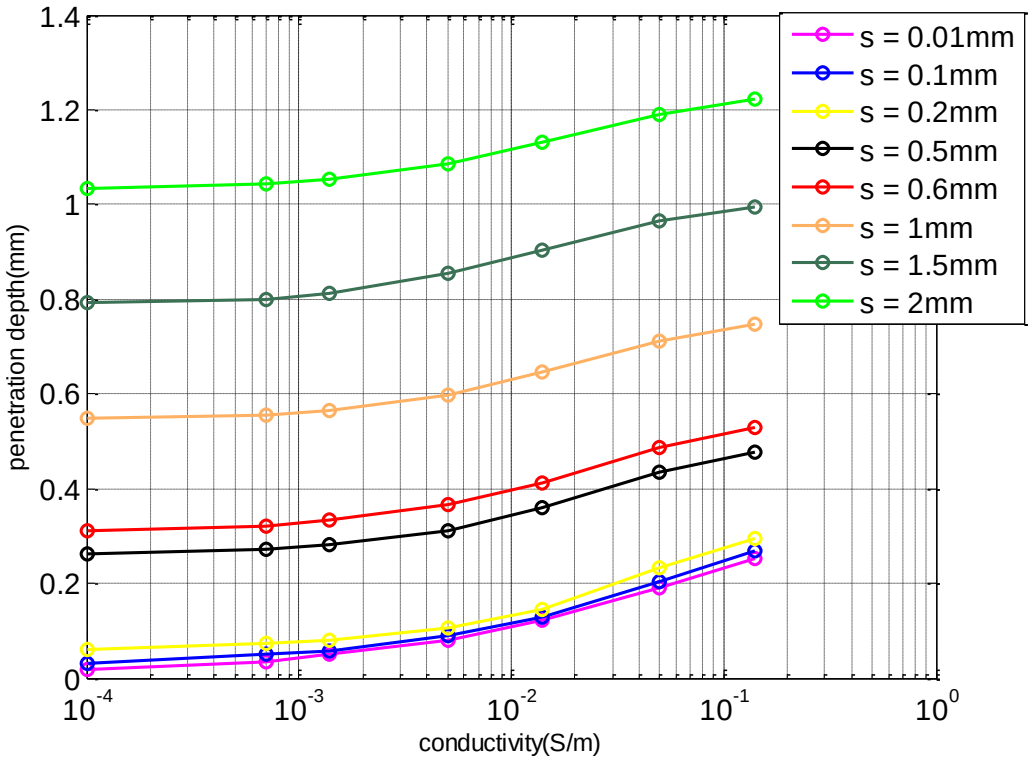
(b)

Figure 3.20: Voltage difference between inhomogeneous and homogeneous case with object depth for a volume conductivity of 0.14 S/m (b) penetration depth for different probe separations

Figure 3.21 investigates the effect of varying the conductivities from 0.14 S/m (high conductivity) to 0.0001 S/m (low conductivity). The voltage differences obtained for different object positions are shown in Figure 3.21a. The penetration depth of an equally spaced electrode for s = 0.1mm can be calculated from Figure 3.21a and is shown in Figure 3.21b with different separation s = 0.1 mm to s = 2mm.



(a)



(b)

Figure 3.21: a) Voltage difference between inhomogeneous and homogeneous case versus object depth using a fixed probe separation (s) of 0.1mm, b) corresponding penetration depths. The conductivity of the volume is varied from 0.14 S/m to 0.0001 S/m

As seen in Figure 3.21b the model is simulated with different conductivities from high to low value i.e. 0.14 S/m to 0.0001 S/m based on the literature review of the conductivity of skin tissue. The penetration depth of different separations can be seen to be nonlinear and depends on the conductivity of the medium.

3.3.5 Electrode optimisation

From the above results, it can be seen that the penetration depth is dictated by the probe separation of the four point probe. The larger separation will provide the larger penetration depth. However, there is a trade-off since the larger separation also makes the voltage difference (between inhomogeneous and homogeneous case)

smaller in the four electrode configuration. A larger separation probe could make it difficult for instrumentation design in term of detectable signal. A smaller separation probe could have better SNR, but achieve lower depth. In addition, the penetration depth is dependant on the conductivity of the medium i.e. the penetration depth is greater in the high conductivity medium, and shallower in the low conductivity medium.

In the human skin, the stratum corneum is typically 50 µm with a conductivity of 0.0001 S/m. Below the stratum corneum is the epidermis and dermis layer, which has a thickness from 0.3 mm to 2 mm. The stratum corneum, epidermis and dermis thickness vary considerably from person to person. Therefore, choosing a separation of electrodes that reach into a certain depth for all patients is difficult. The depth of interest in this thesis for skin cream application is defined as the stratum corneum and the upper part of the epidermis. Hence the penetration depth of interest should be at ~ 0.1 mm (about stratum corneum depth) and therefore an optimum separation s = 0.1mm would represent a preferred choice.

It should be noted that for this work a probe separation of 0.6mm was chosen because there is a hypothesis that the effects of creams could possibly affect deep inside the underlying skin tissue i.e. at epidermis or even dermis (0.3mm from skin surface). In this case the pentration depth is ~0.53 mm in a high conductivity medium (0.14 S/m) and ~0.3 mm in low conductivity medium (0.0001 S/m). At a penetration depth of 0.1mm with a probe separation of 0.6mm the voltage distribution has reached 90 % of the surface value (Figure 3.20a) and hence it is still probing a large proportion of the medium of interest i.e. the stratum corneum and upper epidermis. Figure 3.20b shows the same plot as Figure 3.21 but this time with penetration depth vs conductivity in the function of probe separation. This graph

shows that the different conductivities can affect the penetration depth of the probe i.e. at s = 0.6mm, the penetration depth varies from 0.3mm to 0.53mm, however at s = 0.1mm, the depth is from 0.05mm to 0.23mm. In other words the 0.6mm separation may not be the optimal configuration, however, it is still probing 90% of the volume of interest and is highly dependent on the stratum corneum depth and skin conductivities that vary considerably from subject to subject.

3.3.6 Conclusion

Several conclusions can be drawn from these simulations.

- The addition of the EIDORS simulation has greatly assisted understanding of the voltage distribution throughout the skin.
- The larger the separation, the smaller the voltage difference in a four electrode configuration.
- The skin depth of different separations is nonlinear and is dependant on the conductivity of the medium.
- When the probe separation increases, the penetration depth also increases.
- The probe separation used of 0.6mm although not optimal it still probes 90% of the intended volume

Also, the low conductivity medium makes the penetration depth smaller and high conductivity medium makes the depth larger.

3.4 Digital signal processing: Digital Filter, Lockin Amplifier and Discrete Fourier Transform

Noise and signal distortion at the input of the ADC can cause errors in the recorded values. Several methods are available to capture the amplitude of the signal whilst removing noise and distortion, such as a digital filter lock-in amplifier or filtering via

a discrete Fourier transform (DFT). Three programs carrying out these processing methods have been embedded in the digital signal processing part of the system.

3.4.1 Digital Filter

The signal received at the ADC is contaminated by noise and distortion. Noise can be derived from the power supply, op-amp, shot noise, thermal noise and flicker noise from components and devices. Even though an analogue anti-aliasing filter is used, there is a need to use a digital filter to reduce the noise and hence increase SNR. Digital filters are classified by the duration of their impulse response, which can be finite or infinite. Advantages of infinite impulse response (IIR) filters are less memory storage, the number of coefficients decreases, and less time is needed to perform the calculation compared with finite impulse response (FIR) filters. However, IIR filters have the disadvantage that the response can be unstable, therefore it is necessary to design carefully to eliminate the instability. Since the IIR filter is more efficient on processor resources than FIR, it is used to design the low pass filter in this system. In Figure 3.22, the IIR Chebyshev 2^{nd} order low pass filter is simulated as an example. The coefficients produced by Matlab via a command [B,A]= cheby1(2,0.1,0.1/1.6) are B_0=0.0251, B_1=0.0502, B_2=0.0251, A_0=1, A_1=-1.5292, A_2=0.6308.

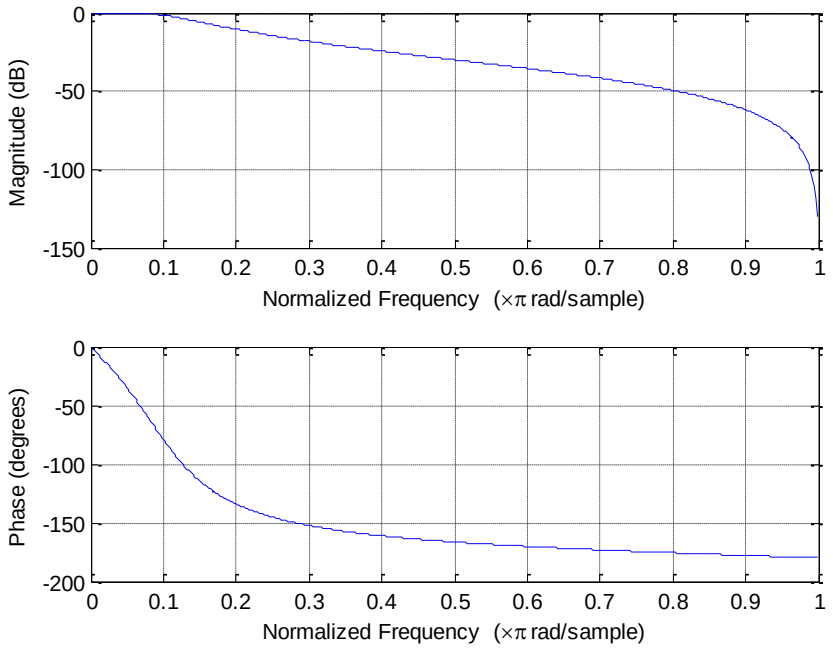


Figure 3.22: Matlab simulated response of the low pass filter

The corresponding equation of this low pass filter is therefore:

$$y[n] = 0.0251x[n] + 0.0502x[n-1] + 0.0251x[n-2] + 1.5292y[n-1] - 0.6308y[n-2] \quad (3.4.1).$$

This equation (3.4.1) is then embedded into a DSP processing function. So, after the ADC Buffer receives full data, this data will be multiplied and divided by the transfer function above in order to reduce noise in the signal. The ADC Buffer utilises 10-bit data therefore input x[n] is also 10-bit digital number. As shown in Figure 3.23, the effect of the low pass filter is seen directly from the ADC input data of DSP before and after low pass filtering.

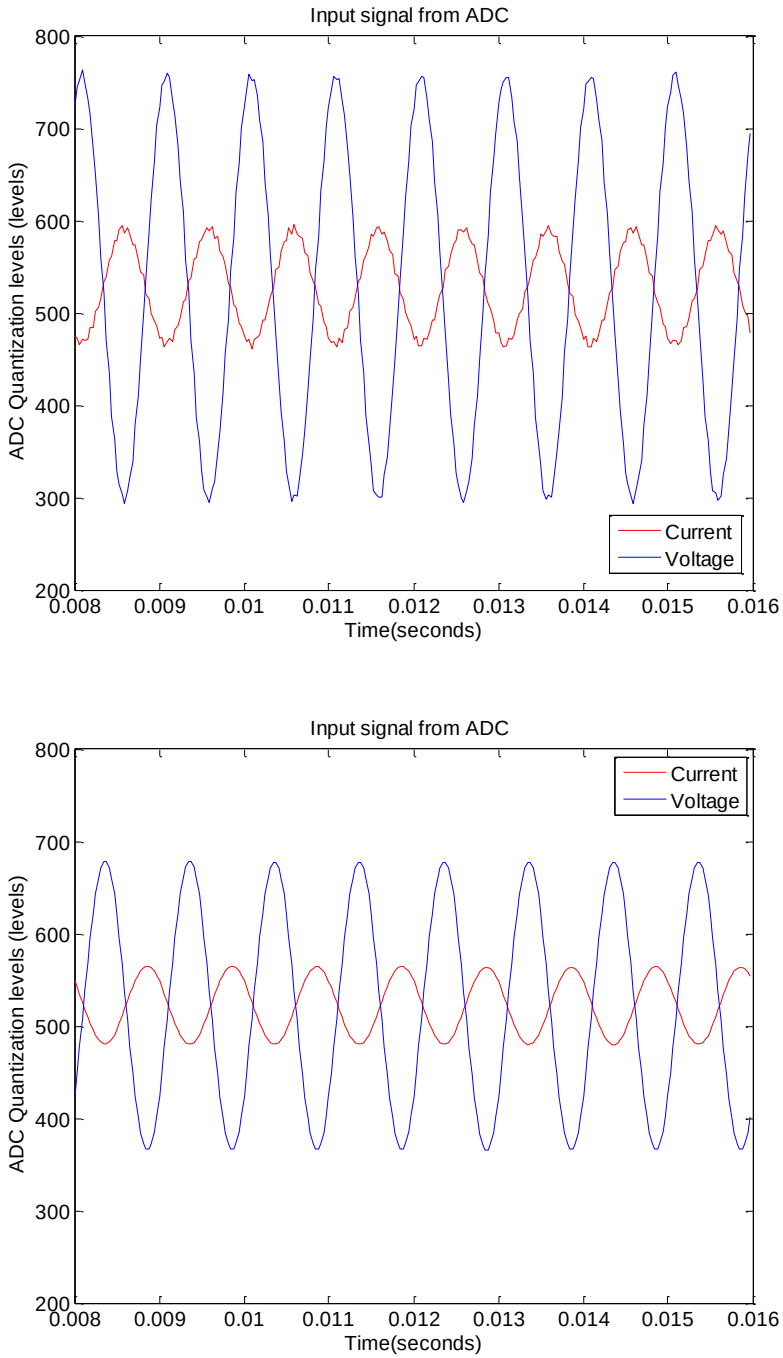


Figure 3.23 : ADC input data before (top) and after (bottom) low pass filtering, signal frequency at 1 KHz, sampling frequency at 32 KHz, N_{DFT} is 512 points

This figure shows that the ripples from the ADC raw data have been removed quite well. For example, in the current signal from ADC (in red) before low pass filter, the amplitude of the signal A_{signal} is about 120 levels and the amplitude of noise A_{noise} is 15 levels. The signal to noise ratio is calculated by

$$\text{SNR} = 20\log_{10}\left(\frac{A_{signal}}{A_{noise}}\right) \quad (3.2)$$

From the equation (3.2), the SNR from ADC input before the low pass filter is 18 dB. After passing through the low pass filter, the A_{signal} = 85 levels and A_{noise} = 0.1 levels and hence SNR = 58.5dB. Similar to the current signal from the ADC, the SNR from the voltage signal (in blue coming from the inner two probes) is improved from 20 dB to 65 dB. Both signals are then passed to the next stage for amplitude and phase detection using a lock-in amplifier.

3.4.2 Lock-in Amplifier

The design reported here uses lock-in detection with quadrature demodulation to capture the amplitude and phase signals.

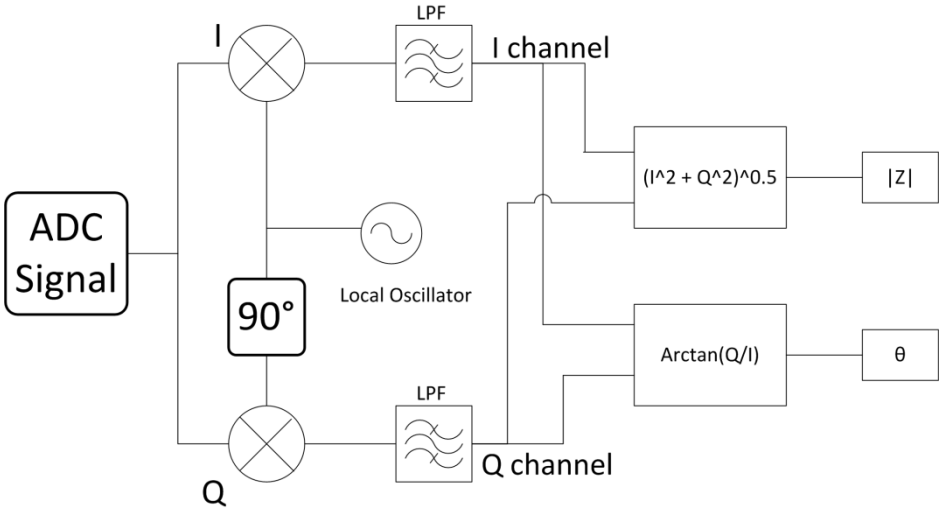


Figure 3.24: Block diagram of a quadrature demodulator

Assuming the ADC Signal is a sine wave with equation $S_1(t) = A_1\sin(\omega t + \theta_1)$. The DSP generates two local oscillators: one in phase with equation $I(t) = \sin(\omega t)$, and another 90 degree out of phase $Q(t) = \sin(\pi/2 - \omega t) = \cos(\omega t)$. By multiplication of the ADC signal and two local oscillators, there are two outputs called the in-phase channel and quadrature channel. In the in-phase channel, the signal is

Ichan = $S1(t) * I(t) = A1 * sin(\omega t + \theta 1) * sin(\omega t) = A_1 * \left(\frac{\cos(\theta 1) - \cos(2\omega t + \theta 1)}{2}\right)$

Qchan = $S1(t) * Q(t) = A1 * sin(\omega t + \theta 1) * cos(\omega t) = A_1 * \left(\frac{\sin(\theta 1) + \sin(2\omega t + \theta 1)}{2}\right)$

The I and Q channel are passed through a low pass filter to remove the high frequency components at 2ωt. Therefore, after going through the low pass filter, there are only $A_1\frac{sin(\theta 1)}{2}$ and $A_1\frac{\cos(\theta 1)}{2}$ in the in-phase channel and quadrature channel respectively. By applying the square root equation, the absolute impedance can be obtained by $|Z| = \sqrt{I^2 + Q^2} = \frac{A1}{2}$. In addition, the phase can be derived by $\theta_1 = \tan\frac{Q}{I}$. As said above, two ADC results were simultaneously, one ADC channel was used for capturing current sense and another channel was used for measuring voltage drop in the inner two probes. After going through the lock-in process, absolute amplitudes of current and voltage were obtained along with the phase shift of voltage $\theta_{voltage}$ and current $\theta_{current}$. By taking the ratio between voltage and current, the absolute impedance can be calculated:

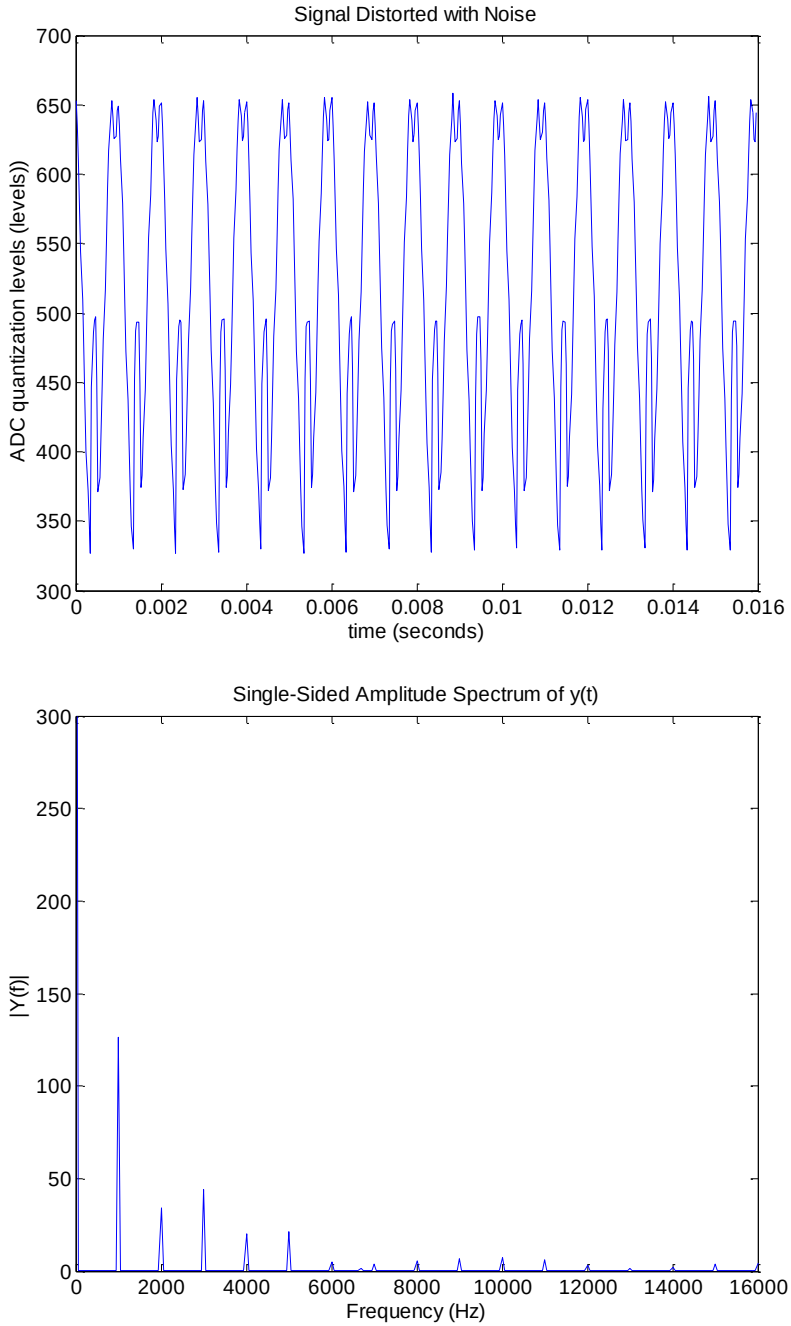
$$|Z| = \frac{|V|}{|I|} \tag{3.3}$$

The phase shift between voltage and current is also calculated by using the subtraction of voltage phase $\theta_{voltage}$ and current phase $\theta_{current}$.

$$\theta_{diff} = \theta_{voltage} - \theta_{current} \tag{3.4}$$

As the waveform generator can sweep the frequency from 20Hz to 100 KHz, the lock-in amplifier was programmed to change the frequency of the local oscillator to lock at the desired frequency and remove unwanted frequency and noise. However, the lock-in amplifier technique could only detect the amplitude of the locked

frequency but could not detect effectively the harmonic distortions that occur in the input signal. In order to detect the harmonic distortion, the lock-in amplifier's local oscillator frequency needs to be changed and repeat the multiplication so that it can calculate the distortion at the second harmonic 2f, third harmonic 3f,… up to the sixth harmonic 6f. However, this is time consuming and hence inefficient. An example of harmonic distortion of a signal at modulation frequency = 1 KHz, sampling frequency at 32 KHz and N_{DFT} is 512 is shown in Figure 3.25



distorted ADC data -> THD = ($P_2 + P_3 + P_4 + P_5 + P_6$) / P_1= 24.91%

Figure 3.25: Harmonic distortions in the ADC input signal

Clearly, the input signal to the ADC contains considerable harmonic distortion at 2 KHz, 3 KHz, 4 KHz, 5 KHz and 6 KHz. By multiplying with in-phase and quadrature phase coefficients, these harmonics also contribute to the low frequency parts before going through the low pass filter. So, even after going through the low pass filter, this harmonic distortion still affects the fundamental frequency and

decreases SNR. By detecting the distortion in early stage, the distorted signal can be discarded or adjusted to reduce the distortion (i.e. reduce the amplitude of the current), hence improving the robustness of the data processing. In order to detect effectively the presence of this distortion, the Discrete Fourier Transform was used.

3.4.3 Discrete Fourier Transform

The lock-in technique does not give an efficient way to detect the distortion. The solution was to use a Discrete Fourier Transform (DFT) and to calculate the total harmonic distortion (THD immediately at the early stage. This should be taken when ADC Buffer is full of samples to avoid passing data into late processing stage such as low pass filter or lock-in. The THD calculation is given by:

$$\text{THD} = \frac{P2+P3+P4+\cdots+P\infty}{P1} = \frac{\sum_{i=2}^{\infty} Pi}{P1} \tag{3.5}$$

In which P_1 is the power of the fundamental frequency, P_2 is the power of the 2nd harmonic frequency, P_3 is the power of the 3rd harmonic frequency, P_4 is the power of the 4th harmonic frequency and P_i is the power of the ith harmonic frequency. In the practical measurement shown in this thesis, the DFT is used to calculate only up to 6th harmonic:

$$\text{THD} = \frac{P2+P3+P4+P5+P6}{P1} \times 100\% \tag{3.6}$$

Measurements for calculating the THD are made at the ADC output of the custom-made bio-impedance analyzer i.e before the lock-in stage. In order to detect the distortion, the input signal from the voltage source will be set at certain amplitude for fixed current level. The current passes through an unknown impedance DUT, and depending on the high or low impedance from the DUT, will cause distortion at the ADC input. For example, because the high input current going through the high

impedance load, the output signal from the sense circuit will be distorted and detected by DFT calculation. In Figure 3.26, the graph with undistorted ADC data is presented.

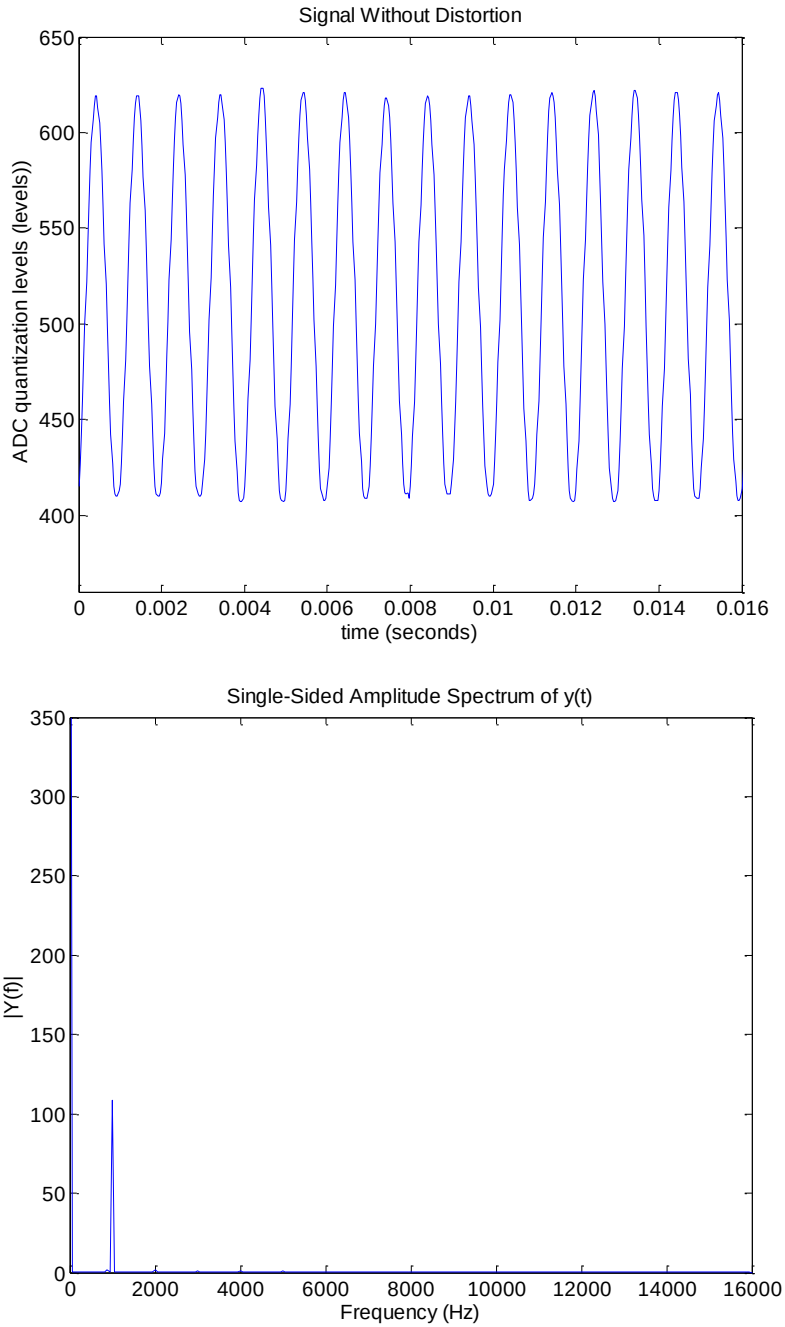


Figure 3.26: THD calculation in undistorted ADC data -> THD = ($P_2 + P_3 + P_4 + P_5 + P_6$) / P_1= 0.0456 %

In the case of undistorted ADC data, there is a small frequency drift due to the 50/60 Hz from the AC power supply. The custom-made bio-impedance analyzer uses two ADC channels to capture the results from the current sense and voltage drop parts of the circuit. Because of the nonlinearity in distortion of each channel, a THD measurement is used for each channel data in which THD > 1% is discarded. For example, a common cause of distortion was that the current level was set too high at first, which made the voltage higher than the maximum acceptable ADC voltage. As the object's impedance is usually unknown, the applied current level could be higher than necessary. The solution to this problem was therefore to reduce the current level until THD becomes less than an "acceptable" 1%.

3.5 Impedance measurement at multiple frequencies

An automatic frequency scan is implemented into the dsPIC33F to control the waveform generator AD5932 through SPI to generate 10 different frequencies from 20Hz to 100 KHz. At every frequency, the ADC channel will take 1024 samples and then pass them through the Lock-in Amplifier Quadrature Demodulation to determine the amplitude and phase of the output measured from Instrumentation Amplifiers AD8429. The processed data is then captured and sent to a PC through RS232 using a Matlab interface. Figure 3.27 shows the custom-made bio impedance analyzer with the four point probe sensor plugged into the analogue frontend.

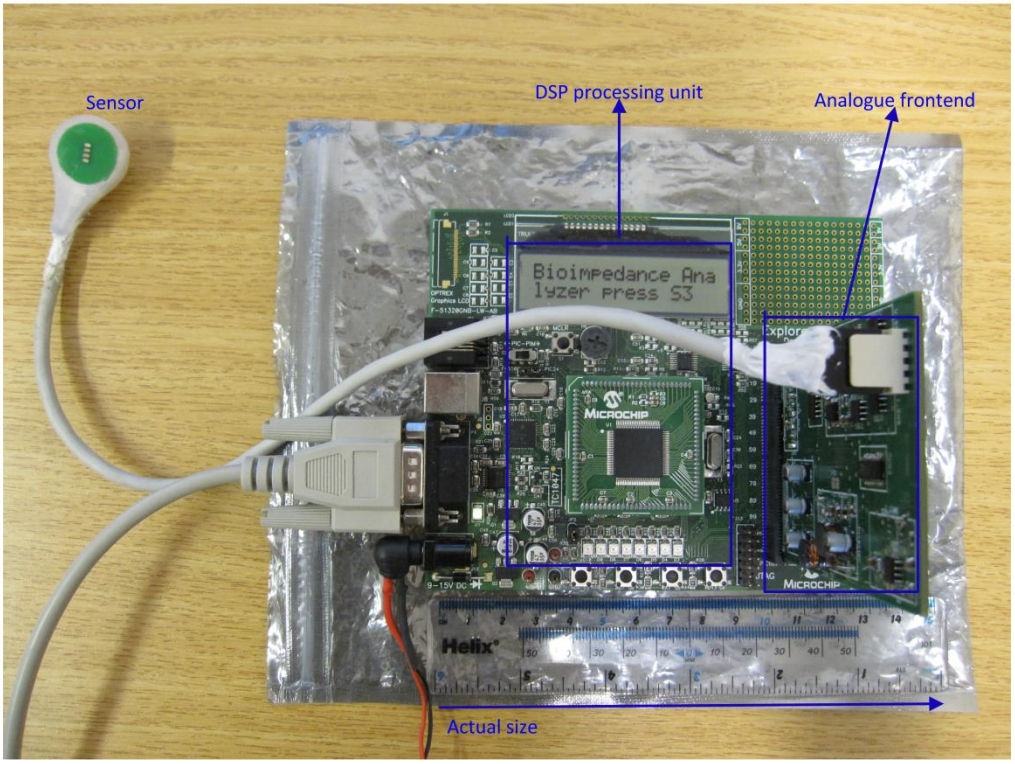


Figure 3.27: the complete custom-made bio impedance analyzer system

In detail, one sweep from 20 Hz to 100 KHz takes about 10 seconds. The frequencies scanned are at 20 Hz, 100 Hz. 200 Hz, 500 Hz, 1 KHz, 2 KHz, 5 KHz, 10 KHz, 20 KHz, 50 KHz, 80 KHz and 100 KHz. The number of data points per frequency sweep was held fixed at 1024 samples (N_{data}). Also, the sampling frequency is set at 32 x the sweep frequency. For instance, at 20 Hz, the sampling frequency is set at 640Hz (×32 times higher). As N_{data} = 1024, then for 20Hz it takes 1.6 seconds to acquire the data. At a signal frequency of 1 KHz, the sampling frequency is set to 32 kHz (again ×32 times higher), but for 1024 points it takes only 32 milliseconds to complete a 1KHz scan. Three parameters – peak to peak current level (μA), number of scans/ sweep and display the received data in real time, are necessary to control the system using a PC. The main control interface application was written in Matlab to interact with the DSP board through RS232. Figure 3.28 shows the main interface application of the custom-made bio-impedance analyzer.

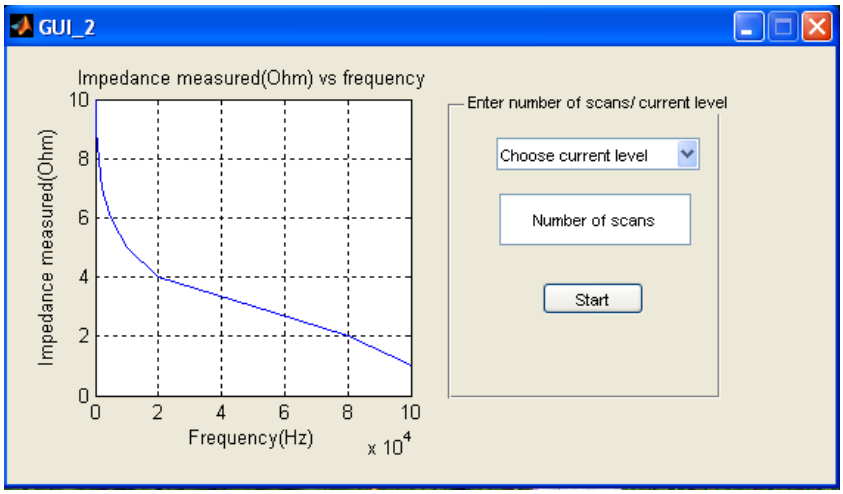


Figure 3.28: Control application – Main interface with PC

In the interface application, the real-time measurement is shown as impedance versus frequency. Also, the drop down bar is made to select the current level (in µA peak to peak) and input data bar to enter the number of scans. Characterisation using samples of known impedance is necessary before the sensor is applied to measurements on human skin. The purpose of these calibration measurements are firstly because it is necessary to understand the accuracy of the frequency response of the impedance analyzer system; secondly there is a need to make sure the programmable current generator and instrumentation amplifier are working correctly and give coherent answers; finally, these measurements provide confidence before moving onto skin analysis as the human skin has unknown frequency dependent impedance. Therefore it makes sense to work firstly with known passive resistor and capacitor networks and with a known ionic calibration solution.

3.6 Characterization with DUT (Device under test)

In four terminal measurment, stray impedances could be introduced into the measurement circuit by cable, electrode and sample. In Figure 3.29, the waveform generator generates a sine wave to the four point probes sensor through the sample impedance Z_{sample}/ Z_{dut} and the stray impedances are shown by Z_{1stray} and Z_{2stray}.

These impedances Z_{1stray} and Z_{2stray} act in series with the sample impedance (DUT) as a potential divider, which affects the voltage across the sample impedance.

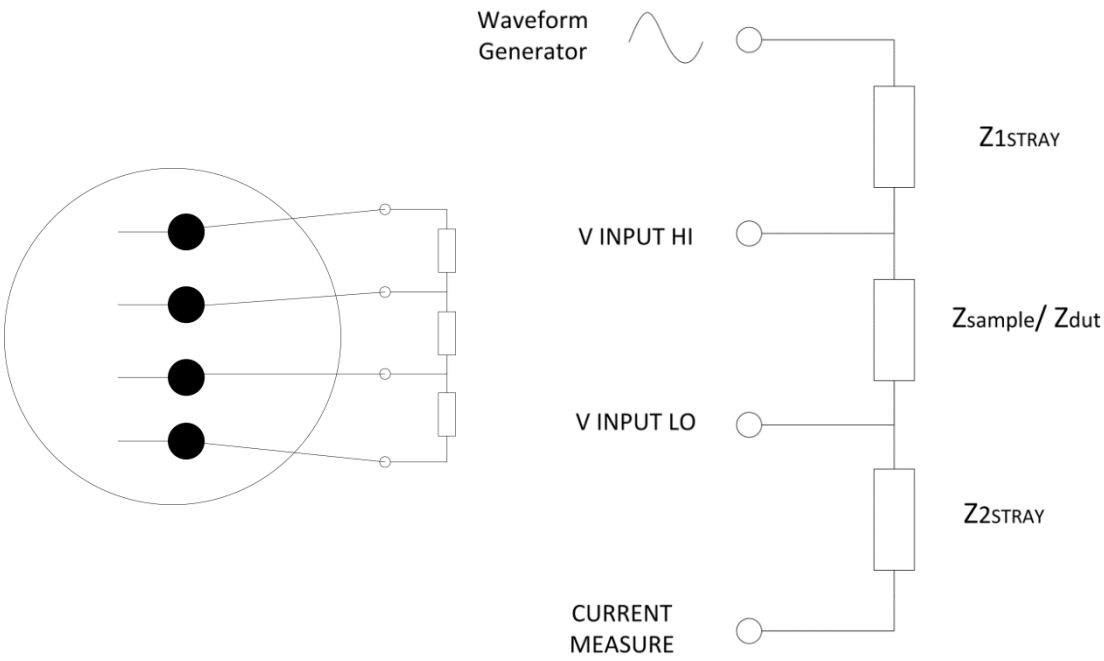


Figure 3.29: Measurement model of the four point probe system

The voltage developed across the sample is then measured by the instrumentation amplifier at two points: Vinput High and Vinput Low. At the last point of the four point probe sensor, there is a current sense part in order to measure the current I passing through the impedance network. The current flowing through the sample is converted to a voltage drop V_d across Vinput HI and Vinput LO by an instrumentation amplifier:

$$V_d = V_{input}(\text{HI}) - V_{input}(\text{LO}) \tag{3.6.1}$$

$$|Z_{dut}| = \frac{V_d}{I} \tag{3.6.2}$$

in which V_d is the difference between the voltage across V_{input} HI and V_{input} LO, I is the current passing through the sample and $|Z_{dut}|$ is the absolute impedance value of the DUT.

3.6.1 Calibration resistor and capacitor network

Three resistors or three resistors combined with a capacitor are soldered into the probe sensor (Figure 3.30). Three resistors (carbon resistors) were used with eight different values: 3x1kΩ, 3x10kΩ, 3x100kΩ, 3x380kΩ, 3x470kΩ, 3x800kΩ, 3x1MΩ, 3x10MΩ and 3x30MΩ (5% tolerance). A range of capacitor (polymer film capacitors) values were used: 1.5nF, 3.3nF, 4.7nF, 6.8nF and 10nF (10% tolerance).

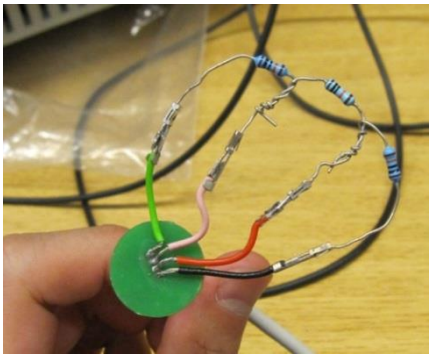


Figure 3.30: Calibration resistors and capacitors networks

3.6.2 Calibration with solution

Five kinds of calibration solution were used, namely: de-ionized water (7 µS/cm), calibration solution (46 µS/cm), Hanna Instrument HI7033 calibration solution (92 µS/com), tap water (580 µS/cm) and Hanna Instrument HI7031 calibration solution (1376 µS/cm). The calibration solution is tested independently before applying the four point probe sensor using a conductivity meter. The conductivity is at a specific temperature, therefore, by using a Hanna Instrument Conductivity Meter HI8733 with temperature compensation, the conductivity of the solution can be estimated accurately.



Figure 3.31: Calibration solution is checked by Hanna Instrument conductivity meter before measurement.

Figure 3.32 illustrates how the four point probe electrodes were immersed in the liquids in order to make the measurements.

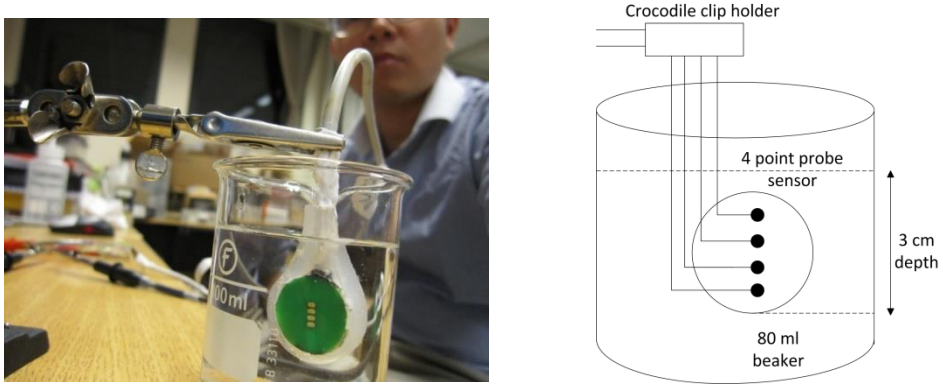


Figure 3.32: Four point probe electrodes set up to measure the calibration solution.

As shown in Figure 3.32, the calibration solution was put into an 80 ml solution. Then, electrodes were held by a crocodile clip and placed into a glass beaker at the allocated position 3 cm below the water surface. The sensor probe was connected to the analogue frontend and measurements were taken. The frequency was swept from 20 Hz to 100 KHz and all data was stored to a PC via the RS232 link.

3.7 Results from resistors and capacitors networks

All the resistors and capacitors were measured independently by a digital multimeter in order to confirm the real value.

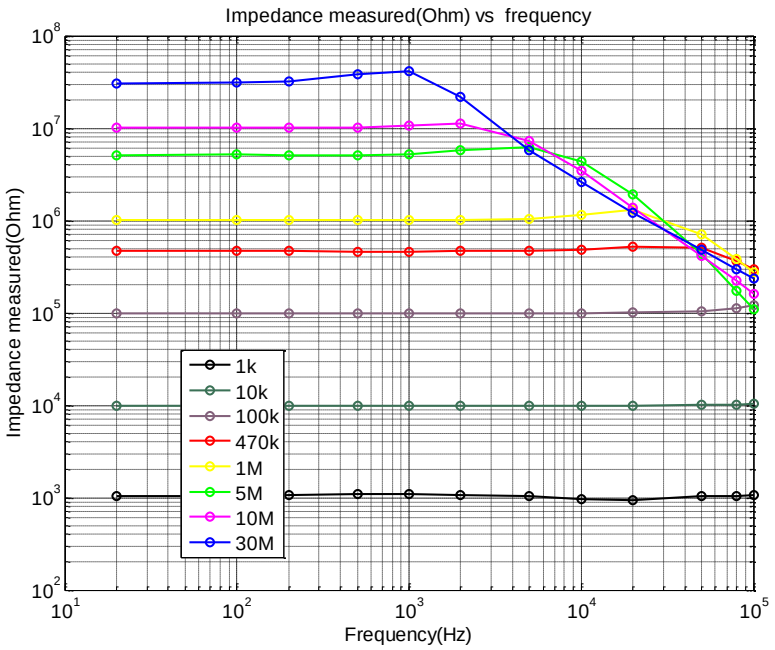


Figure 3.33: Calibration with resistors networks

As shown in Figure 3.33, the measurement system can measure the impedance up to 30 MΩ at 20 Hz and greater than 250 KΩ at 100 KHz. However, the errors increase as the load impedance is increased. The impedance measurement error is frequency dependent as stray capacitances reduce the performance of the high load measurement at high frequency. For the load of 100KΩ, the bandwidth was flat up to 100 KHz. The 3dB bandwidth of 1MΩ load impedance dropped down at 50 KHz. Similar to 1 MΩ load, the impedance load 10 MΩ reached -3dB at 5 kHz.

The correlation coefficient r is calculated by

$$r = \frac{\sum_{i=1}^{n}(x_i-\bar{x})(y_i-\bar{y})}{\sqrt{\sum_{i=1}^{n}(x_i-\bar{x})^2}\sqrt{\sum_{i=1}^{n}(y_i-\bar{y})^2}} \qquad (3.7.1)$$

where one data set [$x_{1...}x_n$] containing n value, another data set [$y_{1...}y_n$] containing n value, $\bar{x}$ is the mean of dataset x, and $\bar{x}$ is the mean of dataset y. -1 ≤ r ≤ 1, 1 represents strongly positively correlated, -1 represents strongly negatively correlated, 0 represents no correlation. For example: x is the set of measured data from multimeter and y is the set measured data from custom made device.

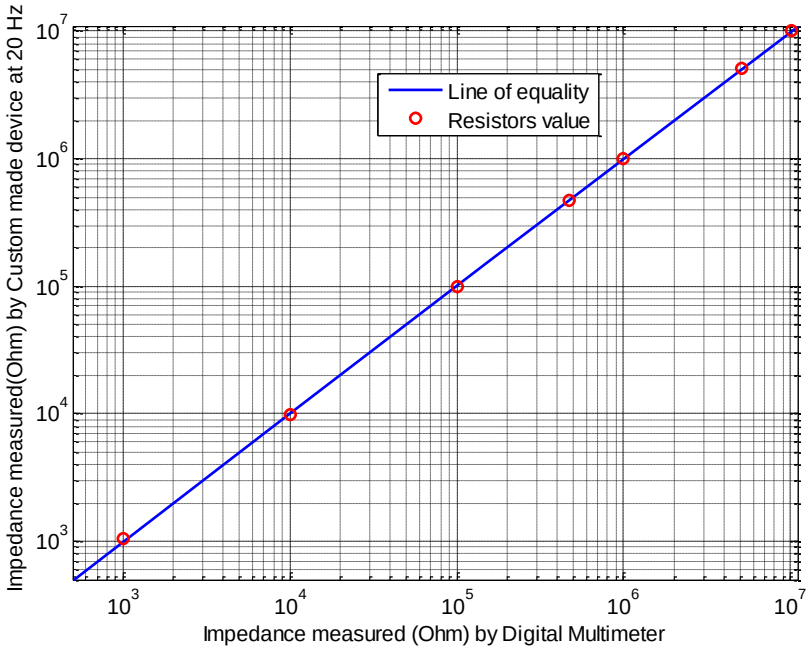


Figure 3.34: Digital meter measurement vs custom made device measurement (20 Hz). Correlation coefficient calculated is 0.999

The independent measurement results between digital multimeter and custom made device are plotted in Figure 3.34. As can be seen, the results of two devices are very well correlated over the resistor range from 1kΩ to 10MΩ as can be seen in correlation coeffient of 0.999.

Figure 3.35 shows the results from the measurement of the combination of resistor and capacitor networks.

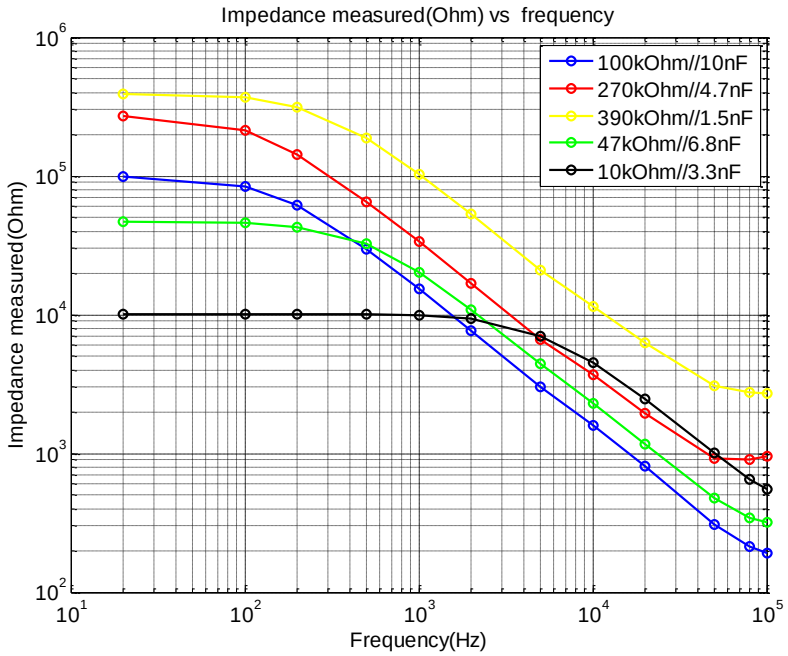


Figure 3.35: Characterisation with resistor and capacitor networks

The impedance network of 10 KΩ // 3.3 nF dropped down to -3dB at about 5 KHz. An impedance load of 47 KΩ // 6.8 nF reached -3dB at 500 Hz. The three impedance networks 100 KΩ//10 nF, 270 KΩ//4.7 nF and 390 KΩ//1.5 nF rolled off to -3dB at 150 Hz, 125 Hz and 270 Hz respectively.

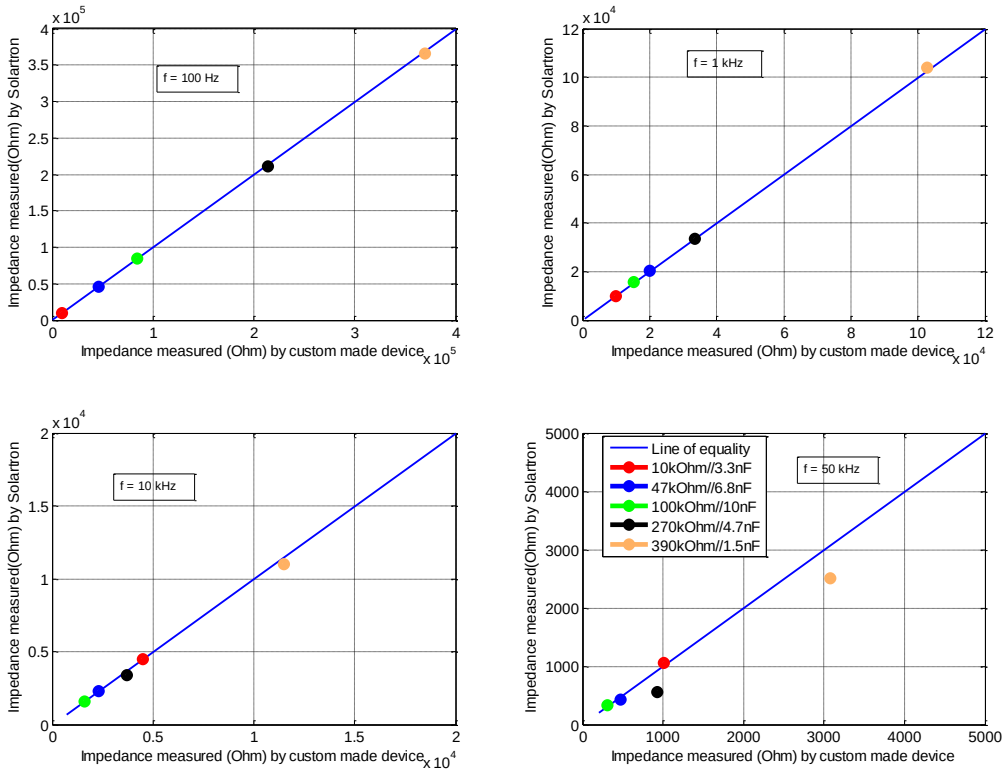


Figure 3.36: Impedance correlation between custom made device and Solartron in RC load measurements at frequency 100 Hz, 1kHz, 10kHz and 50 kHz. Correlation coefficient calculated at 100 Hz is 0.999, at 1kHz is 0.999, at 10 kHz is 0.999 and at 50 kHz is 0.985.

As shown in Figure 3.36, the correlation coefficient between Solartron and custom made device is quite high (>0.98). The correlation decreases when the frequency increases.

The cut-off frequencies from the capacitors and resistors networks are quite close (within 5% error) compared to a theoretical calculation of $f = \frac{1}{2\pi RC}$. Despite the existence of a small stray parasitic capacitance (about 5 pF) from the Printed Circuit Board, the capacitance from the impedance networks was dominant in the impedance measurement. For additional validation, the results from the custom made device were also compared with the Solartron "Impedance Analyzer 1260 + 1294"Solartron Analytical, Farnborough, UK .

3.8 Results in calibration solution

As described in the previous section, the calibration solutions were measured using a Conductivity Meter HI8733 (Hanna Instrument) with temperature compensation. Five values of solution were measured with this meter: de-ionized water (7 µS/cm), calibration solution (46 µS/cm), Hanna Instrument HI7033 calibration solution (92 µS/cm), tap water (580 µS/cm) and Hanna Instrument HI7031 calibration solution (1376 µS/cm). The calibration solutions were measured using the four point probe sensor connected to the custom made bio-impedance analyzer.

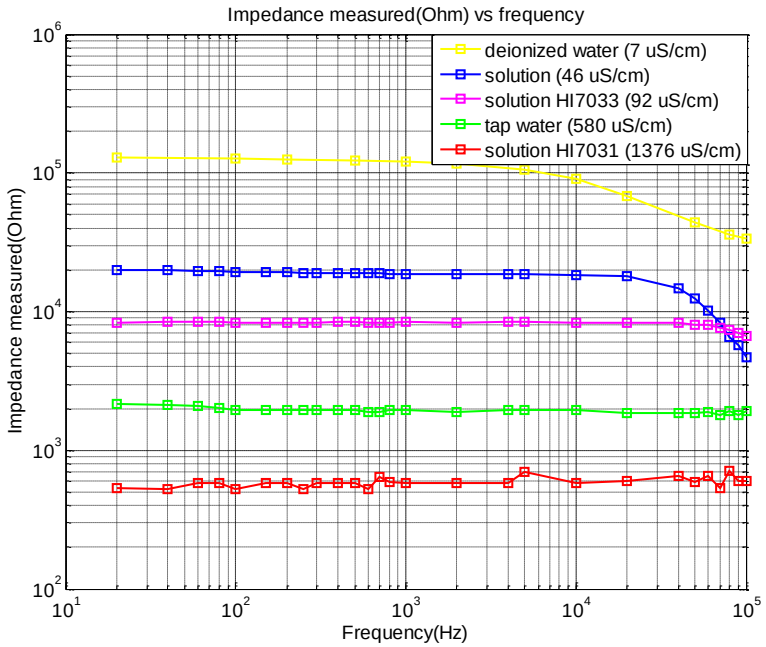


Figure 3.37 : Calibration with five different calibration solutions

As seen in Figure 3.37, the impedance from de-ionized water is about 135 KΩ, the impedance from solution at 46 µS/cm is about 20 KΩ. The value measured on this calibration solution indicated that the bulk uniform resistance of the liquid is about 20 KΩ. It also showed that at higher frequency the frequency response reduced the bandwidth due to the capacitive loading. In the calibration solution 92 µS/cm, the measured impedance was about 9 KΩ. The bulk resistance measured in tap water

580 µS/cm was about 2 KΩ. The bulk resistance measured in a calibration solution of 1376 µS/cm was about 600-700 Ω.

The resistivity value was obtained by inversing the conductivity value from the Hanna Instrument HI7031 1376 µS/cm, the resistivity is 726 Ω.cm. The results were encouraging because the ratios of the impedance values measured from calibration solutions nearly matched the measured conductivity values obtained using the conductivity meter (Table 3.1).

	De-ionized water	Solution 46 µS/cm	Solution HI7033	Tap water	Solution HI7031
Conductivity meter HI8733 measurement	7µS/cm (142857Ω.cm)	46µS/cm (21739Ω.cm)	92µS/cm (10869Ω.cm)	580µS/cm (1724Ω.cm)	1376 µS/cm (726 Ω.cm)
Custom made device measurement	135000 Ω	20000 Ω	9000 Ω	2000 Ω	600 Ω
Ratio (meter/device)	1.0582	1.08695	1.207	1.16	1.21

Table 3.1: Comparison of the conductivity measured between Conductivity meter and Custom made device (frequency 100 Hz).

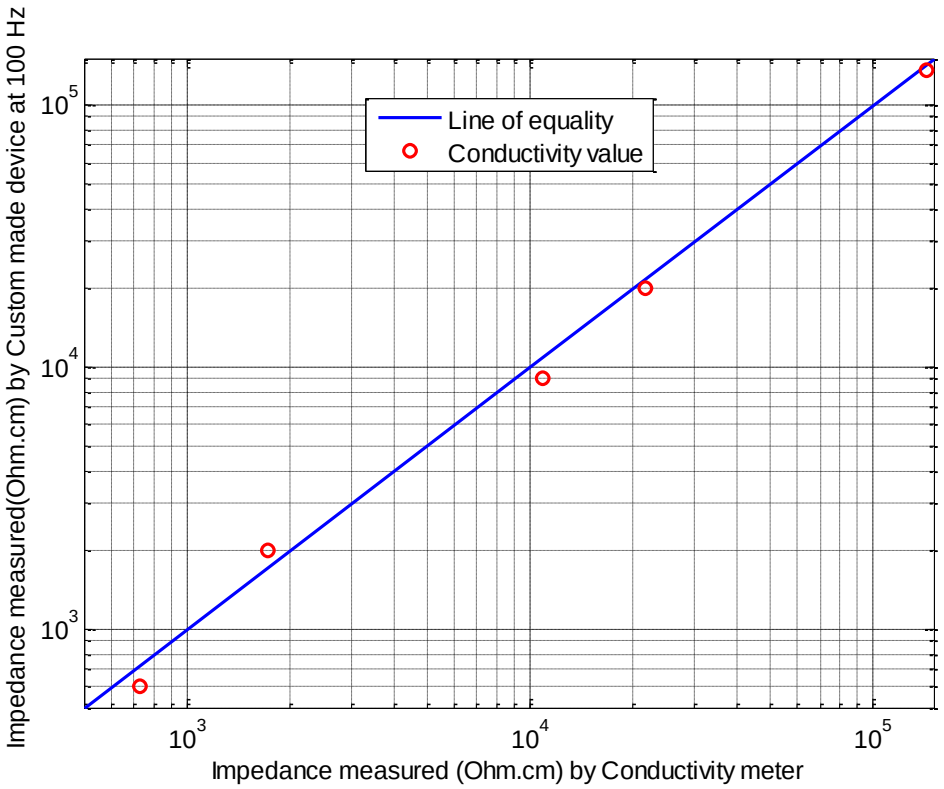


Figure 3.38: Conductivity meter measurement (Ω.cm) vs custom made device measurement (100 Hz). The correlation coefficient result is 0.999

In table 3.1, however, there are differences between measurement by Conductivity Meter and Four point Probe Sensor, for example, using the Conductivity Meter, there is a fixed volume tube outside the electrodes in order to measure the constant volume of liquid for every usage; in contrast, the bioimpedance analyzer used a four point probe with a larger measurement volume. The conductivity meter HI8733 (Hanna Instrument) has accuracy at 20˚C of ± 1% Full Scale excluding probe error. For example in full scale 0 to 1999 µS, if the conductivity measure at 1376 µS/cm, it means that the possible value is 1376 ± 19.99 µS. In Figure 3.38, the correlation coefficient result also shows that the custom made device and conductivity meter are well correlated.

3.9 Validation of data measurement using the Solartron impedance analyser

In order to validate the measured results, the Solartron Impedance Analyzer 1260 + Impedance Interface 1294 was compared with the custom made device. The Solartron system was capable of measuring an impedance load up to 1 GΩ. In addition, there are two configurations: 2-terminal measurement (two probes/ Kelvin probes) and 4-terminal measurement (four point probes). According to the Solartron manufacturer in Figure 3.39, four terminal measurement of the Solartron can be measured within 1% accuracy from 10 KΩ to 1 MΩ and within 10% accuracy from 1 MΩ to 10 MΩ. All of the tests were based on the biomedical terminal measurement only. The biomedical terminals on Solartron 1294A ensure the safety current afforded by Medical Standard EN60601, in which connections must be made only through this current limited terminal. The specifications of the Solartron 1260 + 1294 are given in Table 3.1.

Solartron 1260 impedance/gain phase specification		
Generator	**Voltage mode**	**Current mode**
AC amplitude	0 – 3 V rms	0-60 mA rms
Resolution	5mV	100 µA
DC bias range	±40.95V	±100mA
Max DC resolution	10 mV	200 µA
Output impedance	50Ω	>200kΩ at <1kHz
Frequency	10µHz to 32MHz, max resolution: 10µHz, error: ±100ppm, stability	
Sweep types	frequency (logarithm or linear), ac/dc voltage, ac/dc current	
Measures impedance	Able to achieve >100MΩ depends on 2-, 3- and 4-terminal measurement configurations	
Accuracy	0.1%, 0.1° accuracy	

Table 3.1: Specification of Solartron 1260 impedance gain/phase analyzer

The specification in Table 3.1 is a noise free analysis. Solartron 1260 uses Solartron Analytical's patented single-sine correlation technique, which inherently removes the

noise and harmonic distortion which they claim affects competitors' instruments (Solartron Analytical, Farnborough, UK).

Solartron 1294 impedance interface specification		
Generator	**Voltage mode**	**Current mode**
AC amplitude (normal)	0 – 7 V rms	0-30 mA rms
DC bias range (normal)	±10V	±45mA
Max AC + DC (normal)	±10V peak	±45mA peak
AC amplitude (IEC601)	0 – 7 V rms	10 mA rms
DC bias range (IEC601)	±10V	±10µA
Max AC + DC (IEC601)	±10V peak	±14mA peak
Measurement parameters	Impedance, real, imaginary, phase, tanθ, frequency, time, ac level, bias, complex plane.	
Measurement range **(using in conjunction with 1260)**	Sensitivity **1µV, 1pA**; impedance range from 0.01 to $> 10^9\Omega$; frequency up to 750 kHz.	
Output resistance	50Ω	

Table 3.2: Specification of Solartron 1294 impedance interface

For human biological measurement, the current limit is at ±10µA DC and up to 10 mA AC dependent on the applied frequency (Solartron Analytical, Farnborough, UK).

Figure 3.39 is useful as it is provided by the manufacturer and allows the operating range of the Solarton to be determined. The aim of the characterization carried out here was to conduct a series of experiments to allow us to plot a similar graph for the custom made device.

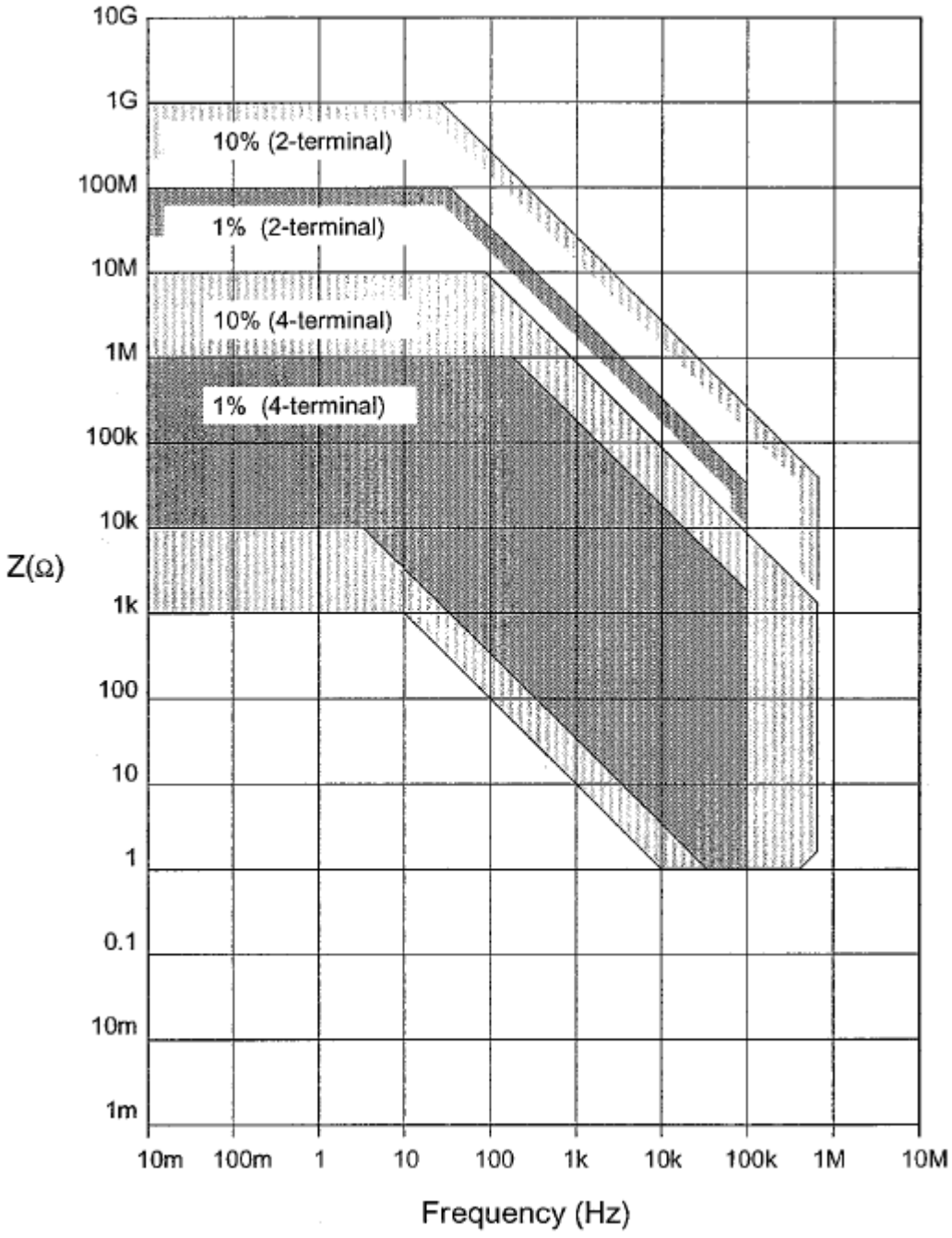


Figure 3.39: Typical accuracy of 2-terminal and 4-terminal biomedical (IEC601-1/ EN60601) impedance measurement, using 1 meter cables (Solartron Analytical, Farnborough, UK).

The measurement frequency of the Solartron can span from 10 mHz to 1 MHz. However, the frequency of the custom made device was from 20 Hz to 100 KHz, therefore the testing results on the Solartron were conducted from 10 Hz to 100 KHz in order to compare the two instruments.

Figure 3.40 shows the combination of Frequency Response Analyzer 1260 combined with Impedance Interface 1294. The previously described resistor networks, resistor-capacitor networks and calibration solutions were again investigated.



Figure 3.40: Solartron Impedance Analyzer 1260 (lower device) combined with Impedance Interface 1294 (upper device) for extended range of impedance measurement

3.9.1 Validation with resistors network

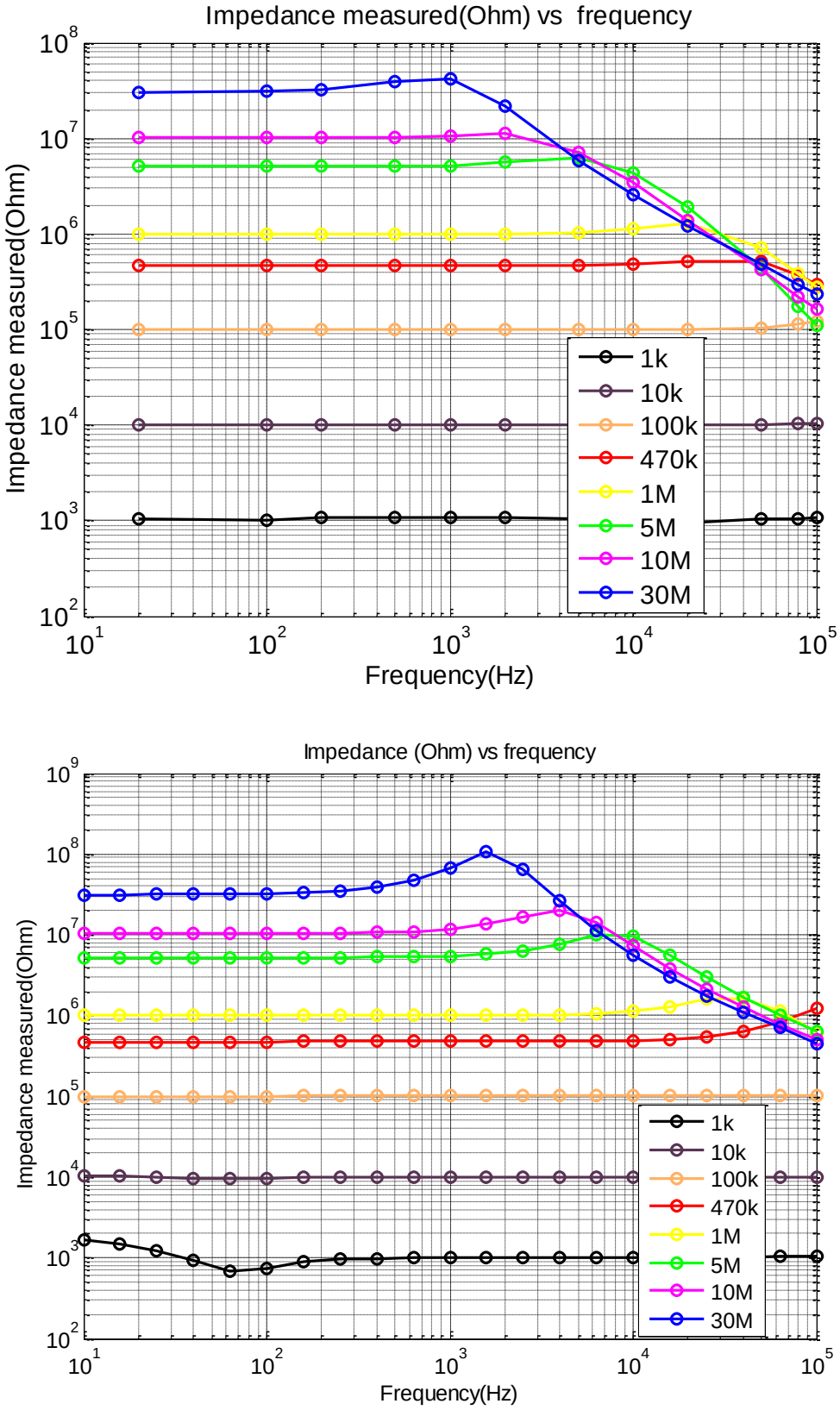


Figure 3.41: Comparison between Device (top) and Solartron (bottom) in impedance measurement of resistors network

Figure 3.41 shows comparison between the custom made device and the Solartron in impedance measurement. In general, in the low frequency range from 20Hz to 10 KHz, there is only a 5% difference in the impedance results between the custom made device and the Solartron. However, in the higher frequency range above 10 KHz, the impedance load from 1 MΩ, 5 MΩ, 10 MΩ and 30 MΩ dropped to about 400 KΩ at 100 KHz compared with a drop of about 250 KΩ at 100 KHz for the custom made device. As a result, it is assumed that the output impedance of the Solartron is about one and a half times that of the custom made device.

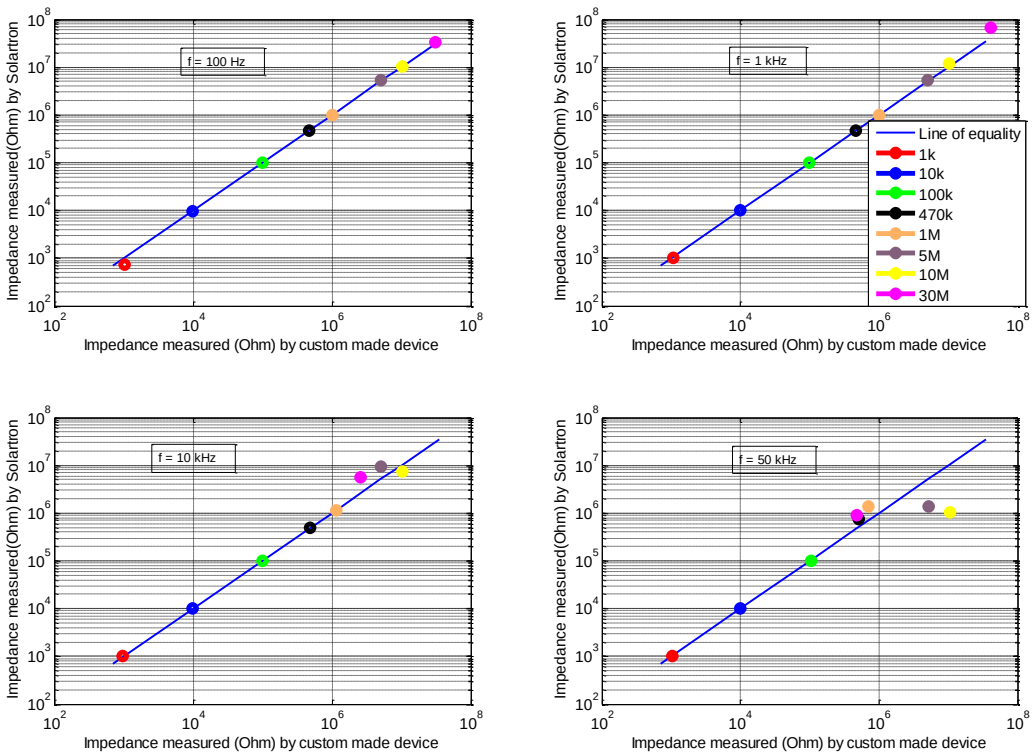
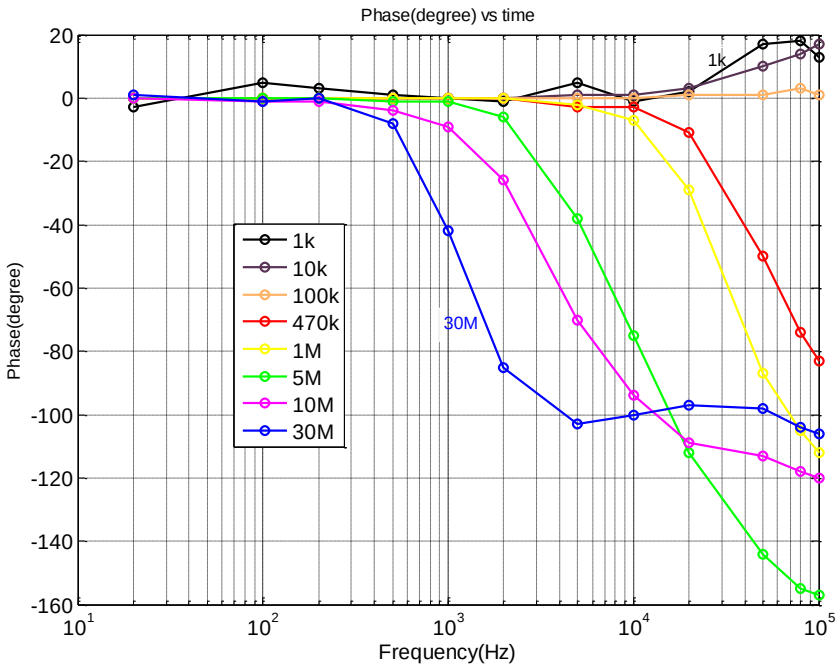


Figure 3. 42: Impedance correlation between custom made device and Solartron in resistor load measurements at frequency 100 Hz, 1kHz, 10 kHz and 50 kHz. Correlation coefficient calculated at 100 Hz is 0.999 at 1kHz is 0.996, at 10kHz is 0.992 and at 50 kHz is 0.917.

The output impedance is clearly frequency dependent due to the stray capacitances present in the circuit which reduces the performance of the high load measurement in the high frequency range. These results above show that both the Solartron and custom made device followed this trend.

In Figure 3.43, a comparison between the custom made device and the Solartron in phase measurement of the resistor networks is shown.



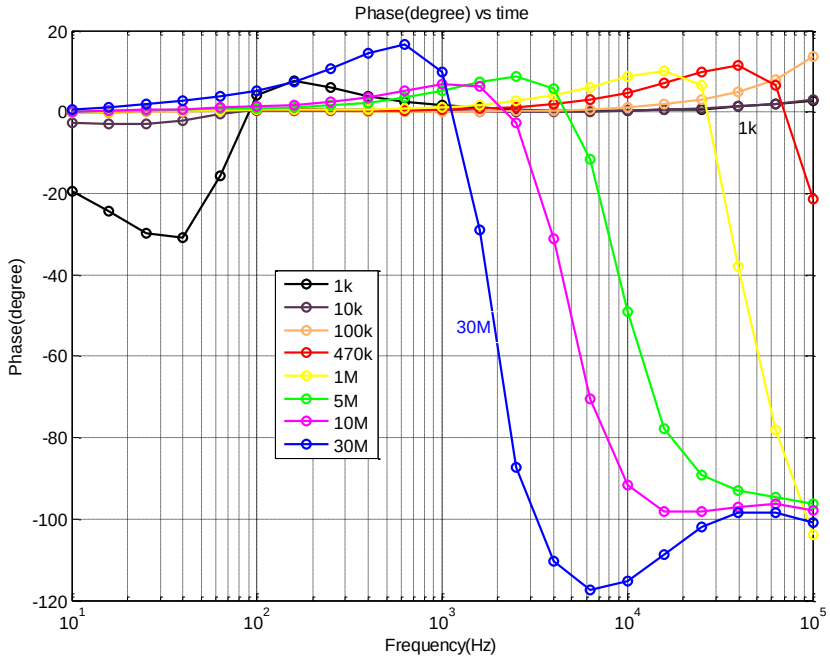


Figure 3.43: Comparison between Device (top) and Solartron (botom) in phase measurements of resistor networks

The results presented in Figure 3.43 show the phase comparison between the custom made device and the Solartron. In both devices, the phase measurements of most impedance loads always started about 0˚ at 20 Hz and fell to negative phase when the frequency was increased. This is because a small stray capacitance existed in the circuit and the DUT becomes gradually dominant as the frequency increased. The phase drop could be seen easily in high impedance loads (such as 1MΩ, 5MΩ, 10MΩ and 30MΩ), however the phase was flattened to about 0˚ in low impedance load (1kΩ, 10kΩ, 100kΩ).

In the frequency range from 20 Hz to 10 KHz, the phase measurements between the custom made device and the Solartron were quite well matched (less than 10 degrees difference) in the impedance range from 10kΩ to 10MΩ as the phase drops from 0 degrees to -100 degrees in both devices. However, there are quite high differences in the low and high impedance boundaries at 1kΩ and at 30MΩ. In fact, the Solartron

has output impedance higher than the custom made device. There are clear differences in the frequency range from 10 KHz to 100 KHz, except for the low impedance load (1kΩ, 10kΩ, 100kΩ) in which the phases were flattened. The high impedance load in the custom made device fell down to -120˚ degree and even as low as -140˚ degree compared with the Solartron's phases, which were maintained at -100˚.

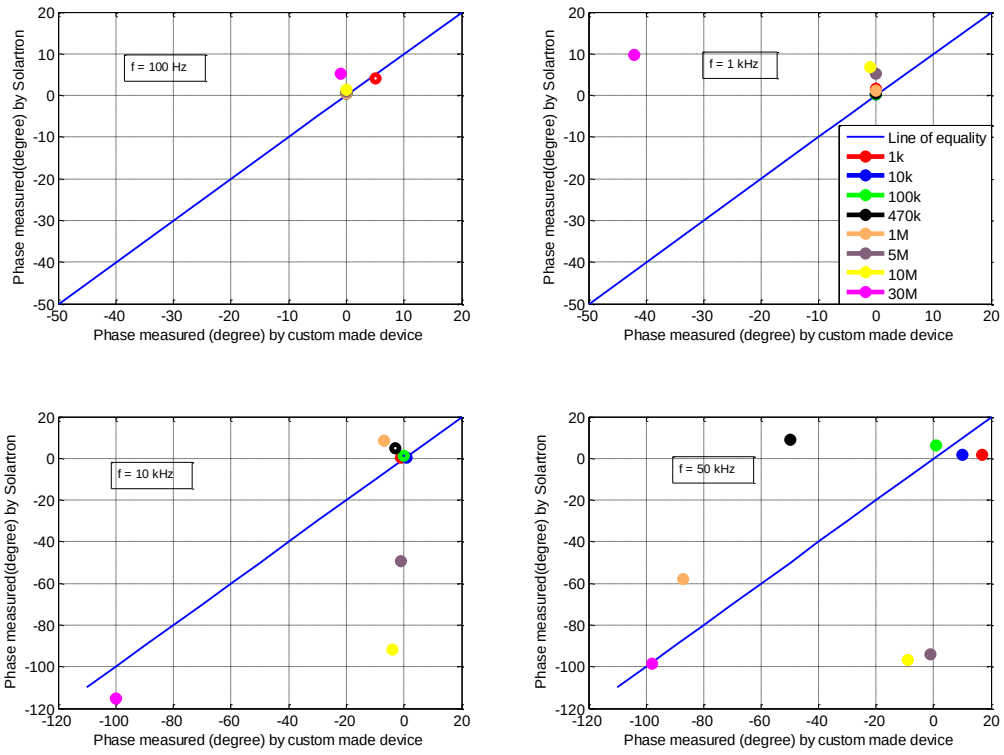
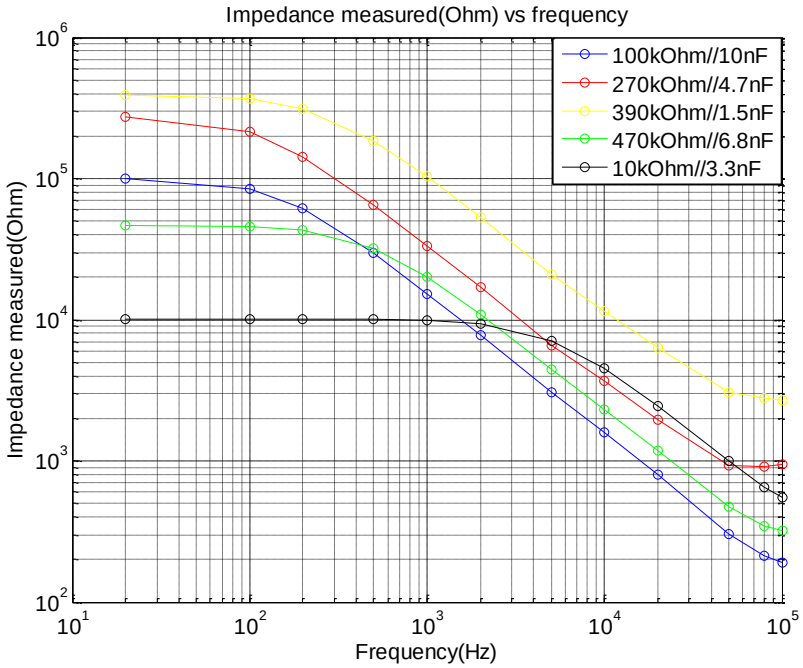


Figure 3.44**:** Phase correlation between custom made device and Solartron in resistor load measurements at frequency 100 Hz, 1kHz, 10kHz and 50 kHz. Correlation coefficient calculated is 0.945 at 100Hz, -0.830 at 1kHz, 0.690 at 10kHz, and 0.753 at 50 kHz

In section 3.9.2, a comparison between the Solartron and custom made device is shown in the impedance and phase measurement of resistor and capacitor networks.

3.9.2 Validation with resistor and capacitor network

After the validation of the resistor networks, RC networks were also used to validate the performance of the custom made device. The purpose of using networks of capacitors combined with resistors was to evaluate how well the system would perform with capacitance in the impedance networks, but also to assess whether the phase measurements were valid.



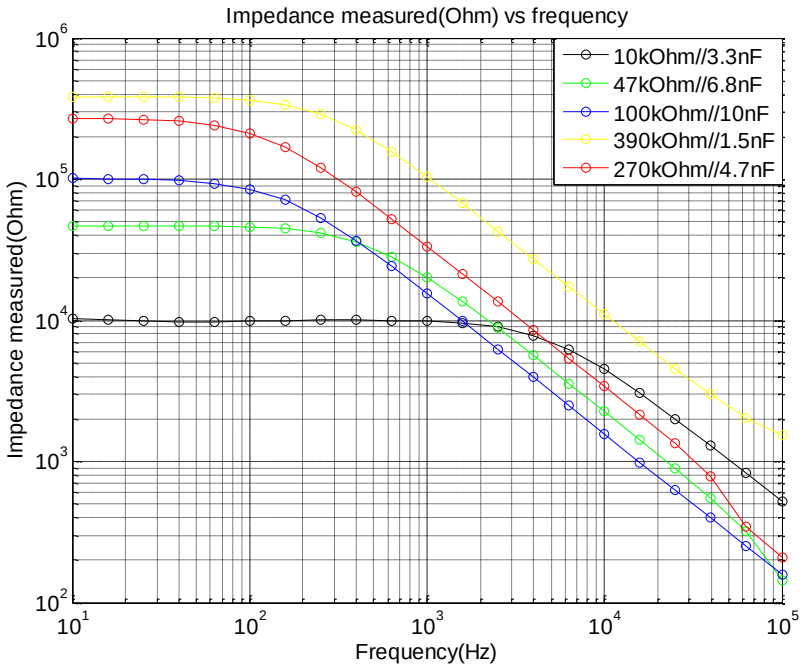


Figure 3.45: Comparison between custom made device (top) and Solartron (bottom) in impedance measurement of RC networks

In Figure 3.45, there were five different capacitive loads used in the impedance measurement. The results showed that the impedance measurement in both devices were similar within 5%. The differences between two device are small (less than or equal 5% difference) in the frequency range 20 Hz to 50 KHz. The impedance load value dropped to -3dB at 5 kHz (10kΩ//3.3nF), 500 Hz (47kΩ//6.8nF), 270 Hz (390kΩ//1.5nF), 150 Hz (100kΩ//10nF) and 125 Hz (270kΩ//4.7nF). There were larger differences (higher than 5%) in the impedance load measurement in the high frequency range above 50 kHz because of the parasitic capacitance at high frequency.

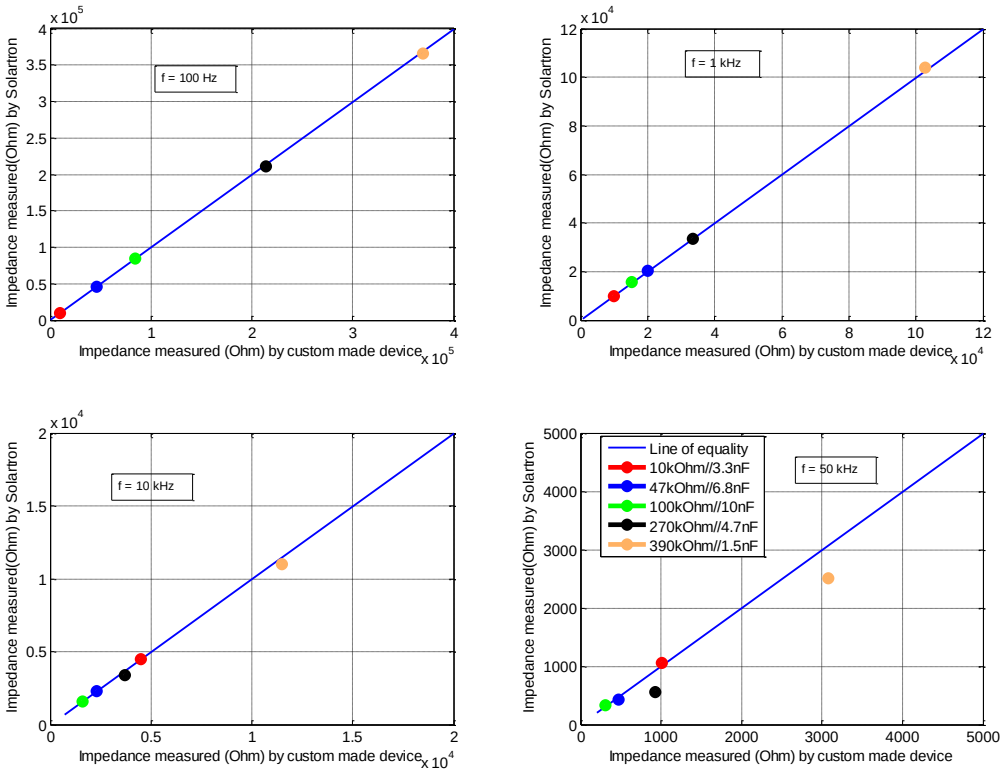


Figure 3.46: Impedance correlation between custom made device and Solartron in RC load measurements at frequency 100 Hz, 1kHz and 10kHz and 50kHz. Correlation coefficient calculated at 100 Hz is 0.999, at 1kHz is 0.999, at 10 kHz is 0.999 and at 50 kHz is 0.985.

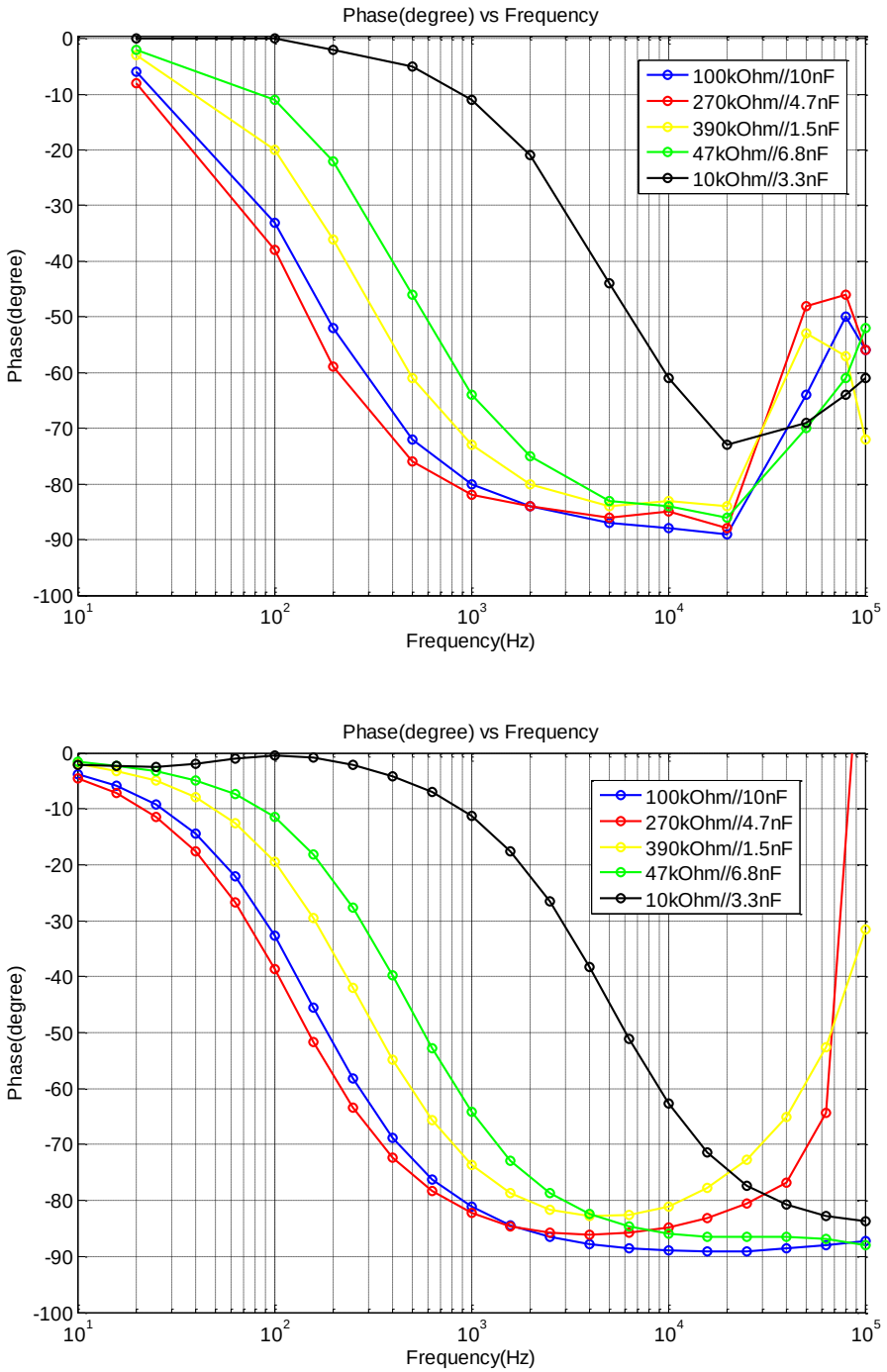


Figure 3.47: Comparison between Device (top) and Solartron (bottom) in phase measurement of RC networks

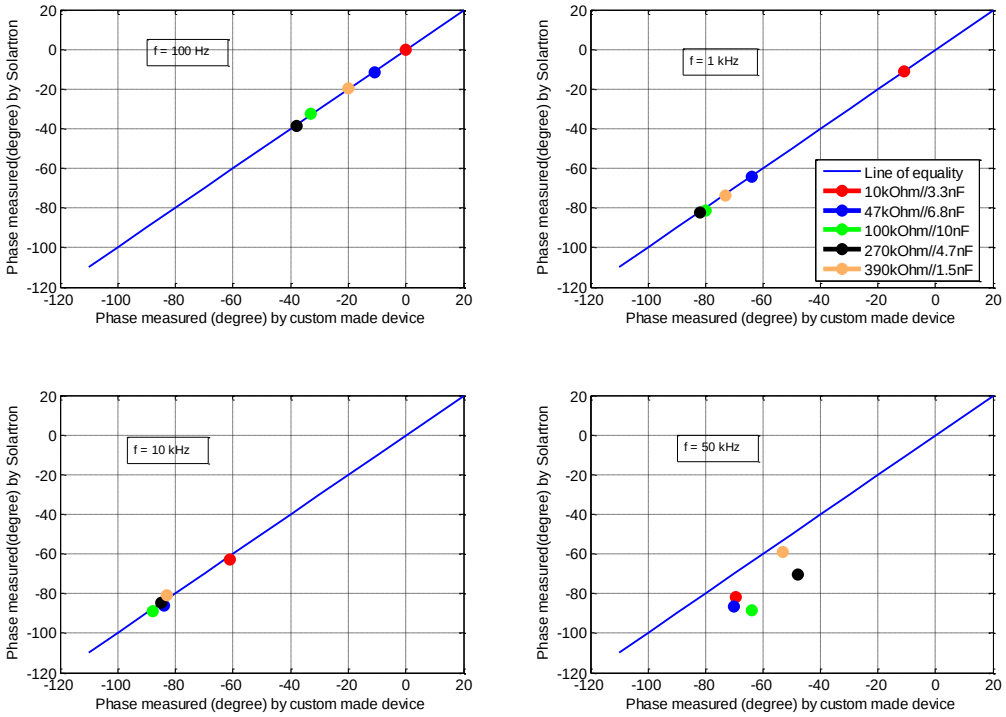


Figure 3.48: Phase correlation between custom made device and Solartron in RC load measurements at frequency 100Hz, 1kHz, 10kHz and 50kHz. Correlation coefficient calculated is 0.999 at 100 Hz, 0.999 at 1 kHz, 0.989 at 10kHz and 0.793 at 50 kHz. It is less fit with the frequency increases.

Figure 3.47 presents the phase results in RC circuits for the custom made device and the Solartron. In the frequency range from 20Hz to 10 kHz, the phase results measured by the custom made device are nearly identical (less than 5% difference) to those measured by the Solartron. The phase trends of these RC circuits quickly fell down to negative phase as the additional capacitance was combined with the resistor in the impedance networks.

In contrast to the similarity from 20Hz to 10 kHz, the phase trends of the RC circuits were different in the frequency range above 20 kHz compared between the custom made device and the Solartron. The phase measurements of the RC circuits in the

custom made device went up to -60˚ degree at 100 KHz. However, the phases of 100kΩ//10nF, 47kΩ//6.8nF and 100kΩ//10nF maintained at -90˚ degree, the phases of 270kΩ//4.7nF and 390kΩ//1.5nF went up to 0˚ degree at 100 kHz with the Solartron.

Through the impedance and phase results in RC circuit measurement, it is illustrated that the output impedance and impedance range of the Solartron was higher than the custom made device. The operational characteristics regions (impedance and phase) of the custom made device are defined in the later section.

3.9.3 Validation with calibration solution

For this study, calibration solutions were used to explore the ionic conduction measurement of both of the systems. In contrast to the measurement in resistor and capacitor networks, the measurement on calibration solution focusses on the ability to measure impedance in a volume (bulk resistance) instead of the solid and fixed resistors. Figure 3.49 shows the comparison between the Device and the Solartron in a calibration solution impedance measurement.

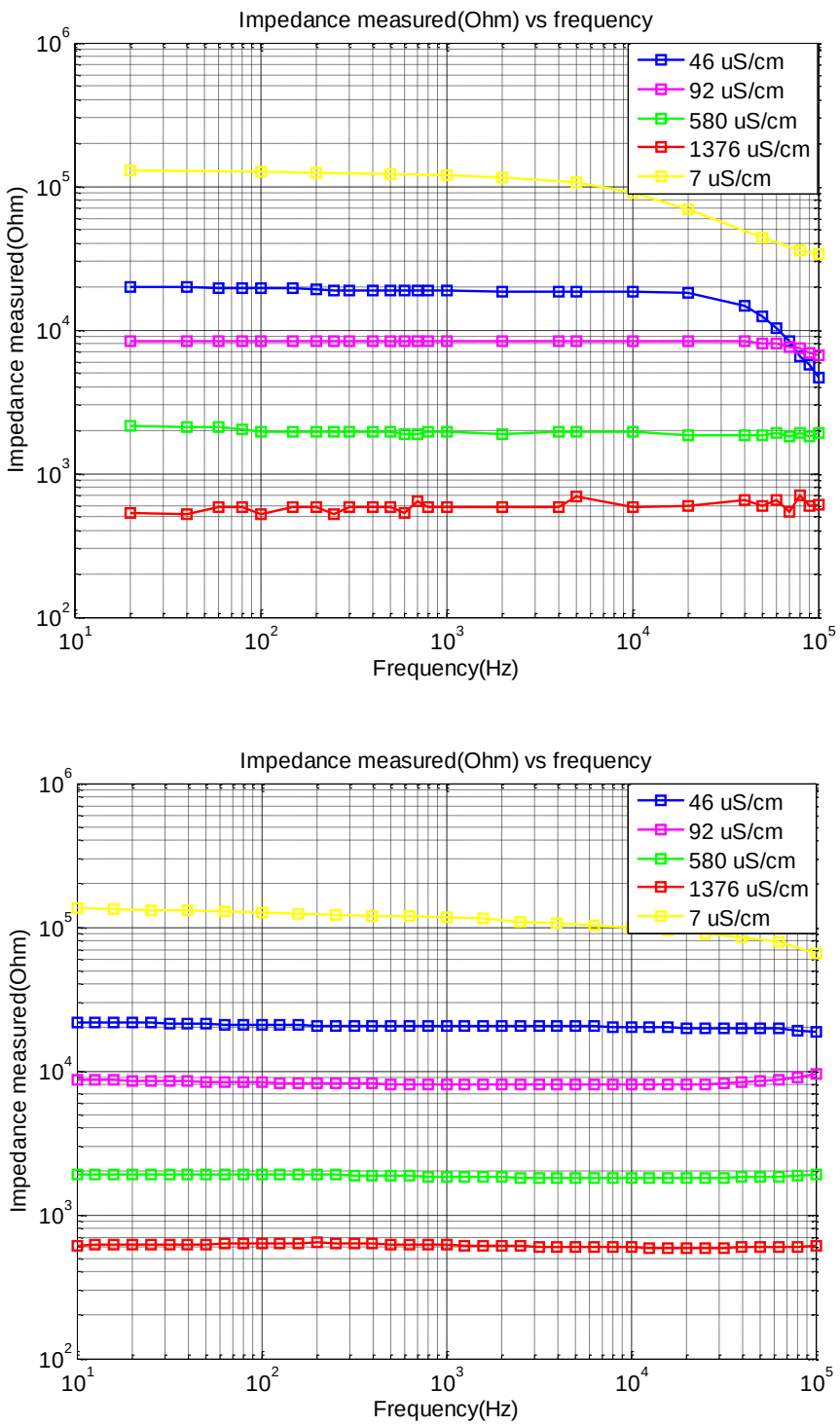


Figure 3.49: Comparison between Device (top) and Solartron (bottom) in an impedance measurement of the calibration solutions

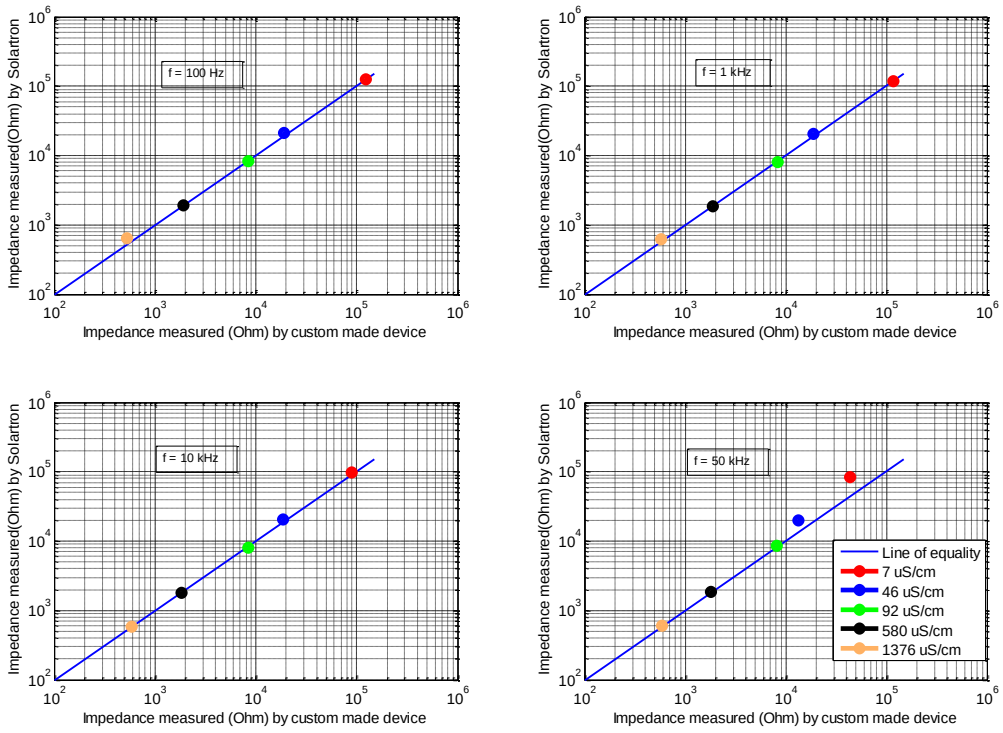


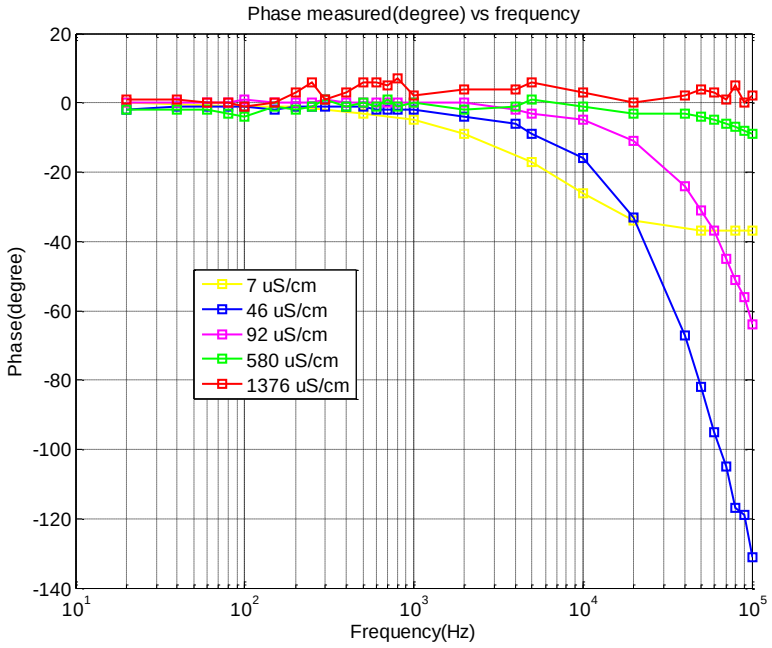
Figure 3.50: Impedance correlation between custom made device and Solartron in calibration solution measurements at frequency 100Hz, 1kHz, 10kHz and 50kHz. Correlation coefficient calculated is 0.999at 100 Hz, 0.999 at 1kHz, 0.999 at 10 kHz, and 0.996 at 50kHz.

In Figure 3.49, three calibration solutions 92 µS/cm, 580 µS/cm and 1376 µS/cm, have impedance results which tend to flatten (up to 100 kHz) and are similar in both of the systems. These three impedance results of the Device are comparable to those of the Solartron as the ratio 600Ω : 2000Ω : 9000Ω is comparable. However, for the de-ionized water 7 µS/cm and calibration 46µS/cm, the impedance values are different between the two devices at high frequency i.e. above 10 KHz.

In contrast to the similarity of the first three calibration solutions, the de-ionized water impedance dropped from 135kΩ to 35kΩ and the calibration 46 uS/cm dropped from 20kΩ to 5kΩ at 100 kHz in the custom made device. The impedance

from calibration 46 uS/cm is flattened and the de-ionized water impedance is slightly dropped in the results from Solartron. Once again, it is illustrated that the output impedance of the Device is lower than the Solartron because the high impedance solution had been used.

Figure 3.51 presents the phase measurement comparison between the two devices.



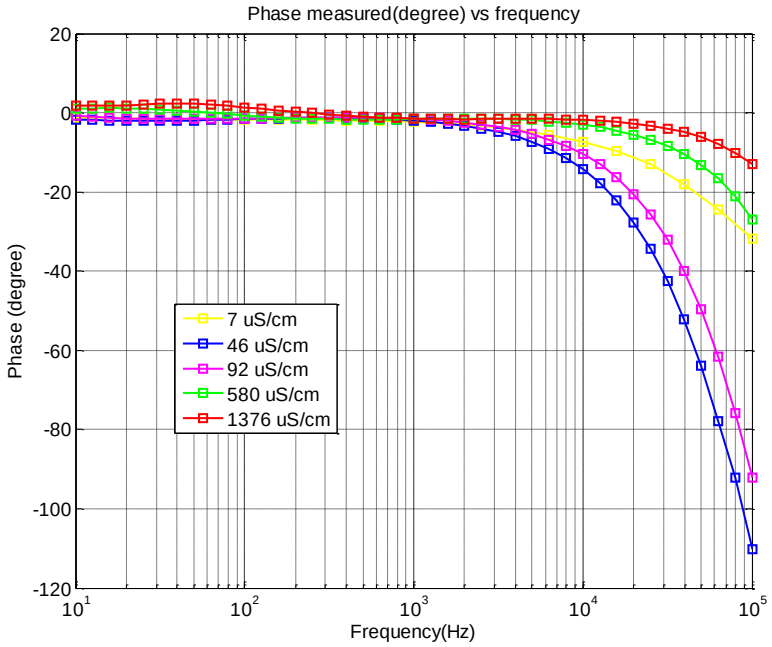


Figure 3.51: Comparison between Device (top) and Solartron (bottom) in phase measurement of a calibration solution

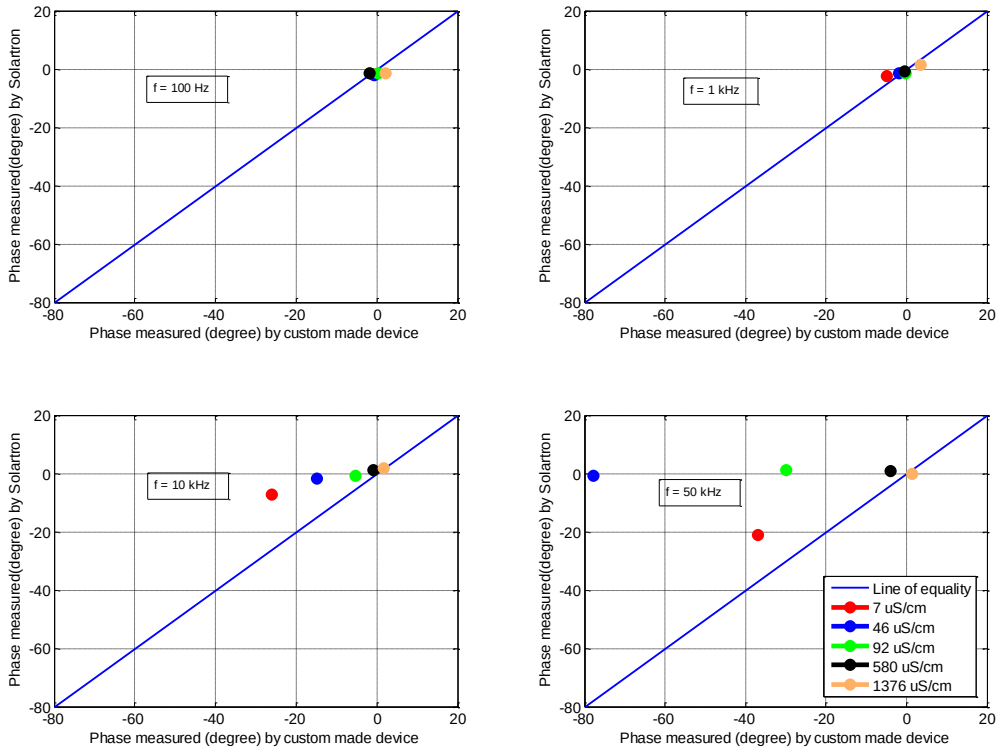


Figure 3.52: Phase correlation between custom made device and Solartron in calibration solution measurements at frequency 100Hz, 1kHz, 10kHz and 50kHz. Correlation coefficient calculated is 0.996 at 100 Hz, 0.936 at 1kHz, 0.972 at 10kHz, and 0.176 at 50 kHz

Figure 3.51 compares the phase measurement between the new Device and the Solartron. In the two graphs, the phases tend to be maintained at 0˚ at low frequencies (20Hz to 1 kHz) and move down to negative phases at higher frequencies (above 10 kHz). The phase of the custom made device dropped to -140˚ degree compared with -120˚ degree for the Solartron at 100 kHz.

The impedance and phase measurement reflected the lower output impedance of the custom made device compared with the Solartron. It is necessary to define the valid

impedance and phase range of the custom made device. In the next section 3.8.4, the comparison between the Solartron and the custom made device is shown in the impedance and phase measurement of human bare skin.

3.9.4 Validation with human skin impedance

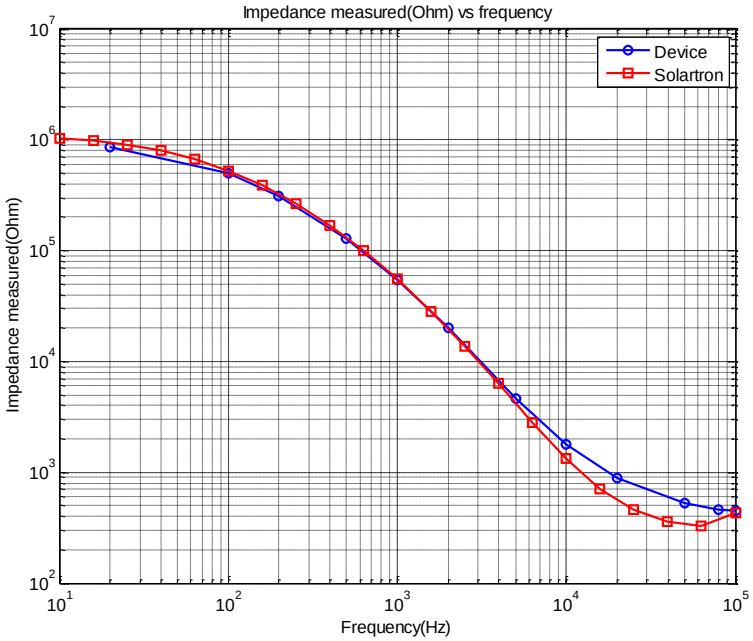


Figure 3.53: Bare skin impedance measurement comparison between Solartron and Custom made device

Figure 3.53 shows comparisons between the custom made device and the Solartron in bare skin impedance measurement. In the frequency range from 20 Hz to 10 KHz, the difference is less than 5% in the impedance results between the two devices. The results from the custom made device followed closely the results of the Solartron. However, in the frequency range higher than 10 KHz, there is a difference of greater than 5% between the custom made device and the Solartron. This is reasonable as this difference has been observed when comparing capacitor and resistor networks with the Solartron system.

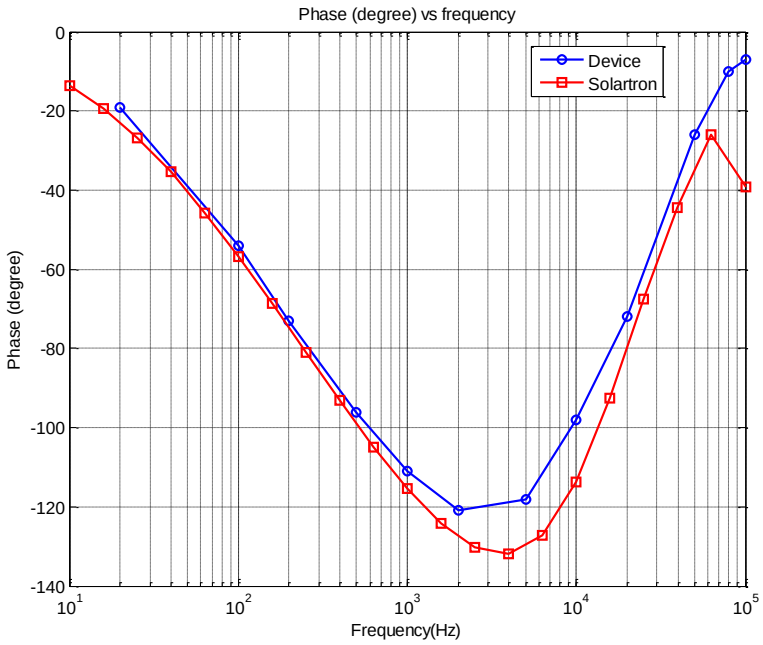


Figure 3.54: Bare skin phase measurement. Comparison between Solartron and Custom made device

In Figure 3.54, the phase different is less than 5% in the frequency range 20 Hz to 1 KHz. In the frequency range higher than 1 KHz, the difference between two devices is greater than 5%, however the trend of the custom made device followed that of the Solartron phase results. In the next section 3.8.5, the operational characteristics of the custom made device are given for the impedance and phase range.

3.9.5 Valid Impedance and Phase Range Measurement

The validation process with impedance networks and calibration solution attempt to determine the valid impedance and phase range of the custom made device, to ensure that the skin measurement results are coherent and reliable.

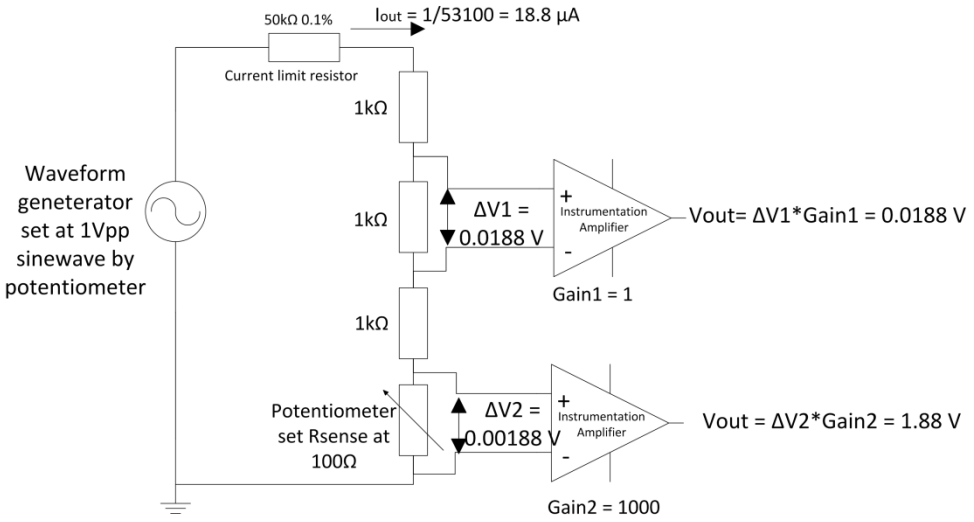


Figure 3.55: Bio-impedance analyser with 3kΩ load measurement

In the In-amp analysis above with gain G = 1000 and bandwidth set at 1 kHz, the total input noise is equal to 11 µV rms (in section 2.5.1) and this is also the minimum detectable signal. For example, in the case of measuring 3 kΩ load (3 x 1kΩ) in Figure 3.55, the voltage measured from INA1 and INA2 are 18 mV and 1.8mV. These values are considerably higher than the minimum detectable signal, therefore the voltage output from the Instrumentation amplifiers are expected to be relatively immune to noise when it reaches the ADC.

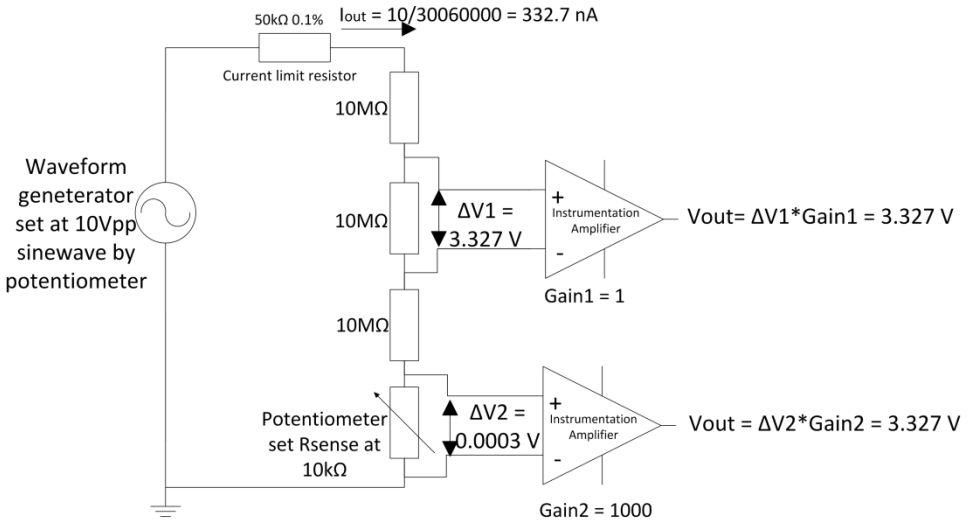


Figure 3.56: Bio-impedance analyser with 30MΩ load measurement

In the case of measuring a 30 MΩ load (3 x 10MΩ) with a gain G = 1000 and bandwidth set at 1 kHz in Figure 3.56, the voltages measured from INA1 and INA2 are 3.327V and 0.3 mV. The ratio between the voltage measured from INA2 and the minimum detectable signal is approximately a factor of 27 (0.3mV/ 11 µV). The voltage measured from INA2 is considerably higher than the minimum detectable signal and hence it is possible to measure a 30 MΩ load. Reducing the bandwidth of lock-in measurement to say 20Hz will improve SNR further. The measurement system can measure the impedance up to 30 MΩ at 20 Hz and ~250 KΩ at 100 KHz. The results were accurate within 3% compared to the actual value of the resistors measured by the Solartron. The percentage error was obtained by

$$\text{Error in (\%)} = \left| \frac{Z \text{ value measured by custom made device} - Z \text{ value measured by Solartron}}{Z \text{ value measured by Solartron}} \right| \times 100\%.$$

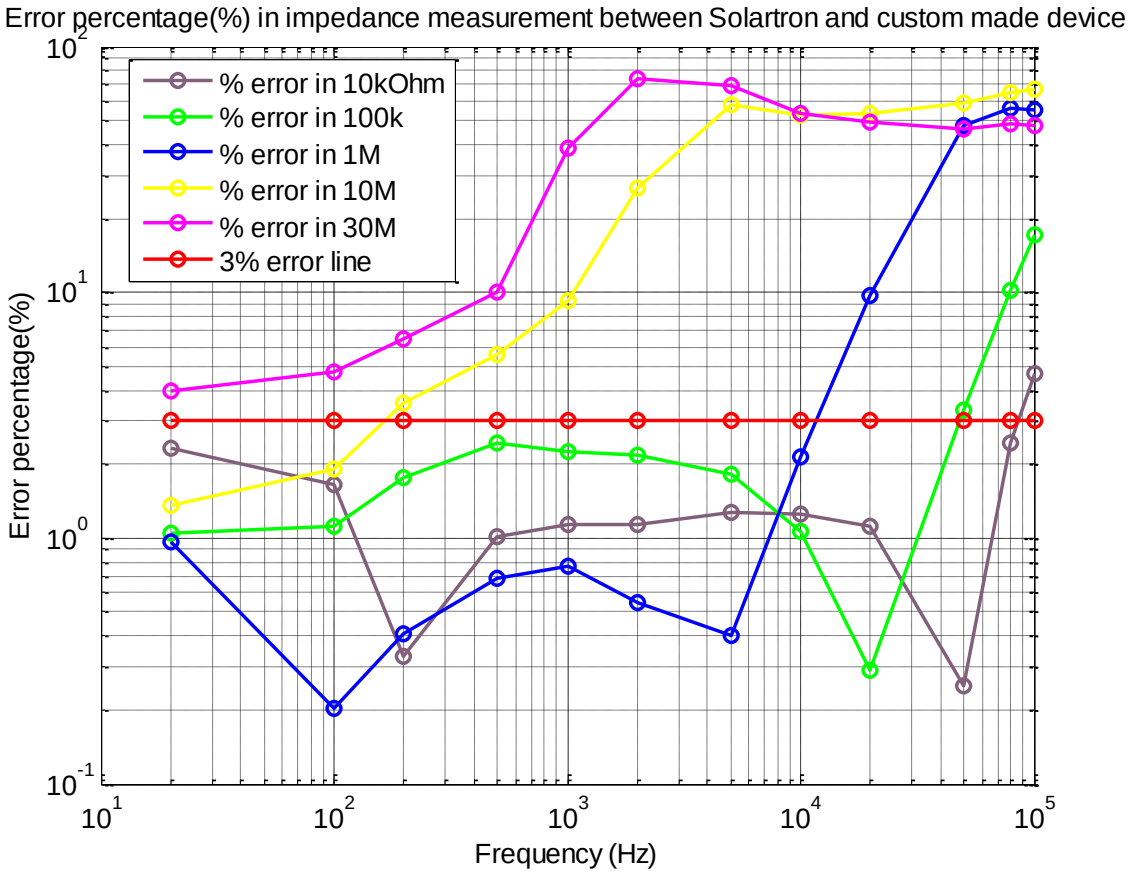


Figure 3.57: Percentage error calculation in impedance measurement between Solartron and custom made device with 3% error line.

In Figure 3.57, less than 3% error (area under the red line) can be achieved in measurement of impedance loads of 10kΩ, 100kΩ, 1MΩ and 10 MΩ but it is highly dependent on frequency. The error percentage increases as the load impedance and the frequency of measurement increases. This is because the output impedance is frequency dependent as stray capacitances reduce the performance of the high load measurement at high frequency. Table 3.3 gives the specification for custom made device.

Custom made device specification	
Generator	**Voltage mode**
AC amplitude	0 – 10 V rms
Resolution	40mV
Current range	200 nA (minimum) – 200 µA max (*)
Current limit 60601	Up to 100 µA AC current at frequency 20Hz – 1kHz & up to 1mA AC at frequency > 1kHz
Output impedance	~10Ω
Frequency	20Hz to 100kHz
Sweep types	frequency (logarithm or linear), ac voltage, ac current
Measures impedance	Able to achieve from 1kΩ to 10MΩ on 4-terminal measurement configurations
Accuracy	3-5% depends on load impedance and frequency (**)

Table 3.3: Specification for custom made analyzer device

(*) Current can sense down to 200 nA in the case of very high impedance load such as 10MΩ, and up to 200 µA in the case of low impedance load (1kΩ).

(**) The accuracy achievement highly depends on load impedance and frequency. i.e. high load such as 10MΩ achieves 3% error at frequency up to 100Hz, but a 100kΩ load achieves a 3% error at a frequency up to 50kHz.

The output impedance is maintained at 10 Ohm (given in datasheet of OPA657) in order to measure the range impedance from 1kOhm to 10 MOhm within 1% error.

For example, when measuring 10kOhm, the error is lower than 1%. The frequency of interest is from 20Hz to 100 kHz, which is the reasonable range to reach to epidermis layers and within the measurable signal range of the system.

Figure 3.58 shows the accuracy divided into three regions based on the impedance network comparison: the first region is within 5% error, the second region is 5-10% error and the third region is above 10% error. It can be seen that for within 5% accuracy, the system can operate from above 1 kΩ up to 1 MΩ (in the frequency from 20 Hz to 10 KHz) to 100 kΩ (at 100 KHz).

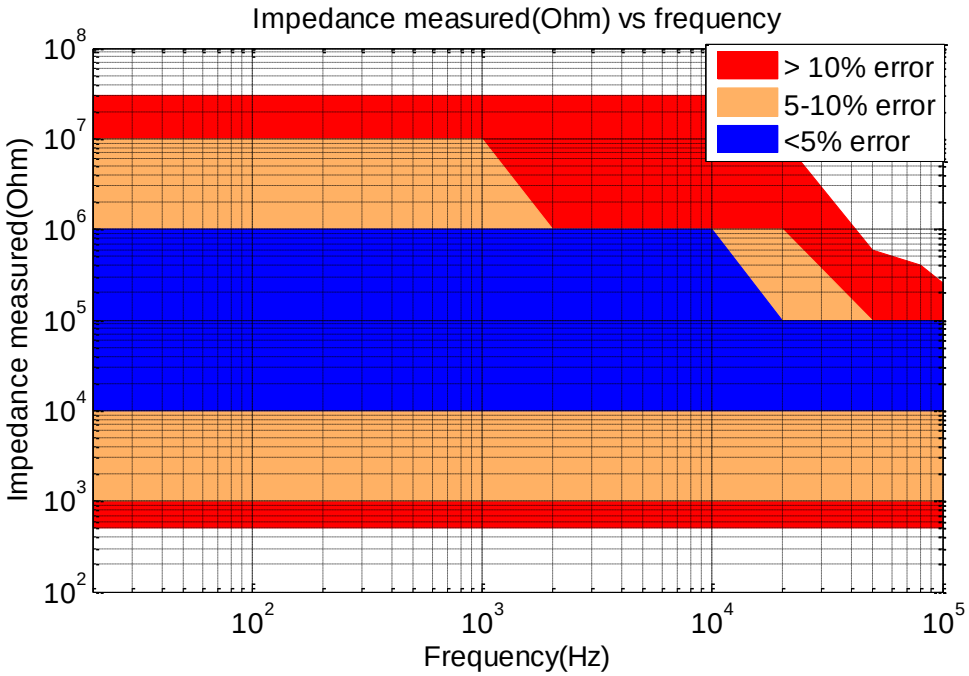


Figure 3.58 : The operational impedance range of the custom made system

In the impedance load region above 1MΩ to 10MΩ and below 1kΩ, the device can measure within 5-10% accuracy. The critical region with greater than 10% accuracy is the impedance load above 10MΩ and below 500Ω. In addition, the operational phase range of the system needs to be evaluated and is shown in Figure 3.59. The

phase range is similar to the impedance range as it is divided into three regions: above 10% accuracy, 5-10% accuracy and within 5% accuracy.

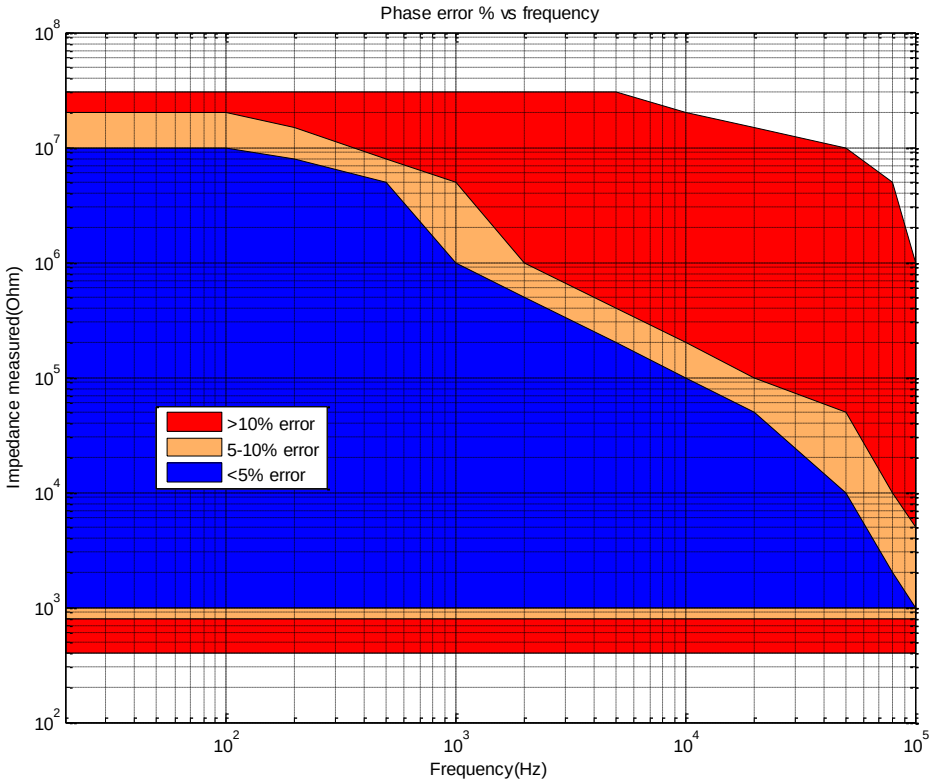


Figure 3.59: The operational phase range of the custom made system

As shown in Figure 3.59, the <5% accuracy is covered from 1kΩ (frequency up to 100 kHz) to 10MΩ (frequency up to100Hz). The regions below 1kΩ and above 10MΩ fell into 5-10% accuracy and above 10% accuracy. Again, the critical region above 10% accuracy is the impedance load above 10MΩ and below 500Ω.

3.10 Conclusion

In this chapter, a custom-made bioimpedance analyzer has been demonstrated. It contains a DSP board combined with designed analogue frontend connected to a four point probe sensor. In order to increase the accuracy of the results, a digital filter, a

lock-in amplifier and FFT are programmed and embedded into the DSP. Moreover, the system is implemented to sweep from 20 Hz to 100 KHz. The application interface is also programmed in Matlab to provide real-time results on a PC.

Test results of resistor and capacitor networks have been illustrated, from the resistor networks only to resistor combined with capacitor networks (within 5% accuracy). Test results in calibration solution are comparable to the Solartron (less than 5% difference) and correspond to the ratio of the calibration solution. There are differences in the measurement of resistors and capacitor networks compared with the calibration solution. However, the impedance and phase results shown are promising and an operating range has been obtained from 20 Hz to 100 KHz. This will help to determine the reliability of the results when measurements are taken on human skin.

In addition, the system can be battery-powered, thereby allowing the users more flexibility and portability without the need of a bulky system like the Solartron. It is possible to take this system away from the lab and make measurements over 24 hours in an ambulatory setting offering the possibility of long term monitoring at home.

The custom made system currently contains some limitations in bandwidth and accuracy. The bandwidth of the system is reduced when making the measurements of very high impedances (such as 3x10 MΩ) but it showed adequate performance (within 10% error in the accuracy regions) for high impedances (up to 3x10MΩ).

Chapter 4 Skin Measurements

4.1 Introduction

This chapter discusses the experimental results obtained by the 4 point probe EIS measurements on subjects using various skin creams. The primary objective of this study is to determine whether EIS can be used to assess the effects of moisturizer on skin. Sections 4.2 provides the introduction to skin impedance measurement and materials, methods and set up protocols for instantaneous, short term and long term measurement. Sections 4.3-4.6 give the details about the measurement results for instantaneous, short term (up to 2 hours) and long term measurement (>5 hours). Sections 4.6 and 4.7 provide discussion and conclusions of the experimental results.

4.2 Methodology

The common parts and differences of the methodology for the 3 experiments: instantaneous measurement, short term measurement and long term measurement are described in this section.

4.2.1 Materials

Four different commercial skin creams are used: Bio-oil (for ageing skin & dehydrated skin), Nivea Express Hydration (for normal & dry skin), Palmer's Cocoa Butter with SPF (Sun Protection Factor) 15 (UVA & UVB Protection) and Palmer Olive Butter (Anti-Aging Peptide Complex).

For a brief introduction, these skin creams contains different chemical constituents (see details in Appendix G). For example, Nivea is a water based moisturizer containing a high concentration of water combined with Glycerin and other constituents. Cocoa Butter and Olive Butter from Palmer's are cream based moisturizers containing Glycerin and other constituents such as Olive oil or Cocoa oil. Bio-oil is an oil based moisturizer that contains high concentrations of oil such as

flower oil, leaf oil and seed oil. Figure 4.1 shows four different kinds of moisturizers used in the experiments.



Figure 4.1: Four kinds of moisturizers were used in the experiments.

4.2.2 Experiment Protocol

The design protocol for skin impedance measurement with and without (control) moisturizers was taken on allocated positions on the arm. Depending on the experiments, there are three measurements: instantaneous measurement, short-term measurement (up to 2 hour) and long term measurement (5 hours). The groups of volunteers (together with Case Report Form information) in different experiments are given in Appendix H.

Volunteers arrive and the experimental protocol was explained to them (using Participant Information Sheet in Appendix C). Temperature in the room was kept constant at 20˚ C (using air conditioning) and 15 minutes was allowed for acclimatizing. Once the protocol is explained, the volunteers sign a consent form

shown in Appendix D. Depending on the experiment to be carried out, different sites of the arm are marked as shown in Figure 4.2b (different colors for illustrative purposes only). The marked areas are red for Bio-oil, blue for Nivea, green for Olive, orange for Cocoa and black for bare skin. Next, the skin creams were applied on 4 points as shown in Figure 4.2b. 0.1 ml of skin cream is applied using a syringe and is rubbed in gently until it is not visible. A paper tissue is used to remove any excess skin cream deposited on the 4 point probe and to clean the probe before taking each measurement. Figure 4.2 shows the whole process of skin impedance measurements using different moisturizers on human skin.

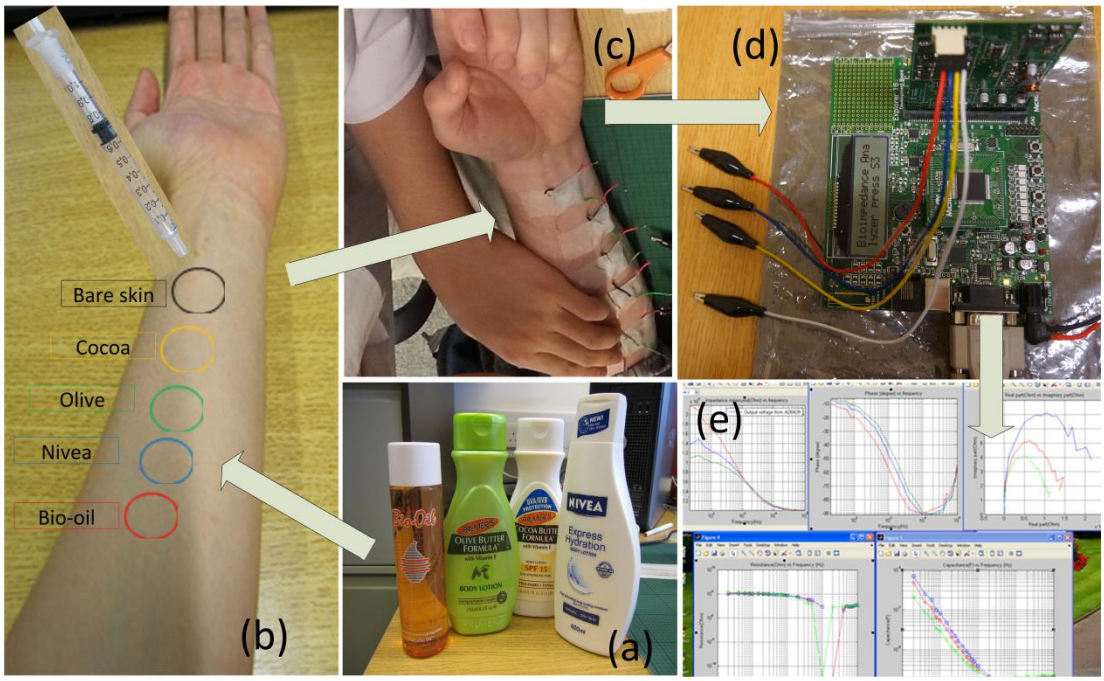


Figure 4.2: Skin measurement (intermittent) on arm with different moisturizers. (a) the four different skin creams . (b) skin cream application sites on arm for experiments using syringe.(c) electrodes are applied on skin with tape. (d) The custom made bio-impedance analyzer is connected to the electrodes for making measurements. (e) Real-time display on PC/laptop.

After the skin creams' application, the electrodes are taped on to the skin as shown in Figure 4.2c. Four terminals from the custom made bio-impedance analyzer are then

connected with the four connections of the electrode sensor as seen in Figure 4.2d. The measurement is taken immediately after the program starts and the real time results are shown on the PC/ Laptop (Figure 4.2e). A measurement will take about 10 seconds, and three measurements are taken on each site.

The previous text describes aspects common to all experiments. The following describes the specific protocols for instantaneous measurement, short term measurement and long term measurement.

- **Protocol for instantaneous measurement:**

Step 1: Apply four different skin creams in the order shown in Figure 4.2b.

Step 2: After the application of skin cream, wait 1 min before taking the measurement.

Step 3: Tape the four electrodes onto the regions of interest using micropore tape as shown in Figure 4.2c.

Step 4: Connect the four terminals from the bio-impedance analyzer to the four connectors of the electrode sensor

Step 5: Start the program and take the measurement for approximately 30 seconds.

Step 6: Repeat step 3 to step 5 for the next electrode sensors until the last electrode sensor is reached.

Step 7: After finishing the measurement, sensors are removed from skin and any surplus skin cream on the probe is wiped off.

There is no timing diagram for instantaneous measurement as the measurements are taken immediately after the skin cream application.

- **Protocol for short term measurement:**

Step 1: Before the skin cream application, the bare skin impedance was measured at locations to which moisturizer will be applied later. This bare skin impedance measurement is necessary for reference.

Step 2: The skin cream is applied to the skin and rubbed in gently until it is not visible. After the application of the skin cream, wait 1 min, remove all the excess using a paper tissue and then take the measurement.

Step 3: Tape the electrode sensors onto applied cream areas on skin using micropore tape.

Step 4: Connect the four terminals from bio-impedance analyzer to four connectors of the electrode sensors.

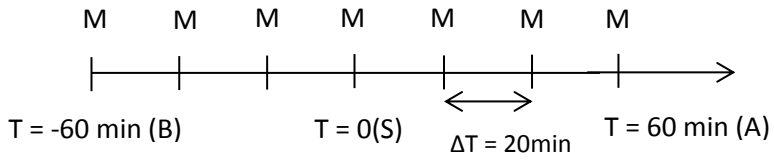
Step 5: Start the program and take three measurements on the same site for approximately 30 seconds, each of measurement takes 10 seconds.

Step 6: Repeat step 3 to step 5 for the next electrode sensors until the last electrode sensor is reached.

Step 7: Lift the tape off to one side to allow the skin to breathe in the ambient environment and to allow easy accurate replacement on the skin. Sensors are cleaned using a paper towel.

Step 8: After 20 min, tape the sensors onto the skin again at the same position and repeat the measurements from step 4 to step 7 following the timing diagram on Figure 4.3 for short term measurement.

Step 9: After finishing the measurement, sensors are removed from skin and cleaned



M: take three measurements, each measurement takes 10 seconds.

(B) Before skin cream application. **(S)** Start skin cream application. **(A)** After skin cream application.

Figure 4.3: Timing diagram of the short term measurement

- **Protocol for long term measurement:**

Step 1: Before the skin cream application, the bare skin impedance was measured at the locations where different moisturizers will be applied later.

Step 2: The skin cream will be applied on the skin and rubbed in gently until it is not visible. After the application of the skin cream, wait 1 min, remove all the excess using a paper towel and then take the measurement.

Step 3: Tape the electrode sensors onto the cream area on the skin using micropore tape.

Step 4: Connect the four terminals from the bio-impedance analyzer to the four connectors of the electrode sensors.

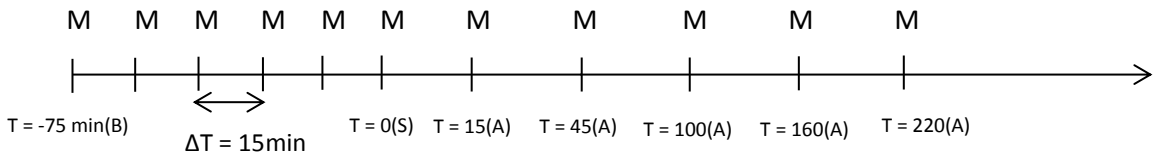
Step 5: Start the program and take three measurements, each measurement takes 10 seconds.

Step 6: Repeat step 3 to step 5 for the next electrode sensors until the last electrode sensor is reached.

Step 7: Lift the tape off to one side to allow the skin to breathe in the ambient environment. Sensors are then cleaned by paper towel.

Step 8: After 15 min, tape the sensors onto skin again at the same position and repeat the measurement from step 4 to step 7 following the timing diagram on Figure 4.4 for long term measurement.

Step 9: After finishing the measurement, sensors are removed from the skin and cleaned.



M: take three measurements, each measurement takes 10 seconds.

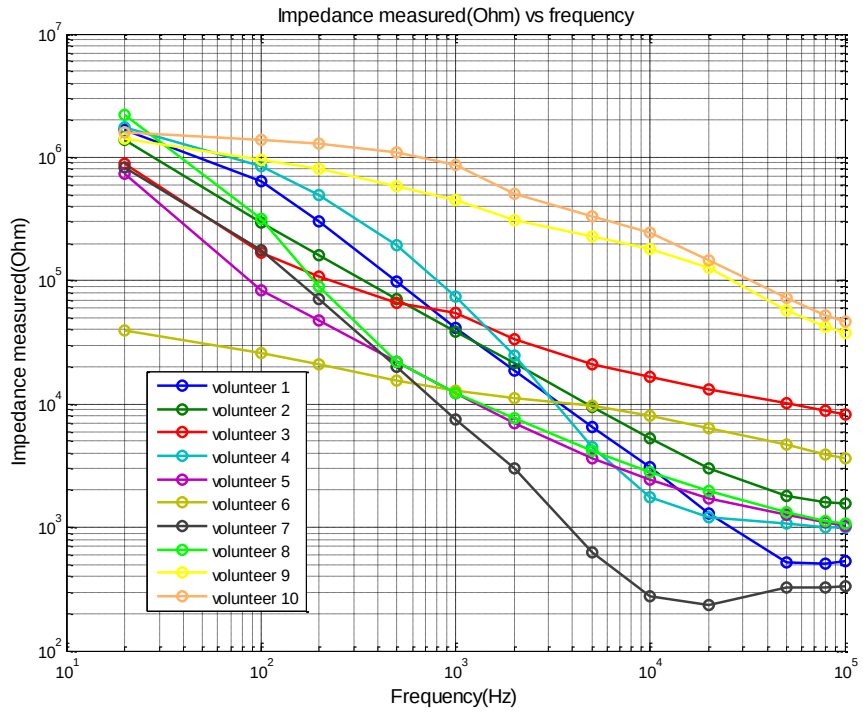
(B) Before skin cream application. **(S)** Start skin cream application. **(A)** After skin cream application.

Figure 4.4: Timing diagram of the long term measurement

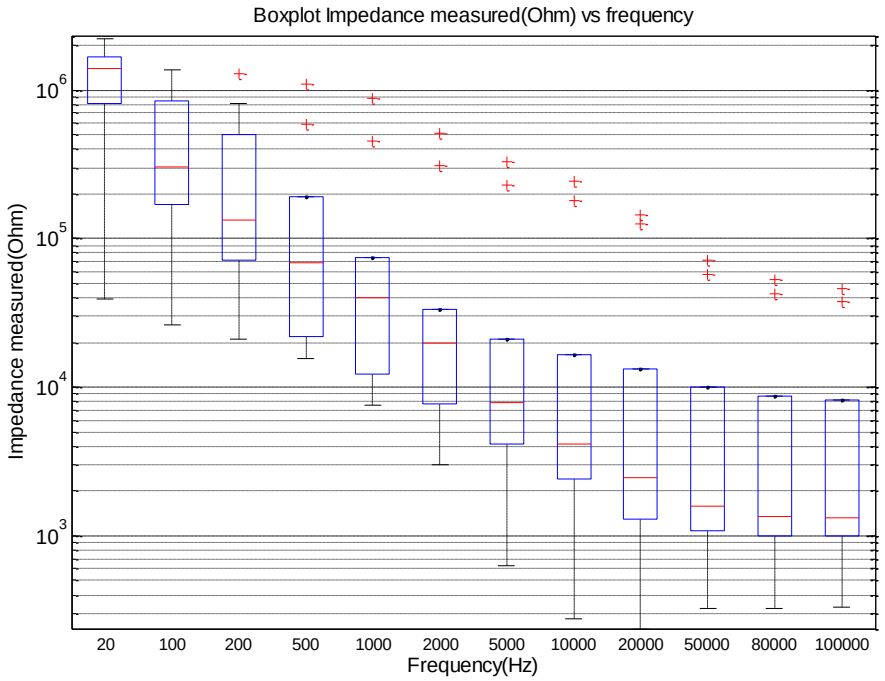
4.3 Instantaneous measurement results

4.3.1 Bare skin impedance:

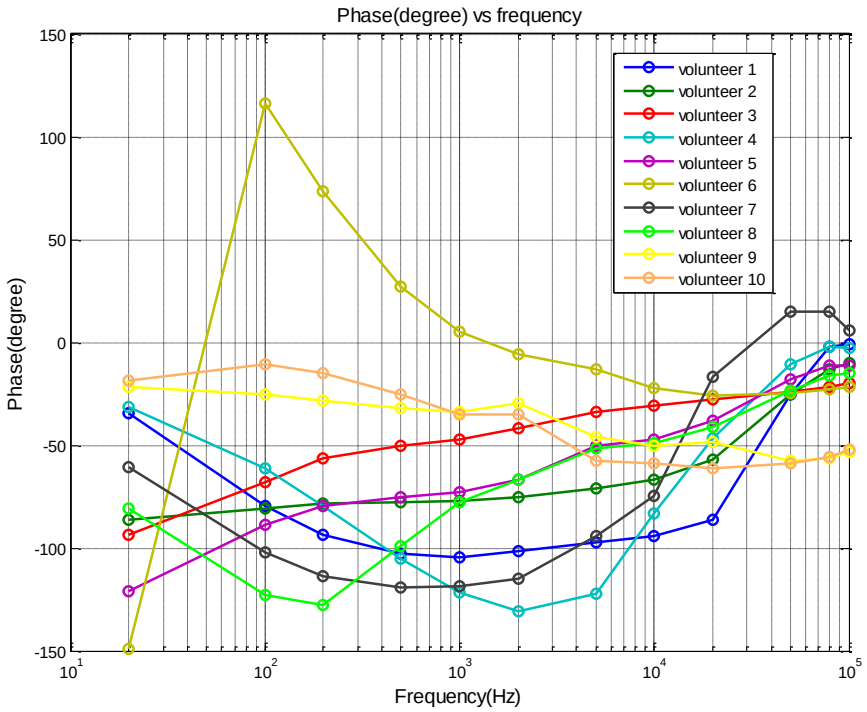
The first measurement is of bare skin on different volunteers in order to get the baseline/ reference. Figure 4.5a shows the skin impedance versus frequency of bare skin measured on 10 volunteers.


Impedance measured(Ohm) vs frequency
Impedance measured(Ohm)
Frequency(Hz)
volunteer 1
volunteer 2
volunteer 3
volunteer 4
volunteer 5
volunteer 6
volunteer 7
volunteer 8
volunteer 9
volunteer 10

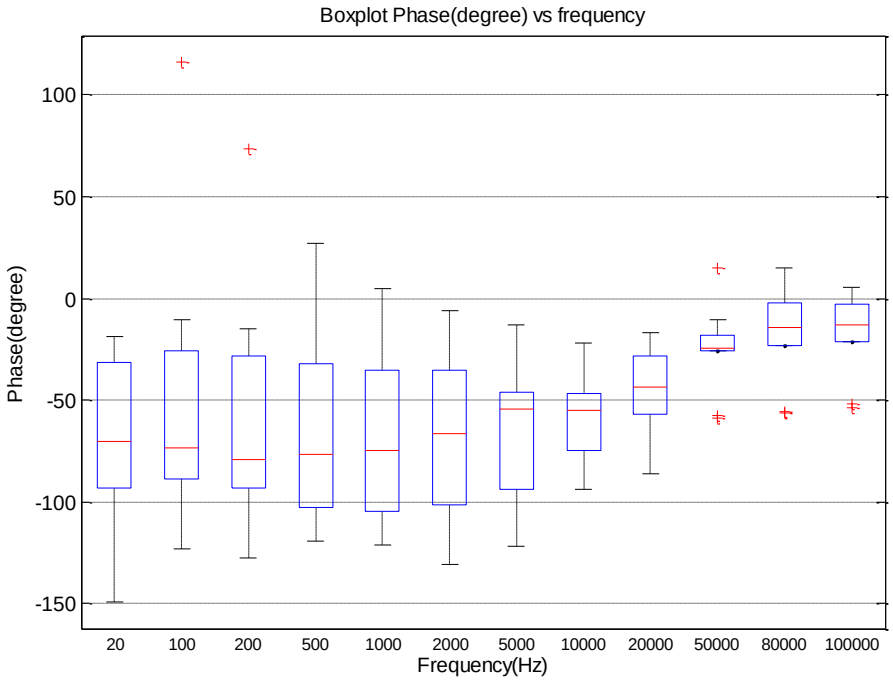
(a)


Boxplot Impedance measured(Ohm) vs frequency
Impedance measured(Ohm)
Frequency(Hz)
20
100
200
500
1000
2000
5000
10000
20000
50000
80000
100000

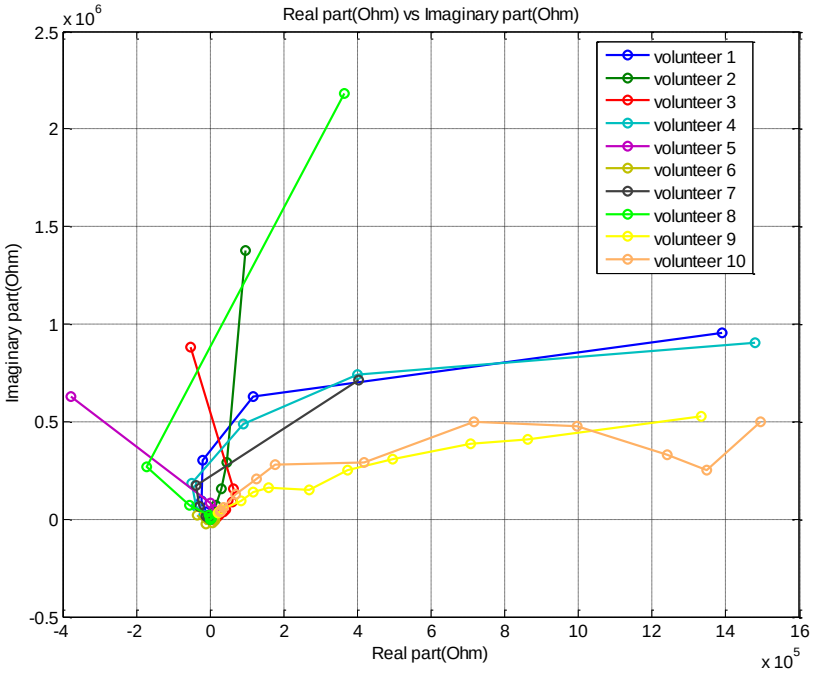
(b)


Phase(degree) vs frequency
volunteer 1
volunteer 2
volunteer 3
volunteer 4
volunteer 5
volunteer 6
volunteer 7
volunteer 8
volunteer 9
volunteer 10
Phase(degree)
Frequency(Hz)
150
100
50
0
-50
-100
-150
10^1
10^2
10^3
10^4
10^5

(c)


Boxplot Phase(degree) vs frequency
Phase(degree)
Frequency(Hz)
100
50
0
-50
-100
-150
20
100
200
500
1000
2000
5000
10000
20000
50000
80000
100000

(d)



(e)

Figure 4.5: Instantaneous skin measurements vs frequency of the bare skin measured on 10 volunteers (group A). (a) Instantaneous Skin impedance vs frequency. (b) The box plot of Instantaneous bare skin impedance. (c) Phase results vs frequency of the Instantaneous bare skin. (d) The box plot of phase results on Instantaneous bare skin. (e) Real versus imaginary plot on Instantaneous bare skin.

In Figure 4.5a, it is clear that each volunteer in this experiment had different skin impedance. However, the impedance results from the volunteers show common points such as at low frequencies (20 Hz) the skin impedance can be high as few MΩ, but at higher frequencies (100 KHz) the skin impedance is as low as a few hundred Ohms. In order to generalize the results for different volunteers, box plots were used to show the median (50% Quartile), upper boundary line (75% Quartile), lower boundary line (25% Quartile), and the variance, minimum and maximum points in the results measured from the 10 volunteers. Outlier values are shown as

red crosses in the boxplot. The box plot explanation is illustrated in the Figure 4.6 below.

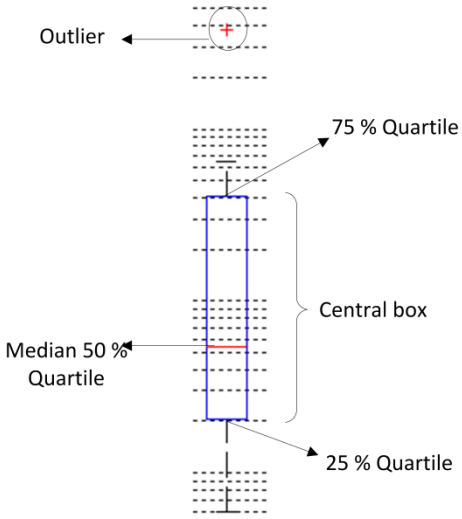


Figure 4.6: The explanation of the box plot

In Figure 4.5b, the box plot of bare skin impedance from 10 volunteers is illustrated. Here, the skin impedance of volunteers at 20Hz was spread from 800 kΩ (25% Quartile) to 1.8 MΩ (75% Quartile) with median (50% Quartile) 1.5 MΩ. The volunteers' skin impedances in turn are: from 170 kΩ to 850 kΩ with median 200 kΩ at 100 Hz; from 14 kΩ to 75kΩ with median 40 kΩ at 1 kHz; from 2.4 kΩ to 16 kΩ with median 4kΩ at 10 kHz; and from 1 kΩ to 8kΩ with median 1.3 kΩ at 100 kHz. However, it is observed that there are two volunteers (volunteer 9 and 10) whose skin impedances are much higher than the main group whilst volunteer 6 had his/her impedance much smaller compared with the others.

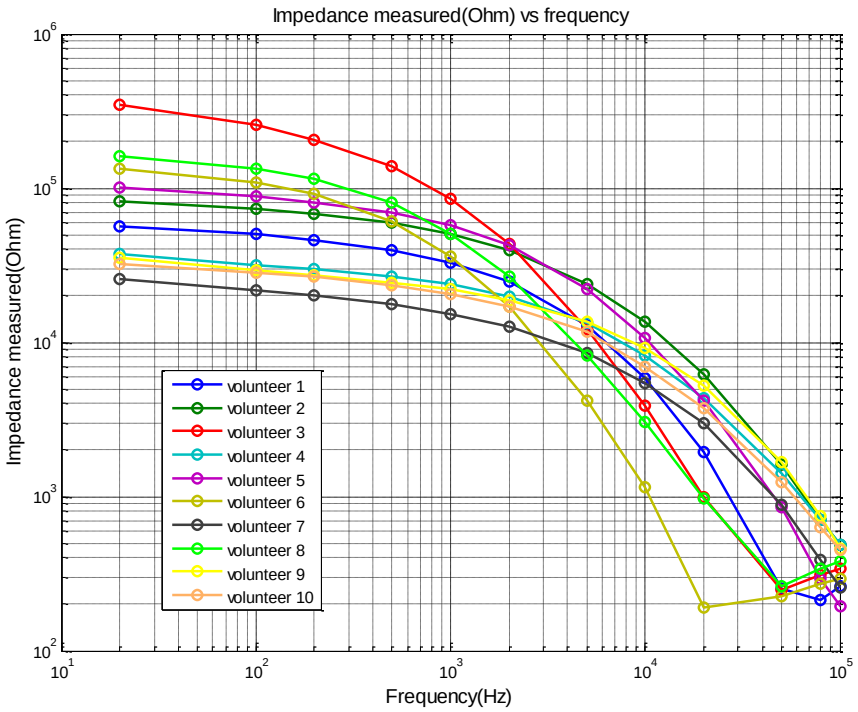
Phase results are shown in Figure 4.5c with the box plot shown in Figure 4.5d. In the frequency range from 20 Hz to 2 KHz, the phase fluctuated from -20 degrees to -90 degrees in 10 different volunteers. The median results (50% Quartile) were around -75˚ to -80˚, which means that in general bare skin measurement results gave more capacitive results than resistive results. On the other hand, in the frequency above 10

KHz, the phase results were less negative than at low frequency. The phase is concentrated in smaller negative range from about -20˚ to -10˚, which means more resistive results can be observed at higher frequency.

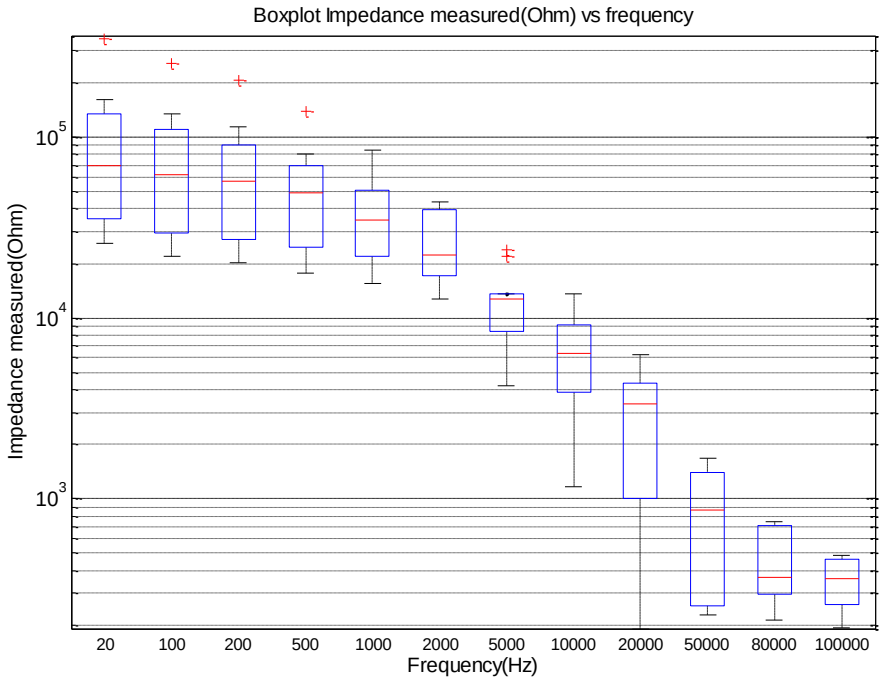
In Figure 4.5e, the real and imaginary plot of Instantaneous bare skin measurement on 10 volunteers is given. The Z plane plot showed the variation in skin impedance from volunteer to volunteer while other sites (with skin cream applied) have skin impedance with less variation as shown in the next sections.

4.3.2 Skin impedance effects of Cocoa Butter Cream:

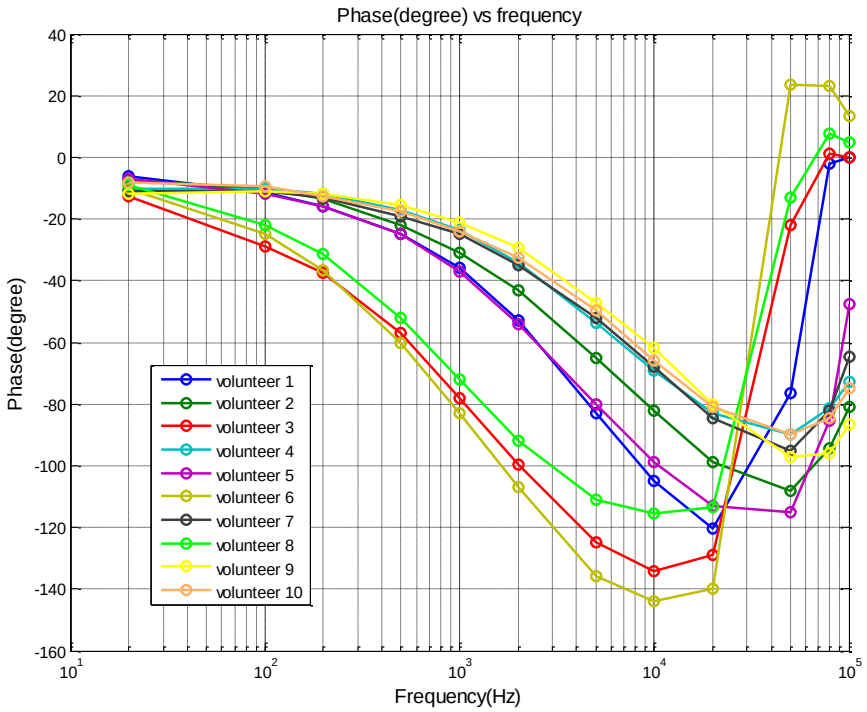
The second measurement is skin impedance using Cocoa Butter on 10 volunteers.


Impedance measured(Ohm) vs frequency
Impedance measured(Ohm)
Frequency(Hz)
volunteer 1
volunteer 2
volunteer 3
volunteer 4
volunteer 5
volunteer 6
volunteer 7
volunteer 8
volunteer 9
volunteer 10

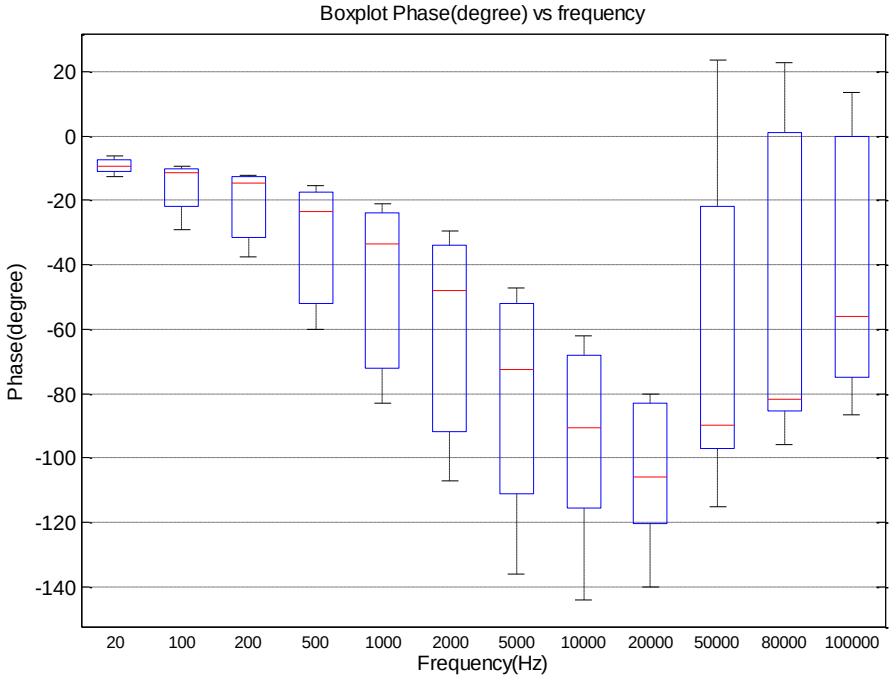
(a)


Boxplot Impedance measured(Ohm) vs frequency
Impedance measured(Ohm)
Frequency(Hz)
20
100
200
500
1000
2000
5000
10000
20000
50000
80000
100000

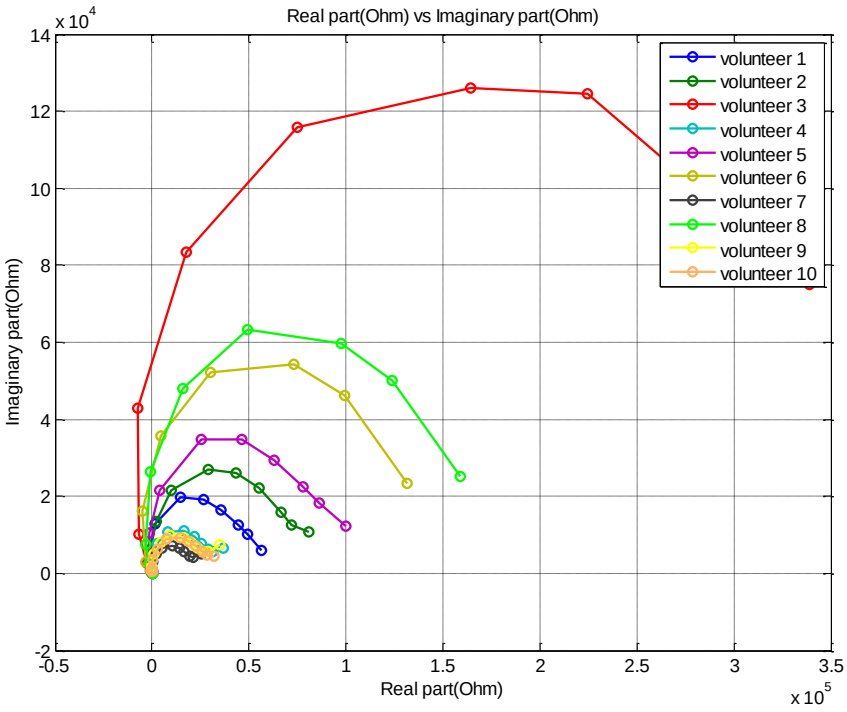
(b)


Phase(degree) vs frequency
Phase(degree)
Frequency(Hz)
volunteer 1
volunteer 2
volunteer 3
volunteer 4
volunteer 5
volunteer 6
volunteer 7
volunteer 8
volunteer 9
volunteer 10

(c)


Boxplot Phase(degree) vs frequency
Phase(degree)
Frequency(Hz)
20
100
200
500
1000
2000
5000
10000
20000
50000
80000
100000

(d)



(e)

Figure 4.7: Instantaneous skin measurements vs frequency using Cocoa Butter measured on 10 volunteers (group A). (a) Instantaneous Skin impedance vs frequency. (b) The box plot of Instantaneous skin impedance. (c) Phase results vs frequency. (d) The box plot of phase results. (e) Real versus imaginary plot.

Figure 4.7a shows skin impedance vs frequency using Cocoa Butter measured on 10 volunteers. The skin impedance was in the range 35kΩ (25% Quartile) to 150kΩ (75% Quartile) at 20 Hz, 30kΩ to 120kΩ at 100 Hz, 20kΩ to 50kΩ at 1 KHz, 3kΩ to 9kΩ at 10 KHz, and 300Ω to 500Ω at 100 KHz. This can also be observed using the boxplot shown in Figure 4.7b.

In Figure 4.7b, it can be seen that the median (50% Quartile) is 70kΩ at 20 Hz, 60kΩ at 100Hz, 35kΩ at 1 KHz, 6kΩ at 10 KHz, and 350Ω at 100 KHz. By comparison with the median of the bare skin impedance in some specific frequencies such as 20 Hz, 100 Hz, 1 KHz, 10 KHz and 100 KHz, the skin impedances measured after applied Cocoa Butter are lower in nearly all of the frequency range from 20 Hz to

100 KHz. In summary, the Cocoa Butter gave a more resistive effect on the skin at low frequencies (approximately from 20Hz to 1 KHz).

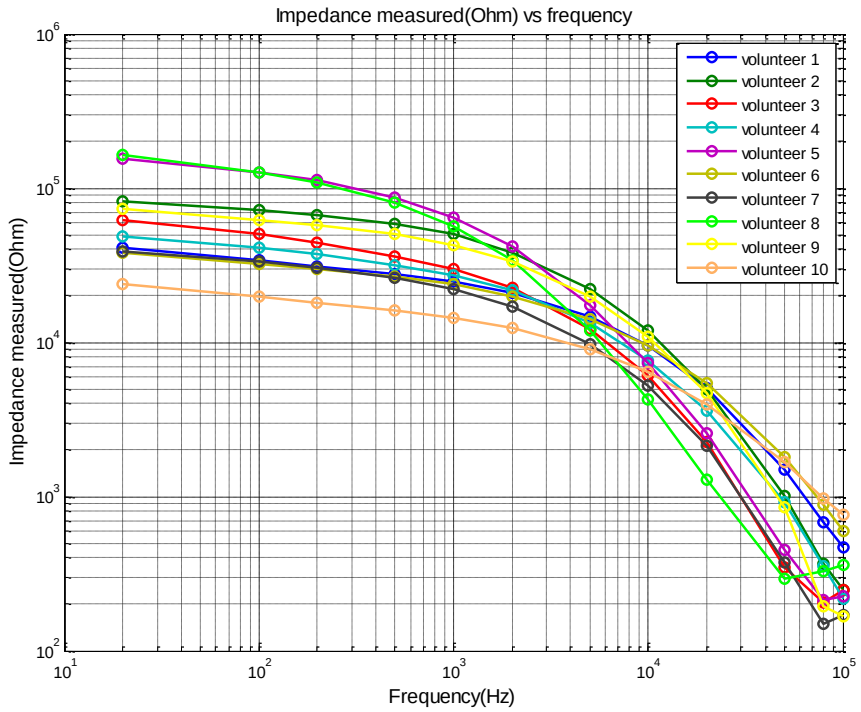
In Figure 4.7c, the phase results versus frequency using Cocoa Butter measured on 10 volunteers are shown. Here, the phase results from 10 volunteers are approximately -10˚ at 20 Hz, and then are spread out at higher frequencies. Figure 4.7d illustrates the box plot.

As shown in Figure 4.7d, after concentrated at about -10˚ at 20 Hz, the phase results spread out from -18˚ (75% Quartile) to -10˚ (25% Quartile) at 100 Hz, -70˚ to -18˚ at 1 KHz, -116˚ to -66˚ at 10 KHz and -74˚ to 0˚ at 100 KHz. Considering the median values, these are -10˚ at 20 Hz, -12˚ at 100 Hz, -34˚ at 1 KHz, -90˚ at 10 KHz and-58˚ at 100 KHz. All the phases in the results of Cocoa Butter are localised at -10 degree at 20 Hz and -12 degrees at 100 Hz compared with the phases spread out between -20˚ to -90˚ in the bare skin at low frequencies. The phases again diverged in the higher frequency in the same way as the bare skin results.

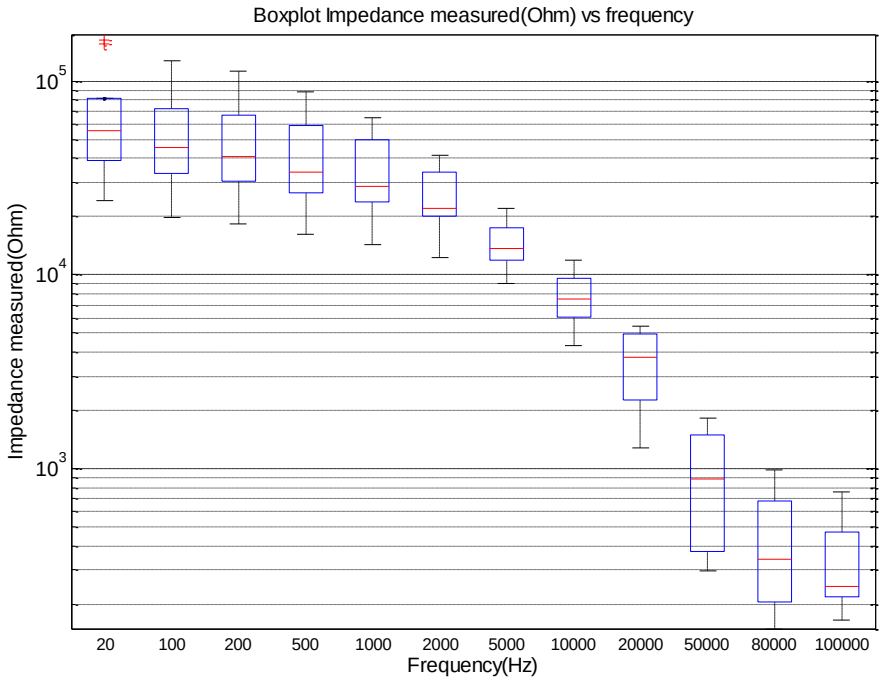
In Figure 4.7e, the real vs imaginary plots of skin impedance using Cocoa Butter formed semicircles. This effect is similar to that of a passive component added to the skin (such as a resistor). This passive component dominated the impedance results, which makes the Z plots of skin impedances become the shape of semicircle (as seen in RC, 2R-1C and Cole models described in section 2.6 of Chapter 2).

4.3.3 Skin impedance effects of Olive Butter Cream:

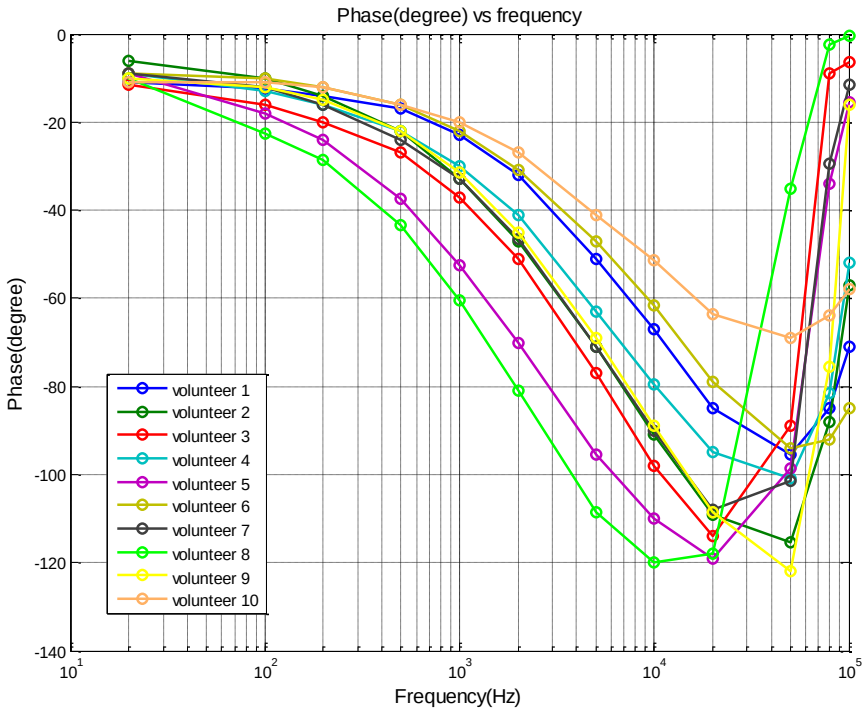
The third measurement is skin impedance using Olive Butter on 10 volunteers.


Impedance measured(Ohm) vs frequency
Impedance measured(Ohm)
Frequency(Hz)
volunteer 1
volunteer 2
volunteer 3
volunteer 4
volunteer 5
volunteer 6
volunteer 7
volunteer 8
volunteer 9
volunteer 10

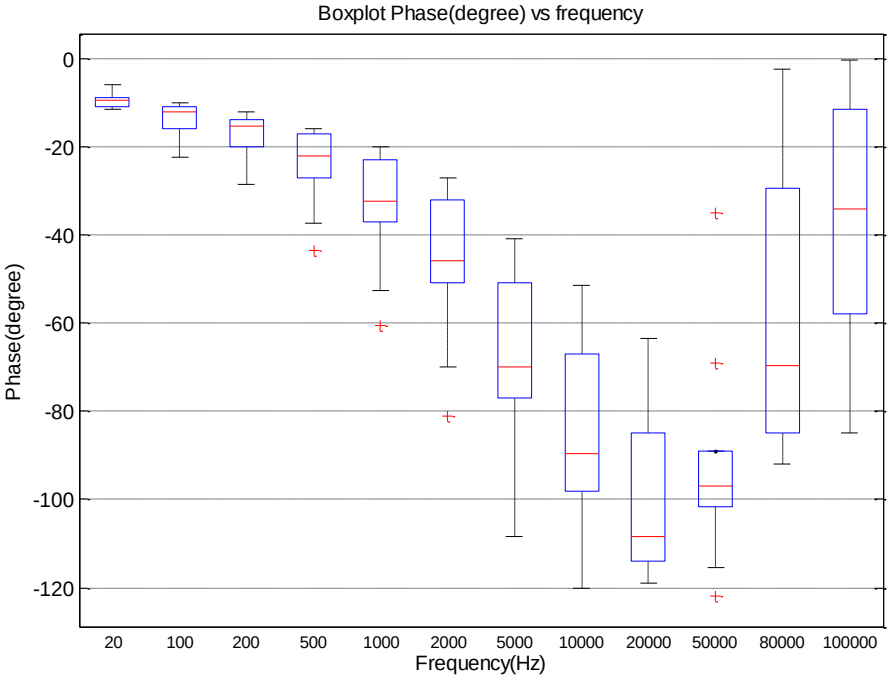
(a)


Boxplot Impedance measured(Ohm) vs frequency
Impedance measured(Ohm)
Frequency(Hz)
20
100
200
500
1000
2000
5000
10000
20000
50000
80000
100000

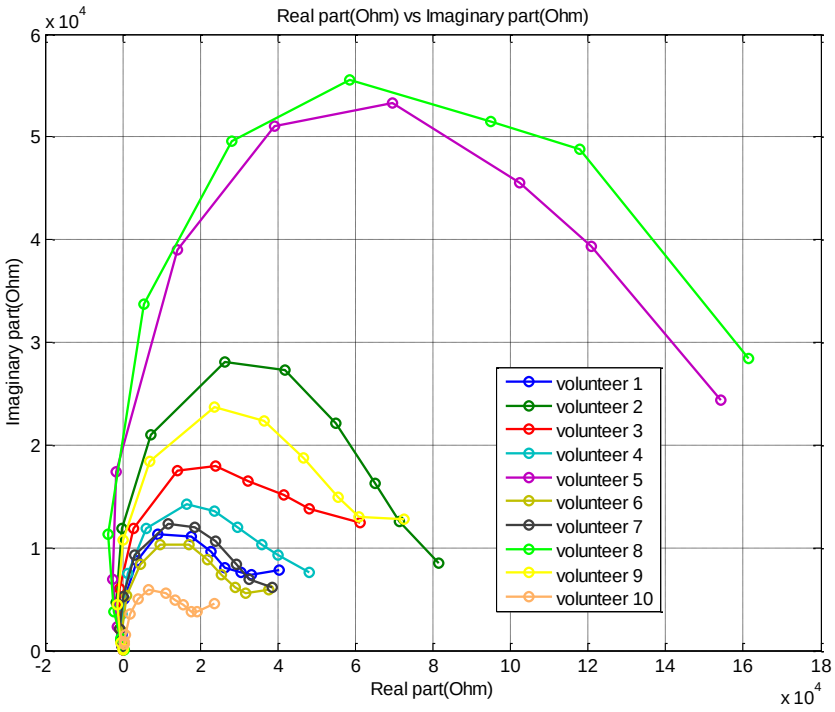
(b)


Phase(degree) vs frequency
Phase(degree)
Frequency(Hz)
volunteer 1
volunteer 2
volunteer 3
volunteer 4
volunteer 5
volunteer 6
volunteer 7
volunteer 8
volunteer 9
volunteer 10

(c)


Boxplot Phase(degree) vs frequency
Phase(degree)
Frequency(Hz)
20
100
200
500
1000
2000
5000
10000
20000
50000
80000
100000

(d)



(e)

Figure 4.8: Instantaneous skin measurements vs frequency using Olive Butter measured on 10 volunteers (group A). (a) Instantaneous Skin impedance vs frequency. (b) The box plot of Instantaneous skin impedance. (c) Phase results vs frequency. (d) The box plot of phase results. (e) Real versus imaginary plot.

In Figure 4.8a and Figure 4.8b, the skin impedance is in the range 40kΩ (25% Quartile) to 80kΩ (75% Quartile) at 20 Hz, 34kΩ to 72kΩ at 100 Hz, 25kΩ to 50kΩ at 1 KHz, 6kΩ to 9.2kΩ at 10 KHz, and 200Ω to 450Ω at 100 KHz.

As shown in Figure 4.8b, the median (50% Quartile) is 54kΩ at 20 Hz, 44kΩ at 100Hz, 29kΩ at 1 KHz, 7.5kΩ at 10 KHz, and 250Ω at 100 KHz. In comparison with bare skin, the Olive Butter has a more resistive effect on skin impedance over nearly the whole range of frequencies. The effect of Olive Butter is similar to that of Cocoa Butter. In Figure 4.8c, the phase results versus frequency using Olive Butter measured on 10 volunteers are shown.

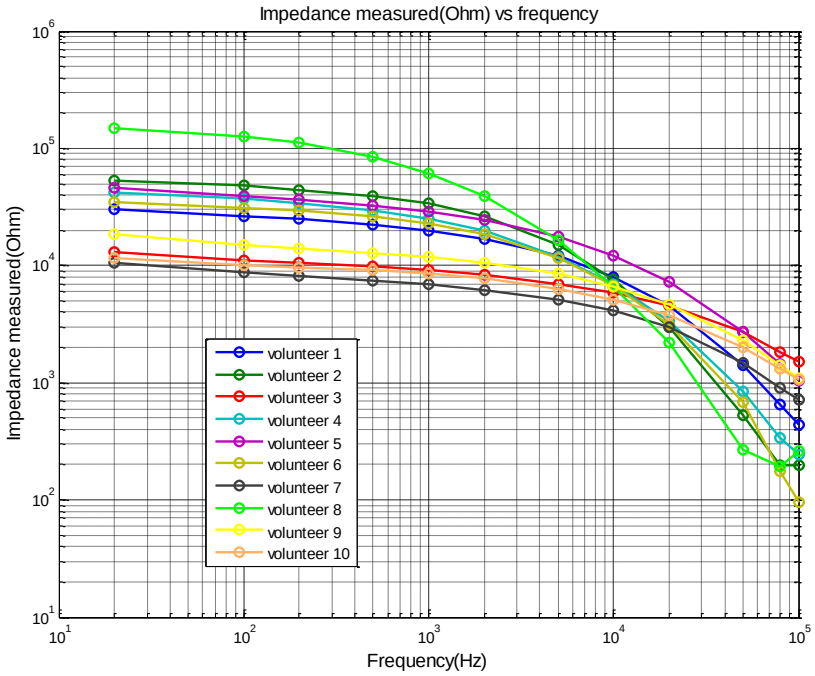
In Figure 4.8c, the phase results from 10 volunteers are about -10˚ at 20 Hz, and then spread out at higher frequencies. Figure 4.8d illustrates the box plot of the phase results on skin using Olive Butter from 10 volunteers.

In Figure 4.8d, after being close to -10˚ at 20 Hz, the phase results spread out in turn from -16˚ (75% Quartile) to -10˚ (25% Quartile) at 100 Hz, -38˚ to -18˚ at 1 KHz, -98˚ to -66˚ at 10 KHz and -58˚ to -12˚ at 100 KHz. Considering the median values, these are -10˚ at 20 Hz, -12˚ at 100 Hz, -34˚ at 1 KHz, -90˚ at 10 KHz and -34˚ at 100 KHz. The phase with Olive Butter are around -10˚ degree at 20 Hz, -12˚ degree at 100 Hz, -34˚ at 1 KHz, -90˚ at 10 KHz. The effects of Olive Butter are comparable with Cocoa Butter.

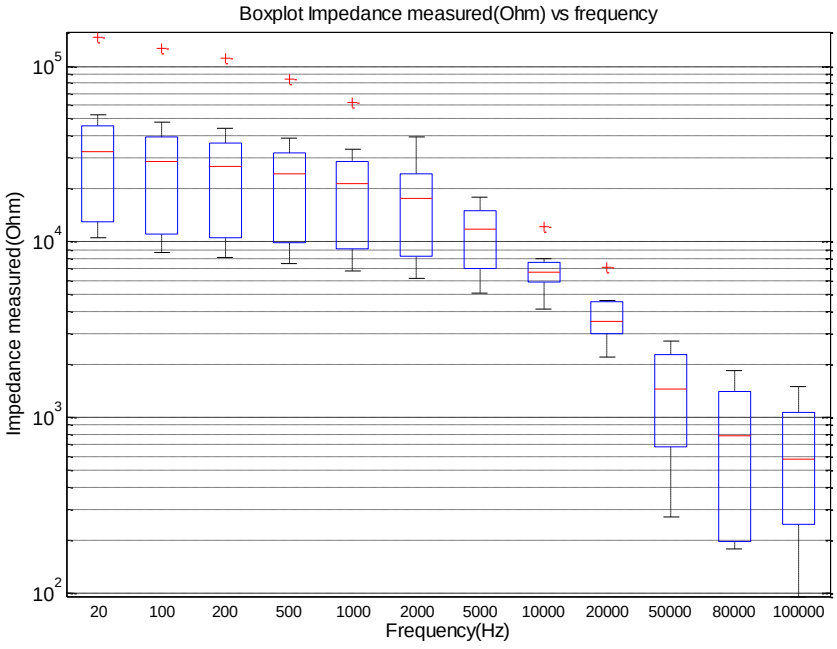
As shown in Figure 4.8e, the real vs imaginary plots of skin impedances using Olive Butter also formed semicircles as seen in the case of Cocoa Butter.

4.3.4 Skin impedance effects of Nivea Cream:

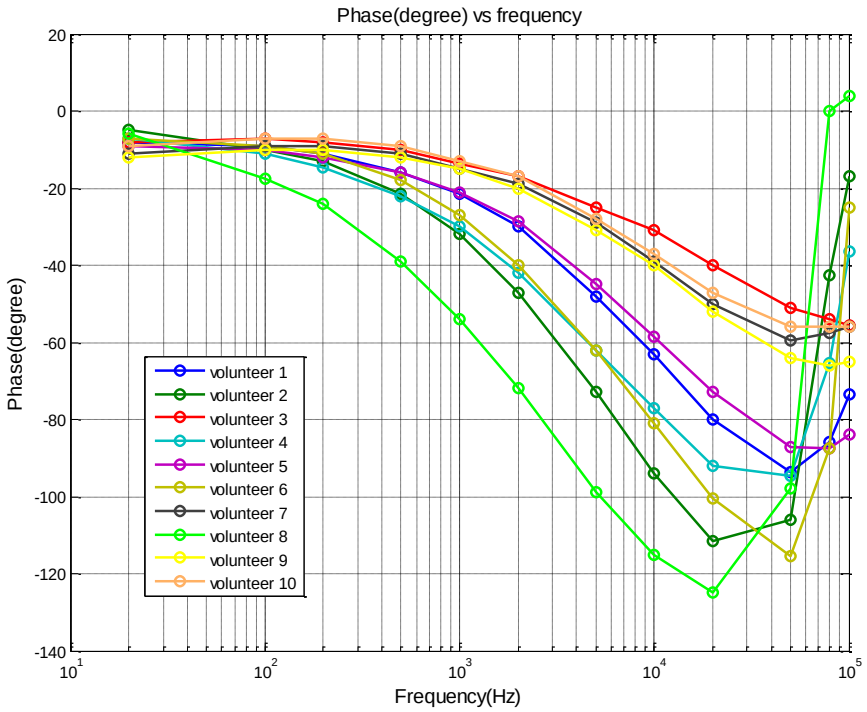
The fourth measurement is skin impedance using Nivea on 10 volunteers.


Impedance measured(Ohm) vs frequency
Impedance measured(Ohm)
Frequency(Hz)
volunteer 1
volunteer 2
volunteer 3
volunteer 4
volunteer 5
volunteer 6
volunteer 7
volunteer 8
volunteer 9
volunteer 10

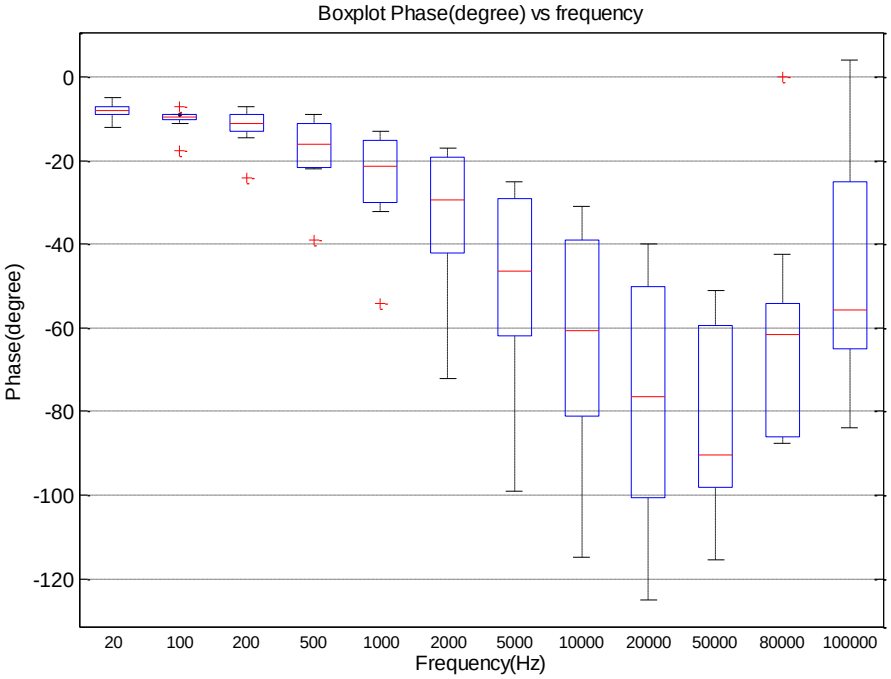
(a)


Boxplot Impedance measured(Ohm) vs frequency
Impedance measured(Ohm)
Frequency(Hz)
20
100
200
500
1000
2000
5000
10000
20000
50000
80000
100000

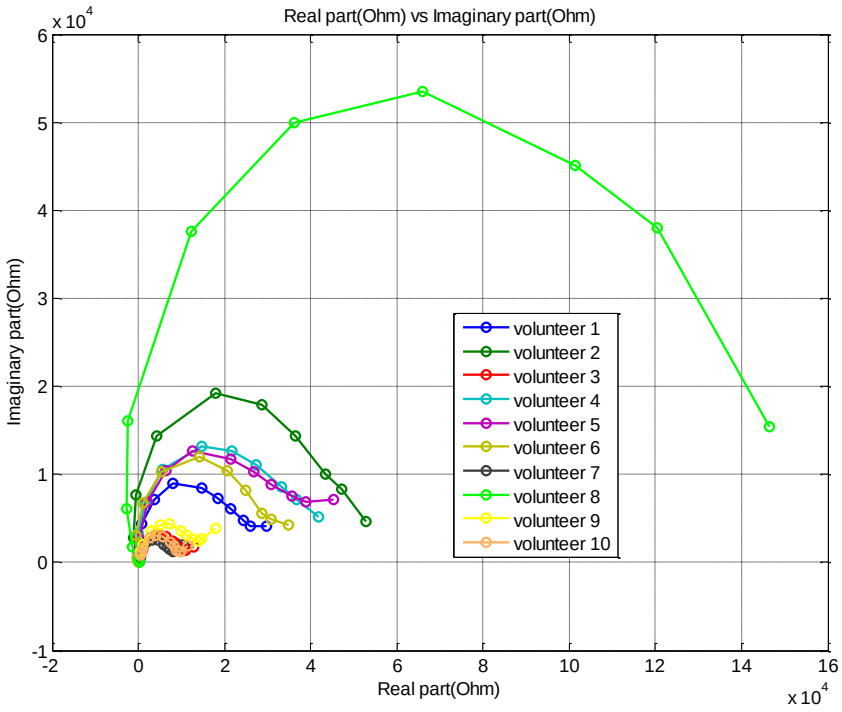
(b)


Phase(degree) vs frequency
Phase(degree)
Frequency(Hz)
volunteer 1
volunteer 2
volunteer 3
volunteer 4
volunteer 5
volunteer 6
volunteer 7
volunteer 8
volunteer 9
volunteer 10

(c)


Boxplot Phase(degree) vs frequency
Phase(degree)
Frequency(Hz)
20
100
200
500
1000
2000
5000
10000
20000
50000
80000
100000

(d)



(e)

Figure 4.9: Instantaneous skin measurements vs frequency using Nivea measured on 10 volunteers (group A). (a) Instantaneous Skin impedance vs frequency. (b) The box plot of Instantaneous skin impedance. (c) Phase results vs frequency. (d) The box plot of phase results. (e) Real versus imaginary plot.

In Figure 4.9a and Figure 4.9b, the skin impedance with Nivea was around 10kΩ to 50kΩ at 20 Hz. The skin impedance was 15kΩ (25% Quartile) to 45kΩ (75% Quartile) at 20 Hz, 12kΩ to 40kΩ at 100 Hz, 9kΩ to 28kΩ at 1 KHz, 6kΩ to 8kΩ at 10 KHz, and 250Ω to 1kΩ at 100 KHz.

As shown in Figure 4.9b, the median (50% Quartile) was 32kΩ at 20 Hz, 28kΩ at 100Hz, 22kΩ at 1KHz, 6.8kΩ at 10KHz, and 600Ω at 100 KHz. Again, in comparison with bare skin, Nivea gave more resistive effect on the skin impedance, which showed that the impedance after Nivea is applied is lower than bare skin for nearly all frequencies and is lower than Cocoa and Olive Butter.

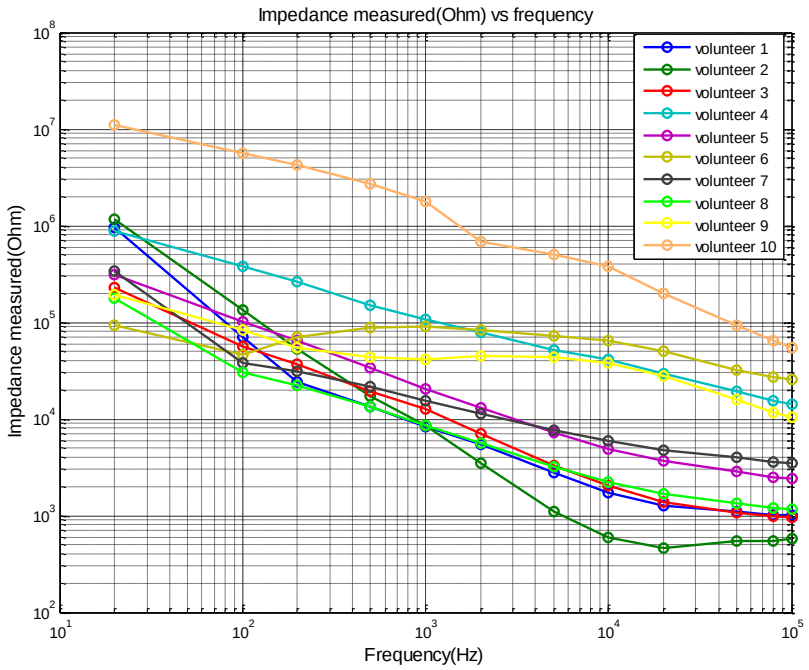
In Figure 4.9c and Figure 4.9d, the phase results versus frequency using Nivea measured on 10 volunteers are shown. In Figure 4.9c the phase results from 10 volunteers are about -9˚ at 20 Hz, and then spread out in higher frequency.

As shown in Figure 4.9d, after being close to -9˚ at 20 Hz, the phase results spread out from -11˚ (75% Quartile) to -10˚ (25% Quartile) at 100 Hz, -30˚ to -15˚at 1 KHz, -81˚ to -39˚ at 10 KHz and -65˚ to -23˚ at 100 KHz. Considering the median values, these are -9˚ at 20 Hz, -10˚ at 100 Hz, -20˚ at 1 KHz, -60˚ at 10 KHz and -55˚ at 100 KHz.

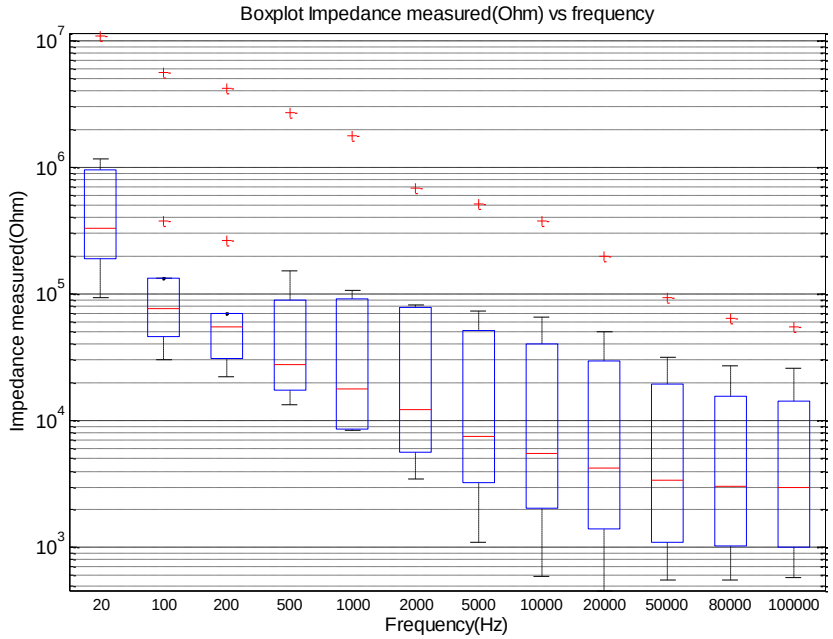
In Figure 4.9e, the semicircle shape from real vs imaginary plots can be seen. It is shown that Nivea also makes the impedance results have less variation in a similar way to Cocoa and Olive Butter.

4.3.5 Skin impedance effects of Bio-oil:

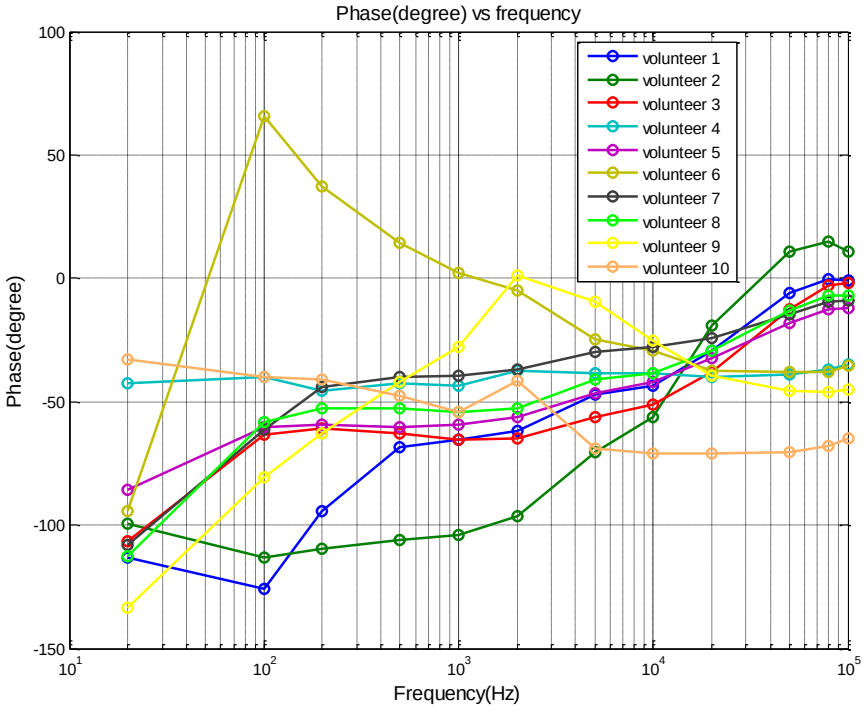
The fifth measurement is skin impedance using Bio-oil on 10 volunteers.



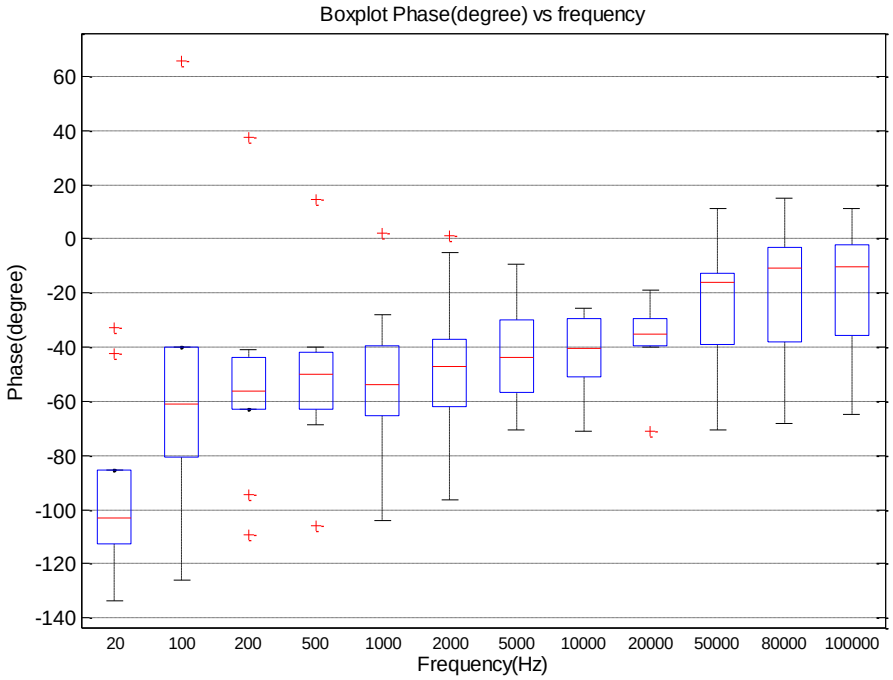
(a)


Boxplot Impedance measured(Ohm) vs frequency
Impedance measured(Ohm)
Frequency(Hz)
20
100
200
500
1000
2000
5000
10000
20000
50000
80000
100000

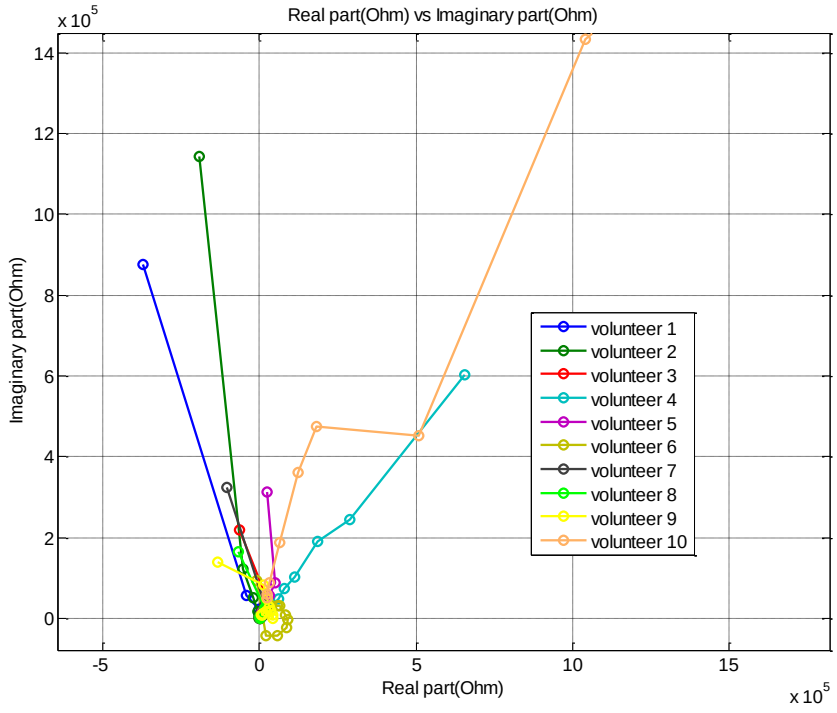
(b)


Phase(degree) vs frequency
Phase(degree)
Frequency(Hz)
volunteer 1
volunteer 2
volunteer 3
volunteer 4
volunteer 5
volunteer 6
volunteer 7
volunteer 8
volunteer 9
volunteer 10

(c)



(d)



(e)

Figure 4.10: Instantaneous skin measurements vs frequency using Bio-oil measured on 10 volunteers (group A). (a) Instantaneous Skin impedance vs frequency. (b) The

box plot of Instantaneous skin impedance. (c) Phase results vs frequency. (d) The box plot of phase results. (e) Real versus imaginary plot.

In Figure 4.10a and Figure 4.10b, Bio-oil adjusts the skin impedance to around 200kΩ - 1MΩ at 20 Hz. The skin impedance was 200kΩ (25% Quartile) to 1MΩ (75% Quartile) at 20 Hz, 45kΩ to 150kΩ at 100 Hz, 9kΩ to 90kΩ at 1 KHz, 2kΩ to 40kΩ at 10 KHz, and 1kΩ to 15kΩ at 100 KHz.

In Figure 4.10b, the median (50% Quartile) impedance result was 320kΩ at 20 Hz, 75kΩ at 100Hz, 18kΩ at 1 KHz, 5.8kΩ at 10 KHz, and 3kΩ at 100 KHz. In comparison with Nivea, Cocoa and Olive Butter, the Bio-oil provided a capacitive effect on skin impedance, which showed that the impedance after applying Bio-oil is similar to that of bare skin for nearly all frequencies. In Figure 4.10c, the phase results versus frequency using Bio-oil measured on 10 volunteers are shown.

In Figure 4.10c, the phase values from 10 volunteers are widely spread out at all frequencies. Figure 4.10c shows that the phase varies on different volunteers.

As shown in Figure 4.10d, the phase values are spread from -85˚ (75% Quartile) to -112˚ (25% Quartile) at 20 Hz, -40˚ to -85˚ at 100 Hz, -40˚ to -65˚ at 1 KHz, -31˚ to -50˚ at 10 KHz and -2˚ to -37˚ at 100 KHz. Considering the median (50% Quartile) values, these are -102˚ at 20 Hz, -61˚ at 100 Hz, -53˚ at 1 KHz, -40˚ at 10 KHz and -10˚ at 100 KHz. The phase results using Bio-oil showed higher negative phases compared with Nivea, Cocoa and Olive Butter. This means Bio-oil gave more of a capacitive effect on the skin than the other moisturizers.

In Figure 4.10e, like the instantaneous measurement results on bare skin, the Bio-oil gave the skin impedance varied between volunteers.

4.3.6 Comparison of skin creams' effect:

In summary, Nivea, Cocoa and Olive significantly reduced the skin impedance with respect to the bare skin impedance. According to the phase results, three skin creams gave lower negative phase than bare skin, therefore they gave more of a resistive effect on skin. On the other hand, Bio oil did not change the skin impedance significantly when compared with the original bare skin. The phase results of Bio-oil showed higher negative phases compared to the other creams, hence it provided more of a capacitive effect on the skin.

In order to see clearly the differences between these skin creams, the results from 10 volunteers has been averaged and plotted. Figure 4.11 shows the average skin impedance using different moisturizers taken from 10 volunteers.

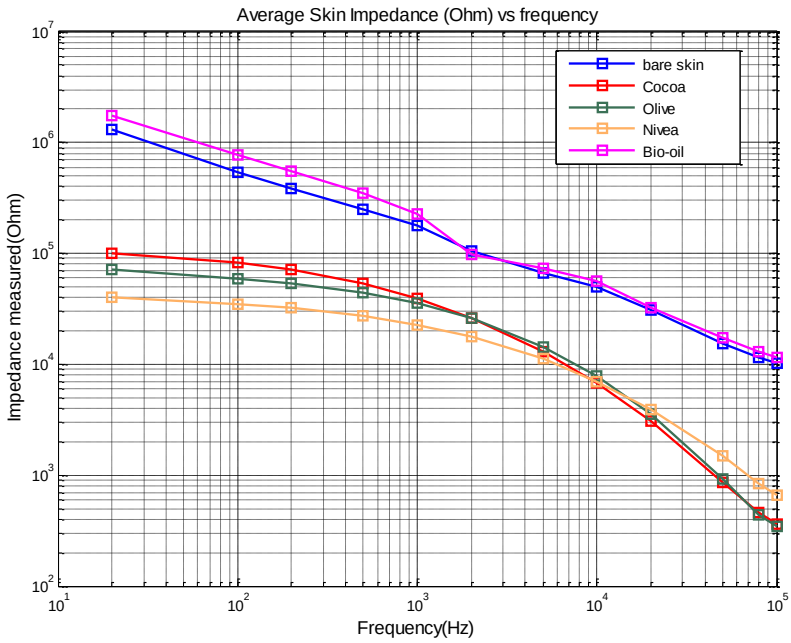


Figure 4.11: The average instantaneous skin impedance using different moisturizers from 10 volunteers

In Figure 4.11, the average impedance results using Bio-oil together with bare skin impedance plotted in the range of frequency from 20 Hz to 100 KHz is higher than

the other skin creams Nivea, Cocoa and Olive Butter. The average impedance results of Bio-oil and bare skin started around 1.25 and 1.5 MΩ (at 20 Hz) to about 10 KΩ (at 100 KHz). On the other hand, the average skin impedance using Nivea, Cocoa and Olive butter is about 40 kΩ - 100 kΩ (at 20 Hz) to 300Ω - 700Ω (at 100 KHz). For the higher impedance result group (including bare skin and Bio-oil), the average skin impedance results are comparable. For the lower impedance group (Nivea, Cocoa and Olive Butter), both Cocoa and Olive gave very similar impedance values and was slightly (about 5-20kΩ) higher than Nivea from 20Hz to 2 KHz. Then, at the high frequencies (above 20kHz), Nivea gave the impedance higher than both Cocoa and Olive. The table 4.1 summarizes the impedance results in details by giving mean and standard deviation (SD) for some specific frequencies.

	Bare skin		**Cocoa**		**Olive**		**Nivea**		**Bio-oil**	
Frequency	Mean	SD	Mean	SD	Mean	SD	Mean	SD	Mean	SD
20Hz	1.25MΩ	±629kΩ	101kΩ	±98kΩ	72kΩ	±49kΩ	40kΩ	±40kΩ	1.5MΩ	±3.3MΩ
200Hz	339kΩ	±414kΩ	71kΩ	±57kΩ	53kΩ	±33kΩ	32kΩ	±30kΩ	483kΩ	±1.3MΩ
2KHz	94kΩ	±173kΩ	26kΩ	±12kΩ	26kΩ	±9.8kΩ	17kΩ	±10kΩ	93kΩ	±208kΩ
20KHz	30kΩ	±56kΩ	3kΩ	±2kΩ	3.5kΩ	±1.4kΩ	3.9kΩ	±1.4kΩ	31kΩ	±60kΩ
100KHz	10kΩ	±17kΩ	360Ω	±107Ω	346Ω	±201Ω	663Ω	±483Ω	11kΩ	±17kΩ

Table 4.1: Summary of impedance versus frequency measured on 10 volunteers using different skin moisturizers.

According to [102], it can be found that Nivea, Cocoa Butter and Olive Butter have a similar response as they are type II humectants, which attract water from deeper dermis to the stratum corneum. Bio oil however, can be classified as a type I [102] occlusive as it blocked water vaporized from the stratum corneum.

In Figure 4.12, the average phase results on different moisturizers taken from 10 volunteers are illustrated.

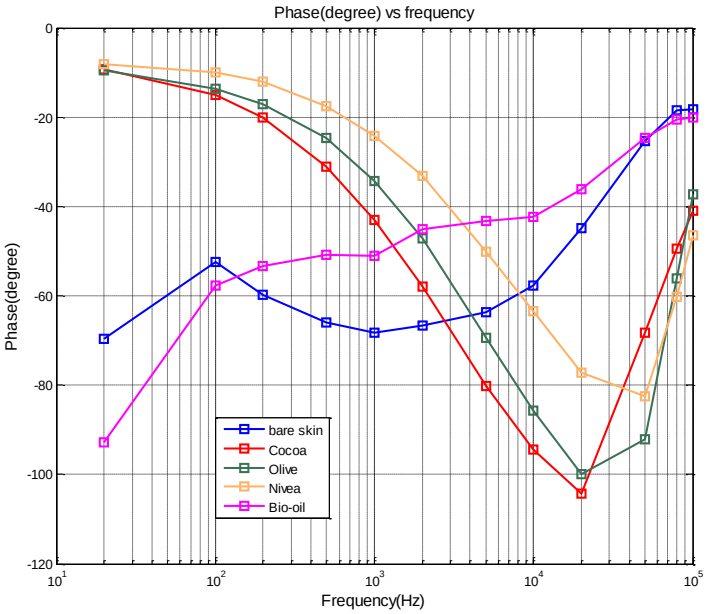


Figure 4.12: Average phase results on different skin creams taken from 10 volunteers (group A).

As seen in Figure 4.12, the average phase results from Bio-oil and bare skin are about -70˚ to -90˚ compared with the average phase of three other skin creams which are around -10˚ at 20 Hz. Also, the phase results in Bio-oil and bare skin had higher negative phase (from -90˚ to -50˚) in low frequencies up to 1 KHz compared with Nivea, Cocoa and Olive Butter (from -40˚ to -10˚). In the higher frequencies about 1 KHz, the phase results from Bio-oil and bare skin tend to decrease to a less negative phase, but Nivea, Cocoa and Olive Butter gave more negative phase. If one assumes that for higher frequencies, the current is injected deeper into the skin layer [1], it can be deduced that Bio-oil gave more capacitive effect as it created a barrier when applied on human skin. However, Nivea, Cocoa and Olive gave more resistive effect compared with Bio-oil.

The table 4.2 summarizes the phase results in details by giving mean and standard deviation (SD) for some specific frequencies.

	Bare skin		Cocoa		Olive		Nivea		Bio-oil	
Frequency	Mean	SD	Mean	SD	Mean	SD	Mean	SD	Mean	SD
20Hz	-69˚	±44˚	-9.3˚	±2˚	-9.5˚	±1.5˚	-8.2˚	±2.1˚	-92˚	±32˚
200Hz	-59˚	±58˚	-20˚	±10˚	-17˚	-5.4˚	-12˚	±4.8˚	-53˚	±39˚
2KHz	-66˚	±40˚	-57˚	±30˚	-47˚	±17˚	-33˚	±17˚	-45˚	±28˚
20KHz	-45˚	±20˚	-104˚	±21˚	-100˚	±18˚	-77˚	±30˚	-36˚	±14˚
100KHz	-18˚	±20˚	-41˚	±40˚	-37˚	±30˚	-46˚	±27˚	-20˚	±24˚

Table 4.2: Summary of phase versus frequency measured on 10 volunteers using different skin moisturizers.

Therefore, the occlusive nature of Bio oil is also revealed in the phase response compared to other moisturizers. The impedance results can discriminate between Bio-oil/ Bare skin (Type I) and other moisturizers Nivea, Olive and Cocoa (Type II) [102]. Phase results demonstrated additional capacitance effects of Bio oil compared to other moisturizers.

Another conclusion that can be drawn from these results is that skin impedance varies greatly from person to person. It can be seen that the standard deviation of impedance and phase results on volunteers has a large variation in bare skin impedance and skin impedance using Bio-oil.

The variation in impedance and phase results can be confirmed from the Z plane plot in the case of bare skin and Bio-oil; while Nivea, Cocoa and Olive tighten the skin impedance values which make semicircles in the real vs imaginary plot.

This experiment was conducted without focusing on the gender or skin sites, but generally skin impedance compared between different people at their arm using moisturizers.

4.4 Short term measurement

This section describes results from several short term measurements i.e. over a period of approximately 240 minutes.

4.4.1 Short term bare skin impedance versus skin temperature:

According to [103][104], the ambient temperature can affect in general the BIA (Bioelectric Impedance Analysis) and specifically the skin impedance. Therefore, the room, where measurements were taken, was kept at a constant temperature 20˚C (using air conditioner) in order to ensure that ambient temperature did not affect the skin impedance results.

In addition, the bare skin impedance was measured together with the temperature of the skin to verify whether the skin temperature is maintained. The experiment was conducted as measuring bare skin impedance using the custom made analyser together with skin temperature in adjacent location using a Nexus 10 mark II [105] for 4 hours. Figure 4.13 shows the bare skin impedance measurement for 4 hours together with the skin temperature with respect to time.

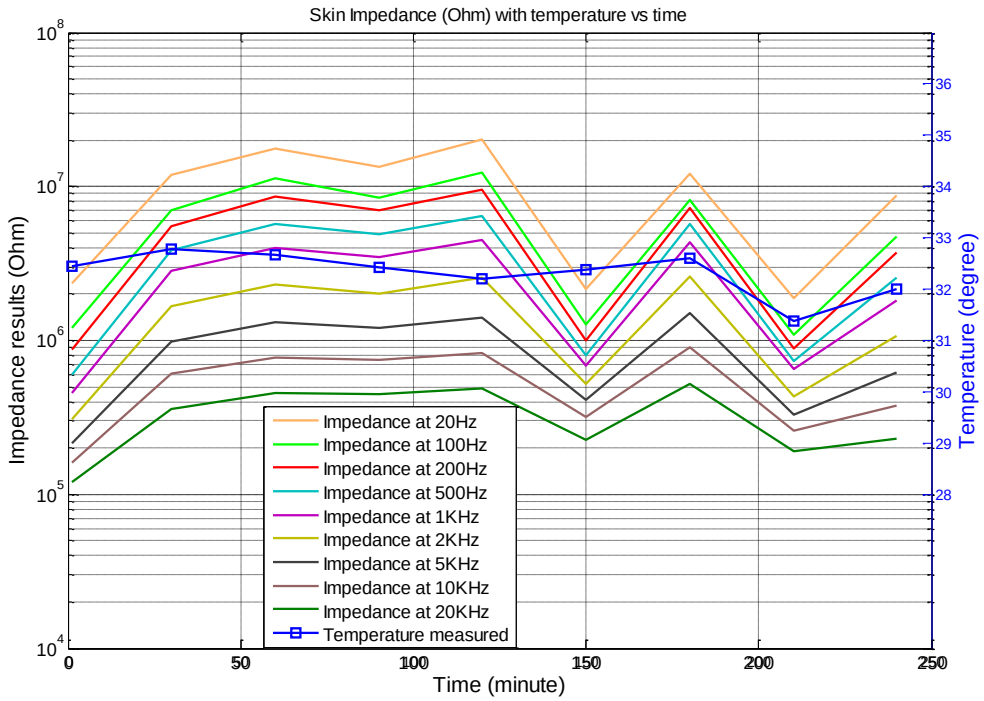


Figure 4.13: Bare skin impedance with temperature measurement for 4 hours (volunteer 1 group B).

As seen in Figure 4.13, the skin temperature varies by around 1˚C (from 31.4˚-32.8˚C) and did not affect the variation in skin impedance. It is observed that skin impedance results fluctuate less at high frequencies and more at low frequencies with respect to time. Grimnes [65] suggests that the sweat gland activity during the time period largely affected the variation in skin admittance mainly because of the change in skin hydration.

4.4.2 Short term skin impedance using moisturizers:

The experiments were conducted in order to investigate how long the effect of the moisturizer is maintained on human skin. This short term measurement was only applied as a pilot before the long term measurement. However, there are several conclusions drawn from the short term measurement, which supports the preparation of the long term measurement.

Before applying the skin cream (Nivea) at t = 0, all three different positions of bare skin are measured three times at t = -60, -40 and -20 minutes and then skin cream is applied and measurements taken for a further 1 hour. The probe was removed between measurements. Figure 4.14 shows the overall skin cream (Nivea) on the measurement results on one volunteer.

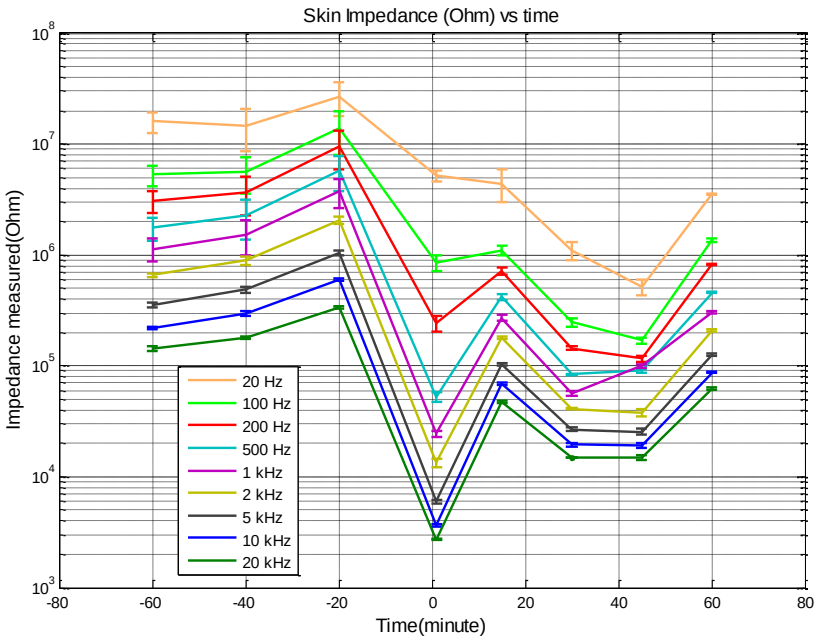


Figure 4.14: Non continuous contact visits each 20 minutes from before (Nivea) application to after application (volunteer 1 group B).

As seen in Figure 4.14 the baseline skin impedance, which is measured three times before skin cream application over one hour, was in the range from around 100 kΩ (frequency = 20 kHz) to over 10 MΩ (frequency = 20 Hz). At time t = 0 after the skin cream was applied, the skin impedance instantaneously falls down to few kΩ (frequency = 20 kHz) and to around 5MΩ (frequency = 20 Hz). After time t = 20, 40 and 60 minutes, skin impedance had a general trend to increase back to the status of the bare skin impedance. However there is a fluctuation of skin impedance in Figure 4.14 which might be due to sweat gland activity [65].

Therefore, in order to investigate the effect of the electrodes on skin, the results from a second site are shown in Figure 4.15. Instead of measuring skin impedance every 20 minutes, skin impedance was measured only one time after skin cream (Nivea) application at t = 60 minutes.

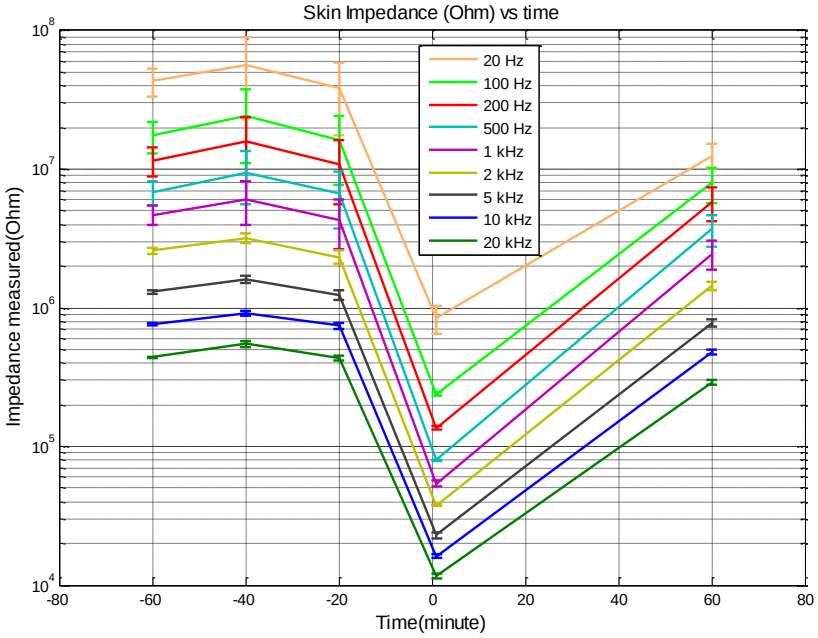


Figure 4.15: Non continuous contact visits only one visit after skin cream (Nivea) application for 60 minutes (volunteer 1 group B).

In Figure 4.15, skin impedance after the drop down at t = 0 minute, increased dramatically after t = 60 minutes. The results showed that the electrodes connected to the skin had a small effect (10% difference) on the skin impedance, which could be caused by sweat glands.

According to Figure 4.14 and Figure 4.15, several conclusions can be drawn. Firstly, continuous contact of electrodes on skin can affect the change in skin impedance because the water contained at the measurement location can be attracted or diffused around skin layers due to the sweat glands. The second conclusion is that skin

impedance dropped down significantly and rapidly after the skin cream application compared with bare skin impedance.

4.4.3 Short term skin impedance with continuous contact of electrodes:

One of the short term experiments conducted was with continuous contact of electrodes on skin as effects of inaccurate placement of electrodes could be removed. However, the results were not reliable (compared with non-continuous contact) since the continuous contact from electrodes attracted moisture from deeper tissue to the stratum corneum and interfered with the skin properties. The results from continuous contact with electrodes are given in Appendix I.

4.5 Long term measurement

Similar to the short term experiments, long term measurements have been conducted to further investigate how long the effect of different moisturizers persisted on human skin. Three skin moisturizers: Bio-oil, Cocoa and Nivea are applied to three adjacent sites of the arm. The fourth adjacent place is used to measure the bare skin as the reference. The probe was removed between measurements. The baseline of skin impedances were measured on all four sites of the arm before applying the skin creams.

At each moment in time, there were four parallel measurements taken at the four different locations i.e. three different creams and bare skin. In total, for long term measurement, there were 44 measurements taken on each volunteer evenly spaced over 5 hours.

4.5.1 Long term bare skin impedance

Figure 4.16 shows the bare skin impedance measurement results for 5 hours on one volunteer.

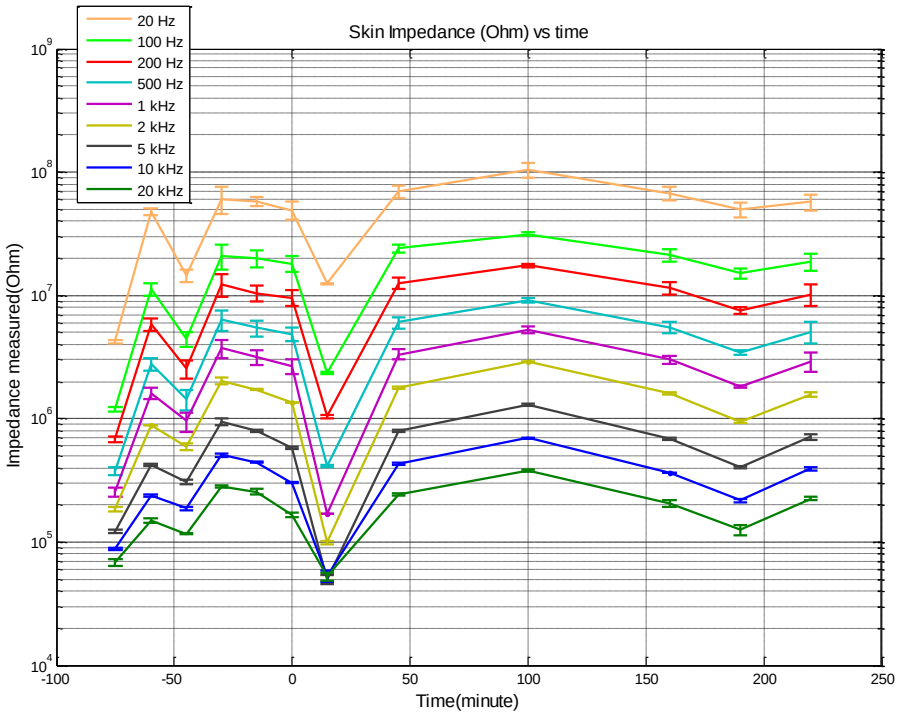


Figure 4.16: Long term measurement with bare skin (volunteer 1 group C).

As seen in Figure 4.16, the baseline skin impedance measured was in the frequency range from 20 Hz to 20 KHz. Skin impedance results fluctuated not only at high frequencies but also at low frequencies. However, there is no large drop or increase in impedance when the nearby other sides have skin cream applied. The fluctuation in skin impedance could possibly be explained by sweat activity changes during the day.

4.5.2 Long term skin impedance using Nivea

Figure 4.17 shows the skin impedance measurement results using Nivea measured for 5 hours on volunteer 1 (group C).

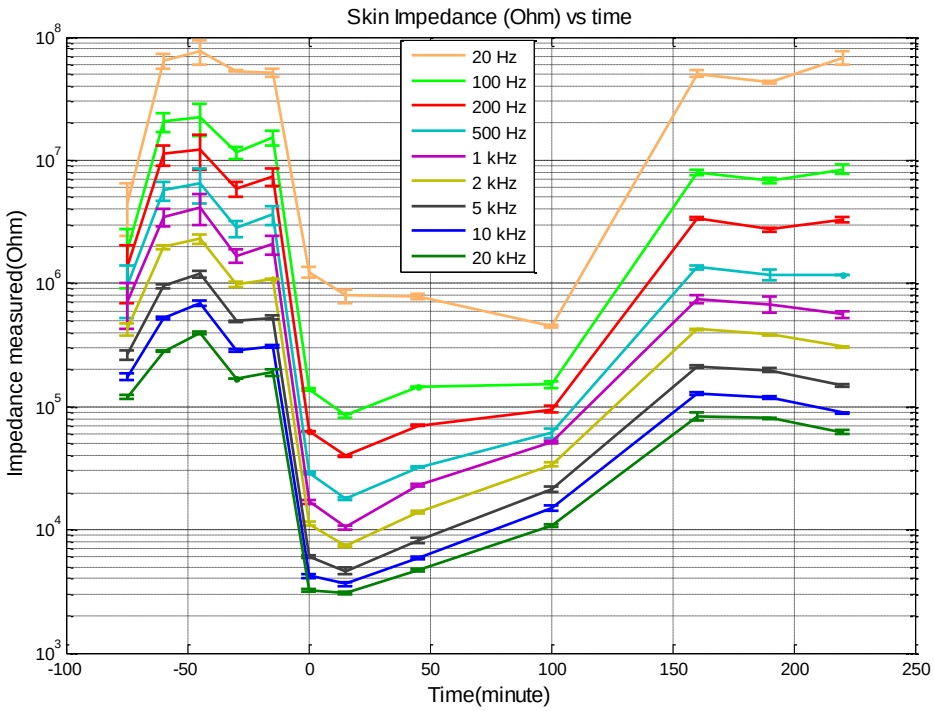


Figure 4.17: Long term measurement with Nivea (volunteer 1 group C).

In Figure 4.17, the base line skin impedance was measured five times before the skin cream application and was in the range from around 200-300 kΩ (frequency at 20 kHz) to over 70-80 MΩ (frequency at 20 Hz). At time t = 0 after the skin cream was applied, the skin impedance instantaneously fell down to about 3 kΩ (frequency at 20 kHz), 4 kΩ (at frequency 10 kHz), 6 kΩ (at frequency 5 kHz), 10 kΩ (at frequency 2 kHz), 17 kΩ (at frequency 1 kHz), 30 kΩ (at frequency 500 Hz), 60 kΩ (at frequency 200 Hz), 150 kΩ (at frequency 100 Hz) and to around 1MΩ (frequency at 20 Hz). After t = 15, 45 and 100 minutes, the skin impedance gradually increased back towards the status of the bare skin impedance. Again, a large variation of skin impedance was seen in the low frequency range. In the high frequency range above 1 kHz, skin impedance results mostly increased with respect to time. After t = 160 minutes, skin impedance results showed that a stable level was being approached. From t = 160 to 220 minutes, there was no large change in skin impedance. At t = 220 minutes the impedance values had returned to approximately 75-80% of the bare

skin impedance level illustrating possibly that the moisturizer was still having a small effect on the skin. Another reason could be that sweat glands or even physiological changes during the day make the return to the bare skin point not possible.

4.5.3 Long term skin impedance using Cocoa:

Figure 4.18 illustrates the skin impedance measurement results using Cocoa measured for 5 hours on one volunteer.

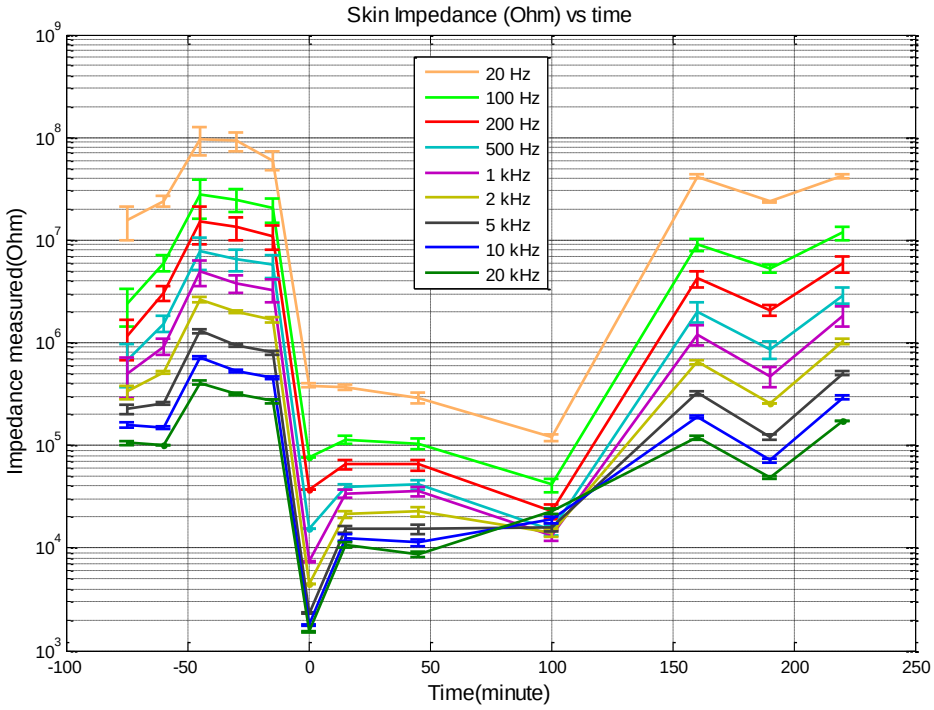


Figure 4.18: Long term measurement with Cocoa butter (volunteer 1 group C).

As seen in Figure 4.18, the baseline skin impedance was in the range from around 100-300 kΩ (frequency = 20 kHz) to over 80 MΩ (frequency = 20 Hz). Similar to the results for Nivea, at t = 0 after the skin cream was applied, the skin impedance decreased sharply. After t = 15, 45 and 100 minutes, the skin impedance had a general trend to return back to the status of the bare skin impedance. At t = 160

minutes, the skin impedance result returned to 80% of the bare skin impedance and fluctuated up to t = 220 minutes.

4.5.4 Long term skin impedance using Bio-oil:

Figure 4.19 illustrates the skin impedance measurement results using Bio-oil measured for 5 hours on volunteer 1 (group C).

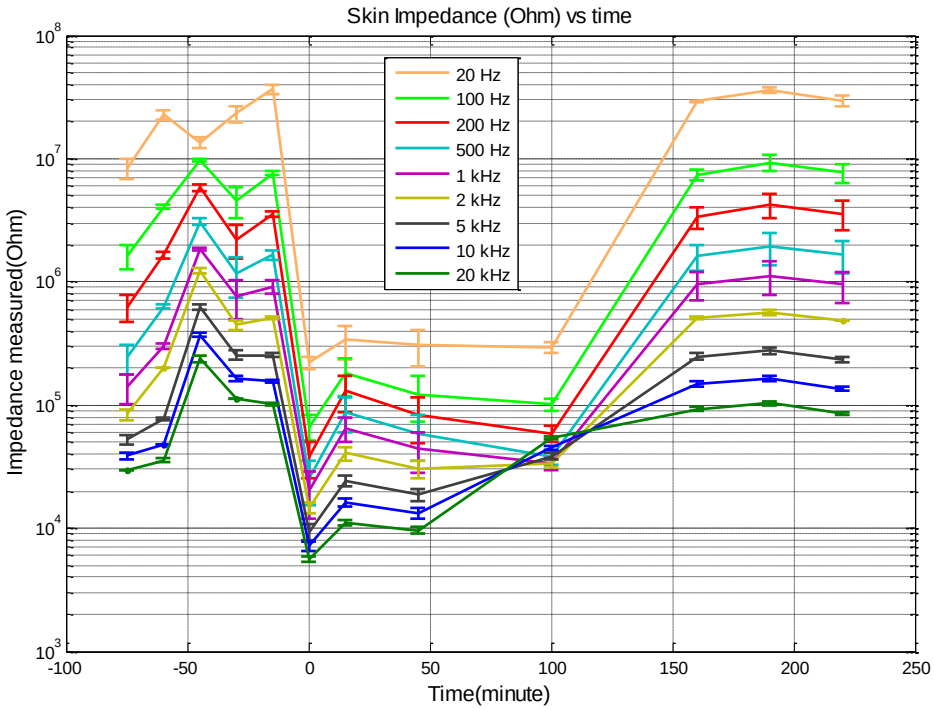


Figure 4.19: Long term measurement with Bio-oil (volunteer 1 group C).

In Figure 4.19, the bare skin impedance measured before the skin cream application was in the range from around 40-200 kΩ (frequency at 20 kHz) to over 20 MΩ (frequency at 20 Hz). At t = 0 after Bio-oil was applied, the skin impedance instantaneously decreased in value. After t = 15, 45 and 100 minutes, the skin impedance had a trend to return back to the status of the bare skin impedance. However the fluctuation of skin impedance was also seen in Figure 4.19, which could be possibly attributed to the sweat glands or physiological effects. At time t = 160 minutes, the skin impedance value returned to the baseline bare skin impedance

and maintained a relatively constant level up to t = 220 minutes. It indicates that the effect of Bio-oil on skin has been significantly reduced.

The long term measurements were conducted on five different volunteers (group C) and the results for all 5 volunteers are shown in Appendix F. The summarized table of impedance results in long term measurement at frequency 1 KHz from 5 volunteers is given in table 4.3.

Long term measurement at 1KHz on volunteer 1								
	Bare skin		Cocoa		Nivea		Bio-oil	
Time (min)	Mean	SD	Mean	SD	Mean	SD	Mean	SD
t = -80	254kΩ	±22.9kΩ	503kΩ	±209kΩ	717kΩ	±294kΩ	139kΩ	±38.2kΩ
t = -10	3.16MΩ	±418kΩ	3.29MΩ	±838kΩ	2.07MΩ	±377kΩ	920kΩ	±112kΩ
t = 0	2.65MΩ	±374kΩ	7.37kΩ	±18Ω	16.8kΩ	±536Ω	20.4kΩ	±8.3kΩ
t = 15	3.33MΩ	±302kΩ	33.9kΩ	±2.8kΩ	10.4kΩ	±264Ω	65.4kΩ	±14kΩ
t = 100	5.26MΩ	±305kΩ	13.2kΩ	±1.6kΩ	51.5kΩ	±1.6kΩ	33.4kΩ	±3.9kΩ
t = 220	2.91MΩ	±530kΩ	1.85MΩ	±410kΩ	562kΩ	±35kΩ	947kΩ	±266kΩ

Long term measurement at 1KHz on volunteer 3								
	Bare skin		Cocoa		Nivea		Bio-oil	
Time (min)	Mean	SD	Mean	SD	Mean	SD	Mean	SD
t = -80	1.26MΩ	±404kΩ	115kΩ	±40kΩ	58.3kΩ	±12kΩ	236kΩ	±74.5kΩ
t = -10	856kΩ	±259kΩ	1.23MΩ	±376kΩ	372kΩ	±113kΩ	1.28MΩ	±510kΩ
t = 0	1.11MΩ	±375kΩ	9kΩ	±29Ω	27.8kΩ	±1.2kΩ	148kΩ	±28.8kΩ
t = 15	648kΩ	±190kΩ	30.2kΩ	±2.5kΩ	7.2kΩ	±298Ω	232kΩ	±81.3kΩ
t = 100	1.93MΩ	±624kΩ	43.9kΩ	±5.2kΩ	10kΩ	±417Ω	387kΩ	±119kΩ
t = 220	1.04MΩ	±342kΩ	33.2kΩ	±3.8kΩ	111kΩ	±13.5kΩ	269kΩ	±100kΩ

Long term measurement at 1KHz on volunteer 2								
	Bare skin		Cocoa		Nivea		Bio-oil	
Time (min)	Mean	SD	Mean	SD	Mean	SD	Mean	SD
t = -80	843kΩ	±586kΩ	2.8MΩ	±485kΩ	700kΩ	±68kΩ	4.2MΩ	±1.08MΩ
t = -10	2.14MΩ	±461kΩ	1.91MΩ	±558kΩ	367kΩ	±20kΩ	1.2MΩ	±195kΩ
t = 0	2.66MΩ	±422kΩ	10kΩ	±467Ω	15kΩ	±100Ω	59kΩ	±7.6kΩ
t = 15	2.54MΩ	±526kΩ	7.8kΩ	±118Ω	25.6kΩ	±2.5kΩ	17.3kΩ	±4.1kΩ
t = 100	1.95MΩ	±220kΩ	1.11MΩ	±194Ω	732kΩ	±46.2kΩ	438kΩ	±8.3kΩ
t = 220	341kΩ	±9kΩ	878kΩ	±106kΩ	496kΩ	±92kΩ	431kΩ	±36.4kΩ

Long term measurement at 1KHz on volunteer 4								
	Bare skin		Cocoa		Nivea		Bio-oil	
Time (min)	Mean	SD	Mean	SD	Mean	SD	Mean	SD
t = -80	407kΩ	±116kΩ	708kΩ	±305kΩ	3.72MΩ	±314kΩ	3.6MΩ	±412kΩ
t = -10	3.72MΩ	±414kΩ	849kΩ	±395kΩ	4.67MΩ	±740kΩ	1.16MΩ	±524kΩ
t = 0	4.3MΩ	±1.6MΩ	7kΩ	±51Ω	16.8kΩ	130Ω	46.2kΩ	±1.4kΩ
t = 15	3.6MΩ	±582kΩ	38.5kΩ	±4.3kΩ	92.5kΩ	±2.8kΩ	226kΩ	±83kΩ
t = 100	3.18MΩ	±344kΩ	86.3kΩ	±26.4kΩ	74.5kΩ	±7.4kΩ	355kΩ	±102kΩ
t = 220	3.70MΩ	±410kΩ	1.4MΩ	±463kΩ	61.4kΩ	±2.7kΩ	834kΩ	±466kΩ

Long term measurement at 1KHz on volunteer 5								
	Bare skin		Cocoa		Nivea		Bio-oil	
Time (min)	Mean	SD	Mean	SD	Mean	SD	Mean	SD
t = -80	1.09MΩ	±399kΩ	198kΩ	±66kΩ	240kΩ	±11.3kΩ	147kΩ	±5.8kΩ
t = -10	1.22MΩ	±404kΩ	1.38MΩ	±295kΩ	166kΩ	±2.3kΩ	125kΩ	±932Ω
t = 0	156kΩ	±16.4kΩ	9.7kΩ	±513Ω	17.5kΩ	±10kΩ	46.9kΩ	±160Ω
t = 15	204kΩ	±53kΩ	17.4kΩ	±74Ω	46.7kΩ	±4.1kΩ	108kΩ	±8.5kΩ
t = 100	153kΩ	±20.5kΩ	59.3kΩ	±3.4kΩ	143kΩ	±15kΩ	1.29MΩ	±498kΩ
t = 220	120kΩ	±16kΩ	157kΩ	±2.8kΩ	203kΩ	±82kΩ	947kΩ	±347kΩ

Table 4.3: Summarized table of impedance results in long term measurement at frequency 1 KHz from 5 volunteers.

4.5.5 Summary of long term monitoring

Generally, in long term monitoring, there are three periods of skin impedance results: first period: before skin cream application t = -75 minutes. Second period: start of the moisturizers application t = 0 minutes, and the third period: after skin cream application up to t = 220 minutes. It is expected that the return times to baseline are different among volunteers and for different skin creams.

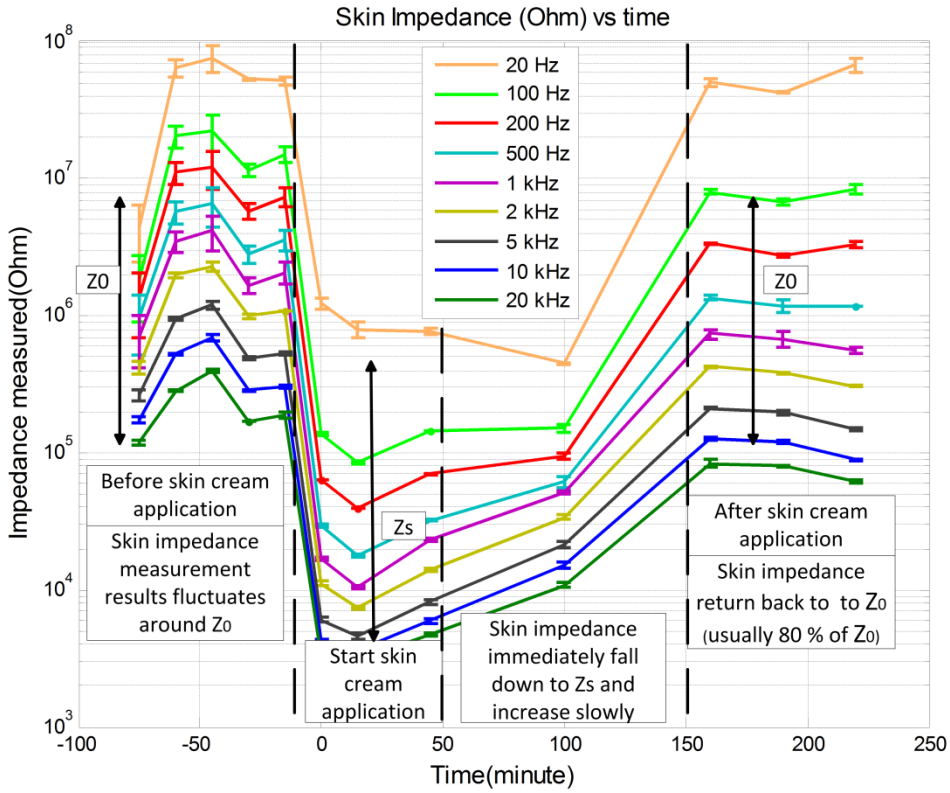


Figure 4.20: Timing diagram long term skin impedance result using moisturizer

In Figure 4.20, the timing diagram shows the process of skin impedance change throughout the experiment. Before the moisturizers application, the skin impedance fluctuates around the initial impedance value called Z_0. Then, after the skin cream has been applied, the skin impedance rapdly falls down to the impedance value Z_S. The skin impedance values then start to increase and return back to at least 80% of the initial impedance value Z_0.

Therefore, according to the long term measurement results which are all included in Appendix F, in comparison among moisturizers used with long term measurements protocol, there are several conclusions to be drawn. Firstly, all moisturizers decreased the skin impedance immediately after being applied to the skin and the effect reduces with time. Secondly, Bio-oil produced a higher skin impedance value than Nivea and Cocoa in the high frequency above 1 kHz. Thirdly, the return time to the baseline was different between volunteers. This indicates that the temporal effect of the moisturizer depends on skin type of different volunteers.

Therefore, it is worth investigating the moisturizer effect time comparison between skin creams on different volunteers to see if any particular cream wears off more quickly than others.

A summary of time returning to 80% of original impedance baseline between volunteers using different creams is given in Figure 4.21.

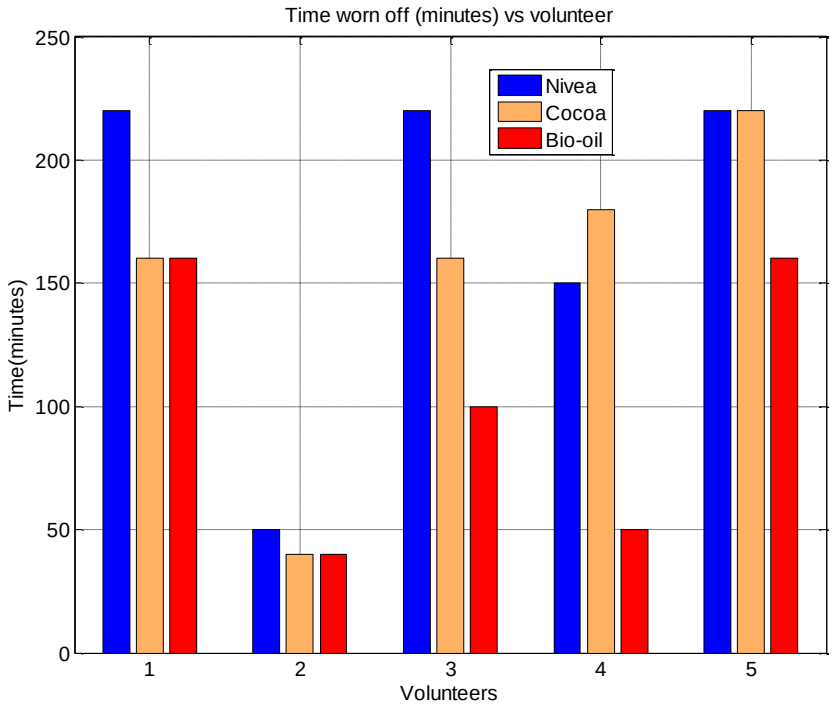


Figure 4.21: Return to 80% baseline for different volunteers using three different skin creams (group C).

As shown in Figure 4.21, through five different volunteers, the Nivea cream effect appears to be longest lasting compared to the two other moisturizers. For example, in volunteer 3, the effect of Nivea on skin lasted up to 220 minutes whilst Bio Oil lasted only 100 minutes. In addition, it can be seen that the time rate order always remained the same between volunteers i.e. Nivea, Cocoa and the shortest was Bio Oil. With patient 2, Bio Oil only appeared to last for 40 minutes before the impedance returned to the baseline value.

4.6 Discussion

Table 4.4 shows a summary of conclusions from three experiments presented in this chapter namely: instantaneous measurement; short term measurements; and long term measurements.

	Materials & Methods	**Results and discussion**
Instantaneous measurement	Measure the effect of different moisturizers immediately after applied skin creams on 10 volunteers. Four different skin creams: Nivea, Cocoa Butter, Olive Butter and Bio-oil. Room temperature kept constant at 20˚C.	- Bio-oil gave the impedance results quite similar to bare skin impedance, whilst Nivea, Cocoa and Olive Butter significantly reduced skin impedance. - Olive and Cocoa have similar effect on skin impedance. - Nivea gave the lowest impedance results while Bio-oil gave the highest amongst the

		four skin creams. -The skin creams except for Bio Oil stabilized in the Z, phase and real vs imaginary plot. - Skin impedance varies greatly between people.
Short term measurement	**First experiment:** Bare skin impedance versus skin temperature with respect to time. No skin cream used on the skin. Room temperature kept constant at 20˚C. Measurements were taken for 4 hours.	- Skin temperature variation of 1˚C did not affect the variation in skin impedance. - It is observed that bare skin impedance fluctuates as a function of time (possibly due to sweat activity or physiological changes).
	Second experiment: Measure the effect of moisturizers on skin for 2 hours. Three skin creams used: Nivea, Cocoa and Bio-oil. Bare skin impedances were measured before skin cream application for 60 minutes. Room temperature kept constant at 20˚C.	- Skin impedance dropped down greatly and rapidly after the skin cream application compared with bare skin. - Skin impedances tend to return to the baseline impedance after the time of skin cream application.
Long term measurement	Intermittently measure the effect of moisturizers on skin for 5	- All moisturizers decreased skin impedance rapidly after

	hours. Three skin creams used: Nivea, Cocoa and Bio-oil. Bare skin impedances measured before skin cream application for 80 minutes. Room temperature kept constant at 20˚C.	application and the effect reduces with time. - Bio-oil gave the highest skin impedance result for frequencies above 1 kHz. - Skin impedance returned to bare skin impedance value after the skin cream application. - However, the return times to the baseline were different from volunteer to volunteer.

Table 4.4: Summary of conclusions from impedance results in different experiments using skin moisturizers.

Instantaneous measurement results on 10 volunteers (group A) using different moisturizers										
	Bare skin (N = 10)		**Cocoa (N = 10)**		**Olive (N = 10)**		**Nivea (N = 10)**		**Bio-oil (N = 10)**	
Frequency	Mean	SD	Mean	SD	Mean	SD	Mean	SD	Mean	SD
20Hz	1.25MΩ	±629kΩ	101kΩ	±98kΩ	72kΩ	±49kΩ	40kΩ	±40kΩ	1.5MΩ	±3.3MΩ
200Hz	339kΩ	±414kΩ	71kΩ	±57kΩ	53kΩ	±33kΩ	32kΩ	±30kΩ	483kΩ	±1.3MΩ
2KHz	94kΩ	±173kΩ	26kΩ	±12kΩ	26kΩ	±9.8kΩ	17kΩ	±10kΩ	93kΩ	±208kΩ
20KHz	30kΩ	±56kΩ	3kΩ	±2kΩ	3.5kΩ	±1.4kΩ	3.9kΩ	±1.4kΩ	31kΩ	±60kΩ
100KHz	10kΩ	±17kΩ	360Ω	±107Ω	346Ω	±201Ω	663Ω	±483Ω	11kΩ	±17kΩ

Short term measurement results on 2 volunteers (group B) using different skin cream @ 1KHz			
Skin creams	**time (min)**	**mean**	**SD**
bare skin (N = 2)	t = -60	453kΩ	±116kΩ
	t = 0	2.9MΩ	±1.36MΩ
	t = 60	2.49MΩ	±1.65MΩ
Nivea (N = 2)	t = -60	1.13MΩ	±267kΩ
	t = 0	24.3kΩ	±1.6kΩ
	t = 60	302kΩ	±6.4kΩ
Cocoa (N = 2)	t = -60	4.67MΩ	±740kΩ
	t = 0	54.1kΩ	±2.6kΩ
	t = 60	2.45MΩ	±584kΩ

Long term measurement results on 5 volunteers (group C) using different skin cream @ 1KHz			
Skin creams	**time (min)**	**mean**	**SD**
bare skin (N = 5)	t = -80	770kΩ	±305kΩ
	t = 0	2.17MΩ	±557kΩ
	t = 220	1.62MΩ	±261kΩ
Cocoa (N = 5)	t = -80	864kΩ	±221kΩ
	t = 0	8.6kΩ	±215Ω
	t = 220	863kΩ	±197kΩ
Nivea (N = 5)	t = -80	1.08MΩ	±139kΩ
	t = 0	18.7kΩ	±2.4kΩ
	t = 220	286.7kΩ	±45kΩ
Bio-oil (N = 5)	t = -80	1.66MΩ	±322kΩ
	t = 0	64.1kΩ	±9.2kΩ
	t = 220	685kΩ	±243kΩ

Table 4.5: The highlight of impedance results in different experiments using skin moisturizers.

4.7 Conclusions

In instantaneous measurement, different moisturizers gave different skin impedance results. Moreover, from the values of impedance measurements one can tell the characteristics of the moisturizer i.e. the Bio-oil gave the highest impedance results compared with other creams; Cocoa Butter and Olive Butter cream had similar skin

impedance effect on skin, and finally Nivea cream gave the lowest impedance. Therefore different chemical substances in the skin creams can create different effects on frequency measurements. The impedance results can discriminate the differences between Bio-oil (Type I) and other moisturizers Nivea, Olive and Cocoa (Type II). Phase results demonstrated additional capacitance effects of Bio-oil compared to other moisturizers. The skin impedance values had a smaller variance than bare skin when all skin creams were applied with the exception of Bio Oil. Furthermore the Bio Oil maintained a CPE type characteristic matching the bare skin whilst the creams Nivea, Cocoa and Olive all showed classical RC behaviour having no CPE.

For short term measurement and long term measurement, several findings had been shown:

- Bare skin impedances fluctuates with time due to possible sweat gland activity or physiological change

- Skin cream immediately affects skin impedance after application

- Skin cream effects reduce with time and the skin impedance tends to return towards the bare skin impedance (or baseline skin impedance).

In conclusion, measuring skin impedance has the potential to verify the effects of the cream on skin. Different creams will have different effects on human skin and therefore understanding skin cream and skin impedance attempts to answer these questions about the skin cream effects. Through these experiments, it is also suggested that a potential custom made bio-impedance analyzer is suitable for home monitoring.

Chapter 5 Data Analysis and Modelling

5.1 Introduction

This Chapter discusses the possible electrical skin impedance models that can be used to fit with practical results. Section 5.2 – 5.3 provides an introduction to biological skin layers, an overview of several skin impedance models, proposed skin impedance modelling and simulation methods. Section 5.4-5.6 compares simulation models with practical results, discussion and indicates the limitations of the models respectively.

5.2 Skin impedance model

5.2.1 Biological Skin Layers

Skin models ideally need to take into account sweat glands, frequency dispersion, hydration and dehydration. It is useful to obtain an electrical equivalent model of skin that has the same frequency characteristics as skin tissue. These models come with different components representing the electrical properties of different layers of the skin.

Human skin is a complex structure containing different layers as illustrated in Figure 5.1[106]

a) Stratum Corneum: this outer layer is called the horny layer and contains fully keratinized, dead cells (corneocytes). This outer-most contains a dense layer of keratin, which can be removed by abrasion. The purpose of the stratum corneum is to form a barrier to protect underlying tissue from infection, dehydration, chemical and mechanical stress.

b) Granular layer (Stratum granulosum): This layer contains flattened cells. It is the transitional stage between the cells of the stratum spinosum and the stratum corneum. These cells have a shrivelled shape.

c) Spinous layer (Stratum spinosum): This layer is composed of cells which have a rounded shape. These cells are loosely packed together and connected by bridges. Clefts exist between the cells.

d) Basal layer (Stratum basale): This layer is composed of a single row of columnar-shaped cells.

f) Dermis: This layer (below the basement membrane) is composed of dense, fibrous connective tissue.

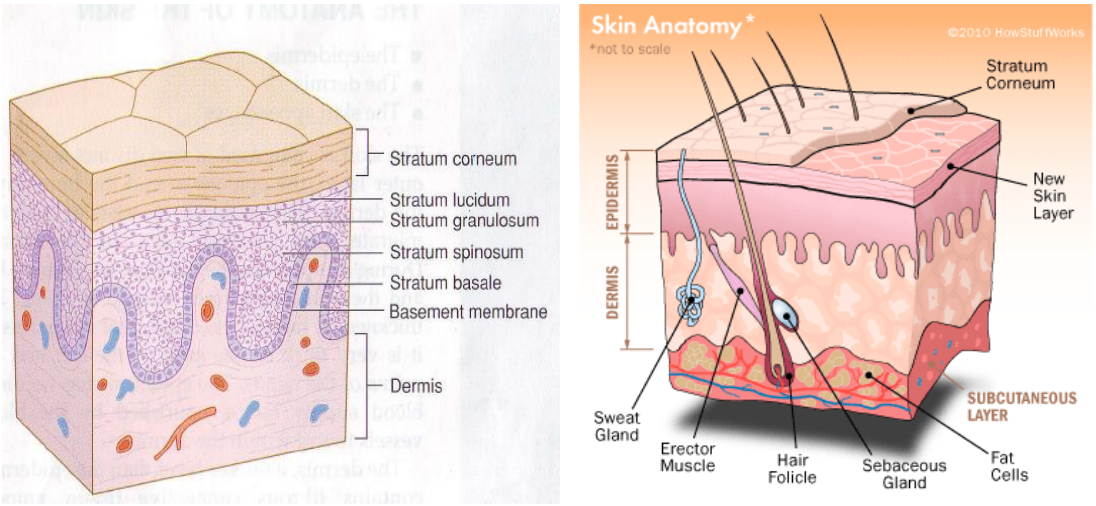


Figure 5.1: The five biological layers of the human skin [106]

In general, it is difficult to electrically model in detail all of these layers of the human skin. The lumped element models, however, cannot totally match the requirement of both theory and experimental measurements. Instead of deploying a very detailed model of the human skin, the models have been chosen to aid comparison with measurements.

5.2.2 Overview of several skin models

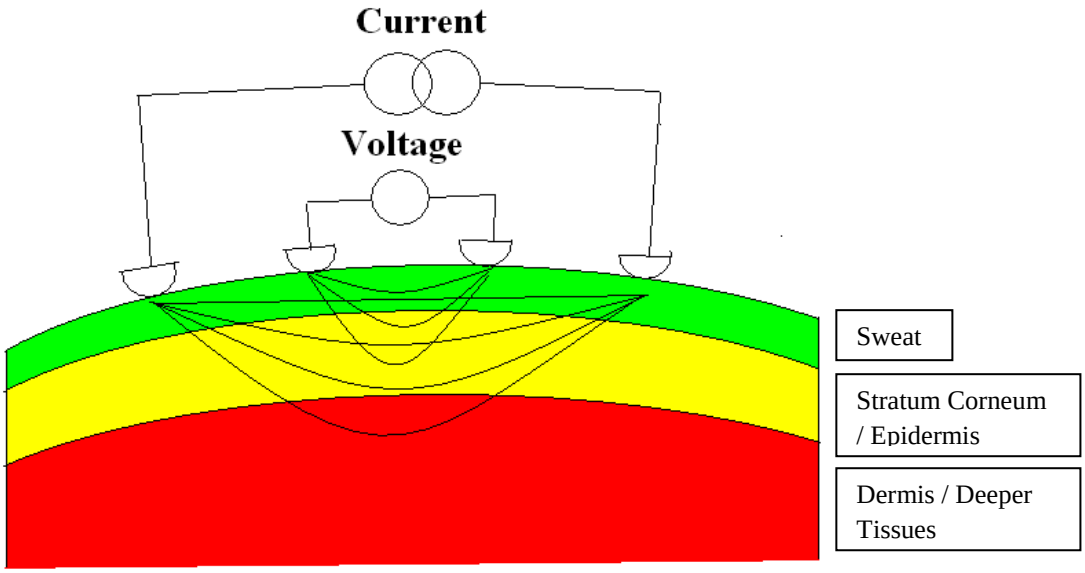


Figure 5.2: General schematic physiological modelling for skin impedance measurement

In Figure 5.2, the four point probe measurement technique has been modelled by using a current source for the two outer probes and two inner probes to measure the voltage drop. Skin layers are illustrated; such as sweat (green layer), stratum corneum/ epidermis (yellow layer) and dermis/ deeper tissue (red layer).

For more details of modelling skin layers, some suggested models have been reported in the literature such as the resistor and capacitor model shown in Figure 5.3 by Baba and Burke [107].

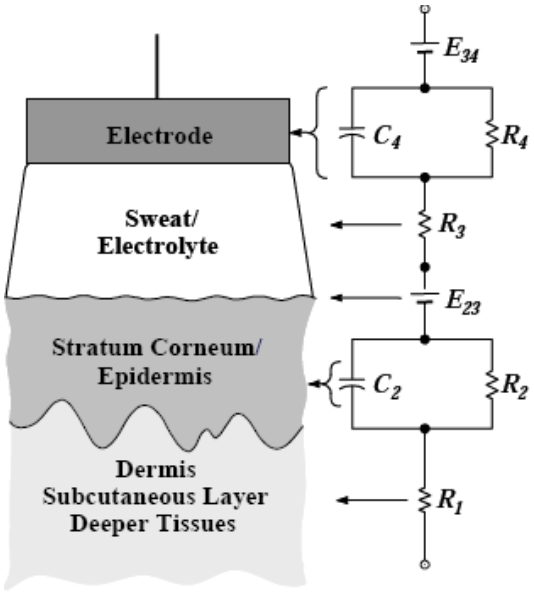


Figure 5.3: Skin-electrode interface and its electrical equivalent circuit [107]

In this model, the resistor R_4 in parallel with the capacitor C_4 models the electrode impedance and R_3 is the model for the sweat or electrolyte interface of a conventional ECG electrode. C_2 and R_2 in parallel model the stratum corneum and epidermis. Finally, the dermis or deeper tissue is modelled by R_1.

An alternative model using variable resistors and capacitors is shown in Figure 5.4 by Ruiz [108].

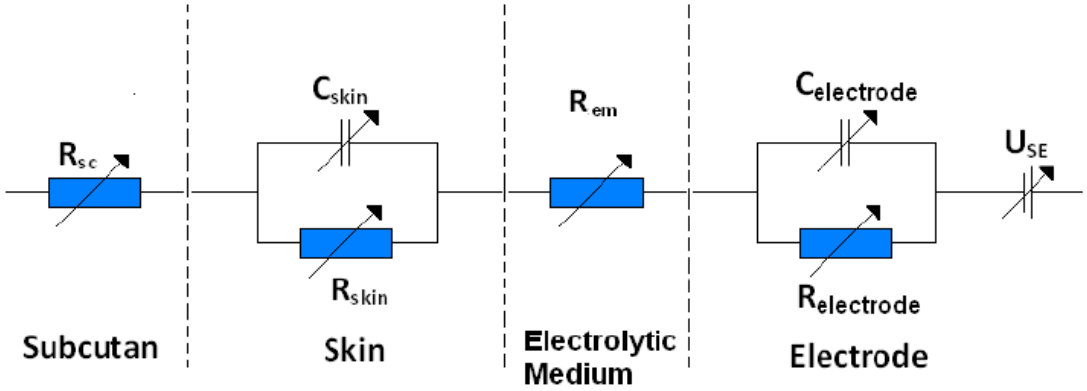


Figure 5.4: Model illustrating the electrical behaviour of the skin-electrode contact [108]

In the model in Figure 5.4, the skin is made of three principal layers: the epidermis, the dermis and a subcutaneous layer. Ruiz [108] used a variable resistor $R_{electrode}$ in

parallel with a variable capacitor $C_{electrode}$ to model electrode impedance. For electrolytic medium (and/or sweat) and subcutan (deeper tissue), only a variable resistor (R_{em} and R_{sc}) was used.

The parallel circuit of R_{skin} and C_{skin} illustrates the epidermis, specifically the stratum corneum. This upper skin layer consists of dead cells that have a large contribution to the total impedance. The dermis and the subcutaneous layer contains a resistive component, therefore they are represented as Rsc in this model. Compared with the first model in Figure 5.3 which used simple resistor and capacitor, the variable resistors and capacitors (in Figure 5.4) can represent the changes in the human skin such as sweat and hydration. However, it may not represent all the frequency response characteristics of the human skin.

A CPA (Constant Phase Angle) model [58], introduced in Chapter 2, has also been used instead of variable resistors and capacitors as shown in Figure 5.5.

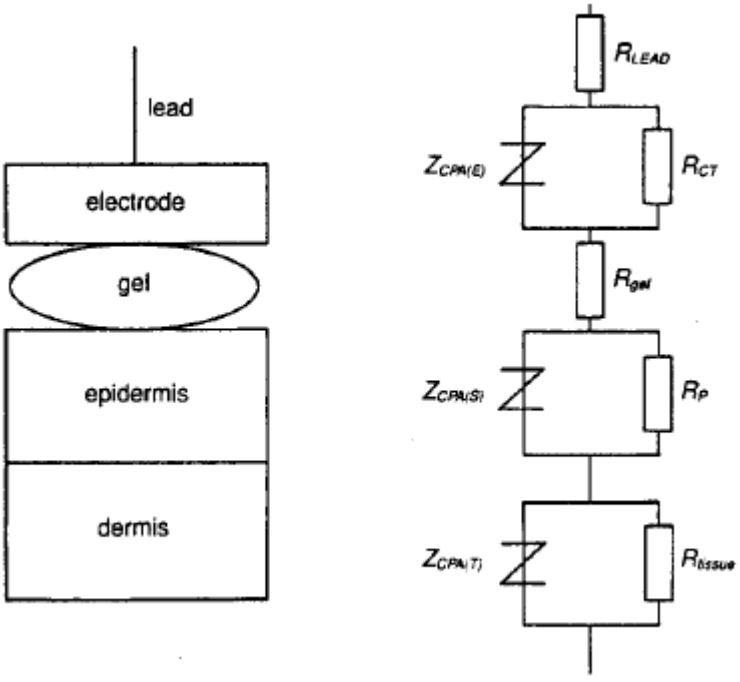


Figure 5.5: Equivalent circuit model of the skin using CPA model [58].

In Figure 5.5, CPA models were used for electrode impedance, epidermis and dermis impedance. The aim was to express the frequency response characteristic of different layers of skin. In the different layers, there are different CPA components and resistors. For the electrode impedance $Z_{CPA(E)}$ is in parallel with R_{CT}. For the epidermis impedance $Z_{CPA(S)}$ is in parallel with R_p, and for the dermis impedance $Z_{CPA(T)}$ is in parallel with R_{tissue}. CPA models give more flexibility in modelling the human skin as they have a better frequency response representation of the skin when compared with a normal resistor and capacitor network.

The Cole model has been used widely to express the frequency response of biological tissue in general and also specifically skin tissue. In the next model, Martinsen [1] used the Cole equations to model all skin impedance layers as shown in Figure 5.6.

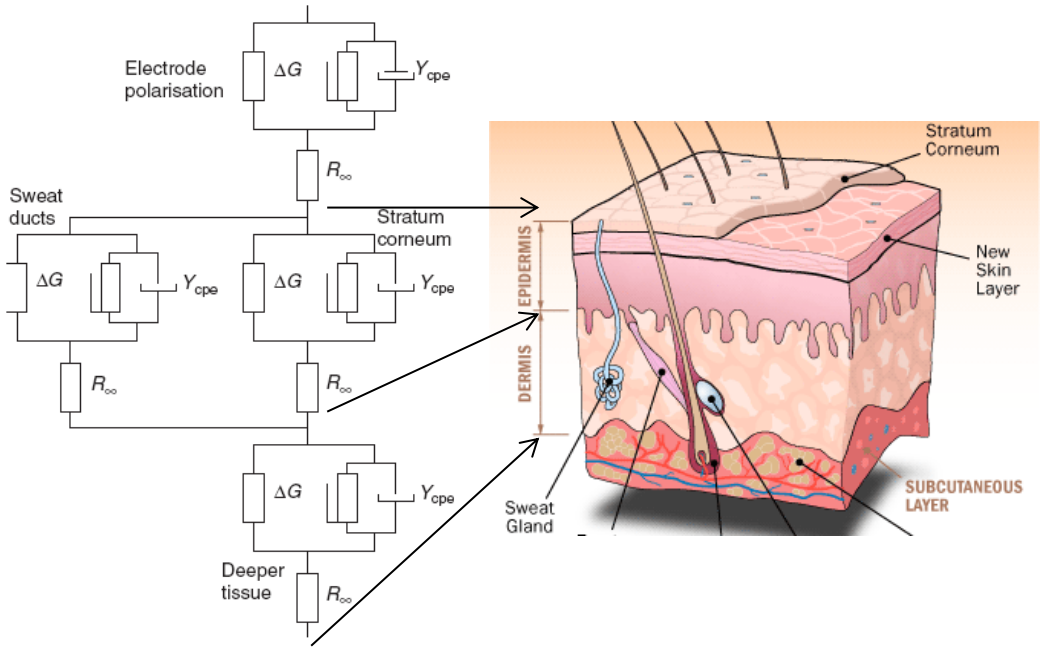


Figure 5.6: Assembly of Cole systems for measurements on skin and illustration of sweat glands [1].

In the Cole model [1], R_∞ is the resistance at high frequency, R_0 is the resistance at low frequency, and $(j\omega\tau_z)^\alpha$ represents an equivalent CPE Y_{cpe}, which consists of both

a frequency dependent resistor and capacitor, together with constant α which represents the exponent factor in a constant phase expression such as $j^{\alpha} = \cos(\alpha\pi/2) + j*\sin(\alpha\pi/2)$.

By introducing $R_0 - R_\infty = 1/\Delta G$ the Cole equation becomes

$$Z = R_\infty + \frac{1}{\Delta G + \Delta G(j\omega\tau_z)^{\alpha}} \qquad (5.2.1)\ [1]$$

In Figure 5.6, the Cole model [1] has been used to model all the skin including the electrodes polarization impedance, sweat ducts, stratum corneum, and deeper tissues. The sweat ducts (or sweat glands) are arranged to be in parallel with the stratum corneum (see in Figure 5.6) instead of in series like in previous models. Grimnes [63] suggested that if the measurement was conducted with biomaterial like human skin in vivo, the impedance model is a good starting point with stratum corneum modelled by CPE together with ideal conductance modelled by ΔG that controls the magnitude of CPE.

However, Grimnes and Martinsen also informed the limitation of Cole models as when the ΔG affects the magnitude of the CPE then the Cole equation does not allow an independent variable DC conductance in parallel with the CPE without disturbing the components of the CPE [1].

In general, there is a need to construct a whole model system for skin tissue measurement using the four point probe technique. The model should be derived from the four electrode interfaces to deeper tissue layer including the stratum corneum, sweat glands, epidermis, and dermis. One approach showing an electrical impedance model of skin layers and measurement system is illustrated in Figure 5.7.

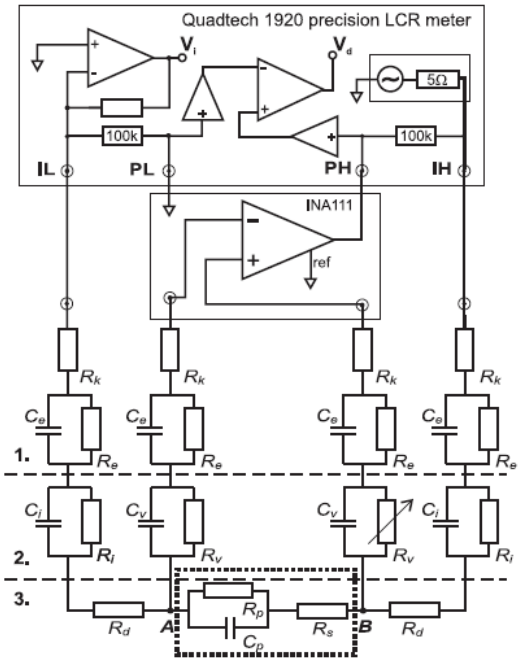


Figure 5.7: Electrical model of skin and electrodes connected to an instrumentation amplifier interface and the LCR-meter. The first part of the model corresponds to electrode impedances, the second to stratum corneum and the third to deeper viable tissues [109].

In Figure 5.7, the author modelled a whole skin impedance system including three different layers: electrode impedance, stratum corneum and deeper tissue. The electrodes' impedance is modelled by a three component model 2R-1C (C_e in parallel with R_e and both in series with R_k). The stratum corneum is represented by a two component model RC (R_i parallel with C_i or R_v parallel with C_v). Finally, the deeper tissue is illustrated as a three component model 2R-1C (C_p in parallel with R_p and both in series with R_s).

5.2.3 Proposed skin models

Through these models from the previous section, there are several main models used for modelling the skin impedance such as the two component model, three component model, CPE model and Cole model containing CPEs (refer to Chapter 2).

The interface between the skin and electrodes can be modelled as a resistor and capacitor network (RC in parallel). The contact between the metallic electrode and skin can be modelled as a resistor. However, the contact area between metal and skin acts likes a capacitor due to the ion-electron exchange with two different layers of charges. Therefore, its interface can be best represented as resistor R_p in parallel with capacitor C_p. There is no model for gel/electrolyte in the proposed model as gel/electrolyte was not used in the experiments.

In the next layer, the sweat, which is created by the sweat ducts, is a resistive component and can be represented as impedance Z_w. The sweat highly depends on the properties of the environment such as temperature and humidity. Therefore, the impedance can be a low value (hot or humid condition) or a high value (cold or dry condition). Usually, the sweat secretes on the surface of the stratum corneum.

The next layer is the stratum corneum / epidermis. This layer has a large contribution to the skin impedance. The stratum corneum / epidermis can be represented as a Cole model containing a CPE component Z_{cpe}, a subtraction value $\Delta R = R_0 - R_\infty$ taken from a resistance value at low frequency R_0 and a resistance value at high frequency R_∞. The stratum corneum and epidermis could be separated into two different model layers. It means that the stratum corneum can be modelled as one Cole model containing a CPE and the epidermis can be modelled as another Cole model with a CPE.

The final layer is the dermis that consists of mostly connective tissue. This dermis layer has resistive electrical properties in biological tissue. Therefore, the dermis layer can be model as a resistor R_∞.

Although more sophisticated layered models (as described above) have been developed, simplified models have been widely used to fit to measured data due to ease of use and simplicity. For example, Brown et al [7] had a modified Cole model (with only three electrical elements R (resistor), S (resistor) and C(capacitor)) in order to fit with his data from cervical cancer results. Yamamoto [17] also combined the stratum corneum layer (modelled by R_2 // C_2) and deep tissue (modelled by R_1 // C_1) into equivalent circuits of total impedance (R_p // C_p). Martinsen and Grimnes [63] also used the simplified model to fit with measured data. Other examples of using simplified models to fit with measurement results can be found by Ferreira [110] and Dorgan [111]. Hence, for comparison with skin measurement results, only specific models are chosen to try fitting. i.e. skin models with/without CPE.

Based on the application of the above simplified models, the following five models have been selected to fit to the measured data of this thesis. These consist of five main models: the two component model; the three component model; the Cole model; a model based on Brown's model called here the Modified Cole model and a constant phase element model (Figure 5.8).

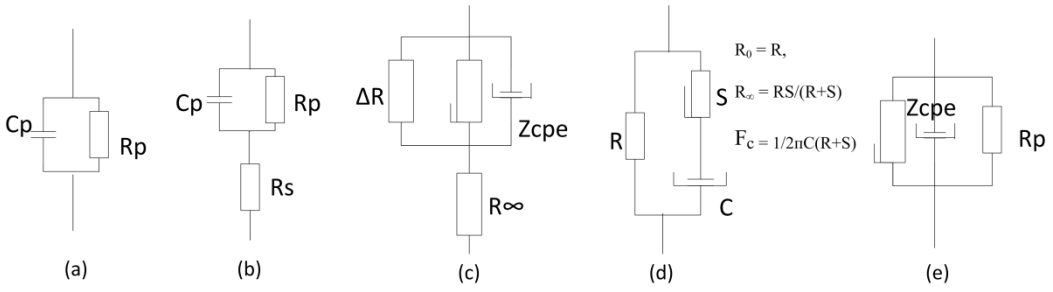


Figure 5.8: Five skin models are used to compare with the skin measurement results. (A) two component model (RC) [1], (B) three component model (2R-1C) [1], (C) Cole model [1], (D) Modified Cole model of Brown [7] and (E) CPE model

There are five models used for fitting: model A (two component model), model B (three component model), model C (Cole model), model D (Modified Cole model) and model E (CPE model). Each of the models in Figure 5.8 is used to compare with the measurement result shown in the next sections. These models may be not the optimum model that can provide a suitable fit to all skin impedance data but are based on those previously applied in research in this field.

5.3 Simulation models and comparison method

As we have seen in section 5.2 (Figure 5.8), there are five main simulation models that can be used to simulate and compare with in vivo skin impedance measurement. The purpose of these simulation models is to find which model achieves the nearest fit to the results of the measurements made in this thesis.

The experiments consisted of recording and storing in-vivo skin impedance and phase data from low frequency (20 Hz) to high frequency (100 KHz). The simulation model results were then generated at the same frequencies as the in-vivo measurement. The two data sets were then compared graphically.

In order to obtain the best fit, the function (in Matlab) called "fminsearch" has been used, which finds the minimum of a scalar function of several variables, starting at an initial estimate. For instance, when the simulation model function is given as complex impedance $Z_{sim} = R_p + j/2\pi fC_p$, in which R is the value of resistor, C_p is the value of capacitor and f is the frequency. The skin impedance measurement in vivo is recorded as Z_{mes}. Fminsearch uses the Nelder-Mead algorithm [112] that attempts to minimize a scalar-valued nonlinear function of n real variables using only function values, without derivative information. This method is therefore used to search the

fitting values with respect to the measured data. The difference ΔD between simulation model values and real skin impedance values are calculated as:

$$\Delta D = \sqrt{(Z_{mes}(f) - Z_{sim}(f))^2} \quad (5.3.1)$$

The function "fminsearch" will handle the function $Z_{sim}(f)$ and generate a range of different simulation results, each with a different ΔD. With sufficient number of function evaluations and number of iterations, the "fminsearch" function will generate and evaluate the minimum results of the difference ΔD to find out how the best fit model compares with the real measurement.

The percentage error between model and practical results is given by:

$$H\ (\%) = \frac{|Z_{fit} - Z_{mes}|}{Z_{mes}} \times 100\% \quad (5.3.2)$$

Even though in some models the measurement result equals the simulation result at one frequency, it is not guaranteed that all measurements results across the whole frequency range equal the simulation results. Therefore, in order to evaluate how best-fit the model is, the average percentage error over the frequency range is given by dividing the sum of the average error between simulation and measurement at each frequency (H_1, H_2, H_3,…,H_N) to number of frequency (N):

$$H_{ave} = \frac{H_1 + H_2 + \cdots + H_N}{N} \quad (5.3.3)$$

H_N is the error percentage of simulation and measurement at the N^{th} frequency. In general, the average error percentage over the frequency range indicates the mismatch between the simulation model and skin measurement

5.4 Comparison between models and skin measurement results

The five simulation model comparisons are used to compare with the absolute measured impedance (bare skin), real versus imaginary impedance and percentage error between simulation and measurement. The measurement results were taken from 16 volunteers.

5.4.1 Two component model compared with measured result

Figure 5.9 shows the impedance of the skin tissue measurement together with the best fit model simulation RC in Figure 5.8(a). The R_p and C_p values used for best fit are 8.9MΩ and 0.262 nF.

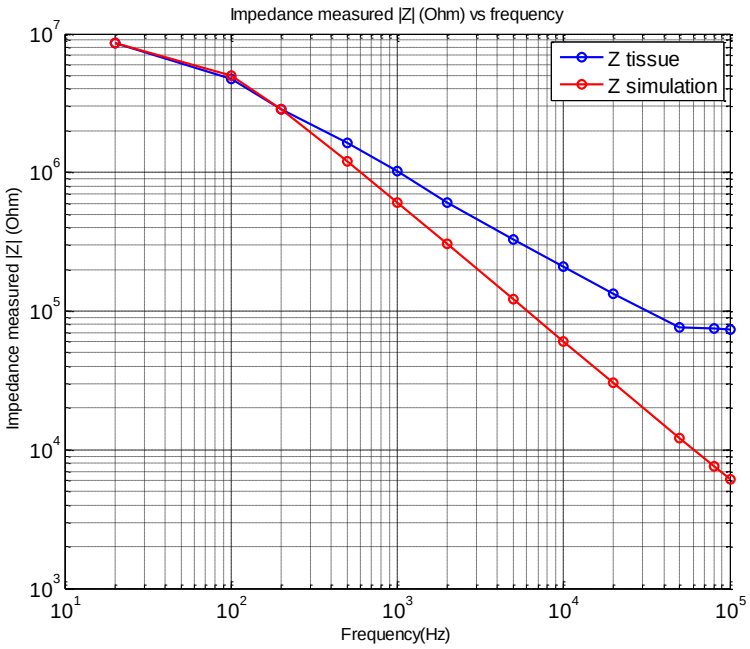


Figure 5.9: Impedance compared between tissue measurement and model simulation using RC model of Figure 5.8(a).

In Figure 5.9, the impedance results from the model simulation only matched with the impedance of skin tissue at low frequencies between approximately 20 and 200Hz. At frequencies > 500 Hz, there is a significant difference between simulation and measurement which increases with frequency.

In Figure 5.10, the real and imaginary parts of the impedance from the skin tissue measured are illustrated compared to the simulation results.

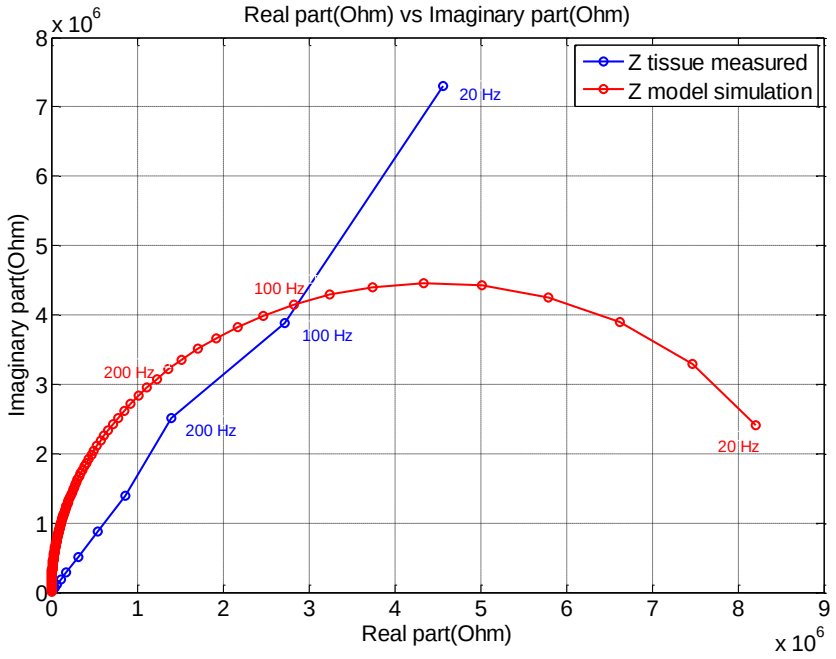


Figure 5.10: Real impedance versus imaginary impedance illustrating comparison between model simulation (red) and bare skin measurement (blue) using RC model of Figure 5.8(a)

As seen in Figure 5.10, the simulation result deviates considerably from the measurement demonstrating that the simple RC model does not provide an accurate model of skin impedance.

The percentage error versus frequency of measured skin impedance versus simulated impedance of the model in Figure 5.8(a) using equation 5.3 is plotted in Figure 5.11.

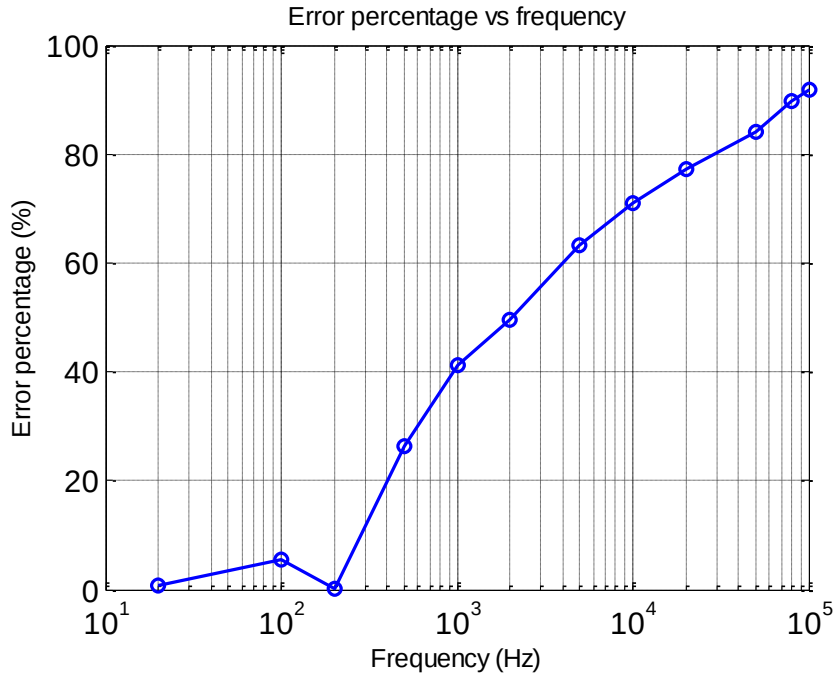


Figure 5.11: Error percentage of simulation and measurement versus frequency taken using the simple RC model of Figure 5.8(a)

In Figure 5.11, it is shown clearly that the percentage error is below 10% at frequencies equal or below 200 Hz. At frequencies above 500 Hz to 100 KHz, the percentage errors are as high as 27% (at 500 Hz), 41% (at 1 KHz), 50% (at 2 KHz), 62% (at 5 KHz), 71% (at 10 KHz), 78% (at 20 KHz), 85% (at 50 KHz), and 91% (at 100 KHz). The average error percentage over the frequency range is ~50 %.

5.4.2 Three component model compared with measured results

The second model used to compare with measured results is the three component 2R-1C network (two resistors and one capacitor) – shown in Fig 5.8(b). The parallel version of the second model had been used to compare with the skin tissue measurement. The impedance of the parallel version in 2R-1C network has been described in detail in Chapter 2 section 2.6.2. In Figure 5.12, the impedance of skin tissue measurement is plotted together with the best fit model of the 2R-1C network

model simulation of Figure 5.8(b). The values used for fitting model are R_s = 186kΩ, R_p = 8.92MΩ and C_s = 0.269 nF.

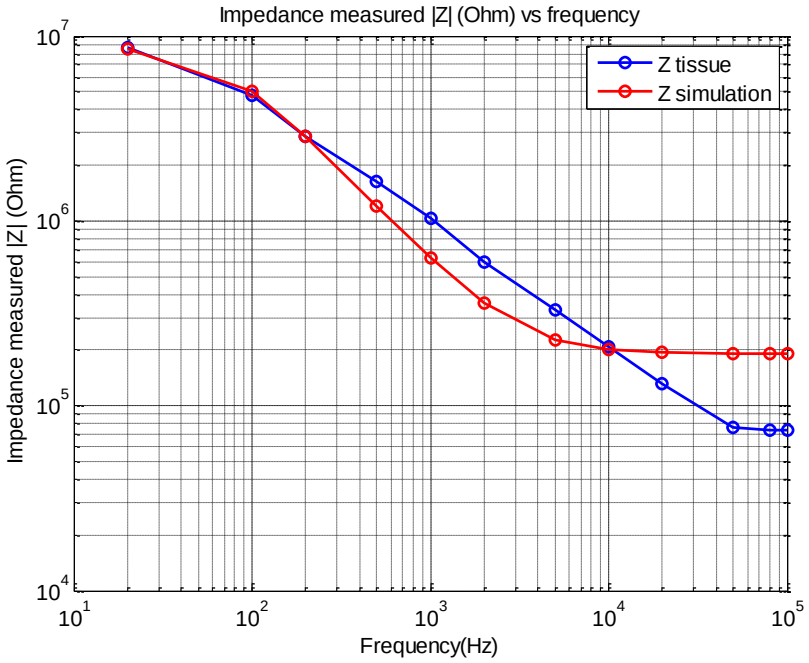


Figure 5.12: Impedance compared between tissue measurement and model simulation using 2R-1C network of Figure 5.8(b).

In Figure 5.12, the simulation impedance curve is close to the measured skin data at the frequencies up to 200 Hz. At the frequency above 500 Hz, the mismatch between simulation model and measured results can be seen, however the difference is not as great compared to the two component model. An intersection of the simulation impedance $Z_{simulation}$ and the measurement impedance Z_{tissue} is seen at 10 KHz. Then, at the frequency higher than 10 KHz, there is a difference between simulation and measurement.

In Figure 5.13, the real and imaginary part of the impedances compared between model simulation and skin measurement is shown.

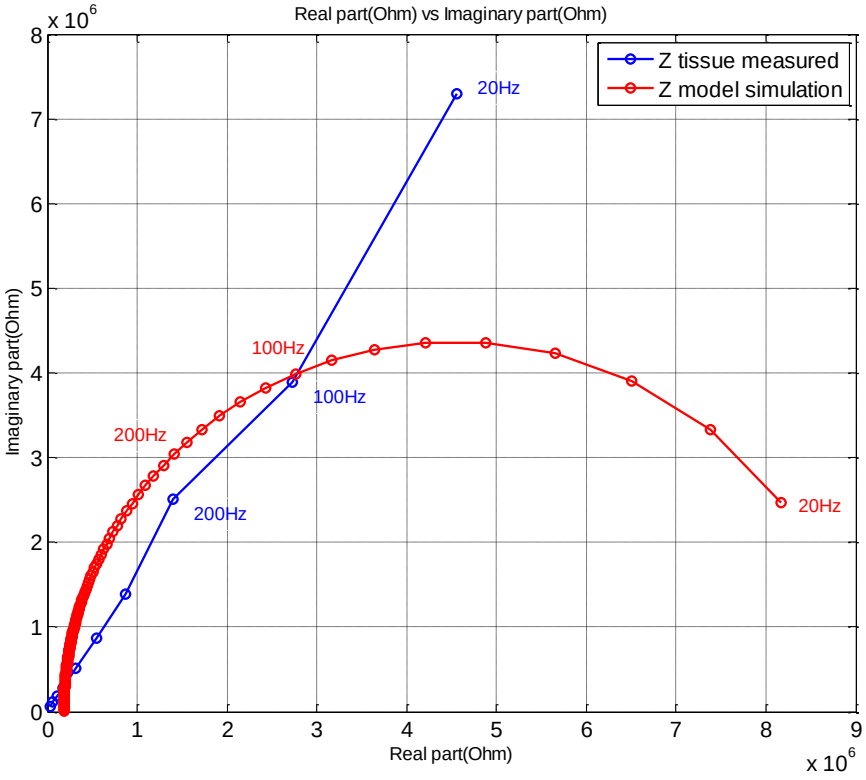


Figure 5.13: Real parts versus imaginary parts of the impedance compared between model simulation (red) and bare skin measurement (blue) using 2R-1C network of Figure 5.8(b).

Figure 5.13 still does not provide an accurate match between simulation and measurement. The difference between the model and measurement can be observed in the percentage error versus frequency plotted in Figure 5.14.

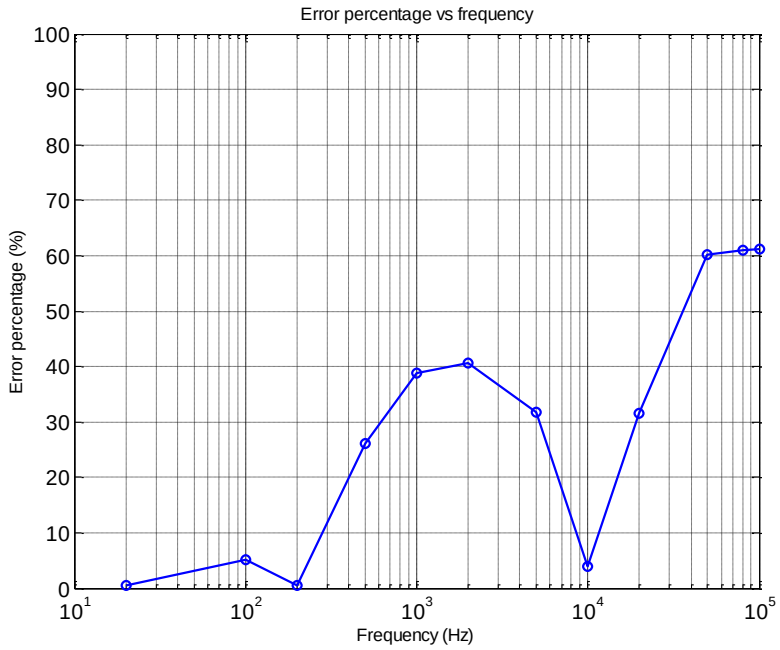


Figure 5.14: Error percentage versus frequency taken between model simulation and tissue measurement using 2R-1C network Figure 5.8(b).

As seen in Figure 5.14, the percentage error is initially 2% (20 Hz) and is below 10% up to 200Hz. The average error over the range is 30.8 %.

Compared with the two component model, the three component model is a better fit with the skin measurement. However, the average error percentage is still high.

5.4.3 Cole model vs measured data

The third model is the Cole model based on Equation 2.18 in Chapter 2. The model is created by CPE elements i.e. containing frequency dependent components. In Figure 5.15, the impedance of skin tissue measurement is plotted together with the best fit Cole model simulation from Figure 5.8(c). The values used for fitting are R_∞ = 8.2kΩ, R_0 = 11.2MΩ, f_c = 44.68 Hz and α = 0.766.

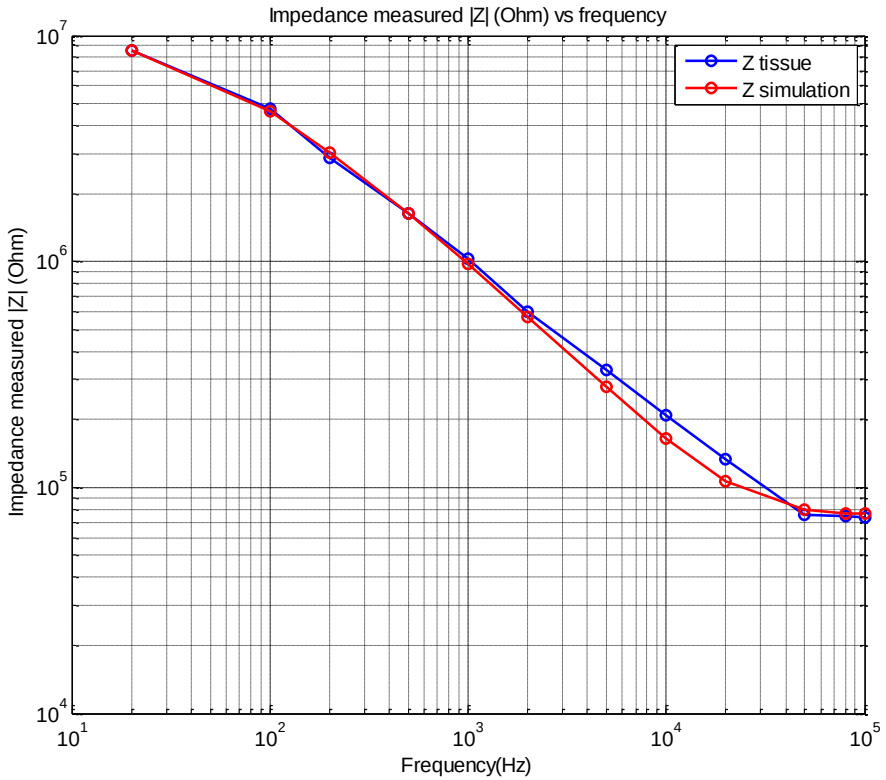


Figure 5.15: Impedance of tissue measurement and model simulation by Cole equation model of Figure 5.8(c).

As seen in Figure 5.15, the simulation impedance values are well matched with the measurement results over the whole frequency range. Above 2 KHz, there are small differences between the simulation and measurement. Compared with the two previous models, the Cole model gave a better fit model compared with the two and three component models.

In Figure 5.16, the real part versus imaginary part of simulation and measurement are plotted together for comparison. However a semi-circular plot is not observed in the experimental data. The error versus frequency using equation 5.3 is plotted in Figure 5.17.

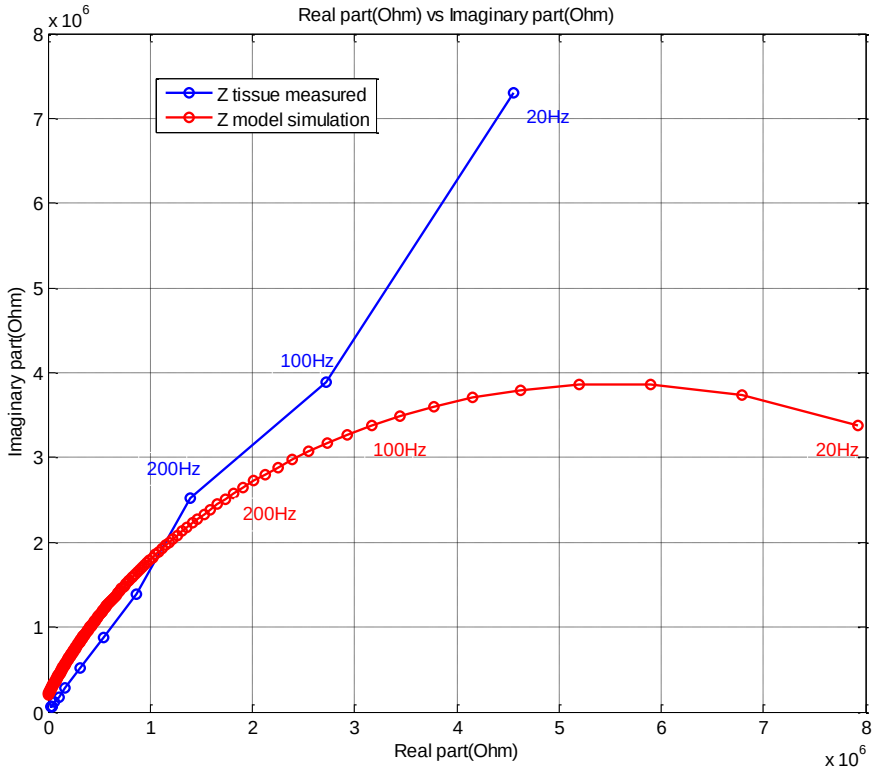


Figure 5.16: Real parts versus imaginary parts of the impedance compared between model simulation (red) and bare skin measurement (blue) using Cole model of Figure 5.8(c).

.

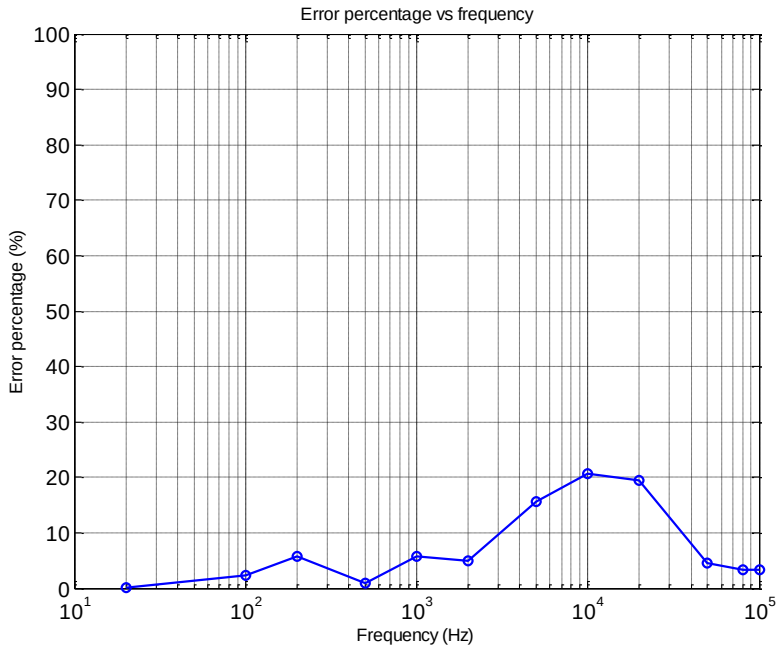


Figure 5.17: Error percentage versus frequency taken between model simulation (using Cole model of Figure 5.8(c)) and tissue measurement.

In Figure 5.17, the percentage errors are below 25% in the frequency range from 20Hz to 100 KHz. The average error percentage was calculated as 7.23%.

From the value of average error percentage above, the Cole model provides an improved fit model for the skin measurement results over the simple two components RC and the three components 2R and 1C models.

5.4.4 Modified Cole model vs measured data

The Modified Cole model is based on Equation 2.9 by using 'a least square deviation method' to the Cole equation and derivation of the formula for impedance by Brown et al [7]. In Figure 5.18, the impedances compared between model simulation and tissue measurement are shown. The parameters used for fitting are R = 9.28 MΩ, S = 4.49 kΩ, C = 0.413 nF and alpha = 0.29.

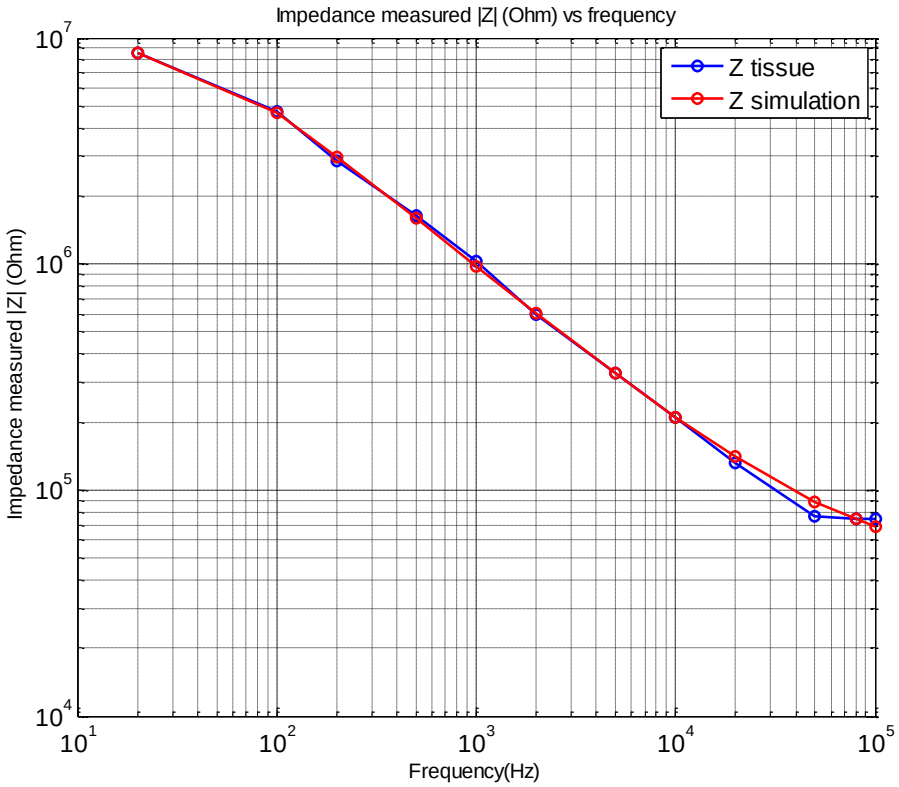


Figure 5.18: Impedance of tissue measurement and model simulation by Modified Cole model of Figure 5.8(d)

As seen in Figure 5.18, the impedances from the Modified Cole model are comparable to the impedance from skin measurement. Figure 5.19 illustrates the real versus the imaginary plot of the comparison between the Modified Cole model and skin measurement.

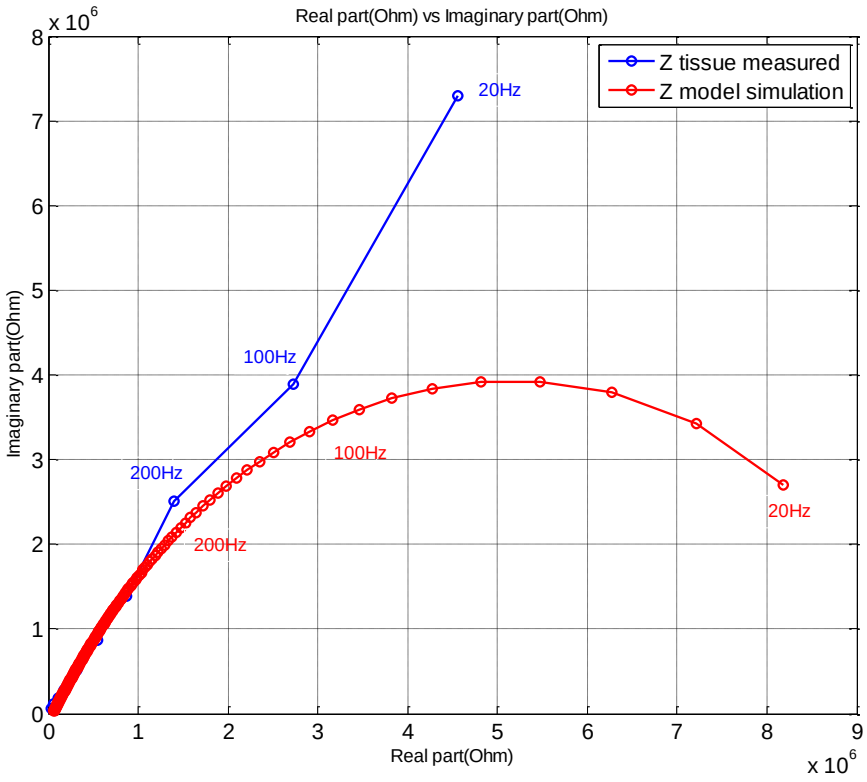


Figure 5.19: Real versus imaginary plots comparing the model simulation (using the Modified Cole model of Figure 5.8(d)) and tissue measurement.

Similar to the results from the Cole model, the differences are highest at the beginning of the two plots when the frequency is 20 Hz. The percentage error versus frequency of the Modified Cole mode compared with skin measurement is shown in Figure 5.20 with an average percentage error of 3.6%.

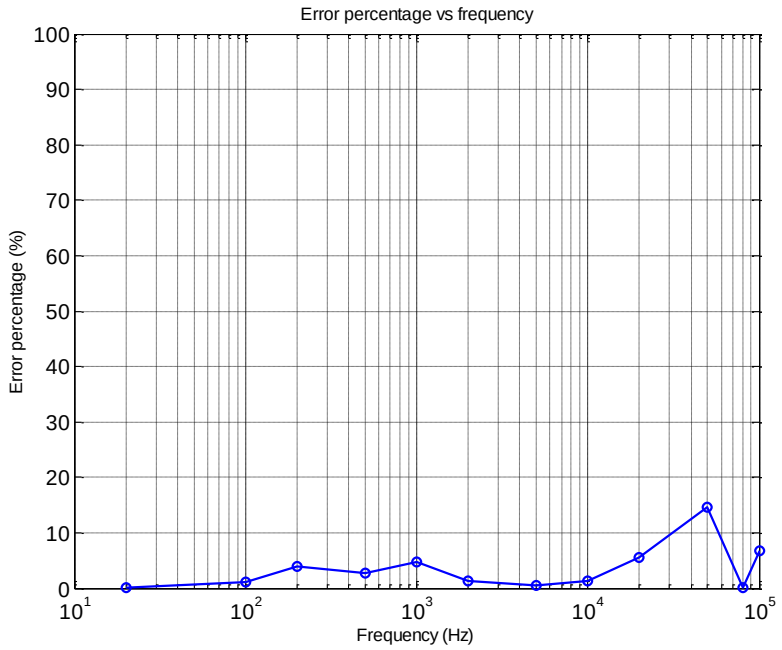


Figure 5.20: Error percentage versus frequency taken between model simulation (using the Modified Cole model of Figure 5.8(d)) and tissue measurement.

Overall, the Modified Cole model gave an average error percentage lower than the Cole model in this case. However, the Modified Cole model may not represent the best fit for all tissue samples.

5.4.5 CPE model vs measured data:

The fifth model is created by only the CPE elements i.e. containing frequency dependent components. In order to present more flexibility for this model, the CPE model is placed in parallel with a resistor R_p. In Figure 5.21, the impedance of skin tissue measurement is plotted together with the best fit CPE model simulation from Figure 5.8(e). The values used for fitting are R_p = 1.11MΩ, R_{cpe} = 172MΩ, C_{cpe} = 1.06×10^{-9} (F) and $\alpha = 0.60746$.

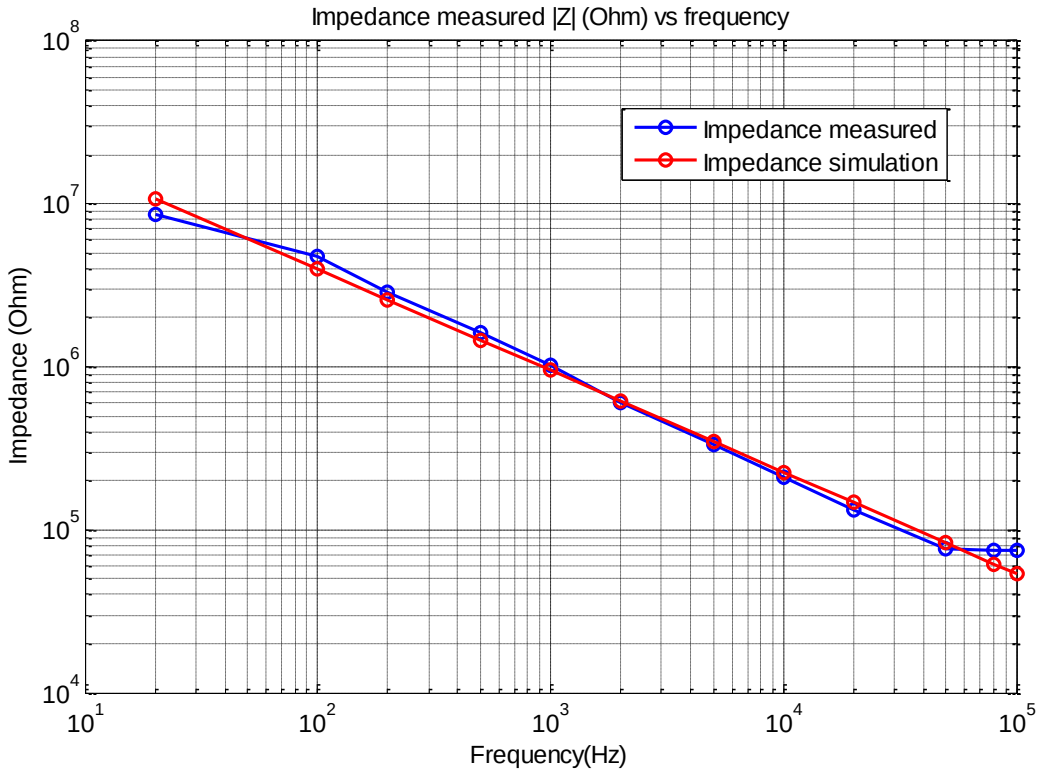


Figure 5.21: Impedance of tissue measurement and model simulation using model E on one volunteer.

As can be seen in Figure 5.21, the CPE model presents a good fit to the measurement data. There is only small difference in the impedance fitting results at the low frequency (20 Hz) and high frequency (above 80 kHz). In Figure 5.22 the real versus the imaginary plot of the comparison between the CPE model and skin measurement is shown.

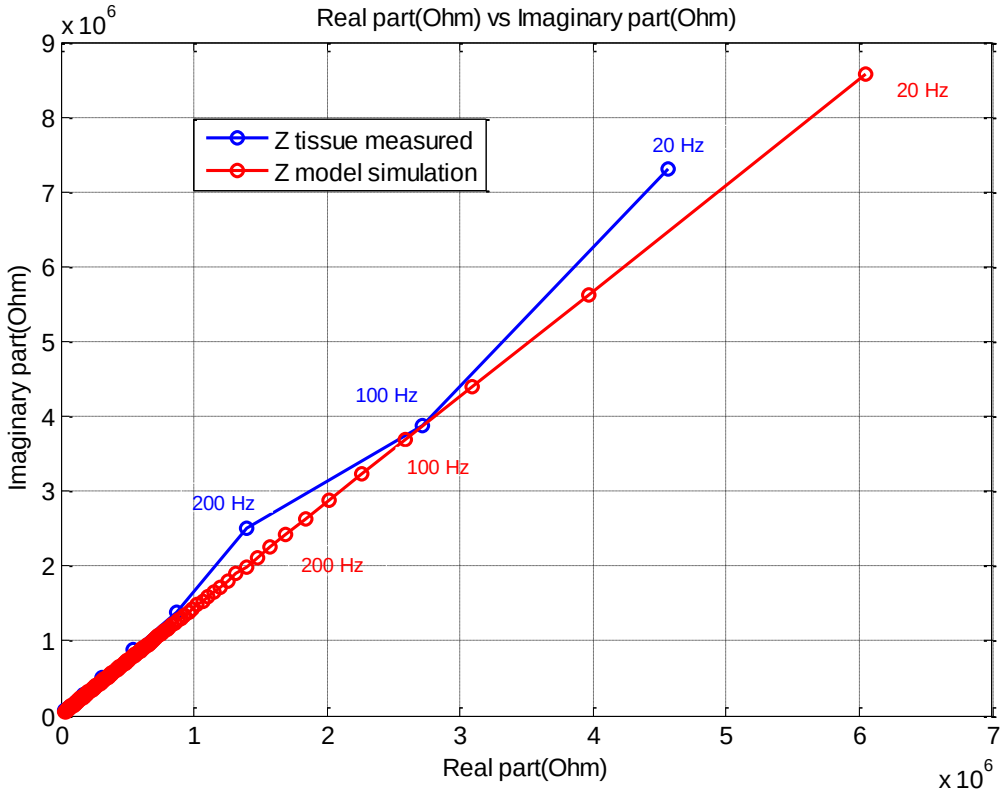


Figure 5.22: Real versus imaginary plots comparing the model simulation (using model E) and tissue measurement.

The CPE model generates a straight line fit of the data measurement. Similar to the results from the Cole model and Modified Cole model, the differences are at the beginning of the two plots when the frequency is 20 Hz (on the right hand side), albeit not as significant as the other two models. The percentage error versus frequency of the Modified Cole mode compared with skin measurement is shown in Figure 5.23 with an average percentage error of 8.82%.

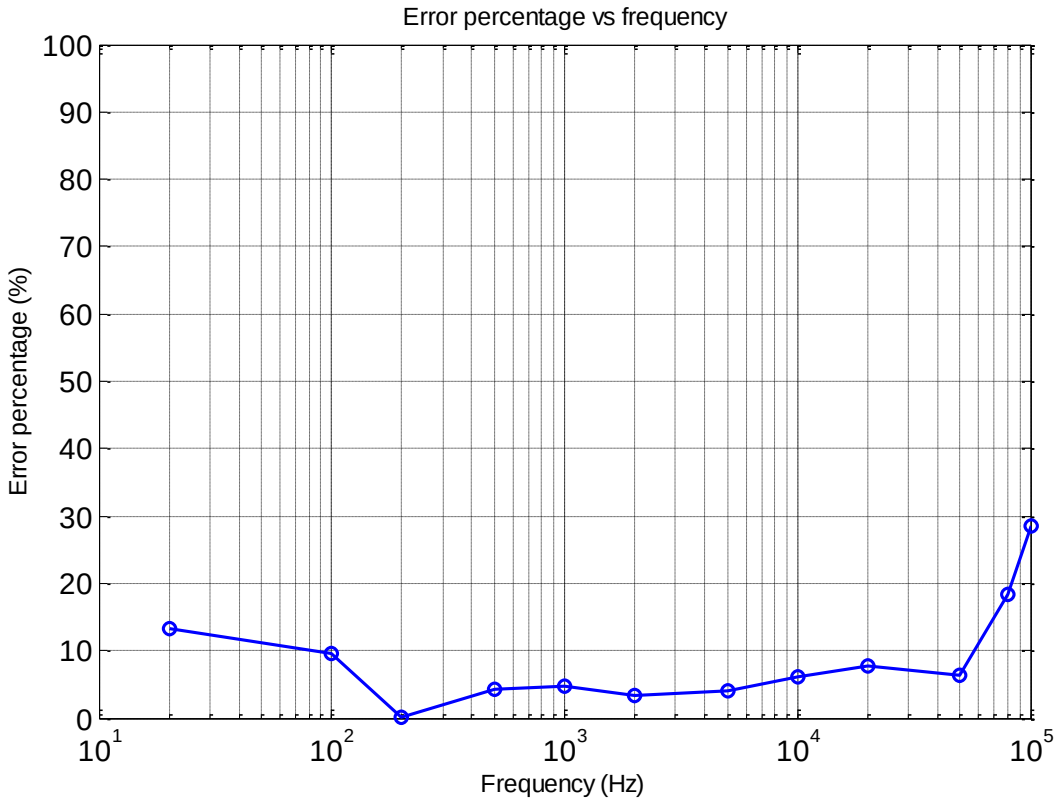


Figure 5.23: Error percentage versus frequency taken between model simulation (using model E) and tissue measurement

In Figure 5.23, it is shown clearly that the percentage error is below 10% at frequencies from 100 Hz to 50 kHz, although the percentage is about 13 % at a frequency of 20 Hz. At frequencies above 50 KHz, the percentage errors are as high as 19% (at 80 kHz), 29% (at 100 KHz). The average percentage error over the frequency range is 8.82%. It is a much better fitting with data measurement when compared with two and three components models.

In the next section, a summary table is provided to compare the average percentage error of the five different models with various tissue sample measurement results.

5.5 Discussion about the simulation model and practical results

The summary table for the above results is shown in Table 5.1. This is based on the average percentage error of each model for the skin sample results of 16 different volunteers. For this overall comparison of the models, the average fit percentage error is calculated for each model over all volunteers.

Volunteer (group D)	Average error (%)Model A (RC model)		Average error (%) Model B (2R-C model)		Average error (%) Model C (Cole model)		Average error (%) Model D (Modified Cole model)		Average error (%) Model E (CPE Model)	
1	50.01		30.77		7.23		3.55		8.82	
2	31.59		31.59		31.15		29.49		34.27	
3	32.2		32.2		20.61		13.48		29.49	
4	31.5		31.5		31.48		27.57		31.06	
5	32.68		22.87		6.16		8.7		5.9	
6	32.61		19.66		13.46		13.54		14	
7	53.1		25.66		5.87		5.86		8.55	
8	63.12		31.68		29.05		26.83		14.38	
9	35.32		22.3		10.53		13.76		14.93	
10	53.25		35.74		8.98		12.22		6.95	
11	42.21		42.21		18.25		7.86		42.64	
12	51.23		34.45		4.16		1.53		4.96	
13	29.4		16.43		4.97		19.21		7.10	
14	53.37		17.63		8.11		8.4		23.35	
15	32.02		17.38		6.66		20.18		7.35	
16	39.65		20.32		4.29		12.9		5.88	
Average fit percentage	**Mean** **41.45%**	**SD** **±10.85%**	**Mean** **27%**	**SD** **±7.74%**	**Mean** **13.18%**	**SD** **±9.84%**	**Mean** **14.06%**	**SD** **±8.51%**	**Mean** **16.22%**	**SD** **12.06%**

Table 5.1: Error table of bare skin measurement on 16 volunteers (group D) by fitting with 5 models of Figure 5.8.

As seen in table 5.1, through the investigation of 16 different tissue samples, the two component model (model A) gave an average fit percentage error of ~42%. The maximum average error percentage of model A is at volunteer 8 for 63.12%, the minimum average error percentage is at tissue volunteer 13 for 29.4%. The results

from the two component model suggest that this is not a good fit to skin measurement results.

The three component model (model B) represents a better fit compared with the two component model as the average error is now ~27 %. The maximum average error percentage of model B is from volunteer 11 at 42.21% and the minimum average error percentage is volunteer 13 at 16.43 %.

The Cole model (model C) gave an average fit error of ~13 %. The maximum average error percentage of model C is volunteer 4 at 41.48%, and the minimum is volunteer 12 at 4.16 % thus providing a better fit compared with model A and model B.

The Modified Cole model (model D) gave an average fit of 14.06 %, which is very near to the Cole model. The maximum average error percentage of model D is volunteer 2 at 29.49% and the minimum average error percentage is volunteer 12 at 1.53 %. Model D represents a better fit model than model A and model B, however is comparable with model C.

The fifth model (model E - CPE model) gave an overall average fit of 16.22 %. It should be noted that compared to the other models the CPE model gave a clear straight line in the real vs imaginary plot. This result is confirmed by Martinsen [1] and Yamamoto [17] when measuring the stratum corneum layer. Otherwise, other volunteers are a much better fit to the semicircle curve from the Cole model. This can be explained by the stratum corneum layer of some volunteers being thicker than others. As a result the measurement data is dominated by the stratum corneum layer results instead of combination between stratum corneum and epidermis/ dermis layer.

The average percentage error of different models is plotted using a statistical boxplot in Figure 5.24.

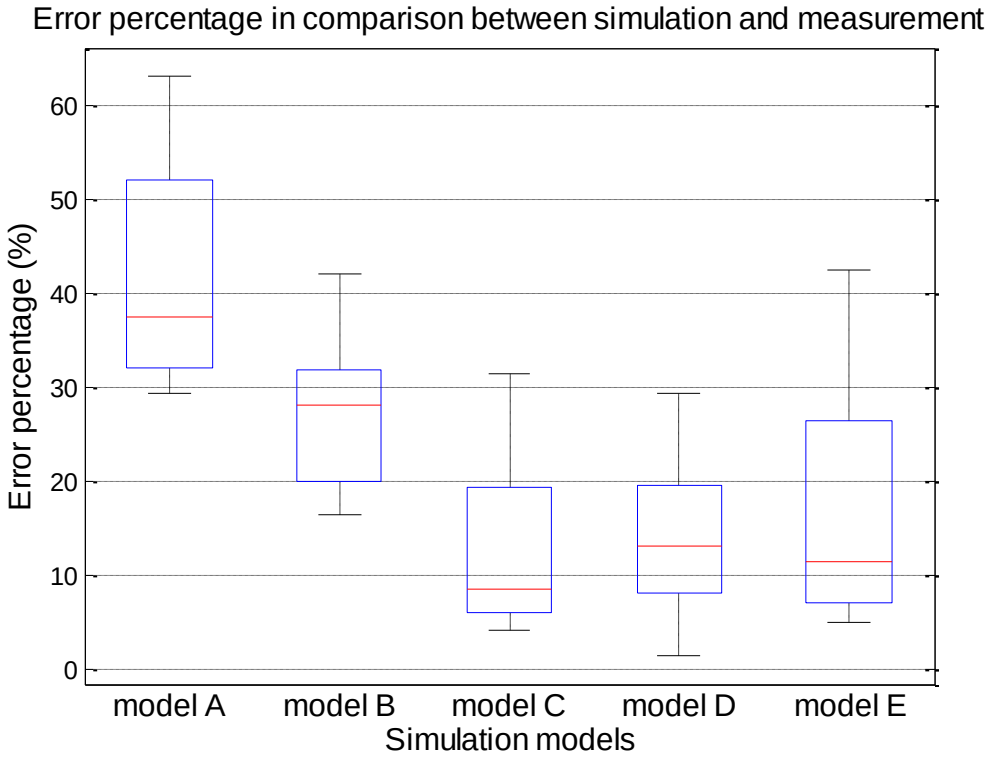


Figure 5.24: The statistical box plot of average error percentages compared between the five models and skin measurement from 16 different volunteers.

In Figure 5.24, the medians (50 % quantile) of the average percentage errors using models A, B, C, D and E are approximately 37%, 28%, 9%, 14% and 12% respectively.

Therefore, it can be seen that model C (Cole model) achieved better fit results with skin measurement among the five different simulation models used. Model D (Modified Cole model) or the model E (CPE model) achieves an average fit very close to the Cole model, Model C. The two and three component models (model A and B) are not good models for fitting skin impedance measurements.

Other conclusions that can be drawn is that the models which contain the CPE model present a much better overall fit compared to the other models that use only passive components such as classical resistors and capacitors. Also, it is likely to get a better fit when the models have more free parameters, but maybe not realistic values of the fitted parameters. i.e. only CPE model (model E) could not get better average fit compared with Cole model (model C and D) because more free parameters together with CPE.

5.6 Limitation of the simulation results with results data.

Through the results of the average percentage error in fitting from different volunteers, it is shown that even the more complicated models (C and D) have a mismatch with the measurement results. For example, for some tissue volunteers, the average percentage error can be as high as 31.48% even when using the Cole model. However, the average error can be as small as 1.53%, an excellent fitting with another volunteer. Therefore, these mismatches could be caused by other factors i.e. parasitic capacitance, abrupt changes in the experimental setup and Z plane fitting process.

As a result the mismatches between measurement and simulation can be divided into two main causes: i.e. either from the simulation models or the experimental setup.

5.6.1 Limitation in practical measurement results

There are a number of potential causes of mismatch between the modelled and measured impedance results. Firstly, in the case of the two and three component models it can be simply said that the model is too basic.

However, even the more complicated models (C,D & E) containing frequency dependent components still have some level of mismatch with the measured results.

A possible reason is that they do not include unwanted parts such as parasitic capacitance that resides between probes as seen in Figure 5.25. These capacitances result in an alternative current path away from the tissue. This obviously means that the current flowing through the tissue is smaller than the current measured from the source. Scharfetter [113], Bolton [114] and Mirtaheri [115] proposed electrical equivalent models based upon these parasitic capacitances. Figure 5.25 shows a basic schematic of this parasitic capacitance with tissue impedance.

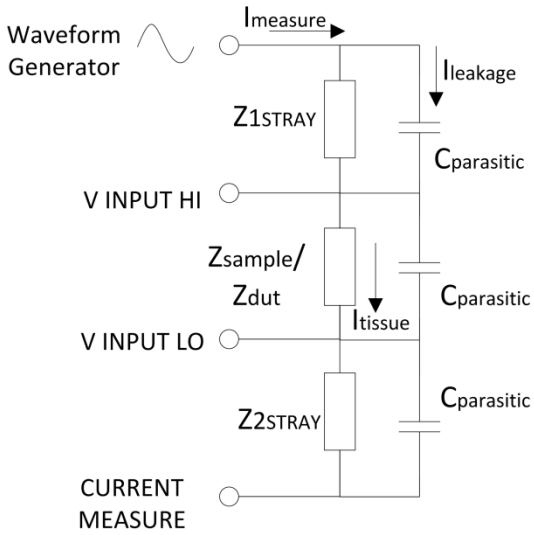


Figure 5.25: Capacitive leakage model in four point probe measurement

In Figure 5.25, the parasitic capacitance $C_{parasitic}$ creates an admittance in parallel with the tissue impedance Z_{tissue}. Moreover, the admittance created by the parasitic capacitance increase with frequency. Therefore it makes the leakage current $I_{leakage}$ flowing through parasitic capacitor even higher, which attenuates the current flowing through the tissue I_{tissue}. Because of the existence of the parasitic capacitance, a mismatch can be seen very clearly at the high frequencies such as in Figure 5.18 and Figure 5.20.

Scharfetter et al. [113] recommended avoiding the use of the high frequency values for fitting to a model by limiting the curve fitting below an upper frequency limit.

The reactance of stray capacitance decreases with respect to frequency, hence the effect increases and distorts the models. Therefore, it decreases the robustness of the Cole fitting approach.

5.6.2 Limitation in experimental setup experiment

Another cause of errors is abrupt changes of experimental measurements. These abrupt changes come from losing connection between the skin and the electrodes. Even though the lock-in amplifier attempts to remove these, some random signals still remain. This can be improved by implementing a coil spring into the electrodes to maintain the force at the interface between electrodes and skin. For example, an introduction of flexi force sensor to monitor force at the surface together with electrical sensor could be included in future work.

5.6.3 Limitation in Z plane fitting process

The limitation of the models leads to errors in fitting as can be seen in Figure 5.19. It is expected that the plot appears as a semicircle in the complex impedance plane. However, even when fitting the measured data to a semicircle using the Cole model, the accuracy of the fitting is still poor - such as volunteer 2,3,4 and 8 with more than 20% fit as shown in Table 5.1. The model can lead to an inaccurate fitting as it can always be seen at the beginning points of the circle, where the value of reactance is high. For example, in Figure 5.19, the plot shows a large difference at the beginning of fitting model compared with measurement. In addition, according to Martinsen [1], the stratum corneum does not necessarily produce a semicircle in real vs imaginary plot (Z plane). Hence, the data from multi-frequency measurement on skin may not derive the circular arc like the Cole parameters.

5.7 Conclusion

Skin layers can be modelled by electrical equivalent circuits. The simplest model is a two component model, followed by the three component model, Cole model, modified Cole model and CPE model. Proposed models are then constructed in order to fit with the results of the practical measurements. Much research has been conducted in the literature to ascertain the best fit model for skin impedance measurement. Including layered models, due to their prevalence in previous published works, five specific models were evaluated.

In order to compare between simulation models and measured results, the average percentage error has been calculated for five different models and 16 different in-vivo skin sample volunteers. The best fit is the Cole model, and closely followed by the Modified Cole model and CPE model. The two and three component models do not fit with the measured results as they are too simple and biological tissue contains frequency dependent components.

Limitations in fitting simulation models and measured results came from not only simulation models but also experimental setup. The non-modeled parasitic capacitance caused an inaccuracy in fitting with measurement results especially at high frequencies. In addition, abrupt changes from experimental setup and Z plane fitting process also affected the fitting approach.

Chapter 6 Discussion and Conclusions

6.1 Introduction

Portable medical devices make it possible to measure human physiological parameters in the long term. One example is in monitoring the effects of cosmetic products (e.g. moisturisers) on the skin. This can be useful for cosmetics companies in new product development where users of their cosmetic products could use such a device in their own home during the developmental process. Another potential application is in monitoring of hydration because the hydration state can be estimated based on the resistivity of skin and water fluid inside the body[116][117].

In this research, four electrode sensors were constructed to measure the skin impedance with and without moisturizers. Frequencies swept through the range from 20 Hz to 100 KHz by a custom made bioimpedance analyser, in order to evaluate the effects of different creams on the skin. Before carrying out measurements on human skin, calibration processes were conducted on different phantoms such as resistors and capacitors networks and calibration solutions. The results from this custom made device were also compared with the results from a commercial Solartron system (Solartron Analytical, Farnborough, UK). Errors were particularly large at the high frequencies, which are limited by the stray/ parasitic capacitance on both systems.

The overall objective of this research was to investigate the effects of different moisturizers on skin across both short term and long term measurements. To achieve this, a low cost and portable system was developed for non-invasive, fast and accurate monitoring of human skin impedance. The strategy to achieve the main aim was divided into six aspects: sensor design, hardware, software, application protocol, in vivo measurement, and modelling. These aspects are discussed in the following sections.

6.2 Sensors design

According to the four point probe electrodes designed by Campbell [100] and Brown et al [7], custom made four point electrodes were implemented with different spacing in order to measure bulk and sheet resistance. The four point probe electrodes were created by gold PCB tracks in order to make sure that the measurement was conducted without any interruption and to minimize destruction due to oxidation or electrochemical reaction. The top gold layer of the four point electrode sensor is the interface that connects to the human skin whilst the bottom copper layer is the part that connects to the cabling leading to the electronics.

As seen in Chapter 3, the four electrode sensors were designed to be small and portable, which is useful when applied to skin and for measuring the skin volume of interest. The sensors were calibrated using resistor and capacitor networks, and various values of calibration solution. In addition, the small size of the sensors helped in investigating several moisturizers on the skin at one time instead of sequentially.

However, the stray / parasitic capacitance on Printed Circuit Board (about 5 pico-farad (pF) mentioned in Chapter 3) reduced the bandwidth of the system at high frequencies around 100 KHz.. Another problem was that the four point probe sensors are attached continuously on the skin (mentioned in Chapter 4); therefore they can affect the sweat gland activity for long term contact creating an unbreathable skin.

It could be concluded that the design of the sensor is good for this specific application, however it still has some disadvantages, such as the effect it has on the skin of making unable to breath and parasitic capacitances, both of which can be improved. This is mentioned later in the Suggestion for Future work section.

6.3 Analogue frontend design

In Chapter 3, the custom-made bio-impedance analyzer was demonstrated. This system includes DSP controlled automatic frequency scanning and ADC automatic sampling. The system was implemented to sweep the voltage controlled current source from 20 Hz to 100 KHz using a programmable waveform generator (AD5932) in order to measure the frequency spectrum of the skin tissue. Instrumentation Amplifiers (AD8429) were used to measure the reference current and voltage across the load, so the transfer impedance could be calculated. A digital filter, lock-in amplifier technique and FFT were programmed into the DSP that allowed the signal to be measured in the presence of noise.

The system was tested with resistors, capacitor networks and calibration solutions. The results of the custom made device were also comparable with the Solartron Impedance Analyzer, which achieved less than 5% error tested with RC networks and less than 10% for calibration solutions. The impedance and phase results compare well with the Solarton over an operating range from 20 Hz to 100 KHz. This helps to determine the reliability of the results when measurements are made in human skin. Furthermore, the system developed can be battery-powered, thereby providing the users with flexibility and portability making it suitable for home monitoring.

The custom made system shows limitations in bandwidth and accuracy especially in high impedance loads (>3 x 10MΩ) and high frequency measurements (>50 kHz). However, this system permitted skin measurements to be performed and the aims of the thesis to be investigated.

6.4 Software for real time measurement

The application interface was implemented and programmed in DSP and Matlab to provide real-time control of the system on a PC. The frequencies scanned were in the range 20 Hz - 100 KHz. Three adjustable parameters - current level, number of scans/ sweep and display of the received data in real time, were necessary to control the system using a PC. The main control interface application was written to interact with the DSP board through RS232. In the interface application, the real-time measurement was shown as: impedance versus frequency; phase versus frequency; and the current applied versus frequency.

The control interface provided the main control required in order to send commands to the DSP. After sending the request, the interface also opens the port and retrieves the data from the DSP and displays it in real time. This routine helped in the automatic sweeping and scanning in order to obtain the impedance spectrum from skin tissue measurement.

The interface was relatively simple and could be improved by providing more control options such as choosing one frequency measurement only or displaying the Z plane plot automatically i.e. real versus imaginary part.

6.5 Application Protocol

In order to conduct this experiment, participants were recruited to take part in a short term or long term skin measurement session using the custom made bio-impedance analyzer. (see Appendix C Participant Information Sheet).

For the skin cream protocol, the temperature of the room was kept constant (using air conditioning). Only 0.1 ml of skin cream was applied. Four different skin creams

were used to conduct these experiments i.e. Nivea, Palmer's Cocoa Butter, Palmer's Olive Butter and Bio-oil (see Appendix G). The protocol was followed step by step together with a timing diagram of the measurement. Skin impedances were measured before application of the moisturizers in order to capture the reference points. After the skin creams had been applied for 1 minute, the skin impedances were measured up to 2 hours for short term or 5 hours for long term. The data was stored in real time on a PC, which included skin impedance, phase and current level.

The application protocols were designed in order to measure the different results from instantaneous measurement, short term measurement and long term measurement as seen in Chapter 4. These protocols were carried out on the volunteers, and defined to collect results for a specific time interval.

Therefore, designing a good protocol helped to minimize the errors from the measurement.

6.6 Summary of in-vivo measurement results

In the instantaneous measurements, different moisturizers gave different skin impedance results. Moreover, the values of impedance measurements can indicate the characteristic of the moisturizer i.e. Bio-oil gave the highest impedance results compared with other creams; Cocoa Butter and Olive Butter cream had similar skin impedance effect on skin, and finally Nivea cream give lowest impedance. The skin creams with the exception of Bio-oil produced impedance values that were well controlled and highly comparable between volunteers and showed no CPE dependance.

For short term and long term measurement, several findings were highlighted (1) bare skin impedances fluctuates with time potentially due to sweat gland activity; (2) skin cream affects skin impedance immediately after application; (3) skin cream effects reduce with time and therefore skin impedance tends to return to the bare skin impedance or baseline skin impedance. In addition, the impedance value varied quite widely between volunteers on bare skin but these tended to demonstrate the CPE nature of skin.

In conclusion, measuring the skin cream and then skin impedance could possibly be used to investigate the effects of the cream on skin. Different creams have different effects on human skin and therefore understanding skin creams and skin impedances could answer these questions about the effects of the skin cream. Also, the return times to the base line are also different from person to person and from skin cream to skin cream (such as Nivea has a tendency to last longer than other skin creams).

6.7 Modelling

The simulation used five different kinds of model in order to fit with 16 different volunteers. The best average fit was shown to be a Cole model, closely followed by a Modified Cole model and CPE model. As far as other models were concerned, those with two or three components were relatively simple but they do not accurately fit with the measurement results because biological tissue contains frequency dependent components.

Limitations in fitting the simulation model and the measured result came from not only the simulation models but also from the experimental setup. The non-modeled parasitic capacitance is likely to have caused an inaccuracy in fitting with the measurement results especially at high frequencies. In addition, several factors such

as abrupt changes to the experimental setup and Z plane fitting could also possibly have affected the fitting approach.

6.8 Suggestions for future work

Various suggestions to improve the potential of this kind of device exist such as:

- Combining the electrodes with a data acquisition system on a single PCB (such as a wearable sensor connected to a DSP) to decrease the parasitic capacitance by shortening the connecting wires.
- Re-designing the sensor to be breathable, so as to determine whether the sweat gland activity affects the measurements. Figure 6.1 shows a proposed breathable four point probe sensor to measure skin impedance.

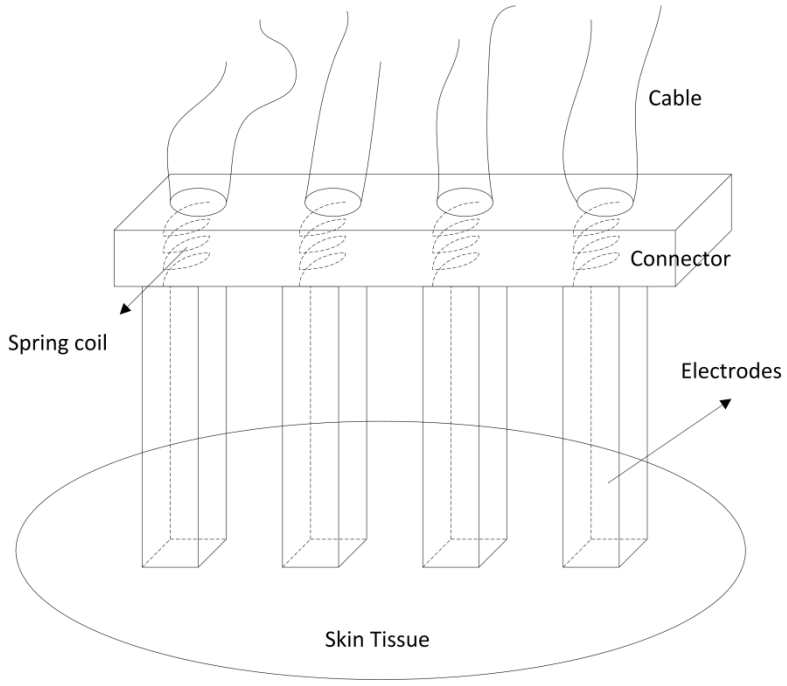


Figure 6.1: The proposed breathable sensor

- An optical sensor could be integrated with the electrical sensor (such as ECG electrodes) to either capture the photoplethysmography (PPG) signal to calculate heart rate or measure electrical skin impedance to calculate impedance plethysmography (IPG), which also related to heart rate. Both PPG and IPG can be used to capture heart rate and therefore increase the reliability by comparison of two data sets.
- Further miniaturization of the device and using a Bluetooth connection instead of a wired cable. Wireless communication will help to improve the portability of measurement unit.
- Further investigation of the reproducibility of this technique with more volunteers.
- Another possible method such as an optical CCD sensor [118] separated from the electrical approach could be used to monitor the sweat gland activity in order to confirm the effect of sweat ducts on skin impedance.
- Based on the properties of human skin layers, a whole model of skin impedance measurement is shown in Figure 6.2, which is the complete proposed model for best fit using the four point probe technique measurement in future work.

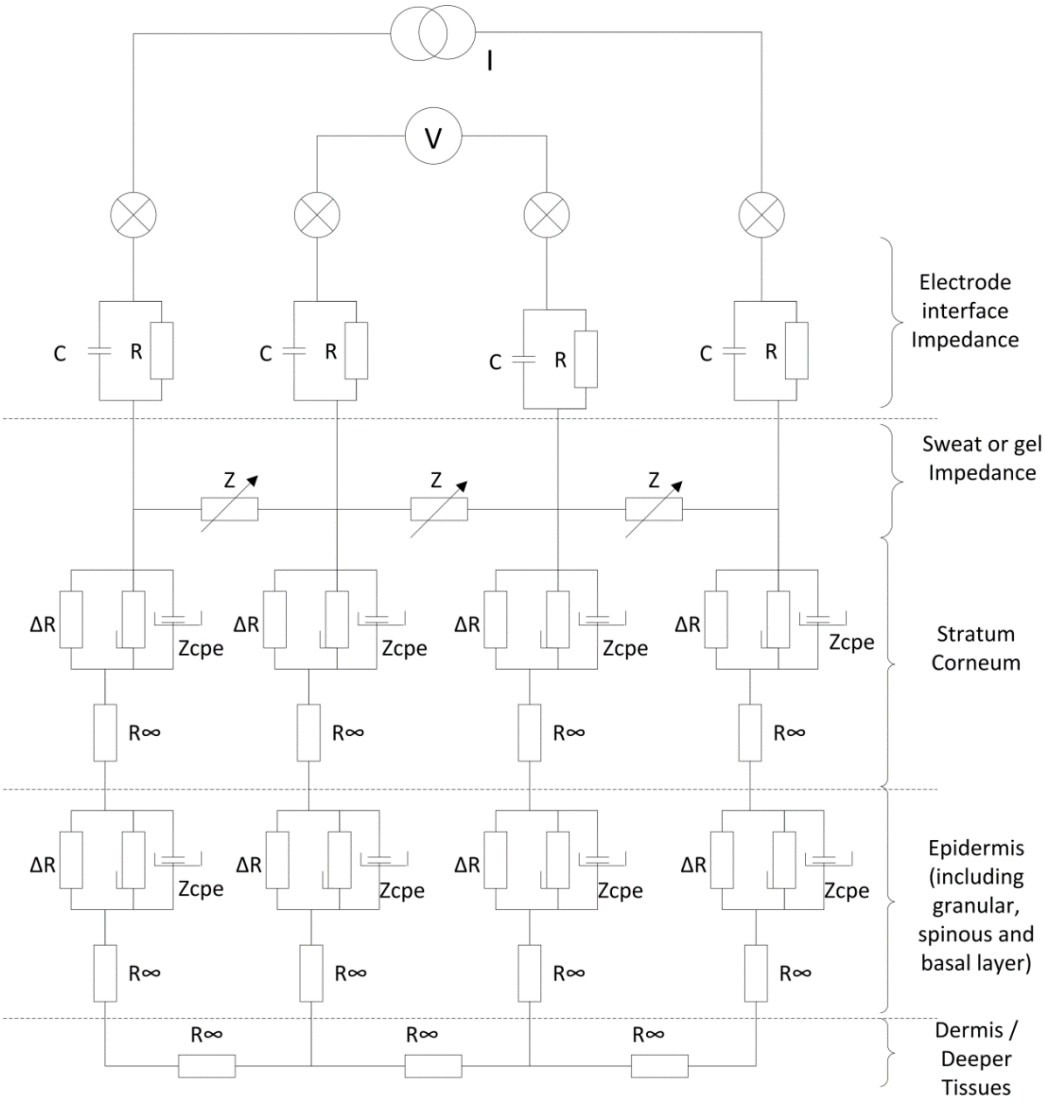


Figure 6.2 The complete proposed modelling system for skin measurement

- The proposed modelling system could be improved by including the electrode interface, sweat, stratum corneum / epidermis and dermis with each skin layer represented by electrical equivalent models.

Suggestion for future experimental work:

These preliminary experiments set the same order and location of the creams on different volunteers for both short and long term measurements. By setting the same

order and locations in all volunteers, the aim is to ensure that the experiments deliver uniform results allowing for accurate comparison between the different skin creams. However, it is possible to randomly allocate the location of creams at each location however care must be taken that the effect of application of one skin cream does not affect the other.

It is suggested that for future work, the random allocation of the location of creams should be carried out and compared with the measured impedance results using the same order location of the creams.

Statistical Analysis for future work

This chapter illustrates prelimary experiments on the effects of skin cream on the human body and the aim was not to identify confounding variables such as volunteers' ethnicity, gender and age but simply to ascertain if impedance changes could be detected. For example, the difference in skin impedance between genders can be considered by calculation the mean impedance of male and female, the standard deviation impedance of male and female volunteers where:

Mean $\mu_{male/female} = \sum_{i=1}^{N} \frac{Z_{male/female\ volunteers}}{number\ of\ male/female\ volunteers}$

Standard deviation $\sigma_{male/female} = \sqrt{\frac{1}{N}\sum_{i=1}^{N}(Z_{male/female} - \mu_{male/female})^2}$

Table 4.6 shows the mean and standard deviation in skin impedance between male and female as a function of frequency for bare skin with no skin cream.

Frequency	**100Hz**	**1kHz**	**10 kHz**	**50kHz**

Mean/SD	Mean	SD	Mean	SD	Mean	SD	Mean	SD
Male (8)	450kΩ	467kΩ	139kΩ	297kΩ	35kΩ	84kΩ	11kΩ	24kΩ
Female (2)	636kΩ	450kΩ	232kΩ	310kΩ	92kΩ	126kΩ	29kΩ	40kΩ
All volunteers (10)	487kΩ	445kΩ	157kΩ	284kΩ	46kΩ	88kΩ	15kΩ	26kΩ

Table 6.1: the mean and standard deviation impedance values for male and females for bare skin with no skin cream.

As can be seen the mean and standard deviation of skin impedance results of females are slightly higher than those of male. However, this cannot be guaranteed because the number of females is small (N=2) compared with males (N=8). Needless to say if the affect of gender and other confounding variables is to be explored then an adequate number of patients must be recruited in future.

By using normal distribution, the measured results of different groups will be analysed in detail in the future work along with volunteers' age and ethnicity will also be analysed.

6.9 Summary of Findings

- It has been confirmed that the four point probe technique is the preferred method for measuring the skin impedance rather than the two point probe.
- The four point probe electrodes should be made with gold-layered PCBs in order to minimize the destruction at an electrochemical interface (human skin) as mentioned in Chapter 3.
- The custom designed small sensors made it possible to measure different effects from moisturizers in several places at the same time.

- Adequate performance can be obtained from small, portable or handheld devices. Therefore, this kind of device is comparable with the large form factor Solartron system.
- Calibration processes using RC networks, and calibration solutions are needed to determine the electrical characteristics of the system.
- Designing a suitable protocol helped to collect the data efficiently from volunteers and to avoid conditions that could affect the measurement.
- Oil-based cream makes the skin impedance high; however the water-based cream reduces the skin impedance. Bio-oil gave the highest impedance results compared with other creams; Cocoa Butter and Olive Butter cream had similar skin impedance effect on skin, and finally Nivea cream give the lowest impedance all with classical RC behavior i.e. no CPE.
- The skin impedance values of volunteers were much tighter than bare skin when all skin creams were applied except for Bio Oil.
- The skin impedance contains CPE that possibly may not produce a circular arc in the Z plane plot as seen in the case of bare skin and Bio-oil. On the other hands, Nivea, Cocoa and Olive added the frequency independent components on skin that tightened the skin impedance and derived the semicircles in real versus imaginary plots.
- Skin impedance tends to return to the base line impedance after applying moisturizers after a time in excess of 2.5 hours, however the return time is different among volunteers and/or skin creams.
- There are several factors that can affect the skin measurement such as the experimental setup, which possibly creates the unwanted parasitic

capacitances. Another factor is physiological changes such as sweat gland activity that can also affect the measurement.

- The Cole model was the best fitting model used in this research.

This work has demonstrated the effect of various skin creams on the EIS properties of human tissue and has illustrated that skin has a widely variable EIS property whilst the application of some skin creams can reduce this variability and present a highly classical RC behavior having no CPE behaviour.

References

[1] Grimnes, S. and Ø. G. Martinsen (2008). Bioimpedance and Bioelectricity Basics, Elsevier's Science & Technology Rights Department. ISBN: 978-0-12-374004-5.

[2] Aberg, P. (2004). "Skin Cancer As Seen By Electrical Impedance". The Divison of Medical Engineering, Department of Laboratory Medicine. Stockholm, Sweden, Karolinska Institutet. Thesis submitted for the degree of Doctor of Philosophy.

[3] McAdams, E. T. and J. Jossinet (1995). "Tissue impedance: a historical overview." Physiological Measurement **16**: A1 - A13.

[4] Fricke, H. and S. Morse (1925). "The electric resistance and capacity of blood for frequencies between 800 and 4½ million cycles." The Journal of General Physiology **9**: 153-167

[5] Cole, K. S. and R. H. Cole (1941). "Dispersion and Absorption in Dielectrics I. Alternating Current Characteristics." Journal Of Chemical Physics **9**: 341-351.

[6] Armstrong, L. E. (2007). "Assessing Hydration Status: The Elusive Gold Standard." Journal of the American College of Nutrition **26**(5): 575S–584S.

[7] Brown, B. H., et al. (2000). "Relation between tissue structure and imposed electrical current flow in cervical neoplasia." The Lancet **355**: 892-895.

[8] Caduff, A., et al. (2006). "Non-invasive glucose monitoring in patients with diabetes: A novel system based on impedance spectroscopy." Biosensors and Bioelectronics **22**: 598–604.

[9] Amaral, C. E. F. and B. Wolf (2007). "Effects of Glucose in Blood and Skin Impedance Spectroscopy." AFRICON 2007 Conference cited by IEEE: 1-7.

[10] Bayford, R. H. (2006). "Bioimpedance Tomography (Electrical Impedance Tomography)." Annu. Rev. Biomed. Eng. **8**: 63–91.

[11] Kerner, T. E., et al. (2002). "Electrical Impedance Spectroscopy of the Breast: Clinical Imaging Results in 26 Subjects." IEEE Transactions On Medical Imaging **21**(6): 638-645.

[12] Zou, Y. and Z. Guo (2003). "A review of electrical impedance techniques for breast cancer detection." Medical Engineering & Physics **25**: 79–90.

[13] Saulnier, G. J., et al. (2007). "An Electrical Impedance Spectroscopy System for Breast Cancer Detection." Annual International Conference of the IEEE: 4154-4157.

[14] Filho, P. B. (2002). "Tissue Characterisation using an Impedance Spectroscopy Probe". Department of Medical Physics and Clinical Engineering, University of Sheffield. A thesis submitted for the degree of Doctor of Philosophy.

[15] Gabriely, S., et al. (1996). "The dielectric properties of biological tissues: II. Measurements in the frequency range 10 Hz to 20 GHz." Phys. Med. Biol **41**: 2251–2269.

[16] Schwan, H.P. (1957), "Electrical properties of tissues and cell suspensions", Adv. Biol. Med. Phys. **5**: 147–209.

[17] Yamamoto, T. and Y. Yamamoto (1976). "Electrical properties of the epidermal stratum corneum." Medical and Biological Engineering **14**(2): 151-158.

[18] Blank IH (1952). “Factors which influence the water content of the stratum corneum”. J Invest Dermatol. Vol.**18**: 433-40.

[19] Blank IH (1953). “Further observations on factors which influence the water content of the stratum corneum”. J Invest Dermatol. Vol.**21**: 259-71.

[20] Martinsen, Ø. G. and S. Grimnes (2008) "Long-Term Effect of Some Skin Moisturizers." Dermatology **2**: 87-89.

[21] Plonsey R, Fleming DG (1969). Bioelectric Phenomena, New York, McGraw-Hill, p358. ISBN 10: 0-07-050342-7.

[22] Pallàs-Areny, R. and Webster, J. G. (2001). Sensors And Signal Conditioning. New York: Wiley. ISBN: 9780471332329

[23] Medical electrical equipment. General requirements for safety BS EN 60601-1:2006, IEC 60601-1:2005 (Accessed: 17 June 2014)

[24] Martinez, F. S. (2007). “Electrical Bioimpedance Cerebral Monitoring: Fundamental Steps towards Clinical Application.” Department of Signals and Systems Division of Biomedical Engineering, Chalmers University of Technology & University College of Borås, Sweden. Thesis for the degree of doctor of philosophy.

[25] Rahal, M., J. M. Khor, et al. (2009). "A comparison study of electrodes for neonate electrical impedance tomography." Physiol. Meas. **30**: S73–S84.

[26] Dozio, R., A. Baba, et al. (2007). "Time Based Measurement of the Impedance of the Skin-Electrode Interface for Dry Electrode ECG Recording." Proceedings of the 29th Annual International Conference of the IEEE EMBS: 5001-5004.

[27] Schwan, H. P. (1963) “Determination of Biological Impedances.” In W. L. Nasduk(Ed.), Physical Techniques in Biological Research. NewYork: Academic Press. Vol. **4**, pp. 323-407.

[28] Ackmann, J. J. (1993). "Complex Bioelectric Impedance Measurement System for the Frequency Range from 5 Hz to 1 MHz." Annals of Biomedical Engineering **21**: 135-146.

[29] Grimnes, S., et al. (2010). "Mutual localization of electrode pairs in a 4-electrode measuring system." International Conference on Electrical Bioimpedance **224**: 1-4.

[30] Wang, Y., Schimpf, P. H., Haynor, D. R., and Kim, Y. (1998), “Geometric effects on resistivity measurements with four-electrode probes in isotropic and anisotropic tissues,” IEEE Trans. Biomed. Eng., **45**: 877–884.

[31] Tsai, J.-Z., H. Cao, S. Tungjitkusolmun, E. J. Woo, V. R. Vorperian, J. G. Webster (2000). “Dependence of apparent resistance of four-electrode probes on insertion depth.”, IEEE Transactions on Biomedical Engineering, **47**, 41-48.

[32] Hinton, A. J. and B. Sayers (1998). ”Advanced Instrumentation for Bioimpedance Measurement”. Solartron, Victoria Rd, Farnborough, Hampshire UK, Solartron Analytical.

[33] Texas Instrument, Application Note 1515 A Comprehensive Study of the Howland Current Pump.

[34] Charles Kitchin and Lew Counts (2006), “A Designer Guide to Instrumentation Amplifiers*”* 3rd edition, Analogue Device, USA.

[35] Hank Zumbahlen (2006). “Basic Linear Design”. Analogue Device, ISBN: 0-915550-28-1.

[36] Walter G. Jung (2002). “Op Amp Applications”. Analogue Device, ISBN 0-916550-26-5.

[37] Lu, l and Brown, B. H. (1994). The electronic and electronic interface in an EIT spectroscopy system. Innov. Tech. Biol. Med., 15 (1), 97-103.

[38] Bertemes-Filho, P., et al. (2000). "A comparison of modified Howland circuits as current generators with current mirror type circuits." Physiol. Meas. **21**: 1-6

[39] Wilson, A. J., et al. (2001). "Mk3.5: a modular, multi-frequency successor to the Mk3a EIS/EIT system." Physiol. Meas. **22**: 49–54.

[40] Oh, T. I., et al. (2007). "Multi-frequency EIT system with radially symmetric architecture: KHU Mark1." Physiol. Meas. **28**: S183–S196.

[41] Yerworth, R. J., et al. (2002). "Design and performance of the UCLH Mark 1b 64 channel electrical impedance tomography (EIT) system, optimized for imaging brain function." Physiol. Meas. **23**: 149–158.

[42] Cook, R. D., et al. (1994). "ACT3: A High-speed, High-Precision Electrical Impedance Tomograph." IEEE TRANSACTIONS ON BIOMEDICAL ENGINEERING **41**(8): 713-722.

[43] Yang, Y., et al. (2006). "Design and preliminary evaluation of a portable device for the measurement of bioimpedance spectroscopy." Physiol. Meas. **27**: 1293–1310.

[44] Hong, H., et al. (2009). "Comparison of a new integrated current source with the modified Howland circuit for EIT applications." Physiol. Meas. **30**: 999–1007.

[45] Hartov, A., et al. (2001). "Dartmouth's next generation EIS system: preliminary hardware considerations." Physiological Measurement **22**: 25-30.

[46] Ryan Halter, A. H. a. K. D. P. (2004). "Design and implementation of a high frequency electrical impedance tomography system." Physiol. Meas. **25**: 379–390.

[47] Halter, R. J., et al. (2008). "A Broadband High-Frequency Electrical Impedance Tomography System for Breast Imaging." IEEE TRANSACTIONS ON BIOMEDICAL ENGINEERING **55**(2): 650-659.

[48] Yoo, P. J., et al. (2010). "Wideband Bio-impedance Spectroscopy using Voltage Source and Tetra-polar Electrode Configuration." International Conference on Electrical Bioimpedance, Journal of Physics **224**: 1-4.

[49] Mohamadou, Y., et al. (2012). "Performance evaluation of wideband bio-impedance spectroscopy using constant voltage source and constant current source." Measurement Science And Technology **23**: 1-10.

[50] Saulnier, G. J., et al. (2006). "A high-precision voltage source for EIT." Physiol. Meas. **27**: S221–S236.

[51] W.Sansen, B. Geeraerts, et al. (1992). "Voltage Versus Current Driven High Frequency EIT Systems." International Biomedical Engineering Days, IEEE: 102-106.

[52] Hartov, A., E. Demidenko, et al. (2002). "Using voltage sources as current drivers for electrical impedance tomography." Measurement Science And Technology **13**: 1425–1430.

[53] Qureshia, T. R., C. Chatwina, et al. (2013). "Bio-Impedance Excitation System: A Comparison of Voltage Source and Current Source Designs." APCBEE Procedia 7: 42 – 47.

[54] Faes, T. J. C., H. A. v. d. Meij, et al. (1999). "The electric resistivity of human tissues (100 Hz–10 MHz): a meta-analysis of review studies." Physiol. Meas. **20**: R1–R10.

[55] Birgersson, U. (2012). Electrical impedance of human skin and tissue alterations: mathematical modeling and measurements. Department of clinical science, intervention and technology. Stockholm, Sweden, Karolinska Institutet.

[56] Rosell, J., et al. (1988). "Skin Impedance from 1 Hz to 1 MHz." IEEE Transactions On Biomedical Engineering **35**(8): 649-652.

[57] M. R. Neuman, (1998). "Biopotential Electrodes," in Medical Instrumentation. Application and Design, 3rd ed., J. G. Webster, Ed. New York : John Wiley and Sons pp. 183–232. ISBN: 9780471676003.

[58] McAdams, E. T., et al. (1996). "Factors affecting electrode-gel-skin interface impedance in electrical impedance tomography." Medical & Biological Engineering & Computing **34**: 397-408.

[59] Fricke, H. (1932). "The theory of electrolytic polarization." Philosophical Magazine, **7**:310-318.

[60] Cole, K. S. (1928). "Electric Impedance of Suspensions of Spheres." The Journal of General Physiology **12**: 29-36.

[61] Cole, K. S. (1932). "Electric Phase Angle of Cell Membranes." The Journal of General Physiology **15**: 641-649.

[62] Cole, K. S. (1934). "Alternating Current Conductance and Direct Current Excitation of Nerve." Science **79**: 164-165.

[63] Grimnes, S. and Ø. G. Martinsen (2005). "Cole Electrical Impedance Model—A Critique and an Alternative." IEEE Transactions On Biomedical Engineering **52**(1): 132-135.

[64] Cardu, R., et al. (2012). "Electrode contact impedance sensitivity to variations in geometry." Physiological Measurement **33**: 817-830.

[65] Grimnes, S. (1983). "Impedance measurement of individual skin surface electrodes." Med. & Biol. Eng. & Comput **21**: 750-755.

[66] Geddes, L. A. and M. E. Valentinuzzi (1973). "Temporal Changes in Electrode Impedance While Recording the Electrocardiogram with "Dry" Electrodes." Biomedical Engineering **1**: 356-367.

[67] O'Connell, M. P., et al. (2000). "An in vivo comparative study of the pregnant and nonpregnant cervix using electrical impedance measurements." British Journal of Obstetrics and Gynaecology **107**: 1040-1041.

[68] Walker, D. C., et al. (2000). "Modelling the electrical impedivity of normal and premalignant cervical tissue." Electronics Letters **36**(19): 1-2.

[69] Walker, D. C., et al. (2002). "Modelled current distribution in cervical squamous tissue." Physiological Measurement **23**: 159–168.

[70] Walker, D. C., et al. (2003). "A study of the morphological parameters of cervical squamous epithelium." Physiological Measurement **24**: 121–135.

[71] Brown, B. H., et al. (2005). "Detection of cervical intraepithelial neoplasia using impedance spectroscopy: a prospective study." International Journal of Obstetrics and Gynaecology **112**: 802–806.

[72] Abdul, S., et al. (2006). "The use of electrical impedance spectroscopy in the detection of cervical intraepithelial neoplasia." Int J Gynecol Cancer **16**: 1823–1832.

[73] Balasubramani, L., et al. (2009). "The detection of cervical intraepithelial neoplasia by electrical impedance spectroscopy: The effects of acetic acid and tissue homogeneity." Gynecologic Oncology **115**: 267–271.

[74] Huang, X., et al. (2012). "Epidermal Differential Impedance Sensor for Conformal Skin Hydration Monitoring." Biointerphases **7**(52): 1-9.

[75] Oppliger, R. A. and C. Bartok (2002). "Hydration Testing of Athletes." Sports Med **32**(15): 959-971.

[76] Cheuvront, S. N. and M. N. Sawka (2005). "Hydration Assessment of Athletes." Sports Science Exchange **18**(2): 1-12.

[77] Lodén, M. et al. (1999). "Improvement in skin barrier function in patients with atopic dermatitis after treatment with a moisturizing cream (Canoderm)." British Journal of Dermatology **140**: 264–267.

[78] Gitis, N. and R. Sivamani (2004). "Tribometrology of Skin." Society of Tribologists and Lubrication Engineers **47**: 1-9.

[79] Sivamani, R. K., et al. (2003). "Friction coefficient of skin in real time." Skin Research and Technology **9**: 235-239.

[80] Lodén M, Maibach HI. (2000). Dry skin and moisturizers – chemistry and function. CRC Press, Boca Raton. ISBN: 9780849375200.

[81] Sivamani, R. K., et al. (2003). "Tribological testing of skin products: gender, age, and ethnicity on the volar forearm." Skin Research and Technology **9**: 299-305.

[82] Martinsen, O. G., et al. (1995). "Electrical Methods for Skin Moisture Assessment." Skin Pharmacol **8**: 237-245.

[83] Martinsen, Ø. G., et al. (2008). "Gravimetric Method for in Vitro Calibration of Skin Hydration Measurements." Biomedical Engineering **55**(2): 728-732.

[84] Yamamoto, Y., et al. (1986). "Characteristics of skin admittance for dry electrodes and the measurement of skin moisturisation." Medical & Biological Engineering & Computing **24**: 71-77.

[85] Yamamoto, T. and Y. Yamamoto (1981). "Non-linear electrical properties of skin in the low frequency range." Med. & Biol. Eng. & Comput **19**: 302-310.

[86] Yamamoto, Y., et al. (2003). "Evaluating object and region of concentric electrode in bio-electrical impedance measurement." IEEE: 282-283.

[87] Lodén, M., et al. (2001). "Instrumental and dermatologist evaluation of the effect of glycerine and urea on dry skin in atopic dermatitis." Skin Research and Technology **7**: 209–213.

[88] Lodén, M., et al. (2002). "A Double-Blind Study Comparing the Effect of Glycerin and Urea on Dry, Eczematous Skin in Atopic Patients." Acta Derm Venereol **82**: 45–47.

[89] Buraczewska, I., et al. (2006). "Changes in skin barrier function following long-term treatment with moisturizers, a randomized controlled trial." British Journal of Dermatology **156**: 492-498.

[90] Vauhkonen, M., et al. (2001). "A MATLAB package for the EIDORS project to reconstruct two-dimensional EIT images." Physiol. Meas. **22**: 107–111.

[91] Polydorides, N. and W. R. B. Lionheart (2002). "A Matlab toolkit for three-dimensional electrical impedance tomography: a contribution to the Electrical

Impedance and Diffuse Optical Reconstruction Software project." Measurement Science And Technology **13**: 1871-1883.

[92] Filho, P. B. (2002). Tissue Characterisation using an Impedance Spectroscopy Probe. Department of Medical Physics and Clinical Engineering, University of Sheffield. **A thesis submitted for the degree of Doctor of Philosophy.**

[93] Bertemes-Filho, P., B. H. Brown, et al. (2003). "Stand-off electrode (SoE): a new method for improving the sensitivity distribution of a tetrapolar probe." Physiol. Meas. **24**: 517–525.

[94] Frerichs, I., et al. (1998). "Electrical impedance tomography in monitoring experimental lung injury." Intensive Care Med **24**: 829-836

[95] Frerichs, I., et al. (2003). "Electrical impedance tomography: a method for monitoring regional lung aeration and tidal volume distribution?" Intensive Care Med **29**: 2312–2316.

[96] Heinrich, S., et al. (2006). "Body and head position effects on regional lung ventilation in infants: an electrical impedance tomography study." Intensive Care Med **32**: 1392–1398.

[97] Gómez-Laberge, C., et al. (2012). "A Unified Approach for EIT Imaging of Regional Overdistension and Atelectasis in Acute Lung Injury." IEEE Transactions On Medical Imaging **31**(3): 834-842.

[98] Adler, A., et al. (2009). "GREIT: a unified approach to 2D linear EIT reconstruction of lung images." Physiol. Meas. **30**: S35–S55.

[99] ADLER, A., et al. (1994). "Imaging Of Gastric Emptying With Electrical Impedance Tomography." Canadian Medical and Biolological Eng. Soc. **20**: 14-15.

[100] Campbell, S. D., K. K. Kraning, et al. (1977). "Hydration Characteristics and Electrical Resistivity of the Stratum Corneum using a noninvasive four point microelectrode method." The journal of Investigative Dermatology **69**(3): 290-295.

[101] Ferreira, J., F. Seoane, et al. (2011). "AD5933-Based Electrical Bioimpedance Spectrometer. Towards Textile-Enabled Applications." 33rd Annual International Conference of the IEEE EMBS: 3282-3285.

[102] Lynde, C. W. (2001). "Moisturizers: What They Are and How They Work." Skin Therapy Letter **6**(13): 3-5.

[103] Buono, M. J., et al. (2004). "The effect of ambient air temperature on whole-body bioelectrical impedance." Physiol. Meas.**25**: 119-123.

[104] Caton, J. R., et al. (1988). "Body composition analysis by bioelectrical impedance: effect of skin temperature." Medicine & Science in Sports & Exercise **20**(5).

[105] Begum S, Barua S (2013). "EEG sensor based classification for assessing psychological stress." Studies in Health Technology and Informatics, 89:83-8.

[106] Hughes, E. (2001). "Skin: its structure and function and related pathology." In Dermatology Nursing: A Practical Guide, Churchill Livingstone, London. ISBN: 978-0443062094.

[107] Baba, A. and M. J. Burke (2008). "Electrical Characterisation of Dry Electrodes for ECG Recording." 12th WSEAS International Conference on CIRCUITS, Heraklion, Greece,: 1-6.

[108] Ruiz, J. C. M. (2013). "Sensor-Based Garments that Enable the Use of Bioimpedance Technology: Towards Personalized Healthcare Monitoring." School of Engineering & School of Technology and Health, KTH, Stockholm, Sweden, University of Borås, Borås, Sweden. A thesis submitted for the degree of Doctor of Philosophy.

[109] Zagar, T. and D. Krizaj (2007). "An instrumentation amplifier as a front-end for a four-electrode bioimpedance measurement." Physiol. Meas. **28**: N57–N65.

[110] Ferreira, D. M., et al. (2007). "Electrical impedance model for evaluation of skin irritation in rabbits and humans." Skin Research and Technology **13**: 259–267.

[111] Dorgan, S. J., et al. (1999). "A model for human skin impedance during surface functional neuromuscular stimulation." 19th International Conference - IEEE **7**(3): 1770-1773.

[112] Lagarias, j. C., et al. (1998). "Convergence properties of the nelder-mead simplex method in low dimensions." Siam Journal of Optimization **9**(1): 112-147.

[113] Scharfettery, H., et al. (1998). "A model of artefacts produced by stray capacitance during whole body or segmental bioimpedance spectroscopy." Physiol. Meas. **19**: 247-261.

[114] Bolton, M. P., et al. (1998). "Sources of error in bioimpedance spectroscopy." Physiol. Meas. **19**: 235–245.

[115] Mirtaheri, P., et al. (2004). "A new biomedical sensor for measuring PCO2." Physiol. Meas. **25**: 421–436.

[116] Piccoli A, Rossi B, Pillon L, Bucciante G (1994). "A new method for monitoring body fluid variation by bioimpedance analysis: the RXc graph." Kidney International, Vol. **46**:534-539,

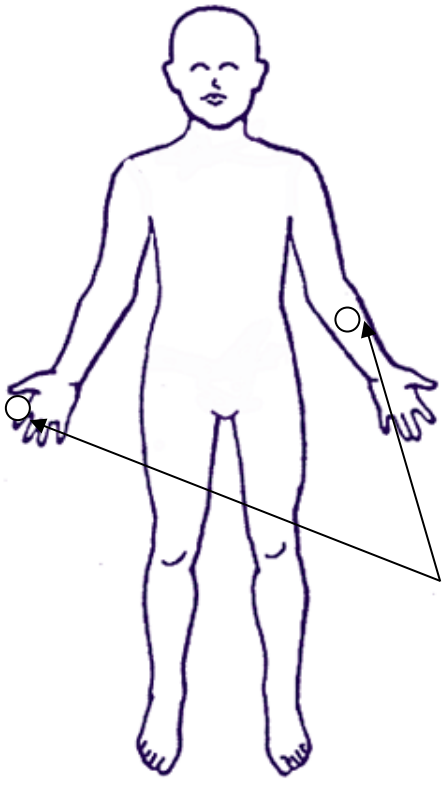
[117] Ellis, K. J. (2000) "Human Body Composition: In Vivo Methods." Physiological Reviews **80**: 649–680.

[118] Kamei, T., et al. (1997). "Instrumentation of a handy microscopic probe for concurrent observation and measurement of active sweat secretion, and its applications." Journal of Pharmaceutical and Biomedical Analysis **15**: 1563-1569.

[119] Charles F. Dalziel and W. R. Lee (1968). "Reevaluation of Lethal Electric Currents." IEEE Transactions On Industry And General Applications **IGA-4**(5): 467-476.

[120] Brown, B. H., et al. (1999). "Medical Physics and Biomedical Engineering." Medical Physics and Biomedical Engineering: Bristol, Institute of Physics Publishing Ltd.

Appendix A: Exploratory research on skin impedance

Study reference	**Exploratory research on skin impedance**
Study aim	The aim of this study is to determine in what manner skin moisturizers affect the electrical properties of human skin.
Tested products	Custom made bio-impedance analyser with different skin creams.
Primary objective	Assess electrical impedance spectroscopy to show differences on skin impedance between with and without moisturizers.
Secondary objectives	Develop a method with suitable ways for long-term monitoring the skin impedance of volunteers.
Design	 Measurements taken on allocated position on fingers, hands and arms. The measurements are: ▪ Skin impedance with/ without moisturizers ▪ Skin cream effects on skin impedance ▪ Skin impedance in short-term recording ▪ Skin impedance in long-term monitoring ▪ (please see the study design for more detail)

Study duration	Depend on the experiments there are two measurements: short-term (up to 2 hours) and long term (from 1 day up to a week)
Start date required	16th December 2012
Study population	N = 8, male N = 2, female Experiments will be made on different skin types (white yellow and brown skin colour). Also, the studies will focus on the age from 18-50.
Body area	Different allocated positions on fingers, hands, and arms,
Product availability date	N/a
Study techniques	Bio-impedance analyzer: Device developed at University of Nottingham, allows measurement of skin impedance. Skin moisturizers: Four different commercial skin creams are used for this experiments: Bio-oil (for ageing skin & dehydrated skin), Nivea Express Hydration (for normal & dry skin), Palmer's Cocoa Butter with SPF 15 (UVA & UVB Protection), Palmer Olive Butter (Anti Aging Peptide Complex). Method: Volunteer arrives and hands in consent form Volunteer get used to the atmosphere and is measured the temperature (10 mins) Allocate position of skin measurement on volunteer's skin by marker (1 min) Clean the probe using Q-Tips with alcohol (1 min) Start with Case Report Form (5 mins) Next, measure the skin impedance of volunteer without moisturizers (5 mins) Measure the skin impedance of volunteer with different moisturizers on different allocated position (please see the study design for more detail) (5 mins) Depend on the experiment such as long-term or short-term, volunteer can be asked

	for taking the measurement.
Analyzing methods (if known)	Impedance spectroscopy: using Electrical Impedance Spectroscopy plots showing the impedance(Z) with phase (θ), Real part (Real) vs imaginary part (Imag), derive the resistance (R) and capacitance (C) vs frequency (f) together with current applied (I). Moisturizers effects: Differences in skin impedance between with and without moisturizers to be analysed on real and imaginary part together with the resistance and capacitance. Different effects between skin creams: Differences in effects on human skin impedance among different skin creams to be analysed All of the above to be analysed through data collected between volunteers.

Appendix B: Case Report Form

Question	Answer
Study case number If allowed, name:	
Age	
How are you today ? General appearance.	
Have you got any diseases recently ?	
Have you got any internal electronic device in the body ?	
Have you suffer from any skin allergy ?	
Are you currently using some kind of skin care at the moment ? If yes, what is it ?	
Do you feel thirsty ? Have you taken any drink before come to the study ?	
Dry/ normal/ sensitive or aging skin ?	

Appendix C: Participant Information Sheet

Effects of moisturizers on human skin impedance measurement in vivo

Why do this study? - It is important to measure how moisturizers affect human skin impedance and EIS (Electrical Impedance Spectroscopy) is a promising approach. Moisturizers' companies claim their effects over long periods e.g. Nivea long lasting effect 24hours. Therefore, it is interesting to monitor the change in the skin properties over time after the moisturizer has been applied.

What do we need? - Measured data will be processed on a DSP and transferred to a PC through USB cable. Data will be arranged by age, ethic, and gender of participants. No personally identifiable information will be stored with the data. A hard copy of consent form will be stored in research office cabinets.

What will participation involve? - In order to do this experiment, participants will be asked to take part in one short skin measurement session. This session should not last more than 2 hours. A custom made bio-impedance analyser will be used to record the skin impedance by passing a small current signal through the skin and measuring the voltage drop using the four point probe technique. The electrodes will be attached to the participant's skin during the experiment. The records will be repeated after 5, 10, 20, 30, 60 minutes and up to 120 minutes. The custom made impedance analyser is classified as non-invasive method and no harm is done to the skin. You may withdraw from the study at any time, in which case all data relating to your measurements will be discarded.

How will my data be used? - Volunteers will be recruited verbally or by email communication. Participants will be made aware of the nature of study and can

choose to withdraw at any stage. In addition, all files of data from volunteers will be kept as anonymous.

What else do I need to know? - Devices being used will satisfy particular requirements for safety (British Standard 60601) for medical device apply current to patents. This sensor will be applied to skin to measure skin impedance. You may be asked whether any implant you have in the body. The data will appear in real time on the PC or Laptop including Skin impedance, Phase and Current Level by using a Matlab interface.

Contact: Son Nguyen
eexsn@nottingham.ac.uk
Room 1003 Tower Building
Department of Electronic and Electrical Engineering

Appendix D: Consent Form



Consent Form - Skin impedance for moisturizers' effects monitoring

I understand the risks associated with the use of current flow on the skin and have been provided with adequate safety training. I consent to the use of Skin Impedance Monitoring devices on my skin in order to test the Skin Impedance Monitoring devices being developed as part of the research within the Electrical Systems and Optics Research Division, Faculty of Engineering.

Print Name .....

Signature .....

Date .....

Appendix E: Safety regulations

In 1968, it was generally accepted that the safe let-go currents are 9 and 6 mA for men and women respectively [119]. This test had conducted using sinusoidal currents from 5 Hz to 10 KHz.

For safety consideration for biomedical devices, British Standard IEC 60601-1 covers all the general requirements for electrical medical (or electromedical) products [23]. The IEC 60601-1 standard, "Medical Electrical Equipment—Part 1: General Requirements for Safety", is the cornerstone document addressing many of the risks associated with electrical medical equipment. The allowance current to pass through the human body is clearly declared in this standard.

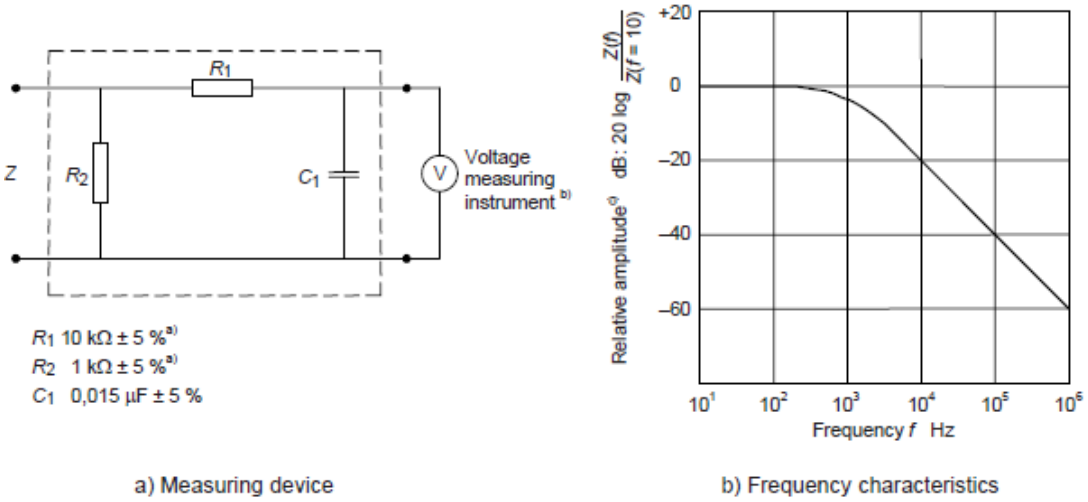


Figure E.1: Example of a measuring device and its frequency characteristics in BS60601 [23]

The custom made system bio-impedance analyser is classified as type B or BF system. Figure E.2 shows allowable values of patient leakage current and patient auxiliary current under normal condition and single fault condition from British Standard 60601-1:2006 [23].

Current in μA

Current	Description	Reference	Measuring Circuit		TYPE B APPLIED PART		TYPE BF APPLIED PART		TYPE CF APPLIED PART	
					NC	SFC	NC	SFC	NC	SFC
PATIENT AUXILIARY CURRENT		8.7.4.8	Figure 19	d.c.	10	50	10	50	10	50
				a.c.	100	500	100	500	10	50
PATIENT LEAKAGE CURRENT	From PATIENT CONNECTION to earth	8.7.4.7 a)	Figure 15	d.c.	10	50	10	50	10	50
				a.c.	100	500	100	500	10	50
	Caused by an external voltage on a SIP/SOP	8.7.4.7 c)	Figure 17	d.c.	10	50	10	50	10	50
				a.c.	100	500	100	500	10	50
Total PATIENT LEAKAGE CURRENT [a]	With the same types of APPLIED PART connected together	8.7.4.7 a) and 8.7.4.7 h)	Figure 15 and Figure 20	d.c.	50	100	50	100	50	100
				a.c.	500	1 000	500	1 000	50	100
	Caused by an external voltage on a SIP/SOP	8.7.4.7 c) and 8.7.4.7 h)	Figure 17 and Figure 20	d.c.	50	100	50	100	50	100
				a.c.	500	1 000	500	1 000	50	100

Key
NC = NORMAL CONDITION
SFC = SINGLE FAULT CONDITION

Figure E.2: Allowable values of patient leakage current and patient auxiliary current under normal condition and single fault condition from British Standard 60601 [23].

For the Patient Auxiliary Current and Patient Leakage Current, the current limit is no more than 10 μA DC current or 100 μA AC passing through the human body. Therefore, according to Standard 60601-1:2006 [23], the current passing through the body needs to be very small and for this safety condition, the device needs to adjust the current to no more than 10μA DC current or 100μA AC current to put through the human body.

However, according to Brown et al [120] in 1999, the transfer impedance of the biological tissue requires the injection of electrical current, which may cause some unwanted effects to the patient such as electrolysis, heating and neuromuscular

stimulation. The sensation occurs at the specific current level called the threshold current. Threshold current rises as well as the frequency increases. Figure E.3 shows the threshold current of sensation as the function of frequency for applied current.

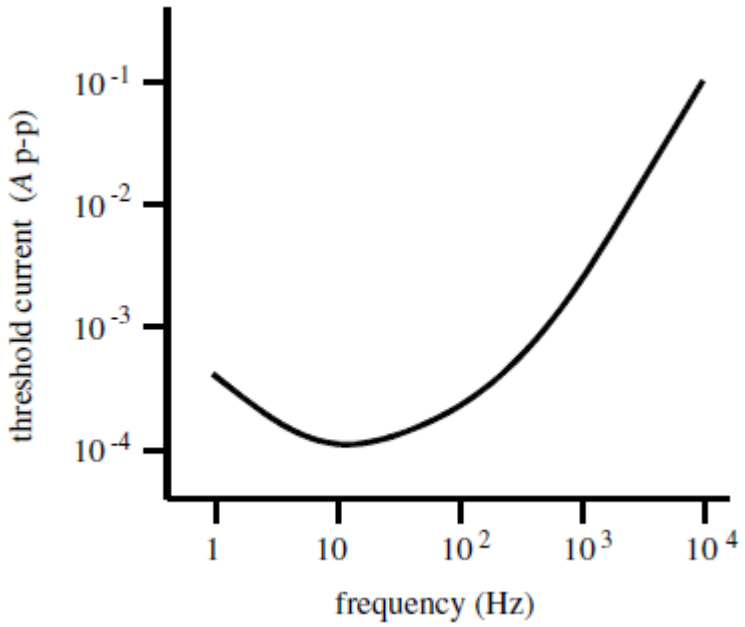


Figure E.3: Threshold current of sensation as the function of frequency for electric current applied between 5mm electrodes [120].

According to British Standard [23], "The RISK is highest and approximately equal for frequencies in the 10 Hz to 200 Hz range. It is lower, by a factor of nearly 5, at D.C. and by approximately 1,5 at 1 kHz. Beyond 1 kHz, the RISK decreases rapidly [45]. The values (in Figure E.2) apply to measured current with the measuring device shown in Figure E.1, which automatically allows for the reduced sensitivity at higher frequencies. SUPPLY MAINS frequencies of 50 Hz and 60 Hz are in the range of highest RISK."

Generally, for frequencies less than 1 KHz where the load impedance is much higher than 10kΩ, the maximum allowable current is around 100 μA. However, for the frequencies higher than 1 KHz, the allowance current can be up to 1 mA as the load

impedance is approximately 1kΩ. The biological tissue is a frequency dependent component. i.e. at low frequency (20 Hz) skin tissue can get higher than 1MΩ and at high frequency (1 KHz), the skin impedance can be low as a few kΩ. Therefore, in order to ensure a good signal to noise ratio in measurement results, the current is usually increased up to 1 mA at high frequency.

Appendix F: Long term skin impedance using moisturizers on five volunteers

Volunteer 1 data:

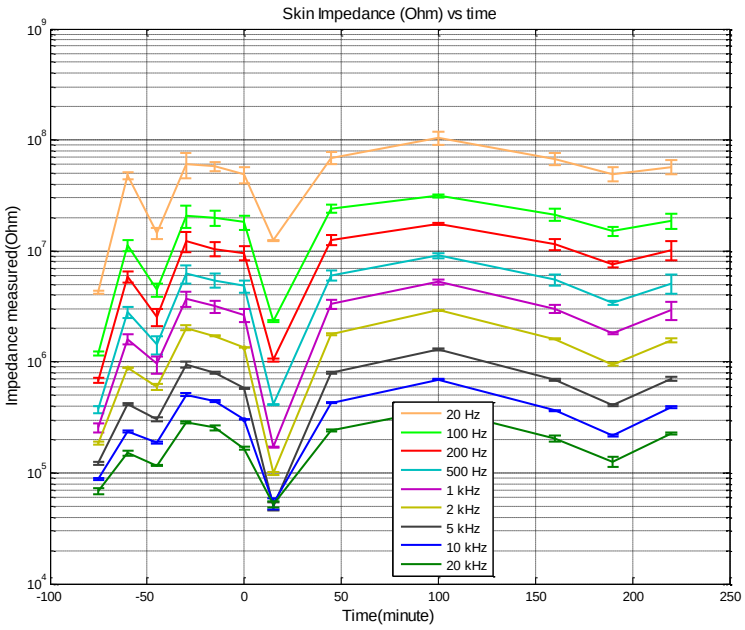


Figure F.1: Long term measurement with Bare skin on volunteer 1

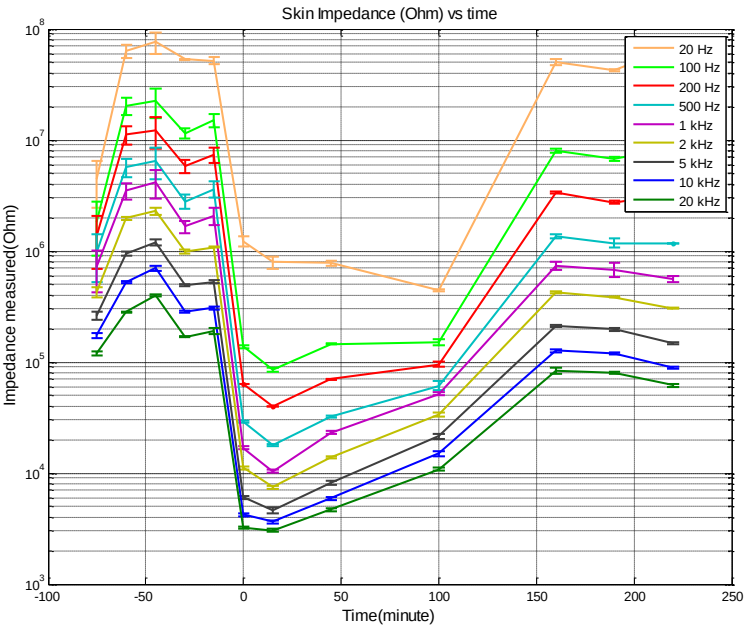


Figure F.2: Long term measurement with Nivea on volunteer 1

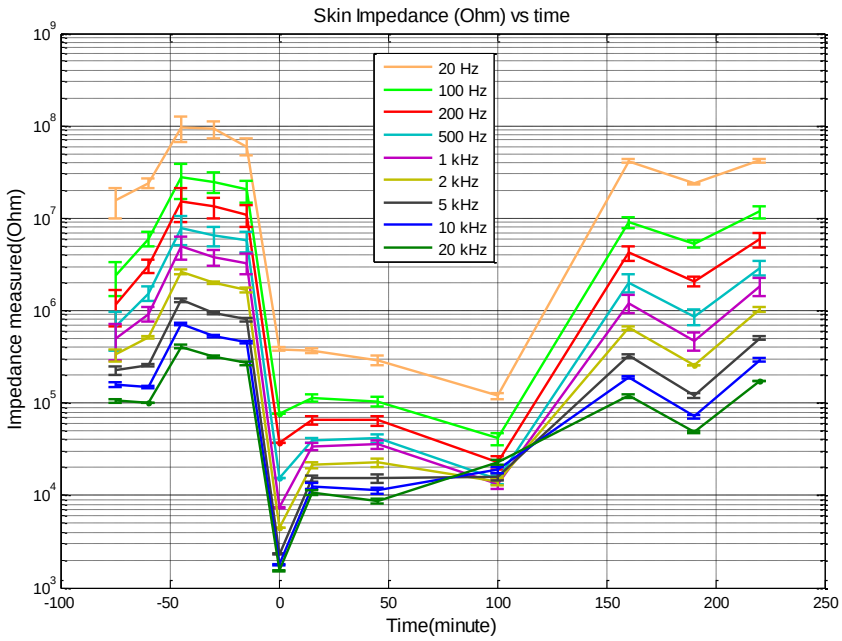


Figure F.3: Long term measurement with Cocoa on volunteer 1

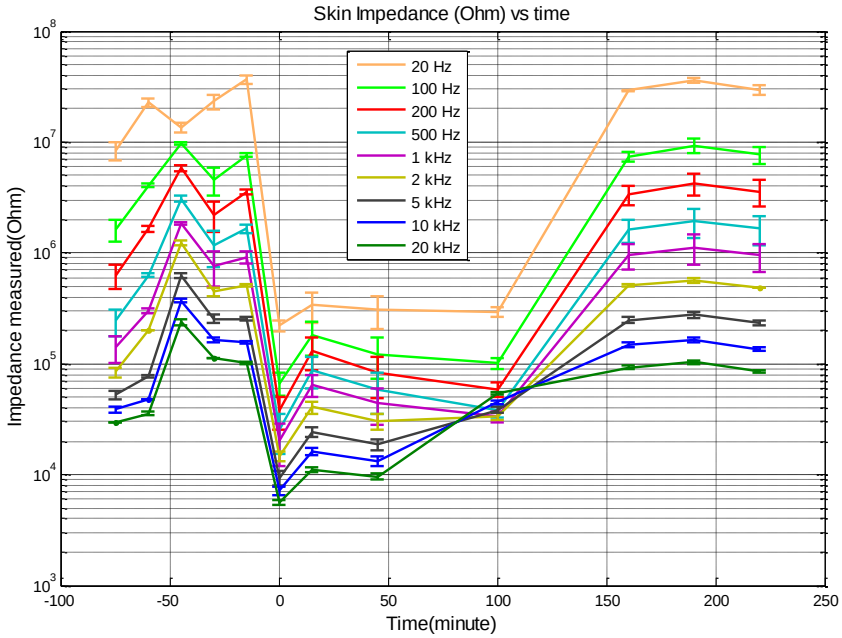


Figure F.4: Long term measurement with Bio-oil on volunteer 1

Volunteer 2 data:

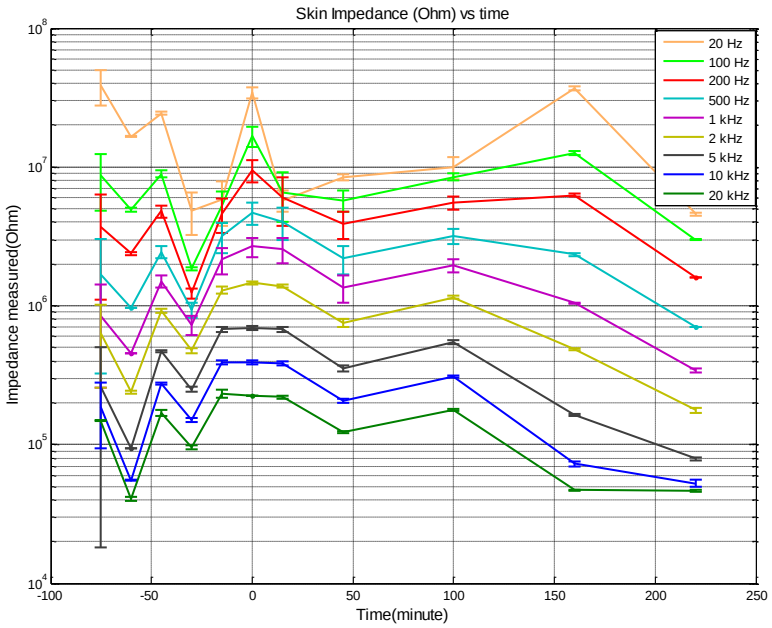


Figure F.5: Long term measurement with Bare skin on volunteer 2

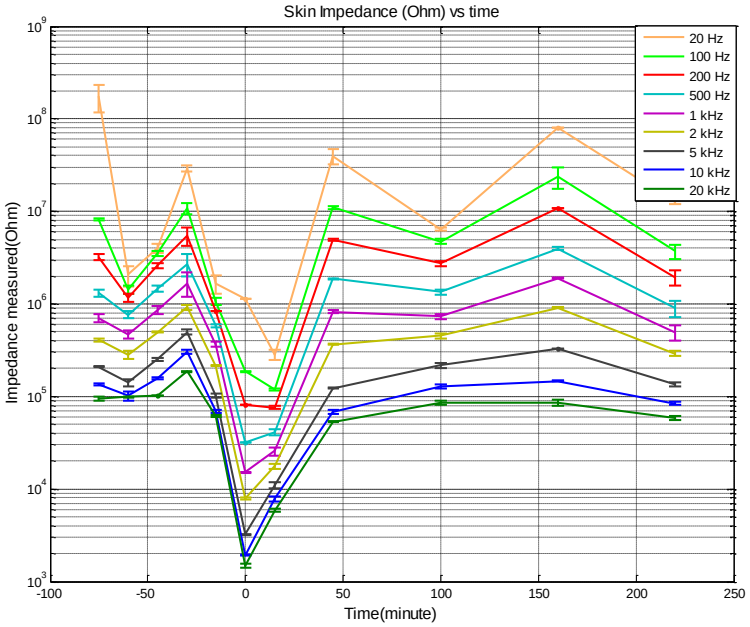


Figure F.6: Long term measurement with Nivea on volunteer 2

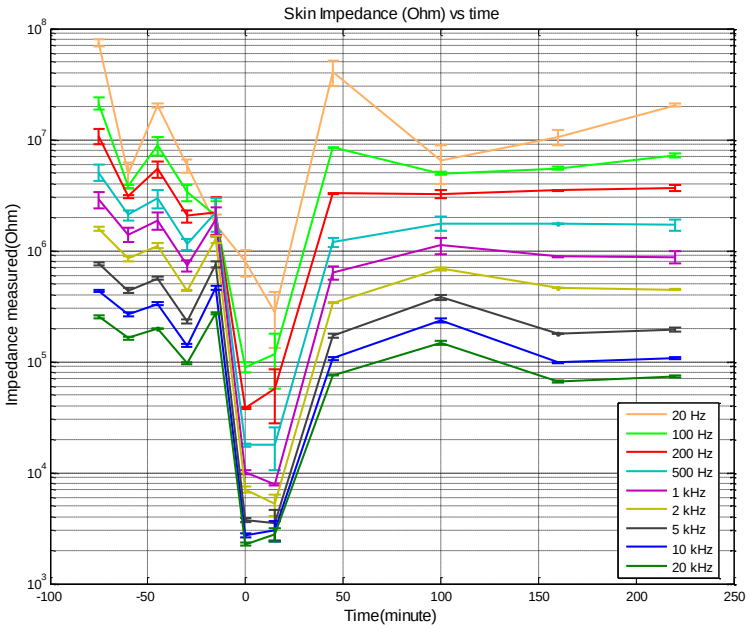


Figure F.7: Long term measurement with Cocoa on volunteer 2

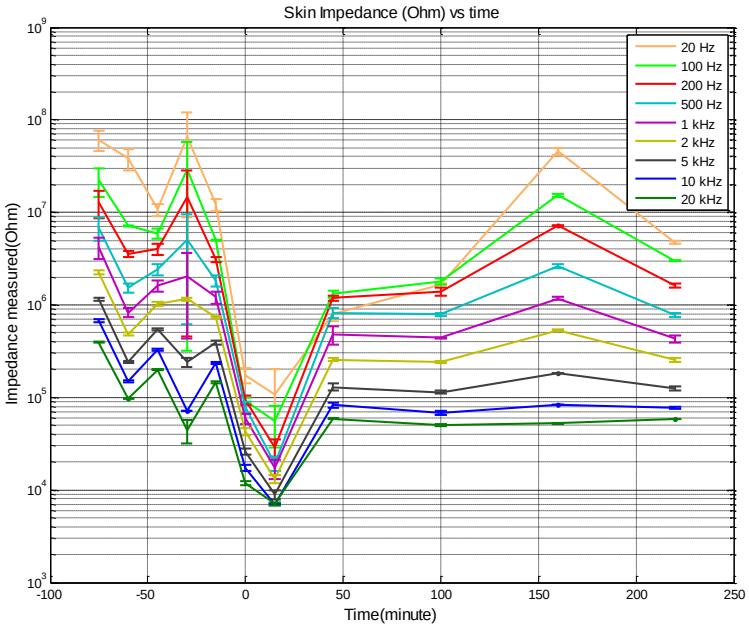


Figure F.8: Long term measurement with Bio-oil on volunteer 2

Volunteer 3 data:

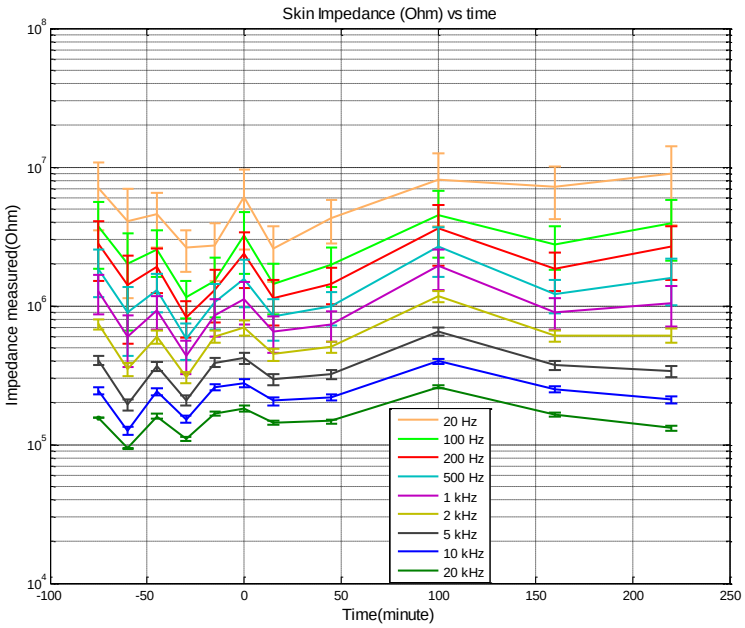


Figure F.9: Long term measurement with bare skin on volunteer 3

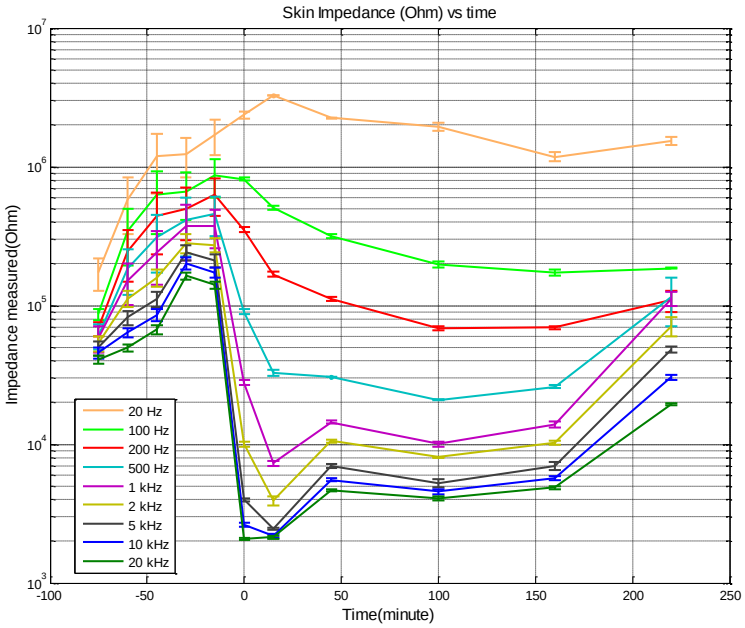


Figure F.10: Long term measurement with Nivea on volunteer 3

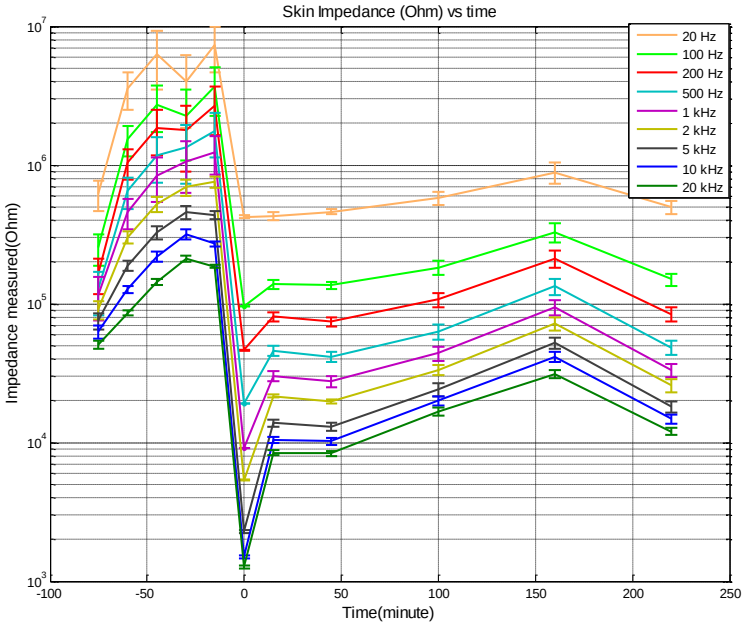


Figure F.11: Long term measurement with Cocoa on volunteer 3

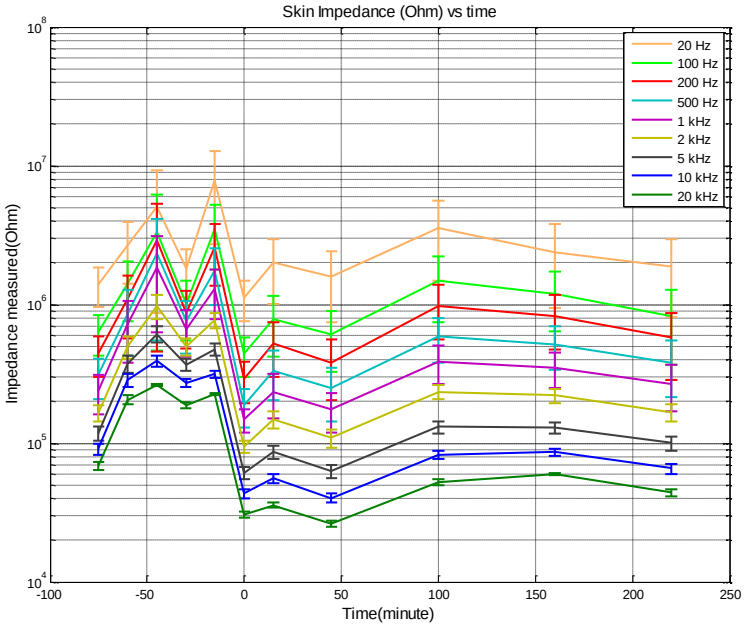


Figure F.12: Long term measurement with Bio-oil on volunteer 3

Volunteer 4 data:

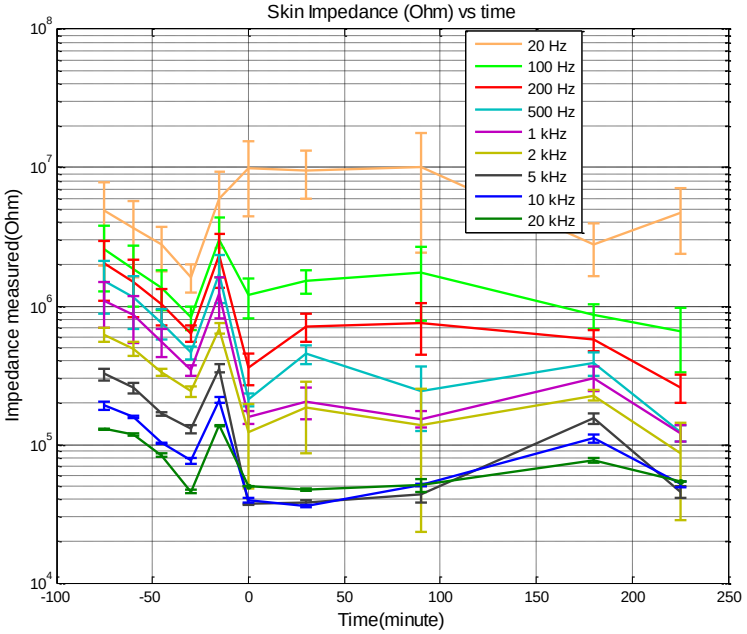


Figure F.13: Long term measurement with Bare skin on volunteer 4

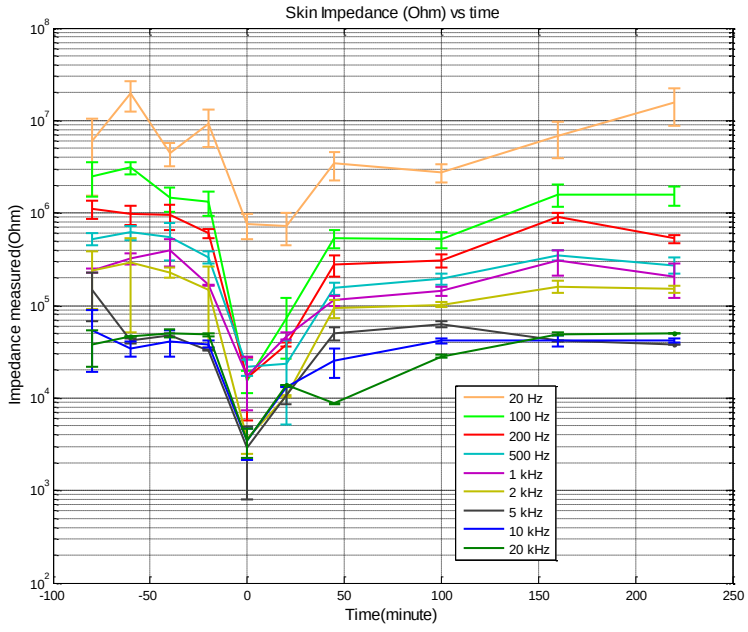


Figure F.14: Long term measurement with Nivea on volunteer 4

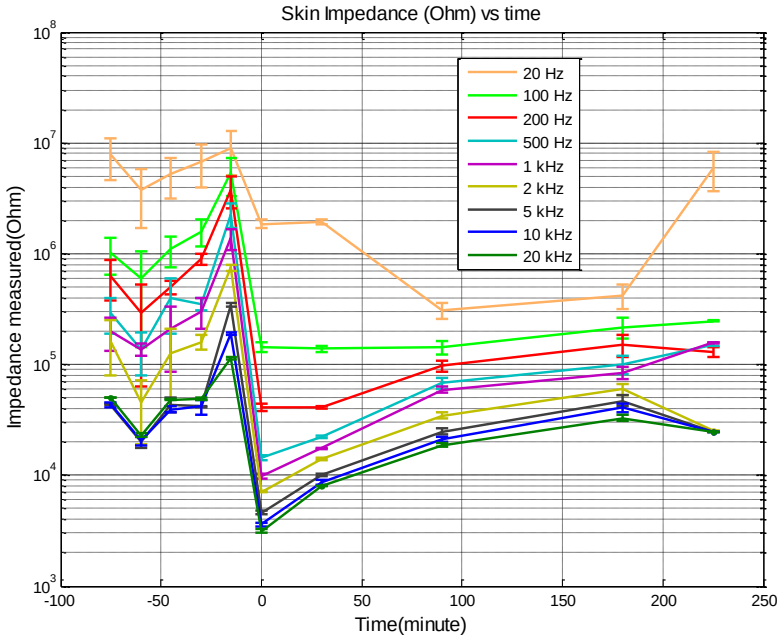


Figure F.15: Long term measurement with Cocoa on volunteer 4

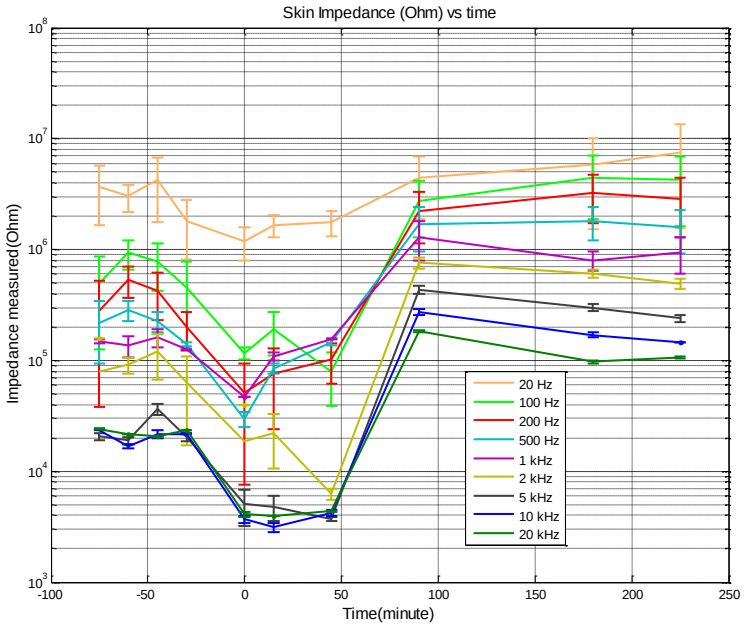


Figure F.16: Long term measurement with Bio-oil on volunteer 4

Volunteer 5 data:

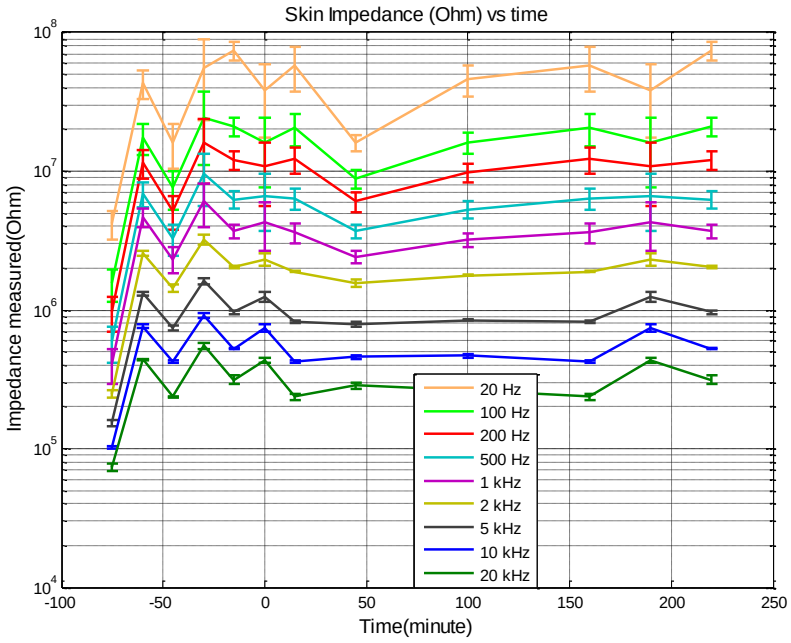


Figure F.17: Long term measurement with Bare skin on volunteer 5

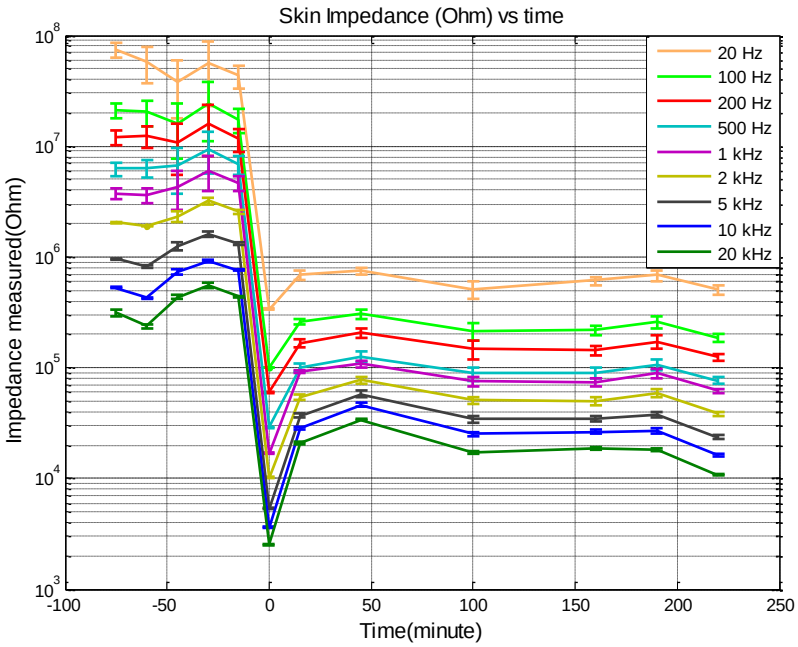


Figure F.18: Long term measurement with Nivea on volunteer 5

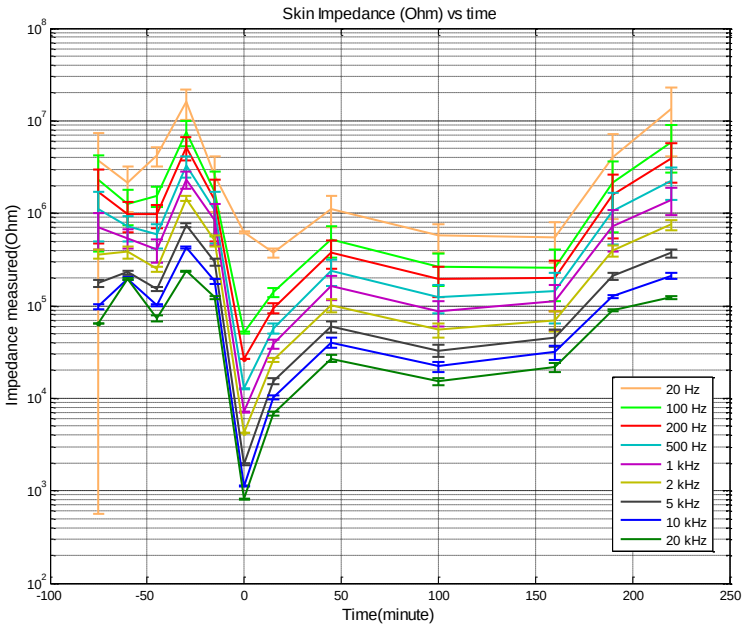


Figure F.19: Long term measurement with Cocoa on volunteer 5

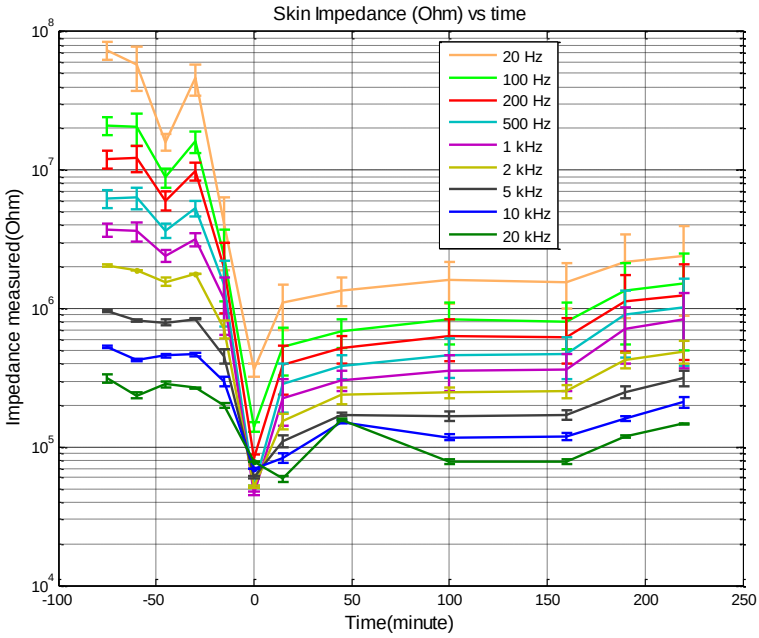


Figure F.20: Long term measurement with Bio-oil on volunteer 5

Appendix G: Details of skin moisturizers using in the experiments

1. Cocoa Butter Formula 250 ml: A year-round essential, this unique formula combines the ultra-moisturising properties of pure Cocoa Butter and Vitamin E with the added benefit of SPF 15 UVA/UVB sun protection. **Ingredients:** Active Ingredients: Octinoxate 7.5%, Octisalate 5.0%, Oxybenzone 4.0%, Avobenzone 1.0%, Inactive Ingredients: Water (Aqua), Theobroma Cacao (Cocoa) Extract, Glyceryl Stearate, Petrolatum, Mineral Oil (Paraffinium Liquidum), Fragrance (Parfum), Propylene Glycol, Cetyl Alcohol, Glycerin, Theobroma Cacao (Cocoa) Seed Butter Extract, PEG-8 Stearate, Dimethicone, Tocopheryl Acetate, Hydroxyethylcellulose, Behentrimonium Methosulfate, Butylene Glycol, Methylparaben, Propylparaben, Yellow 5 (CI19140), Orange 4 (CI15510). Palmer's Cocoa Butter Formula Lotion, http://uk.palmers.com/product/detail.php?ID=23&SUB=260&SID=1.

2. Olive Butter Formula 250ml: Palmer's Olive Butter Formula Lotion is enriched with the powerful antioxidant Vitamin E, which helps to maintain the skin's youthful appearance. The thick rich creamy formula leaves skin feeling instantly soft and soothed. With a deliciously light, fresh fragrance Palmer's Olive Butter Formula Lotion is ideal for those seeking a subtle Mediterranean scent. **Ingredients**: Water, Olea Europaea (Olive) Fruit Oil, Glyceryl Stearate, Propylene Glycol, Glycerin, Mineral Oil (Paraffinum Liquidum), Cetyl Alcohol, Dimethicone, Cocos Nucifera (Coconut) Oil, Behentrimonium Methosulfate, Cetearyl Alcohol, Toocpheryl Acetate, Hydroxyethylcellulose, PEG-8 Stearate, Fragrance (Parfum), Stearalkonium Chloride, Palmitoyl Oligopeptide, Rahnella/ Soy Protein Ferment, PEG-8 Stearate, Glyceryl Acrylate/ Acrylic Acid Copolymer, Phenoxyethanol, Methylisothiazolinone, Yellow 5 (CI 19140), Blue 1 (CI 42090), Red 4 (CI 14700).

Palmer's Olive Butter Formula Moisturizing Lotion, http://uk.palmers.com/product/detail.php?ID=88&SID=1.

3. Nivea Express Hydration 400ml: As skincare experts we believe that it is good to care for your skin everyday, so we have developed this sensationally light feeling formula containing Sea Minerals and blue lotus scent. It provides fast absorbing long-lasting moisture, gives a fresh feeling and scent all day long for 24 hour moisturisation. **Ingredients:** Aqua, Glycerin, Isopropyl Palmitate, Alcohol Denat., Glyceryl Glucoside, Glyceryl Stearate SE, C12-15 Alkyl Benzoate, Cetearyl Alcohol, Maris Sal, Sodium Carbomer, Sodium Cetearyl Sulfate, Dimethicone, Methylisothiazolinone, Phenoxyethanol, Linalool, Benzyl Alcohol, Limonene, Citronellol, Parfum. Nivea Express Hydration Body Lotion, http://shop.nivea.co.uk/express-hydration-body-lotion.html.

4. Bio-oil 200ml: Bio-Oil is a specialist skincare oil that helps improve the appearance of scars, stretch marks and uneven skin tone. It is also effective for aging and dehydrated skin. **Ingredients:** Calendula Officinalis Flower Extract (Calendula Oil)Lavandula Angustifolia Oil (Lavender Oil), Rosmarinus Officinalis Leaf Oil (Rosemary Oil), Anthemis Nobilis Flower Oil (Chamomile Oil), Retinyl Palmitate (Vitamin A), Tocopheryl Acetate (Vitamin E), Paraffinum Liquidum ,Triisononanoin, Cetearyl Ethylhexanoate , Isopropyl Myristate, Glycine Soja Oil, Helianthus Annuus Seed Oil, BHT Bisabolol , Alpha-Isomethyl Ionone ,Amyl Cinnamal ,Benzyl Salicylate ,Citronellol,Coumarin, Eugenol, Farnesol, Geraniol, Hydroxycitronellal, Hydroxyisohexyl 3-Cyclohexene Carboxaldehyde, Limonene, Linalool. Biio-Oil moisturizer, https://www.bio-oil.com/en/product/ingredients.

Appendix H: Group of volunteers for different experiments.

Group A : Instantaneous measurement N = 10				
Volunteer	**Age**	**Sex**	**Skin type**	**Skin alergy**
1	24	Male	Normal	None
2	26	Male	Normal	None
3	28	Male	Normal	None
4	34	Male	Normal	None
5	27	Male	Normal	None
6	23	Male	Normal	None
7	31	Male	Normal	None
8	24	Female	Normal	None
9	26	Female	Sensitive	None
10	42	Male	Normal	None

Group B: Short term measurement (N = 2)				
Volunteer	**Age**	**Sex**	**Skin type**	**Skin alergy**
1	24	Male	Normal	None
2	24	Female	Normal	None

Group C: Long term measurement N = 5				
Volunteer	**Age**	**Sex**	**Skin type**	**Skin alergy**
1	24	Male	Normal	None
2	26	Male	Normal	None
3	24	Female	Normal	None
4	31	Male	Normal	None
5	23	Male	Normal	None

Group D: Bare skin modelling N = 16				
Volunteer	**Age**	**Sex**	**Skin type**	**Skin alergy**
1	24	Male	Normal	None
2	26	Male	Normal	None
3	28	Male	Normal	None
4	34	Male	Normal	None
5	27	Male	Normal	None

6	23	Male	Normal	None
7	31	Male	Normal	None
8	24	Female	Normal	None
9	26	Female	Sensitive	None
10	42	Male	Normal	None
11	24	Female	Normal	None
12	26	Female	Normal	None
13	25	Female	Normal	None
14	29	Female	Normal	None
15	26	Female	Normal	None
16	25	Male	Normal	None

Link table			
Group A	**Group B**	**Group C**	**Group D**
1	1	1	1
2	2	2	2
3			3
4	3		4
5			5
6	4	5	6
7	5	4	7
8	6	3	8
9			9
10	7		10
			11
			12
			13
			14
			15
			16

Appendix I: Short term measurement with continuous contact of electrodes on skin using different moisturizers

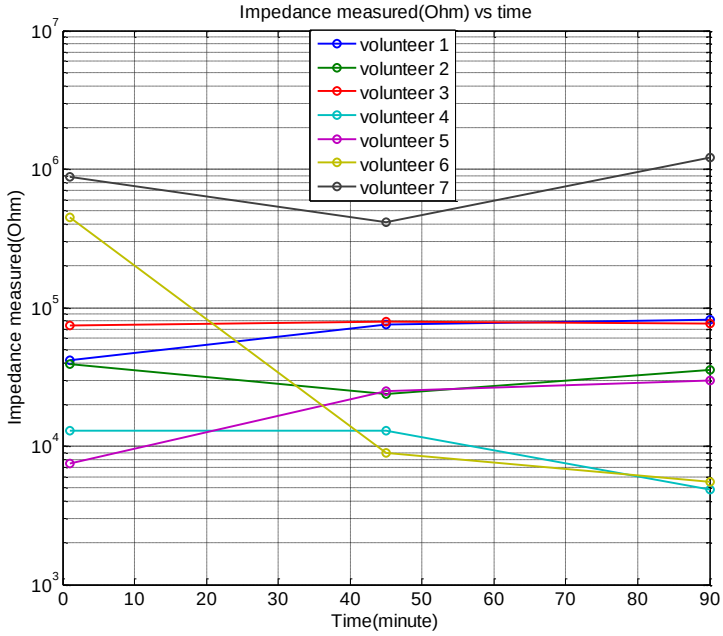


Figure I.1: Continuous contact short term measurement results at 1KHz of bare skin on 7 volunteers

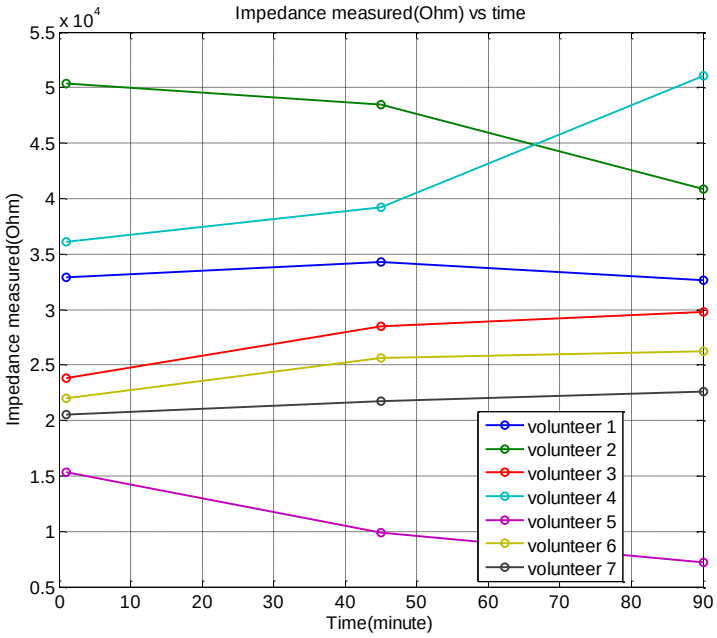


Figure I.2: Continuous contact short term measurement results at 1KHz using Cocoa Butter on 7 volunteers

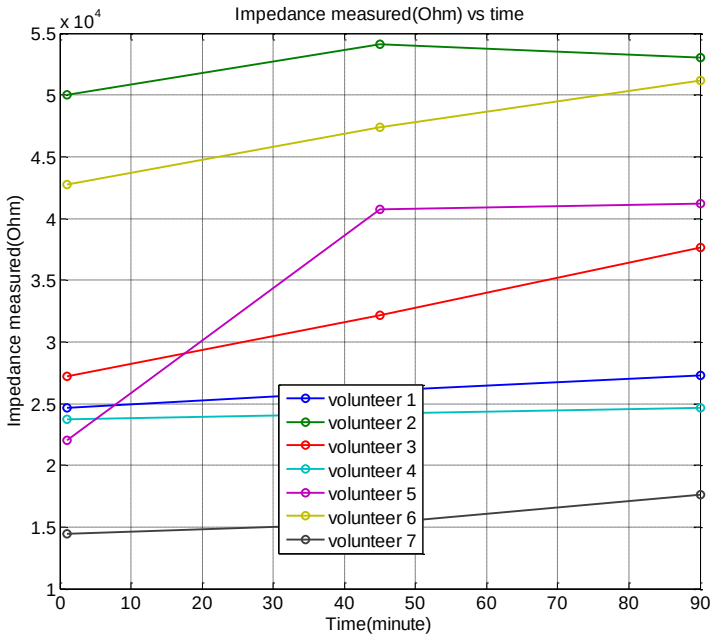


Figure I.3: Continuous contact short term measurement results at 1KHz using Olive Butter on 7 volunteers

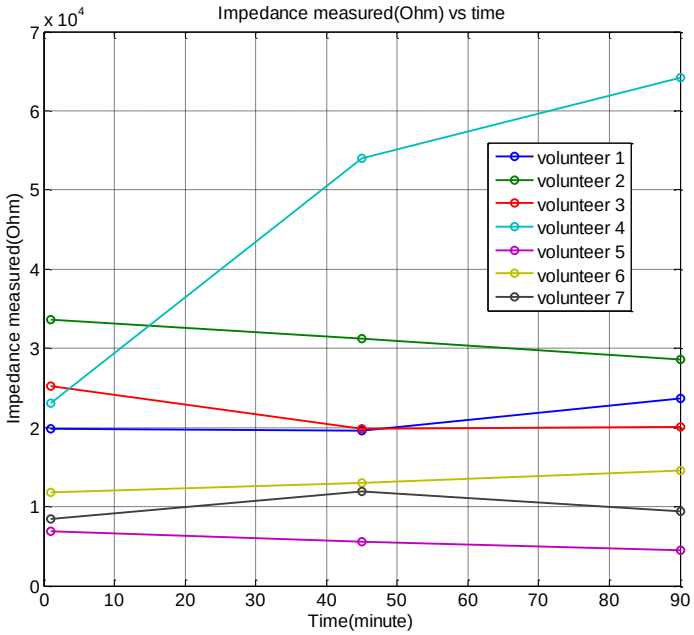


Figure I.4: Continuous contact short term measurement results at 1KHz using Nivea on 7 volunteers

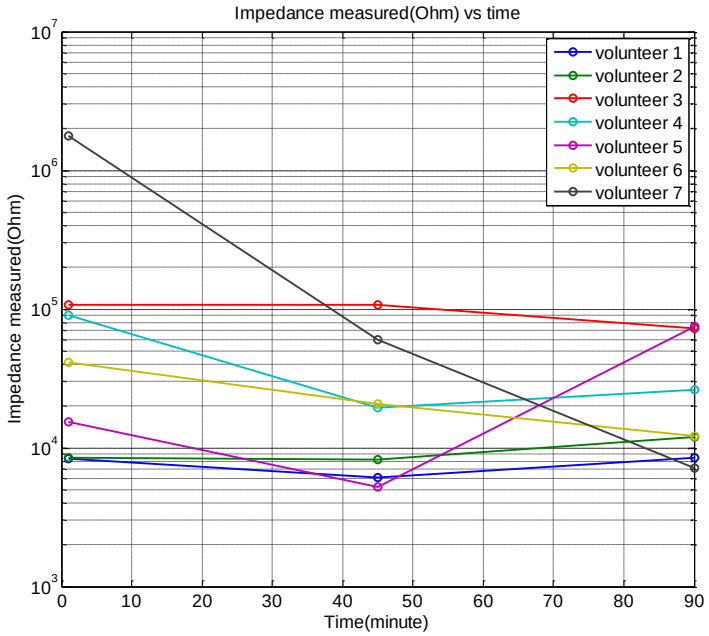


Figure I.5: Continuous contact short term measurement results at 1KHz using Bio-oil on 7 volunteers